

INVESTIGATION OF A CLOSED-LOOP THERMOSYPHON

by

MICHEL A. BERNIER

Department of Mechanical Engineering
McGill University
Montréal, Canada

A Thesis submitted to the Faculty of Graduate Studies and Research
in partial fulfillment of the requirements for the degree of
Doctor of Philosophy

© January, 1991

ABSTRACT

Complementary analytical, numerical, and experimental investigations of fluid flow and heat transfer in closed-loop thermosyphons with vertical heated and cooled sections are presented in this thesis.

A new model is proposed to couple the local results of numerical simulations performed in the heated and cooled section of a thermosyphon with a one-dimensional analytical model. The numerical simulations are based on a finite-volume numerical method which was formulated for the solution of laminar mixed-convection flows in vertical pipes with (or without) conjugate conduction in the pipe wall. Experimentally, a closed-loop thermosyphon was specially designed and constructed for this study. In the closed-loop, the power input is supplied by a semi-transparent gold-film which provides a uniform wall heat flux while enabling flow visualization.

The proposed model was successfully validated against experimental data obtained in this study. Results obtained with the proposed model also indicate that traditional one-dimensional models can significantly overpredict the average velocity in thermosyphons when strong mixed-convection effects are present in the heated and cooled sections. It is also shown that conduction in the pipe wall can significantly affect the velocity and temperature fields in mixed-convection flows. Photographs of flow visualization experiments in mixed-convection flows are also presented.

ACKNOWLEDGMENTS

I wish to express my gratitude to my supervisor, Professor B.R. Baliga, for suggesting this very interesting and challenging project and for the help he provided me throughout the course of this work.

This research was financially supported by the Natural Science and Engineering Research Council of Canada in the form of a Post-Graduate Scholarship and through individual operating and equipment grants awarded to Dr. Baliga. I also received a graduate fellowship award and a teaching assistantship from the Department of Mechanical Engineering at McGill University. In addition, during the course of this work, I have been lecturing in the Department of Mechanical Engineering at Ecole Polytechnique de Montréal. Furthermore, the McGill University Computing Center provided me with free computer time. The financial help provided by all these institutions is gratefully acknowledged.

I am indebted to several individuals for assistance during this research work. I wish to thank Messrs. Arthur Clément and Donald Borland of the Machine Tool Laboratory for their technical assistance in machining some of the critical parts of the experimental apparatus, Mr. Jack Kelly and his staff of the undergraduate laboratory, Messrs. George Dedic and George Tewfic of the DATAC laboratory, and Mr. Shaolin Shi for drawing some of the figures contained in this thesis. Thanks are also due to my friends and competent colleagues, Messrs. Neil Hookey, Christian Masson, Robert McBrien, Stuart Neill, Daniel Rousse, and John Saabas, for their valuable suggestions.

Last but not least, I would like to thank Ms. Réjeanne Burke and my family for their constant support throughout my years of studies. Without them, this work would have been much more difficult.

TABLE OF CONTENTS

	PAGE
ABSTRACT	i
SOMMAIRE	ii
ACKNOWLEDGEMENTS	iii
TABLE OF CONTENTS	v
LIST OF FIGURES	xiii
LIST OF TABLES	xviii
NOMENCLATURE	xix
 1. INTRODUCTION	 1
1.1 AIMS AND MOTIVATION OF THE THESIS	1
1.2 SYNOPSIS OF RELATED INVESTIGATIONS	5
1.2.1 Closed-Loop Thermosyphons	5
1.2.1.1 General papers on closed-loop thermosyphons	6
1.2.1.2 Toroidal thermosyphons vertical heat transfer passages	7
1.2.1.3 Closed-loop thermosyphons with vertical heat transfer passages	12
1.2.2 Conjugate mixed-convection flow and heat transfer in vertical pipes	15
1.2.2.1 Forced and free convection	16
1.2.2.2 Mixed-convection	17
1.2.2.3 Conjugate heat transfer in pipes	26
1.2.3 Previous Studies Related to the Gold-Film Technique.	29
1.2.4 Summary of the Literature Review	31
1.2.4.1 Closed-loop thermosyphons	31
1.2.4.2 Mixed-convection flow in vertical pipes	32

	PAGE
1.2.4.3 Conjugate heat transfer in vertical pipes ..	34
1.2.4.4 The thin gold-film technique	34
1.3 SURVEY OF THE THESIS	34
2. THEORETICAL CONSIDERATIONS	36
2.1 INTRODUCTION	36
2.2 TRADITIONAL ONE-DIMENSIONAL MODEL	39
2.2.1 Assumptions	39
2.2.2 Derivation of the General One-dimensional Momentum Equation	43
2.2.3 Determination of the Friction Factor, $f(s)$	45
2.2.4 Determination of the Temperature Distribution, $T(s)$.	46
2.2.4.1 Derivation of the energy equation	46
2.2.4.2 Thermal boundary conditions	46
2.2.4.3 Solution of the energy equation	47
2.2.5 Solution of the Traditional Model	49
2.2.6 Discussion	50
2.3 THE PROPOSED MODEL	54
2.3.1 Background	54
2.3.2 Two-Dimensional Governing Equations and Boundary Conditions in the Heated and Cooled Sections	56
2.3.2.1 Elliptic forms of the governing equations ..	56
2.3.2.2 Parabolic forms of the governing equations .	58
2.3.2.3 Boundary conditions	59
2.3.2.4 Energy equation and temperature distribution in regions outside the extended heated and cooled sections	61
2.3.2.5 Non-dimensionalization of the governing equations	62

2.3.3 Overview of the Solution of the Proposed model	63
2.4 CLOSING REMARKS	64
3. NUMERICAL SIMULATION OF MIXED-CONVECTION FLUID FLOW AND HEAT TRANSFER IN A VERTICAL PIPES	65
3.1 INTRODUCTION	65
3.2 GOVERNING EQUATIONS AND BOUNDARY CONDITIONS	67
3.2.1 Elliptic Forms of the Governing Equations	67
3.2.1.1 Assumptions	67
3.2.1.2 Governing equations	68
3.2.1.3 Boundary conditions	69
3.2.2 Parabolic Forms of the Governing Equations	70
3.2.2.1 Assumptions	70
3.2.2.2 Governing equations	71
3.2.2.3 Boundary conditions	72
3.2.3 Non-Dimensionalization of the Elliptic Equations ...	73
3.3 INTEGRAL FORM OF THE CONSERVATION EQUATIONS	76
3.4 DOMAIN DISCRETIZATION	77
3.4.1 Elliptic Case	77
3.4.2 Parabolic Case	78
3.5 DISCRETIZATION EQUATIONS	79
3.5.1 Elliptic case	79
3.5.1.1 General convection-diffusion equation	79
3.5.1.2 Fluid flow equation	82
3.5.1.3 Finishing touches	87
3.5.2 Parabolic case	88
3.5.2.1 Convection-diffusion equation	89
3.5.2.2 Fluid flow equation	90

3.6 SOLUTION OF THE NOMINALLY-LINEAR DECOUPLED SETS OF DISCRETIZATION EQUATIONS	93
3.7 COMPUTER CODE IMPLEMENTATION AND VALIDATION	95
3.7.1 Laminar Mixed-Convection in a Vertical Pipe Subjected to a Uniform Heat Flux Boundary Condition	96
3.7.2 Sudden Expansion in a Pipe	97
3.7.3 Mixed-Convection in a Vertical Pipe Subjected to a Constant Wall Temperature Boundary Condition	97
3.7.4 Conjugate Heat Transfer in Axisymmetric Pipe Flows .	98
3.8 CLOSING REMARKS	99
4. SOLUTION OF THE PROPOSED MODEL	100
4.1 INTRODUCTION	100
4.2 OVERVIEW OF THE PROPOSED MODEL	100
4.2.1 One-Dimensional Momentum Equation	100
4.2.2 Incorporation of Two-Dimensional numerical Inputs ..	101
4.3 SOLUTION OF THE PROPOSED COUPLED 1-D/2-D MODEL	104
4.3.1 Preliminary Considerations	104
4.3.2 Solution Methodology	106
4.3.2.1 Step 1: Choice of the starting conditions ..	106
4.3.2.2 Step 2: Numerical simulations in the extended heated and cooled sections	107
4.3.2.3 Step 3: Determination of correction ratios .	109
4.3.2.4 Step 4: Solution of Eq. 4.2 using the secant method	110
4.3.2.5 Step 5: Monitoring of the convergence of V from cycle to cycle	113
4.3.2.6 Step 6: Return to the next cycle	114
4.4 SPECIFIC MODEL FOR THE EXPERIMENTAL APPARATUS	114

	PAGE
4.5 CLOSING REMARKS	116
5. EXPERIMENTAL APPARATUS AND PROCEDURES	117
5.1 INTRODUCTION	117
5.2 EXPERIMENTAL CLOSED-LOOP THERMOSYPHON	118
5.2.1 Overall Design	118
5.2.2 Elements of the Closed-Loop Thermosyphon	119
5.3 DESIGN AND CONSTRUCTION OF THE GOLD-FILM SECTIONS	123
5.3.1 Introduction	123
5.3.2 Characteristics of the Gold-Film	124
5.3.3 Construction Procedures	125
5.3.3.1 Preliminary considerations	125
5.3.3.2 Cutting of the Plexiglass pipe	127
5.3.3.3 Cutting, painting, bending and gluing of the gold-film	128
5.3.3.4 Mating and sealing of the two half sections	132
5.3.3.5 Electrode construction	133
5.3.3.6 Gluing of thermocouples in heated sections no.1 and no.2	135
5.3.4 Determination of the Average Internal Diameter of the Gold-Film Sections	136
5.4 SUPPORTING EQUIPMENT AND INSTRUMENTATION	137
5.4.1 Temperature measurements	137
5.4.1.1 Inlet and outlet bulk temperature measurements, T_{in} and T_{out}	138
5.4.1.2 Ambient temperature measurements, T_a	140
5.4.1.3 Wall temperature measurements in heated section no.2	140
5.4.2 Average Velocity Measurements	141
5.4.3 Current, Voltage, Resistance and Power Measurements	143

	PAGE
5.4.4 Real-Time Data Acquisition System	144
5.5 SYNOPSIS OF THE EXPERIMENTAL PROCEDURE	146
5.6 FLOW VISUALIZATION INSTRUMENTATION AND PROCEDURE	148
5.6.1 Introduction	148
5.6.2 Dye Injection Instrumentation	149
5.6.3 Flow Visualization Procedures	151
5.7 CLOSING REMARKS	154
 6. RESULTS: CONJUGATE CONDUCTION AND LAMINAR MIXED-CONVECTIONN IN VERTICAL PIPES FOR UPWARD FLOW AND UNIFORM WALL HEAT FLUX	155
6.1 INTRODUCTION	155
6.2 PRELIMINARY CONSIDERATIONS	156
6.2.1 Introduction	156
6.2.2 Selection of Non-Dimensional Parameters	156
6.2.3 Grid Independence Checks	158
6.3 RESULTS AND DISCUSSION	161
6.3.1 Introduction	161
6.3.2 Normalized Interface Heat Flux, q_i/q	161
6.3.3 Distributions of Dimensionless Bulk and Wall Temperatures, θ_b and θ_w	164
6.3.4 Velocity Distribution, u/V	165
6.3.5 Fanning Friction Factor-Re Product, fRe	167
6.4 FLOW VISUALIZATION STUDIES ON MIXED-CONVECTION FLOWS	168
6.4.1 Introduction	168
6.4.2 Recirculation cells	169
6.4.2.1 Introduction	169
6.4.2.2 Observations	171
6.4.3 Laminar-Turbulent Transition	174

PAGE

6.4.3.1 Introduction	174
6.4.3.2 Observations	175
6.5 CLOSING REMARKS	177
7. RESULTS: THE PROPOSED MODEL	178
7.1 INTRODUCTION	178
7.2 PRELIMINARY CONSIDERATIONS	179
7.2.1 Presentation of the Two Geometries	179
7.2.2 Grid Independence Checks	181
7.2.3 Determination of the Lengths of the Post-Heated and Post-Cooled Sections	185
7.2.4 Axial Wall Conduction and Heat Losses in the Heated Section of Geometry #1	186
7.3 RESULTS AND DISCUSSION	187
7.3.1 Comparison Between Results of the Proposed Model and the Experimental Data	187
7.3.1.1 Introduction	187
7.3.1.2 Average velocity in the heated section	188
7.3.1.3 Axial wall temperature variations in the heated section	190
7.3.1.4 Problems encountered with the gold-film sections	191
7.3.1.5 Effects of variable properties	193
7.3.2 Results for geometry #2	195
7.3.2.1 Comparison between the results of the propo- sed model and those of Cases 1 and 2 of the traditional one-dimensional model	196
7.3.2.2 Effects of heat losses (gains) from thermosyphons	206
7.4 CLOSING REMARKS	210

	PAGE
8. CONCLUSION	211
8.1 REVIEW OF THE THESIS	211
8.2 SUMMARY OF RESULTS AND MAJOR CONTRIBUTIONS	213
8.3 PROPOSED EXTENSIONS OF THIS WORK	216
REFERENCES	218
APPENDICES	
A. THERMOPHYSICAL PROPERTIES OF WATER	226
B. SOLUTION OF THE TRADITIONAL MODEL	227
C. NON-DIMENSIONALIZATION OF THE GOVERNING EQUATIONS OF THE PROPOSED MODEL	231
D. DETERMINATION OF THE NODAL TEMPERATURES FOR A GIVEN V	236
E. DETERMINATION OF L_{eq} DUE TO FORM LOSSES IN THE 180° BENDS .	238
F. THERMOCOUPLE CALIBRATION PROCEDURE AND RESULTS	240
G. WALL TEMPERATURE CORRECTIONS	244
H. EXPERIMENTAL DETERMINATION OF THE OVERALL HEAT LOSS COEFFICIENT (U)	247
I. DESCRIPTION OF THE OPEN-LOOP CONFIGURATION	250
J. CALIBRATION OF THE AVERAGE VELOCITY MEASUREMENT	255
K. EXPERIMENTAL DATA	257
FIGURES	266
TABLES	309

LIST OF FIGURES

<u>FIGURE</u>	<u>TITLE</u>	<u>PAGE</u>
1.1	Schematic illustration of the closed-loop thermosyphon used in the present study.	266
1.2	Schematic illustration of a toroidal thermosyphon (Lavine, [1984]).	267
1.3	Schematic illustration of a closed-loop thermosyphon with vertical heat transfer passages (Huang, [1987]).	267
2.1	Geometric details and nomenclature used in the proposed model.	268
2.2	Elemental control volume used in the derivation of the general one-dimensional momentum equation.	269
2.3	Elemental control volume used in the derivation of the general one-dimensional energy equation.	269
2.4	Calculation domain and boundary conditions used in the two-dimensional numerical simulations of the proposed model: (a) the extended heated section; and (b) the extended cooled section.	270
3.1	Calculation domain and boundary conditions used in the study of conjugate conduction and mixed-convection in a vertical pipes. Case where the elliptic equations are used.	271
3.2	Calculation domain and boundary conditions used in the study of mixed-convection in vertical pipes. Case where the parabolic equations are used.	272
3.3	Typical grid distribution in the solid and in the fluid for the case where the elliptic equations are used. Also shown is a schematic of the control volume associated with node P along with its corresponding neighbouring nodes.	273
3.4	Staggered momentum control volumes for: (a) radial velocity; (b) axial velocity.	274
3.5	Schematic of the control volume associated with node P along with its corresponding neighbouring nodes. Case where the parabolic equations are used.	275
3.6	Distance between neighbouring nodes and control volume faces.	275

FIGURE	TITLE	PAGE
3.7	Mixed-convection in a vertical pipe subjected to uniform heat flux boundary condition. Results of a Nusselt number comparison among the experimental data of Hallman [1958] and the present numerical codes.	276
3.8	Sudden expansion in a pipe. $Re_d = 40$, $D/d = 2$, $L/D = 2$. The streamlines generated by the present elliptic code are indistinguishable from the ones obtained by Macagno and Hung [1967].	276
3.9	Mixed-convection in a vertical pipe subjected to constant wall temperature boundary condition. Results of a velocity profile comparison among the numerical data of Marner and McMillan [1970] and the present numerical codes.	277
3.10	Conjugate conduction in the wall for the case where the flow is assumed to be fully developed throughout the calculation domain. Comparison of the ratio of the interface heat flux over the applied heat flux obtained by Fithen and Anand [1988] and the present elliptic code.	277
5.1	Schematic of the experimental closed-loop thermosyphon.	278
5.2	Photograph of the experimental closed-loop thermosyphon showing, from left to right: a constant temperature bath; the closed-loop thermosyphon covered with black insulation; a computerized data acquisition system; and an instrument rack holding the power supply, two multimeters, and the data acquisition and control unit.	279
5.3	Elements of the closed-loop thermosyphon: (a) top circular 180° bend showing the flange-spacer-flange arrangement and the transparent expansion chamber; (b) bulk temperature measurement section; (c) cooled section.	280
5.4	Construction of the gold-film sections: (a) cutting in half of the Plexiglass pipe; (b) painting of the extremities of a gold-film strip; (c) pouring of the epoxy glue on the gold side of the film; (d) insertion of the gold-film into the Plexiglass pipe using a brass rod; (e) tightening of the top aluminum block; (f) final assembly showing the protruding excess width of the film.	281
5.5	Construction of the gold-film sections: (a) cutting of the excess width; (b) mating and sealing of two half sections; (c) junction between the copper electrode and the gold-film; (d) close-up view of the thermocouple wires glued inside the Plexiglass pipe; (e) completed assembly of a flow visualization section; (f) completed assembly of a heated section.	282

<u>FIGURE</u>	<u>TITLE</u>	<u>PAGE</u>
5.6	Cross-sectional view of one end of heated section no.2 showing the electrical connection between the copper electrode and the gold-film.	283
5.7	Cross-sectional view of heated section no.2 showing the location of the thermocouples inside the Plexiglass pipe and the various relevant materials and dimensions. Note: the figure is not to scale.	284
5.8	Geometric parameters and nomenclature used in the determination of the average velocity inside the closed-loop thermosyphon.	285
5.9	Schematic diagram of the electrical circuit.	285
5.10	Transfer of a computer screen image (also shown in Fig. 5.2) to a printer showing all the measurements taken in the thermosyphon.	286
5.11	Instrumentation for flow visualization studies: (a) dye injection tube; (b) pressurized dye reservoir; and (c) flow visualization section, with long-wave black lights on each side.	287
5.12	Schematic of the open-loop configuration.	288
6.1	Results of grid-independence checks for $Gr_q/Re = 50$, $Re = 10$, $Pe = 50$, $K = 500$, and $\Delta = 0.05$: (a) effects of axial grid refinements; (b) effects of radial grid refinements.	289
6.2	Axial variation of the ratio of the heat flux at the fluid-solid interface over the applied heat flux (q_i/q) for $Gr_q/Re^2 = 5000$, $Re = 1$, $Pe = 5$.	290
6.3	Axial variation of the ratio of the heat flux at the fluid-solid interface over the applied heat flux (q_i/q) for $Gr_q/Re^2 = 50$, $Re = 10$, $Pe = 50$.	291
6.4	Comparison of q_i/q for two different Re . $Gr_q = 5000$, $Pr = 5$, $\Delta = 0.05$, and $K = 50$.	292
6.5	Axial variation of θ_w and θ_b for $Gr_q = 5000$, $Re = 1$, $Pe = 5$.	293
6.6	Axial variation of θ_w and θ_b for $Gr_q = 5000$, $Re = 10$, $Pe = 5$.	294
6.7	Axial variation of θ_b for cases where axial wall conduction is important ($K = 50$, $\Delta = 0.05$) and where it is non-existent ($\Delta = 0$). $Gr_q = 5000$, $Re = 1$, $Pe = 5$.	295

<u>FIGURE</u>	<u>TITLE</u>	<u>PAGE</u>
6.8	Effects of axial conduction in the wall on the velocity profiles at various axial locations for two different Re. $Gr_q = 5000$, $Pr = 5$.	296
6.9	Axial variation of the fRe product for two different Re. $Gr_q = 5000$, $Pr = 5$.	297
6.10	Recirculation cell in a mixed-convection flow for $Re = 90$, $Gr_q = 0.33 \times 10^6$, $Pr = 5.6$: (a) flow visualization experiments; (b) corresponding numerical streamlines.	298
6.11	Numerically predicted streamlines over the full calculation domain for $Re = 90$, $Gr_q = 0.33 \times 10^6$, $Pr = 5.6$: <u>Note</u> : the scale of the radial direction is 10 times the scale of the axial direction.	299
6.12	Observation of laminar-turbulent transition occurring in a mixed-convection flow for $Re = 72$, $Gr_q = 0.7 \times 10^5$, $Pr = 6.0$. The "x" indicates the start of the transition and is located ≈ 46 cm ($L/D = 25.5$) from the inlet.	300
6.13	Observation of laminar-turbulent transition occurring for $Re = 48$, $Gr_q = 0.95 \times 10^5$, $Pr = 6.0$. Transition was noted at a distance of ≈ 50 cm ($L/D = 28$) from the inlet.	301
7.1	Grid independence checks performed for the conditions of experimental run #8. $Gr_m = 5078$, $Re_{ref} = 163.7$, $Pr = 6.8$, $St_m = 0.34 \times 10^{-3}$, and $\phi_\infty = 0.242$.	302
7.2	Effects of axial wall conduction and heat losses on the interface heat flux. Results of numerical simulations for $Gr_m = 5078$, $Re_{ref} = 163.7$, $Pr = 6.8$, $St_m = 0.34 \times 10^{-3}$, and $\phi_\infty = 0.242$.	303
7.3	Average velocity in the heated section of the closed-loop thermosyphon. Comparison between experimental data and the results of the proposed model.	303
7.4	Axial variation of wall temperatures in the heated section. Comparison between experimental data and the results of the proposed model.	304
7.5	Wall temperature measurements in the male and female half sections of the heated section.	305
7.6	Variation of V^* as a function of Gr_m for $St_m = 0$ and $Pr = 7.0$. Comparison between the traditional and proposed models for geometry #2.	305

<u>FIGURE</u>	<u>TITLE</u>	<u>PAGE</u>
7.7	Axial variation of fRe , T (area-weighted mean temperature), T_b (velocity-weighted bulk temperature) for $Gr_m = 300$, $St_m = 0$, and $Pr = 7.0$. Comparison between the traditional and proposed models for geometry #2.	306
7.8	Axial variation of fRe , T (area-weighted mean temperature), T_b (velocity-weighted bulk temperature) for $Gr_m = 3000$, $St_m = 0$, and $Pr = 7.0$. Comparison between the traditional and proposed models for geometry #2.	307
7.9	Axial variation of Nu in the cooled section of geometry #2. $St_m = 0$ and $Pr = 7.0$.	308
7.10	Effects of heat losses on V^* as a function of the non-dimensional ambient temperatures, ϕ_∞ , for three different values of St_m . $Gr_m = 500$ and $Pr = 7.0$.	308

LIST OF TABLES

<u>TABLE</u>	<u>TITLE</u>	<u>PAGE</u>
F.1	Calibration results for thermocouple T50. Ambient temperature during calibration was $25^{\circ}\text{C} \pm 2^{\circ}\text{C}$.	243
H.1	Results obtained during the experimental determination of U.	249
J.1	Results of the calibration of the average velocity measurement in the closed-loop thermosyphon.	256
5.1	Resistance measurements of the gold-film strips taken at various stages of construction.	309
5.2	Specifications of various instruments used in this study.	310
5.3	Results of the determination of the average internal diameter of the gold-film sections.	311
5.4	Axial location of each thermocouple inside heated section no.2.	312
7.1	Dimensional and non-dimensional lengths related to geometries #1 and #2.	313
7.2	Summary of the average velocities measured experimentally and determined using the proposed model.	314
7.3	Summary of average hot and cold side temperatures and average frictional resistance obtained with the traditional one-dimensional model and the proposed model for $\text{Gr}_m = 300$.	315
7.4	Summary of average hot and cold side temperatures and average frictional resistance obtained with the traditional one-dimensional model and the proposed model for $\text{Gr}_m = 3000$.	315
7.5	Summary of average hot and cold side temperatures and average frictional resistance obtained with the proposed model for three different heat losses (gains) conditions.	316

NOMENCLATURESYMBOLDESCRIPTION

a	coefficient of the discretization equation
A	cross-sectional area of the pipe
b	constant term in the discretization equation
C	dimensionless correction ratio
C_p	specific heat at constant pressure
ds, dV	differential surface and volume element
D	diffusion conductance
D	internal diameter of the pipe
f	Fanning friction factor
f_d	Darcy friction factor
F	mass flowrate across a control volume face
F	function defined in Eq. 4.10
Gr	Grashof number $\left[\frac{g\beta(T_w - T_o)r_i^3}{\nu^2} \right]$
Gr_q	Grashof number based on heat flux $\left[\frac{g\beta q D^4}{\nu^2 k_f} \right]$
Gr_m	modified Grashof number $\left[\frac{D^3 g \beta q}{\nu V_{ref} k_f} \right]$
g	acceleration due to gravity (9.8 m/s ²)
h	heat transfer coefficient
h_o	external heat transfer coefficient
h_m	head loss
i	enthalpy; also axial grid location

<u>SYMBOL</u>	<u>DESCRIPTION</u>
j	radial grid location
\tilde{J}	combined convection-diffusion flux
k_f	thermal conductivity of the fluid
k_s	thermal conductivity of the solid
K	solid to fluid thermal conductivity ratio (k_s/k_f)
K_L	pressure loss coefficient in curved pipes
L	total length of the closed-loop
L_c	length of the cooled section
L_d	length of the downstream section
L_{eq}	equivalent length of pipe
L_h	length of the heated section
L_u	length of the upstream section
L_x, L_y, L_z	various lengths related to Fig 5.8
$L_1 \dots L_{10}$	various lengths of the closed-loop (Fig. 2.1)
$L1$	number of grid points in the axial direction
m	mass
\dot{m}	mass flowrate
\tilde{n}	outward normal vector
Nu	Nusselt number (hD/k_f)
\overline{Nu}	average Nu in the cooled section $\left[\frac{\int_0^{L_c} Nu \, dL}{L_c} \right]$
P, p	pressure
P_w	power input
Pe	Péclet number ($Re \cdot Pr$)
Pr	Prandtl number ($\mu C_p/k_f$)
q	heat flux

<u>SYMBOL</u>	<u>DESCRIPTION</u>
q_i	heat flux at the fluid-solid interface
Q_L	heat losses around the loop
Q_x, Q_y, Q_z	heat losses over lengths L_x, L_y, L_z
Re	Reynolds number $(\rho V D / \mu)$
Re_{ref}	reference Reynolds number $\left[\frac{V_{ref} D}{\nu} \right]$
R	radius of the 180° bends
r	radial coordinate
r_i	internal radius of the pipe
r_x	internal radius of the gold-film sections
$r_2 \dots r_6$	various radii in the heated section (Fig 5.7)
s	axial coordinate around the closed-loop
S	source term
S_c	constant part of the linearized source term
S_p	coefficient of ϕ_p in the linearized source term
St_m	modified Stanton number $\left[\frac{U D}{\rho_m V_{ref} A C_p} \right]$
$s_1 \dots s_{11}$	given values of the axial coordinate, Fig. 2.1
T	temperature; also area-weighted mean cross-sectional temperature
T_a	ambient temperature
T_b	bulk temperature
T_{cold}, T_{hot}	average cold, hot side temperatures
T_{in}, T_{out}	inlet, outlet bulk temperatures
T_m	mean temperature in the closed-loop, $(T_3 + T_4)/2$
T_o	inlet temperature
T_w	wall temperature
\bar{T}_w	mean wall temperature in the cooled section

<u>SYMBOL</u>	<u>DESCRIPTION</u>
$T_1 \dots T_{11}$	nodal temperatures evaluated at $s_1 \dots s_{11}$
u, v	axial and radial velocity components
U	overall heat loss coefficient
V	average velocity; also voltage
V	volume of the control volume
\tilde{V}	velocity vector
V_g	guessed average velocity
V_{ref}	reference velocity $\left[\frac{P_w \beta g \Delta Z}{8 \pi \mu C_p L} \right]^{1/2}$
W	dimensionless parameter $\left[\frac{P_w}{2 \pi r_i L_h} \frac{\rho_m^2 \beta g (2 r_i)^4}{\mu^3 C_p} \right]$
X	parameter used in Eq. 2.14 $\left[\frac{h 2 \pi r_i}{\rho_m V A C_p} \right]$
Y	dimensionless geometric parameter $\left[\frac{\Delta Z L_h}{L_{eq} 2 r_i} \right]$
z	axial coordinate

GREEK SYMBOLS

α	underrelaxation parameter
β	volumetric thermal expansion coefficient
Γ	diffusion coefficient of ϕ
∂	partial derivative
∂A	surface of the control volume
δ	thickness of the pipe
δ_x	distance between grid points in the x-direction
Δ	pipe thickness to diameter ratio (δ/D)
Δs	length of an elemental control volume
Δz	axial dimension of the control volume

SYMBOLDESCRIPTION

Δz	height difference between the middle of the heated and cooled sections, Fig. 2.1
ϵ	length parameter $\left[\frac{L_b}{2} - \frac{1}{X} + \frac{e^{-XL_b}}{[1-e^{-XL_b}]} L_b \right]$
θ	angle of the control volume in the thermosyphon
θ	dimensionless temperature $\left[\frac{T-T_o}{qD/k_f} \right]$
μ	dynamic viscosity
ν	kinematic viscosity
ξ	parameter used in the z-momentum equation
ρ	density
ρ_m	mean density in the closed-loop
Σ	summation
τ_w	shear stress at the wall
ϕ	scalar dependent variable
ϕ	dimensionless temperature $\left[\frac{T - \bar{T}_w}{qD/k_f} \right]$
ϕ_∞	dimensionless ambient temperature $\left[\frac{T_a - \bar{T}_w}{qD/k_f} \right]$
ψ	dimensional streamfunction
Ω	modified heat loss coefficient $\left[\frac{U}{\rho_m VAC_p} \right]$
Ω	electrical resistance

SUBSCRIPTS

b	bulk
cs	refers to the cooled section
e, n, s, w	east, north, south, and west control volume faces

SYMBOLDESCRIPTION

E, N, S, W	pertains to main grid points E, N, S, and W
e	empty
f	full
hs	refers to the heated section
m	cycle number
n	iteration counter in the secant method
nb	neighbour points
o	evaluated at the inlet temperature
p	pertains to pressure
P	pertains to grid point P
x	refers to the gold-film sections
w	wall

SUPERSCRIPITS

fc	pertains to fully developed forced convection
u	refers to the u-velocity component
T	refers to temperature
*	non-dimensional value
#	guessed value
'	correction value
o	refers to the preceding axial station
—	averaged quantity

CHAPTER I

INTRODUCTION

1.1 AIMS AND MOTIVATION OF THE THESIS

This thesis presents complementary experimental, analytical and numerical investigations of a closed-loop thermosyphon with vertical heat transfer sections operating in a steady-state, laminar flow regime. A schematic illustration of this thermosyphon is given in Fig. 1.1.

Closed-loop thermosyphons are natural circulation loops in which fluid flow is induced by buoyancy forces. As an example, consider the geometry shown in Fig. 1.1, where the fluid inside the closed-loop is heated and cooled at certain locations. This creates a temperature difference and consequently a density gradient inside the loop which, in the presence of the gravitational force field, activates the buoyancy force that drives the fluid circulation. Under steady-state conditions, this buoyancy force is balanced by shear forces on the pipe wall.

Closed-loop thermosyphons have numerous practical engineering applications: Examples include buoyancy driven natural circulation loops in small nuclear reactors designed to heat buildings (Glen and Hilborn [1984]); internal combustion engines (Japikse [1973]); emergency cooling of nuclear reactor cores (Zvirin, [1981a]); and solar water heaters (Tabor [1984] and Mertol et al. [1981]). The main advantage provided by closed-loop thermosyphons is that they can transport heat from a source to a sink without a pump. The proper design of all these engineering

systems requires the modelling of closed-loop thermosyphons. For example, in the case of a nuclear reactor, it is crucial to be able to predict the flowrate and the core temperature distribution that would result in the event of emergency cooling using natural circulation. Another example can be envisioned by referring to Fig. 1.1 where one may want to know what heat-exchanger length and wall temperature are required to keep the absolute temperature inside the loop below a certain level.

Of particular interest to this study are the mixed-convection phenomena in the heated and cooled sections of the closed-loop thermosyphon. It may seem surprising to refer to a mixed-convection situation in a natural circulation loop, but this can be rationalized by looking at a packet of fluid as it travels around the loop (Welander [1967]). After completing one revolution, this packet of fluid appears to be "forced" into the heated (or cooled) sections. Since the overall flowrates are usually relatively small (small Reynolds number), buoyancy or free convection effects, caused by heating (or cooling) of the fluid in the heated (or cooled) section, are significant (relatively high Grashof number). Thus the conditions in the heated and cooled sections resemble a mixed-convection situation. In addition, because of the relatively small Péclet number, axial conduction in the fluid and in the pipes of these two sections may be important in certain cases, and the situation is then one of conjugate mixed-convection. Thus, the problem of interest is one of modelling the flow inside a closed-loop thermosyphon in which the vertical heat transfer sections experience conditions akin to conjugate mixed-convection.

Modelling of closed-loop thermosyphons has been studied in the past. So-called one-dimensional models have been used to predict the velocity and temperature distribution in a toroidal thermosyphon (Mertol [1980]) and in a closed-loop thermosyphon with vertical heat transfer sections (Huang and Zelaya [1988]). In the one-dimensional approach, velocities and temperatures are averaged over the cross-sectional area of the pipe and the flow is assumed to be fully developed inside the whole loop. The validity of this approach becomes questionable for cases where buoyancy effects significantly influence the velocity and temperature profiles inside the loop, like the ones considered in this study.

Accurate modelling of closed-loop thermosyphons can be accomplished by solving numerically the three-dimensional differential equations that govern the fluid flow and heat transfer in the entire closed-loop. Lavine [1984] performed such calculations for a toroidal thermosyphon. However, the computational costs involved in these complete three-dimensional simulations are very high.

In this study, a new approach, with accuracy, complexity, and computational costs in between that of the one-dimensional approach and the complete three-dimensional numerical simulations, is proposed to model closed-loop thermosyphons with vertical heat transfer sections. It involves iterative coupling between a one-dimensional model and local results of two-dimensional mixed-convection numerical simulations performed only in the heated and cooled sections of the loop.

The proposed model enables the determination of the average velocity inside the loop, and provides detailed temperature and velocity

profiles in the heat transfer passages of the loop. The two-dimensional numerical simulations of conjugate mixed-convection flow in the heated and cooled sections are carried out using a finite-volume based numerical method.

In order to validate the proposed coupling procedure and the numerical simulations, a complementary experimental investigation was undertaken. An experimental facility was designed and built for this study. One of the novel features of this apparatus is the utilization of a thin semi-transparent gold-film as an electrical heating element in the heated section. This provides a nearly uniform heat flux boundary condition while enabling flow visualization in the heated section.

To summarize, the goals of this thesis are:

- (i) Formulate, implement and test a one-dimensional model of fluid flow and heat transfer in a closed-loop thermosyphon similar to that shown in Fig. 1.1.
- (ii) Formulate, implement, and test a finite-volume based numerical method to simulate two-dimensional conjugate mixed-convection in the heated and cooled sections of the closed-loop thermosyphon.
- (iii) Formulate a method that couples the results of two-dimensional mixed-convection numerical simulations, performed in the heated and cooled sections, with a one-dimensional model in order to predict fluid flow and heat transfer in the closed-loop

thermosyphons, accurately and affordably.

- (iv) Design and construct an experimental apparatus to ascertain the validity of the proposed method to simulate closed-loop thermosyphons. This experimental facility was designed to provide average velocity data, and flow visualization data and local wall temperatures in the heated section.

1.2 SYNOPSIS OF RELATED INVESTIGATIONS

The purpose of this literature review is to present the salient features of previous studies in the areas of closed-loop thermosyphons and conjugate mixed-convection flows. The review also indicates the drawbacks of certain studies and the gaps found in the literature, which provided some of the motivation for the present work.

The review is organized in three categories, which themselves have sub-sections. First, studies of fluid flow and heat transfer in closed-loop thermosyphons are examined. Then, the area of conjugate mixed-convection in pipes is reviewed. Following this, a brief review of the papers pertaining to the thin gold-film technique is presented.

1.2.1 Closed-Loop Thermosyphons

This section is divided into three sub-sections. General papers related to closed-loop thermosyphons are treated first. Then, the review concentrates on two types of closed-loop thermosyphon geometries: Toroidal thermosyphons and closed-loop thermosyphons with vertical heat

transfer passages.

1.2.1.1 General papers on closed-loop thermosyphons

Literature surveys on closed-loop thermosyphons have been published by Zvirin [1981a], Lavine [1984], and Mertol and Greif [1985]. More recently, a thorough review of the subject was done by Greif [1988], and included in a special issue of the ASME Journal of Heat Transfer, commemorating the 50th anniversary of the heat transfer division of the ASME. The inclusion of this "state-of-the-art" review of closed-loop thermosyphons in this issue of the ASME Journal of Heat Transfer certainly reflects the past, present, and future importance of these heat transfer devices.

In the following paragraphs and sections, when reference is made to the stability of natural circulation loops, it should not be confused with the subject of laminar-turbulent transition in pipes. A stable natural circulation loop is one which can sustain a steady, unidirectional flowrate. Even though the subject of closed-loop thermosyphon stability is not specifically addressed in this study, it is important to the understanding of closed-loop thermosyphons and to the justification of certain assumptions in subsequent Chapters. It is, therefore, included in this review.

Japikse [1973] presented an in-depth review of the literature on all types of thermosyphons (open, closed and closed-loop). In his review, however, very little is mentioned on closed-loop thermosyphons, reflecting, as noted by Japikse, the lack of attention given to this area up to

1973. Furthermore, in this review, Japikse [1973] failed to report on the pioneering work of Keller [1966] and Welander [1967] on closed-loop thermosyphon stability.

Keller [1966] studied the stability of a closed-loop thermosyphon geometry, similar to the one presented in Fig. 1.1, operating with a point heat source at the top and a point heat sink at the bottom. He used a one-dimensional model and showed that under certain conditions the loop experiences periodic flowrate oscillations. Welander [1967] pursued the work of Keller [1966] and showed, by doing a transient numerical simulation, that such a loop can experience three modes of oscillations: a stable mode where the flowrate is constant; a neutrally stable case where the flowrate oscillates around a mean value that does not change direction; and an unstable case where the flowrate oscillates with time and may change direction aperiodically.

1.2.1.2 Toroidal thermosyphons

Toroidal closed-loop thermosyphons (Fig. 1.2) have been studied extensively, as they are amenable to relatively simple analytical and numerical treatments. The most relevant papers on toroidal thermosyphons will now be examined.

Creveling et al. [1975] studied experimentally and analytically the flow inside a toroidal thermosyphon operating with a constant heat flux condition in the bottom half and a constant wall temperature condition in the top half. Experimentally, they showed the existence of the three stability modes reported by Welander [1967]. They also found that the

friction factor and the Nusselt number in the cooled section were higher than the standard fully developed forced convection values.

Damerell [1977] and Damerell and Schoenhals [1979] extended the work of Creveling et al. [1975]. They used the same geometry, but with various tilt angles of the heated section. Their work reveals that, for a fixed heat flux and a constant wall temperature cooled section, maximum flowrate is achieved when the heated section is directly below the cooled section, $\alpha = 0^\circ$ in Fig. 1.2. As the angle α is increased, all other parameters remaining the same, the flowrate diminishes towards zero when $\alpha = 180^\circ$. For $\alpha > 60^\circ$, the agreement between their one-dimensional model, which assumes that $Nu = 3.66$ in the cooled section and that $f = 16/Re$ throughout the loop, and their experimental observations is very good. For small tilt angles ($\alpha < 60^\circ$), their model predictions overestimate the experimentally observed flowrates. This is probably due, as they mentioned, to the presence of streamwise flow reversal in the entrance of the cooled section, which could not be accounted for in their one-dimensional model.

Damerell [1977] and Damerell and Schoenhals [1979] also produced an experimental stability map which shows, as was noticed earlier by Creveling et al. [1975], that for small tilt angles ($\alpha \approx 0^\circ$), stable flows are confined to a certain range of heat fluxes: stable at low power levels, unstable at intermediate power levels, and stable again at high power levels. For tilt angles greater than $\alpha \approx 6^\circ$, the flow was always stable, irrespective of the magnitude of the heat flux. Their one-dimensional model also showed that, for a given set of operating conditions, multiple steady-state solutions are possible. Experimentally,

they were unable to reproduce multiple solutions except for the simple case of $\alpha = 0^\circ$.

It was not until the work of Acosta et al. [1987] that the multiplicity of steady-state solutions was experimentally confirmed. Acosta et al. [1987] used a tilted square loop where the heated and cooled sections were in the bottom and top leg, respectively. They observed that, over a certain range of power input and tilt angles, the flow could be either in the clockwise or counterclockwise direction.

Greif et al. [1979], Mertol [1980], and Mertol et al. [1983] carried out transient and stability analyses of the toroidal thermosyphon shown in Fig. 1.2 (with $\alpha = 0^\circ$) for various cooled section configurations: constant wall temperature heat-exchanger; parallel and counterflow heat exchanger. They used a one-dimensional approach, and solved the transient, coupled, momentum and energy equations using a finite difference method. They also carried out stability calculations by imposing small perturbations on the steady-state values of velocities. Greif et al. [1979] report good agreement between the results produced by this technique and those obtained in the linearized stability analysis of Creveling et al. [1975].

Axial heat conduction in the fluid of a toroidal thermosyphon was examined by Mertol [1980]. It is concluded that for small values of the Péclet number, axial conduction in the fluid tends to make the temperature in the thermosyphon more uniform, therefore decreasing temperature gradients. This results in less buoyancy and smaller velocities in the thermosyphon, which also yields more stable systems.

Mertol et al. [1982] carried the one-dimensional analysis of toroidal thermosyphons a step further by studying the two-dimensional aspect of the flow. Their model allowed radial and axial variations of temperature and radial velocity variations. When the governing equations are non-dimensionalized, the Graetz number emerges as a parameter. The friction factor (f) and the Nusselt number (Nu) do not need to be given a priori, but are now outputs of the solution. It was shown that both f and Nu reach their fully developed values when the Graetz number is small. They compared the flowrates, obtained with their two-dimensional numerical simulations, with the experimental results of Creveling et al. [1975]. The agreement is shown to be very good, and better than that obtained with their previous one-dimensional model (Mertol [1980]). Their model fails, however, to predict the streamwise flow reversals observed experimentally by Damerell and Schoenhals [1979].

Lavine [1984, 1986, 1987] performed three-dimensional, steady-state, numerical simulations on the same toroidal thermosyphon for two Grashof numbers (Gr) and three tilt angles. Her results show that the flow is indeed three-dimensional, with streamwise flow reversal in some cases. This corroborates the qualitative observations of Damerrell and Schoenhals [1979] and the quantitative experimental observations of Stern et al. [1988]. Secondary cross-stream motions, which are expected to be present because of pipe curvature, were also obtained. It was found that flow reversals become stronger as Gr is augmented and weaker as the tilt angle is increased. The peripherally averaged quantities, fRe and Nu , are generally greater than the values obtained from correlations for fully developed flows.

Lavine [1984] compared her three-dimensional results to the one-dimensional analysis of Greif et al. [1979] and to the two-dimensional study of Mertol et al. [1982]. In the worst case, the one-dimensional and two-dimensional models overpredict the axial velocity by 47 % and 31 %, respectively. These three-dimensional numerical calculations converged slowly and required CPU times of the order of 1 to 2 days on an IBM 4341 computer, even though the Grashof numbers used were relatively small. For high Gr, finer grids are required due to steeper gradients. For these cases, converged, grid-independent solutions could not be obtained by Lavine [1984]. Unfortunately, this precluded any comparison with the experimental data of Damerell and Schoenhals [1979] and Stern [1988], which were performed at relatively high Gr.

Stern et al. [1988] performed laser-Doppler velocity measurements at the entrance and exit of the heated section of a toroidal loop. These measurements confirmed quantitatively the three-dimensionality of the flow and established a valuable experimental data base. Flow visualization studies also revealed the presence of streamwise flow reversals.

Ronen and Zvirin [1985] extended the analysis of Mertol et al. [1982] by studying the flow inside toroidal thermosyphons for higher values of the Graetz number. They concluded along the same vein as Mertol et al. [1982], re-emphasizing that Nu and fRe approach their fully developed values when the Graetz number is small.

Sen et al. [1985a] studied toroidal thermosyphons with known heat fluxes. The originality of their work lies in the treatment of the time-dependent problem where they reduce the one-dimensional momentum

and energy equations to an infinite set of ordinary differential equations using the 2π -periodicity of the temperature. It is shown that stable, periodic or even chaotic solutions can be obtained.

Sen et al. [1985b] looked at the steady-state velocity of an inclined toroidal thermosyphon with constant flux heating and constant-temperature cooling. They showed that the point of maximum velocity did not necessarily occur for a zero inclination angle ($\alpha = 0^\circ$ in Fig. 1.2), as was previously concluded by Damerell and Schoenhals [1979].

1.2.1.3 Closed-Loop thermosyphons with vertical heat transfer passages

This geometry consists of heated and cooled sections oriented vertically and joined together by a piping system so as to form a closed-loop (Fig. 1.3). Studies on thermosyphon solar water heaters are also reviewed in this section.

Zvirin et al. [1978] examined the stability of natural circulation solar water heaters by perturbing the steady-state results. It was found that loop instabilities could occur for cases of high energy utilization.

Mertol et al. [1981] used a one-dimensional analysis to study the performance of thermosyphon solar water heaters as a function of various parameters. One of their conclusion is that a variation in tank (which is the cooled section in this case) elevation relative to the solar collector (which is the heated section) has no significant effect on the

daily performance of the solar system, as long as the bottom of the tank is higher than the top of the solar collector. When the bottom of the tank is lower than the top of the collector, the daily output of the solar system is reduced since reverse circulation occurs at night. This work represent a classic example of the usefulness of modelling closed-loop thermosyphons.

Zvirin et al. [1981a] used the concept of form losses in their one-dimensional analysis. Their particular interest was in modelling the emergency cooling of nuclear reactor cores. A comparison of data obtained from their one-dimensional model, an experiment on a small scale nuclear reactor, and the operation of an actual nuclear power plant reveal that the agreement among the three sets of data was within 30 %. They speculated that the difference was probably due to experimentally observed three dimensional effects which could not be handled by their one-dimensional analysis.

Hallinan [1983] and Hallinan and Viskanta [1985] conducted a series of experiments on the heat transfer from a vertical tube bundle in a natural circulation loop. They report that the flow remained stable in all cases over a relatively broad range of conditions. They also suggest an empirical correlation, which could be useful in the design of tube bundles in nuclear reactors, to relate the mean Nusselt number to the governing non-dimensional parameters. They experimentally observed a transition from laminar to turbulent flow for Reynolds number (based on hydraulic diameter of the flow passage and on velocity) as low as 340.

Huang [1987a] studied the behavior of a rectangular closed-loop thermosyphon with vertical heat transfer passages. This loop is presented in Fig. 1.3. He obtained empirical mixed-convection correlations for vertically downward cooling flow in a natural circulation loop for various values of hydraulic resistance. Experimentally, the hydraulic resistance was adjusted by using a gate valve located within the loop. He found that for a given flowrate (or Re) the dimensionless group $Nu \cdot Gr / Pr$ increases with an increase in hydraulic resistance. This can be explained by the fact that when the hydraulic resistance is increased it takes more power and, consequently, more cooling to have the same flowrate in the loop. Therefore, the dimensionless group $Nu \cdot Gr / Pr$, which is proportional to the cooling rate will have to increase. His findings reaffirm the conclusion of Holman and Boggs [1960] who performed a similar experiment with Freon 12.

In another article related to the same geometry, Huang and Zelaya [1988] presented analytical and experimental results for various values of the hydraulic resistance. Their one-dimensional model assumed constant flux in the heated and cooled sections and negligible heat losses from the rest of the loop. Analytically, form losses in the gate valve were accounted for by using an equivalent length of pipe. The results obtained with their one-dimensional analysis agree very well with their experiments. This seems to indicate that one-dimensional modelling of closed-loop thermosyphons with vertical heat transfer sections, using the just-mentioned assumptions, can be accurate. Analytical and experimental transient results are also presented. It is shown that, starting from rest, the flow oscillates, much like a damped spring-mass system, to finally reach its steady-state value.

Huang and Zelaya [1987b] also carried out a stability analysis of their loop. They discovered that the loop tends to be unstable for high power input, low friction and high relative height between the cooled section and the heater.

Flow in a rectangular closed-loop thermosyphon with two vertical heat transfer passages, maintained at constant wall temperatures, was also examined experimentally and analytically by Durig and Shadday [1986]. Their one-dimensional model used averaged Nusselt numbers and friction factors obtained from a separate two-dimensional numerical simulation of mixed-convection flow in vertical tubes performed by Shadday [1986]. When compared with their experimental results, they show that the use of these two-dimensional inputs into their one-dimensional model, instead of the fully developed forced convection flow correlations, considerably improves the mass flowrate prediction in the closed-loop. However, since the numerical simulations are not implicitly coupled to the solution to the one-dimensional model, these averaged values have to be known beforehand for a broad range of conditions.

1.2.2 Conjugate Mixed-Convection Flow and Heat Transfer in Vertical Pipes

The following survey of the literature is primarily concerned with conjugate laminar mixed-convection flow and heat transfer inside heated vertical pipes.

Since turbulent flows are not specifically addressed in this study,

the survey is limited to laminar cases. However, the laminar to turbulent transition in mixed-convection flows is reviewed as it pertains to some of the theoretical developments discussed in Chapters 2 and 3 and to some experimental observations obtained during the course of this investigation.

This section is divided into three sub-sections: First, the limiting cases of mixed-convection (forced and free convection) are briefly examined; then, the literature on mixed-convection is surveyed; this is followed by a review of the effects of wall axial heat conduction.

1.2.2.1 Forced and free convection

The forced and free convection regimes can be regarded as particular cases of the more general mixed-convection regime. The subject of pure laminar forced convection flow in ducts, has been treated very thoroughly by Shah and London [1978] in their classic monograph and in a recent article by Shah [1983]. These references contain benchmark results for a number of cases, ranging from fully developed flow to simultaneously developing flow in pipes. Some of these results were used to test the numerical codes developed during the course of the present study. Also worth mentioning is the recent work of Kakaç and Yener [1983] on laminar forced convection in the entrance region of ducts, where both hydrodynamic and thermal boundary layers develop simultaneously.

A few researchers have investigated pure free convection flow in vertical heated passages. Dyer [1975] studied the development of lami-

nar natural convection flow in a vertical duct open at both ends and heated by a constant heat flux. Karki and Patankar [1984] solve the natural convection problem in a vertical shrouded array. Dalbert [1981] investigated natural convection in a vertical channel with symmetric and asymmetric heating. All of these studies basically used the same solution technique. It consists of specifying an inlet velocity, rather than the pipe length, to start the numerical calculations. Then, the momentum and energy equations are solved numerically, using a parabolic marching-type procedure, until the exit pressure is equal to the ambient pressure. This, in turn, determines the length of the pipe for a given inlet velocity.

1.2.2.2 Mixed-convection

The subject of mixed-convection in vertical pipes has been reviewed by a number of authors: Metias and Eckert [1964]; Kays and Perkins [1973]; and, more recently, by Jackson et al. [1989]. It is worth noting that this last reference contains an excellent review of the turbulent mixed-convection regime.

Hallman [1958] studied mixed-convection water flow in a vertical tube heated with a constant heat flux. Analytically, he solved the case of fully developed flow and heat transfer. Experimental data on local Nusselt numbers in the developing region as well as in the fully developed region are also presented. In the fully developed region, the experimentally determined Nu are shown to agree well with his analytical solution. He also shows that the Nu increases and the thermal entrance length diminishes as free convection effects become more important.

In some experimental runs, Hallman [1958] observed a transition from a steady laminar flow to a random eddying flow. This phenomenon was observed for Re as low as 150. The observations of such transitions were based on wall temperature fluctuations since his heating section was made of an opaque tube, thus precluding any flow visualization. As mentioned by Hallman, the accuracy of the transition location was somewhat limited by the fact that thermocouples were located 5 cm apart, and by the damping of wall temperature fluctuations, caused by a high heat capacity Inconel tube.

Hanratty et al. [1958] examined the effect of natural convection on the velocity field for an upward flow in a vertical and transparent tube subjected to a constant wall temperature. By injecting a dye, they were able to detect flow reversals and unstable turbulent flows downstream of these reversals. They also obtained analytically the velocity and temperature profiles in the fully developed region for the uniform heat flux boundary condition. The shape of these profiles is a function of the Gr/Re parameter. As the Gr/Re parameter is increased, the velocity profile at the pipe center is flattened until a value of $Gr/Re = 22$. For larger values of Gr/Re the velocity profile develops a dimple at the pipe center line and the maximum velocity no longer occurs at the tube center.

Scheele et al. [1960] extended the work of Hanratty et al. [1958]. They undertook experimental observations for the constant heat flux case. Their heated section was opaque which prevented any dye filament observations in this section. Observations of transition to turbulence

at the exit of the heated section are in good agreement with the ones of Hallman [1958]. In some cases, transitional flows were noted for Re as low as 100. They also postulated that the velocity profile must be distorted at least to a condition of flatness, $Gr/Re = 22$, just before a point of inflexion is established in the velocity profile, in order for transition to occur. However, they were unable to verify their hypothesis experimentally because for $Gr/Re = 22$, their heating section was not long enough for the velocity profile to reach a flatness condition at the center of the pipe.

Scheele and Hanratty [1962] alleviated this deficiency in the earlier work of Scheele et al. [1960], by using a longer heated section. Transitional flows were detected by measuring the abnormal, but periodic, temperature fluctuations recorded by a thermocouple inserted in the center of the pipe at the outlet of the heated section. They confirmed previous hypotheses by observing that the lowest Gr/Re ratio at which transition was detected corresponds very closely to the Gr/Re ratio calculated by Hanratty et al. [1958], for which the velocity profiles had an inflexion point. Although the flow was unstable at low values of Re , it did not exhibit the characteristic random structure of turbulent flows until the Re was close to 2300.

In a paper related to the same geometry, Scheele and Hanratty [1963] report on experimentally determined Nusselt numbers for fully developed flows. It is shown that for the same Reynolds number the values of the Nusselt number are significantly increased when free convection effects are superimposed on forced convection.

Although the work of Scheele and his colleagues, described in the previous paragraphs, is quite valuable, it pertains mainly to fully developed mixed-convection flow of water. Scheele and Greene [1966] recognized these two limiting factors in a further study. They used shorter pipes and focussed on non-fully developed flows. The experimentally observed values of Gr/Re at which unstable flows occurred were greater than that for fully developed conditions. This is probably because a greater value of Gr/Re is needed for the velocity profile to develop a point of inflexion in such a short distance. Unfortunately, solutions to the developing velocity profile were not available at that time, so that no conclusive evidence could be obtained on the existence of points of inflexion leading to unstable flows.

Kennedy and Somers [1962] reported the presence of "non-laminar" (but not turbulent) mixed-convection flow in a vertically heated circular tube for $Re < 3000$. The existence of these non-laminar flows was inferred by a sudden decrease in the wall temperature and by relatively large temperature fluctuations in the fluid. For the same Reynolds number, this non-laminar condition increased the Nusselt number by as much as 30 % above the laminar value.

Metias and Eckert [1964], using the literature review of Metias [1963], proposed limits of applicability for the different regimes of heat transfer in vertical pipes, ranging from laminar free convection to turbulent forced convection, including the mixed-convection laminar region. Lawrence and Chato [1966] investigated, numerically and experimentally, the entrance effects on an upward flow of fluid in a vertical tube subjected to a constant heat flux condition. Their heated section

consisted of six electrically conducting tubes separated by five transparent Plexiglass couplings. The existence of transitional flows was inferred by temperature fluctuations occurring within the fluid, measured by inserting a temperature probe at the coupling section. They concluded that the axial distance from the entrance at which transition takes place depends on the heat flux and fluid flowrate. By comparing their experimental observations of transition to the velocity field obtained numerically they found that transition always occurred after the velocity profile had developed an inflexion point, thus, confirming the assertion of Scheele and Greene [1966]. Numerically, they used the boundary-layer type conservation equations and accounted for viscosity and density variations. Their numerical results agree very well with those of their experiments, except near the tube entrance where they suspected that the boundary-layer approximations may be at fault.

Marner and McMillan [1970] solved numerically the case of developing laminar mixed-convection in a vertical tube subjected to a constant wall temperature. Their results show that local Nusselt numbers are higher than the ones obtained using a Graetz-type solution. Furthermore, the axial variation of Nu was observed to be non-monotonic with a slight increase near the point of maximum velocity profile distortion from the laminar fully developed Poiseuille shape.

Collins [1971] solved numerically the governing equations for a number of mixed-convection flows for both constant heat flux and constant wall temperature boundary conditions. He used a step-by-step marching procedure to predict the developing velocity and temperature fields. His results are specific to two fluids: air and water. An

interesting comparison is made between the axial centerline velocity variation using these two fluids at the same Grashof and Reynolds numbers. The mixed-convection effects are shown to be more important for water than for air and this, according to Collins, is due to two factors. First, the thermal diffusivity of water ($k_f/\rho C_p$) is much lower than the one for air and, therefore, the core portions of a water-filled vertical pipe will not be heated as much as an air-filled one. Thus, water heating will take place near the wall, thereby accentuating the buoyancy effect in that region. Also, the small increase in air viscosity with temperature slightly reduces the buoyancy effects. But for water, the viscosity decreases substantially with temperature, and in the process aids the buoyancy effects. Collins also concluded, based on his numerical simulations, that changes in the density of water are so small that they can be neglected in every term of the governing equations except, of course, in the buoyancy term, thus validating the Boussinesq approximation.

Zeldin and Schmidt [1972] studied developing mixed-convection flows in constant-temperature vertical tubes. Their numerical solutions, which used the fully elliptic version of the governing equations, were compared with experimental results obtained with air. Agreement is fair and could perhaps be improved by including the temperature dependence of physical properties in their numerical model. In addition, and as noted by Zeldin and Schmidt, axial conduction in the pipe may have heated the fluid prior to its entrance into the test section, which may explain part of the disagreement. They predicted, numerically, that for a given length of the pipe, the centerline velocity would become zero at a critical value of Gr/Re . Beyond this critical value, their iteration

algorithm could not converge, which meant that flow reversals could not be studied. They also mentioned that changes in the temperature and velocity distributions are barely noticeable when $Gr/Re < 1$.

Collins [1980] looked at developing laminar mixed-convection in circular tubes. He used the fully elliptic equations to solve this problem numerically, including density and viscosity variations. The agreement between his numerical results and the experimental data of Zeldin and Schmidt [1972] is generally better than that between the numerical and the experimental results of Zeldin and Schmidt [1972]. This demonstrates the possibility of an improvement in the numerical predictions if the temperature dependence of viscosity and density are included.

Dalbert [1982] and Penot and Dalbert [1983] presented an extension to the work on free convection by Dalbert et al. [1981] by including mixed-convection situations. The forced convection part of the mixed-convection flow is handled by specifying a driving pressure drop between the inlet and outlet of a channel. The solution technique is slightly different than the one described by Dalbert et al. [1981] since the driving pressure drop is not independent of the channel height. Instead, an iterative process on the value of the inlet velocity is repeated until the exit pressure is equal to the ambient pressure.

Chow et al. [1984] did a numerical study on the effects of free convection and fluid axial conduction on forced convection heat transfer inside a vertical channel at low Péclet (Pe) numbers. The inclusion of fluid axial conduction required the use of an elliptic scheme to solve this problem. They show that at low values of Pe , even the entering

velocity profile can be distorted due to axial conduction in the fluid. For the same reason, the bulk temperature increases before the fluid enters the heated section.

Aung and Worku [1986a, 1986b] numerically studied mixed-convection in a vertical channel with asymmetric constant wall temperatures. It is shown that for fixed asymmetric wall temperatures, the flow field experiences a reversal after a certain minimum value of the Gr/Re parameter. For a fixed value of Gr/Re , the flow reversals are observed to move downward in the channel as the wall temperature asymmetry is increased. These flow reversals had been observed experimentally by Sparrow et al. [1984] in a one-sided heated vertical channel for the limiting case of free convection.

In the numerical investigations of Chow et al. [1984] and Aung and Worku [1986a, 1986b], the study of flow reversals is somewhat limited by the fact that they used a parabolic marching scheme, which enables prediction of the onset of flow reversals but which prevents any examination of the flow field past this point. Another important drawback of their studies is that their results are specific to water. Habchi and Acharya [1986] alleviated this lack of generality by including the Prandtl number as a parameter. They show that temperature profiles inside the channel become more uniform when the Gr/Re^2 parameter increases. The resulting Nu are mildly affected, confirming the results of Aung and Worku [1986a]. They did not venture into flow reversal situations as their numerical computations were done using a parabolic marching scheme.

Shadday [1986] solved numerically the time-dependent axisymmetric momentum and energy equations for the case of upward flow in a vertical tube maintained at a constant wall temperature. For small Grashof numbers, the flow is steady, but when Gr is increased, unstable flows are noticed. The unsteady component of the flow was confirmed experimentally in a parallel study done by Durig and Shadday [1986]. Time-averaged results are also presented and used in the closed-loop thermosyphon investigation of Durig and Shadday [1986].

Yao [1987] presents results of a linear-stability analysis of fully-developed upward flow in a heated vertical pipe. His analysis involves the perturbation of the full three-dimensional time-dependent Navier-Stokes equations. He shows that flows can become unstable at low values of Re and mild heating.

Morton et al. [1989] investigated numerically and experimentally flow recirculations in laminar developing mixed-convection in vertical circular tubes, subjected to a constant wall temperature boundary condition. Generally, their elliptic numerical simulations predicted very well the flow recirculation zones observed experimentally. For some cases, though, the flow reversal predictions were further downstream than what was observed experimentally. They postulated that this difference was due to axial conduction in the pipe, which pre-heated the fluid upstream of the heating section and which was not accounted for in their numerical formulation.

1.2.2.3 Conjugate heat transfer in pipes

Axial heat conduction along the walls containing a heated (or cooled) fluid can significantly influence, in some cases, the heat transfer to the fluid. This coupling of heat conduction in the walls and convection in the fluid is referred to as conjugate heat transfer. Most of the papers on this topic deal with forced convection situations, with a minimum of attention given to the simultaneous effects of developing mixed-convection and wall conduction. In the following paragraphs, two non-dimensional governing parameters related to pipe axial conduction are used: Δ , the ratio of wall thickness to pipe diameter; and K , which represents the ratio of the thermal conductivity of the wall to the thermal conductivity of the fluid.

Davis and Gill [1970] studied the effects of wall conduction on heat transfer with Poiseuille-Couette flow between parallel plates. It is concluded that increasing K and Δ enhances wall conduction effects, whereas an increase in Pe diminishes the importance of wall conduction.

Iqbal et al. [1972] solved, using variational calculus, the problem of conjugate heat transfer for the case of laminar fully developed mixed-convection in vertical non-circular ducts. Only circumferential pipe conduction was considered. It is shown that large values of K tend to homogenize the circumferential wall temperature. Conversely, as K approaches zero, the wall heat flux becomes circumferentially uniform.

Mori et al. [1974] investigated numerically the effects of wall conduction in pipes where the flow is hydrodynamically fully developed. It

is concluded that for "sufficiently" thin walls, the condition at the outer surface can be considered to prevail at the fluid/solid interface. In their simulations, the calculation domain was restricted to the heated section, thus, neglecting axial conduction in the upstream and downstream pipes.

Faghri and Sparrow [1980] considered simultaneous wall and fluid axial conduction in laminar pipe-flow heat transfer. The geometry consisted of a directly heated pipe section preceded by an adiabatic pipe section. The flow was assumed to be fully developed from inlet to outlet and the analysis was restricted to thin-walled tubes. This problem was solved numerically using the full elliptic equations. It is shown that a substantial amount of convective heat transfer can occur in the non-directly heated pipe. As the $\Delta \cdot K$ parameter increases, the magnitude of this phenomenon and the extent of the upstream region where it occurs increase. This is further enhanced for small values of the Péclet number for which axial fluid conduction becomes important. At the entrance of the heated section, Nusselt numbers are shown to be lower than the ones obtained by the classic Graetz-type formulation.

In three separate numerical investigations, Zariffteh et al. [1982], Fithen and Anand [1988] and Campo and Schuler [1988] studied the combined effects of wall and fluid axial conduction on laminar heat transfer in circular tubes. In these studies, a hydrodynamically fully developed parabolic velocity profile is assumed throughout the calculation domain and pre-heated and post-heated sections were included. The first study used a Galerkin-type finite element approach to solve the energy equation for both the solid and fluid regions, while the other

two studies used finite differences methods. Fithen and Anand [1988] report that preheating of the fluid (upstream of the heated section) can extend as far as 22 radii for a constant heat flux case and 7 radii for a constant wall temperature case. Zariffah et al. [1982] calculated the ratio of convective heat gain in the heated section to the overall heat added. It is shown that this ratio can be substantially lower than unity for small values of the Péclet number and/or large values of K . Campo and Schuler [1988] showed, much like Davis and Gill [1970] did for parallel plates, that pipe wall conduction effects are important when K and Δ are high and Pe is small.

In the first of a series of papers related to conjugate heat transfer, Barozzi and Pagliarini [1984] experimentally investigated coupled conduction and laminar forced convection in a circular tube, with water. Heat was supplied to the fluid using a wire inserted into an helical groove machined on the outer wall of a copper pipe. The pre-heated section was made of Plexiglass and allowed for the development of the velocity profile. The general agreement between the results generated by this apparatus and numerical simulations performed by these authors is fair. At the entrance, the agreement is reported to be very good despite not allowing for wall conduction in the upstream section, in their numerical simulations. Even though general trends are well predicted, the discrepancy between numerical and experimental results increases with downstream distance. According to them, this is believed to be due to the growing effects of density and viscosity variations on heat transfer.

Barozzi and Pagliarini [1985] did a numerical study on the conjugate heat transfer with hydrodynamically fully developed laminar pipe flow. The heated section was subjected to a constant heat flux condition on the outside surface of a wall with finite thickness. They show that the inner surface heat flux is more uniform when Δ and K are small and when the Péclet number is high. Axial pipe conduction effects are more pronounced at the inlet of the heated section than at the outlet. Thus, pipe axial conduction may be less important, on average, for long tubes. It is also shown that axial pipe conduction may alter the usual linear bulk temperature variation (obtained for a truly uniform heat flux condition) as the heat flux is not distributed equally within the heated section. Recently, Pagliarini [1988] added fluid axial conduction to the just-mentioned analysis. As expected, it is concluded that fluid axial conduction is important for low values of K and small Péclet number.

1.2.3 Previous Studies Related to the Gold-Film Technique

A number of researchers recognized the electrically-heated thin gold-film technique as an attractive source of uniform heat flux for heat transfer experiments. Baughn et al. [1985] evaluated local heat transfer coefficients, using the same type of gold-film as the one used in this study, for three test problems: heat transfer downstream of an abrupt expansion; heat transfer from a cylinder in crossflow; and non-uniform circumferential heating in a pipe. For the problems studied, the conclusions reached are that: (i) wall conduction effects are essentially negligible; (ii) the nonuniformity of the gold coating introduces an error of the order of ± 2 -4 percent; and (iii) the change in resisti-

vity of the gold-film, due to temperature effects, introduces an error of the order of ± 1 percent.

Hippensteele et al. [1983, 1985] used the gold-film technique and liquid crystals composite to obtain qualitative and quantitative results of local heat-transfer coefficients on a turbine blade airfoil. As reported in these studies, if conduction and radiation losses are properly accounted for, the thin gold-film technique provides a relatively simple and accurate way for determining local heat-transfer coefficients. The largest source of error (6-8 percent) is due to the nonuniformity of the gold-film resistivity.

The works of Baughn et al. [1985] and Hippensteele et al. [1983, 1985] pertain to forced convection situations in which heat transfer due to thermal radiation and heat conduction processes is small in comparison with that due to the convective mechanism. In a study undertaken at McGill's Heat Transfer Laboratory, Neill [1989] examined the gold-film technique in the context of natural convection where radiation and conduction must imperatively be accounted for to obtain accurate local heat transfer coefficients. Two test problems were selected: two-dimensional, steady-state, laminar natural convection along a vertical flat plate and in a horizontal concentric annulus. When compared with analytical solutions (in the case of the vertical flat plate) and numerical results (for the annulus), the experimentally determined local heat transfer coefficient agreed within approximately $\pm 10\%$ when radiation and conduction was accounted for appropriately.

1.2.4 Summary of the Literature Review

1.2.4.1 Closed-loop thermosyphons

Analytical, numerical and experimental studies on closed-loop thermosyphons have been reported. A number of geometries were studied with different positioning of the heated and cooled sections. In general, for a given geometry and power input, heating from below and cooling from above leads to the maximum flowrate. It also increases the probability of obtaining unstable flows, where the flowrate varies aperiodically with time. When the heated and cooled sections are vertical, the flowrate is reduced but the flow is much more stable.

The sophistication level of closed-loop thermosyphon models covers a large scale. At one end of the spectrum, there are simple traditional one-dimensional models which assume fully developed flow over the whole loop and $Nu = 3.66$ in the cooled section. While at the other end, the non fully-developed nature of the flow is accounted for in accurate but costly fully three-dimensional numerical models. It has also been shown that one-dimensional models could be improved with more accurate input values of Nu and f .

Experiments have been performed on a number of geometries to ascertain the validity of the aforementioned models. Generally, when experimental conditions approach fully developed flow conditions, the results of one-dimensional models agree well with those of the experiments. But when experimental conditions are such that natural convection effects are strong, the velocity and temperature profiles are distorted from

their fully developed forced convection shapes, and one-dimensional models become inaccurate. Another drawback of past investigations of closed-loop thermosyphons is that, to the knowledge of this author, none of the reported studies analyzed the effects of heat losses (or gains) from sections other than the cooled (or heated) portions.

1.2.4.2 Mixed-convection flow in vertical pipes

The first studies on mixed-convection in vertical pipes did not benefit from the current digital computers. Therefore, a number of simplifying assumptions had to be made which limited the analyses to the study of fully developed mixed-convection flows. However, recent studies have solved numerically the simultaneously developing mixed-convection problem. Marching-type parabolic solution procedures have been used quite successfully, but are limited to conditions where flow reversals are absent. Flow reversals are handled by solving the full elliptic equations. There seems to be a general agreement, supported by numerical and experimental studies, that heat transfer is enhanced in buoyancy-aided flows.

Flow reversals have been studied quite extensively (numerically and experimentally) for the constant wall temperature case. For the constant heat flux case, however, numerical studies have been limited to the prediction of the start of the flow reversal region, neglecting the study of flow reversals downstream of this region.

Experimentally, mixed-convection flows have been studied for both the constant wall temperature case and the constant heat flux case.

Flow visualization has been undertaken for the constant wall temperature case, but it is impossible when an optically opaque electrically heated pipe provides the constant heat flux boundary condition. For this reason, flow reversals have not yet been observed experimentally for the constant heat flux case. Furthermore, observations of flow instabilities (see paragraph below), which can be obtained by looking at the behavior of a dye filament injected in the flow, have been undertaken only at the exit of the heated section where the pipe was made of a transparent material.

As far as stability is concerned, there seems to be a general consensus, supported by analytical and experimental work, that upward mixed-convection flow can become unstable at Re much lower than the corresponding values encountered in isothermal pipe flows. But the flow does not become truly turbulent until the Re has reached a value close to 2300. The instability is attributed to the presence of a point of inflexion in the flow.

Since mixed-convection flows are more likely to occur at small Re , the associated Pe will also be small (for small Prandtl number fluids), which means that fluid axial conduction may be important. Then, it would seem appropriate, to append to the calculation domain of the numerical analyses, sections located downstream and upstream of the heated section. This is often done for forced convection flows, but has not yet been carried out for mixed-convection flows.

1.2.4.3 Conjugate heat transfer in vertical pipes

The studies reviewed in section 1.2.2.3 all revolved around the same theme: the study of laminar hydrodynamically fully developed and thermally developing flow in the presence of wall axial conduction. Numerically, the problem is reduced to the analysis of the energy equation. Generally, for this class of problem, the boundary condition at the inner surface will be different from the imposed boundary condition at the external surface, except in the case of thin pipes where axial conduction has been shown to be negligible. Typically, the inner surface heat flux is more uniform when Δ and K are small and when the Pe is high. It is also revealed that axial pipe conduction may influence the fluid temperature distribution downstream and upstream of the heated section itself.

1.2.4.4 The thin gold-film technique

The thin-gold film technique has been used quite successfully to measure local wall temperatures and determine local heat transfer coefficients for flows ranging from turbulent forced convection to laminar natural convection. In addition, because of its transparency, the gold-film is extremely useful in flow visualization studies.

1.3 SURVEY OF THE THESIS

This thesis has eight Chapters and is organized as follows. Chapter 1 reviews the current knowledge on closed-loop thermosyphons and on mixed-convection in vertical pipes with (or without) axial

conduction in the pipe wall. As well, the goals of the present study have been presented. Chapter 2 is devoted to a presentation and discussion of mathematical models of closed-loop thermosyphons. In addition, an overview of a procedure for the coupling of traditional one-dimensional models with inputs from two-dimensional numerical simulations is presented. This is then followed, in Chapter 3, by a review of the numerical procedures used to simulate conjugate mixed-convection in the heated and cooled sections of the closed-loop thermosyphon. A complete description of the proposed solution methodology, based on a coupling of one-dimensional and two-dimensional models, is given in Chapter 4. Description of the experimental apparatus and procedures is done in Chapter 5. In Chapter 6, the numerical results of conjugate conduction and laminar mixed-convection in vertical pipes are presented along with results of flow visualization experiments. The results pertaining to the proposed model are presented in Chapter 7. Finally, in Chapter 8, the major contributions of the present investigation are summarized and recommendations for future work are made.

CHAPTER II

THEORETICAL CONSIDERATIONS

2.1 INTRODUCTION

The presentation and discussion of mathematical models of closed-loop thermosyphons with vertical heat transfer sections is the subject matter of this Chapter.

Although the analysis is kept general enough to include any type of closed-loop thermosyphon with vertical heat transfer sections, attention is focussed on the geometry shown in Fig. 2.1, as it is the geometry used in the experimental portion of this thesis. The geometry consists of two vertical straight pipes joined together by two circular 180° bends each of mean radius R . All pipes are of circular cross-section with an internal radius, r_i . The circulating fluid is heated by a constant and uniform heat flux, q , in the heated section of the loop, and it is cooled in a cooling section maintained at constant wall temperature, \bar{T}_w . Elsewhere, around the loop, the pipes are insulated from the ambient fluid so as to limit heat gains (or losses). Both the heated and cooled sections are preceded by a sufficient length of straight pipe so that the flow can be assumed to be hydrodynamically fully developed when it enters each of these sections.

The theoretical considerations of closed-loop thermosyphons similar to that shown in Fig. 2.1 are presented here in several successive steps. First, a general one-dimensional mathematical model is derived,

solved and discussed. This model will be referred to as the traditional model. Following this, a novel model involving a coupling of one-dimensional and two-dimensional governing equations will be presented and discussed. This novel approach will be denoted as the proposed model. An overview of the methodology used to solve the proposed model will also be presented in this Chapter. Details of this solution method will be given in Chapter 4.

In the traditional one-dimensional model, described in section 2.2, the general governing equations are solved by assuming: (i) steady fully developed laminar flow throughout the loop; (ii) steady fully developed forced convection heat transfer in the heated and cooled sections; (iii) negligible heat losses (or gains) in sections other than the cooled (or heated) sections. Under these assumptions, the Fanning friction factor is equal to $16/Re$ throughout the loop; the variation of the fluid temperature in the axial direction is linear in the heated section; and the Nusselt number in the cooled section is constant, $Nu = hD/k = 3.66$.

This traditional approach has been presented in the past by a number of researchers (for example, by Mertol [1980] and more recently by Huang and Zelaya [1988]). It is re-examined here for three reasons: (1) it provides a basic understanding of the problem, some aspects of which have been overlooked in the literature, without the added complexities of heat loss considerations and mixed-convection effects; (2) the resulting velocity is a natural choice for the reference velocity in the non-dimensionalization of the governing equations in the proposed model; and (3) it is one of the primary components of the proposed method.

It should also be noted that the traditional model was developed and used in the early stages of this study. This facilitated the design of the experimental apparatus, for the desired range of operating conditions, without the more advanced proposed model, which was developed later.

As mentioned in the introductory Chapter, one-dimensional models are inaccurate under certain circumstances. For example, in the closed-loop thermosyphon shown in Fig. 2.1, the velocities are relatively small (small Re) and buoyancy effects are significant in the heated and cooled sections (high Gr_q). This implies that the heated and cooled sections experience a condition of mixed-convection, including the possibility of local flow reversals. Thus, the velocity and temperature profiles inside these sections could be significantly different from the assumed fully developed profiles. Consequently, the friction factor in these sections can not be assumed equal to the one associated with fully developed Poiseuille flow. In addition, the assumption of a constant Nusselt number in the cooled section becomes questionable. As well, in the heated section, the axial fluid temperature distribution may deviate from the assumed fully developed linear distribution. Yet another source of inaccuracy in such traditional one-dimensional models is the neglect of the influence of heat gains (or losses), from the insulated sections, on the fluid flow and heat transfer inside closed-loop thermosyphons. The proposed model was developed in an effort to alleviate some of these deficiencies associated with traditional one-dimensional models.

The proposed model, described in section 2.3, involves an original

iterative coupling procedure between the local results of two-dimensional numerical simulations performed in the heated and cooled sections and a traditional one-dimensional analysis. With this coupling procedure, the two-dimensional numerical simulations form an integral part of the overall solution procedure and their results do not need to be known a priori. In order to keep the computational effort at an acceptable level, the numerical simulations are performed only in the important sections of the loop, primarily in the heated and cooled sections. Elsewhere, around the loop, the traditional model is used with a proper account of heat losses (or gains).

2.2 TRADITIONAL ONE-DIMENSIONAL MODEL

2.2.1 Assumptions

The assumptions used in the development of the traditional one-dimensional model of the closed-loop thermosyphon depicted in Fig. 2.1 are the following:

- 1) The velocity is fully developed throughout the entire closed-loop;
- 2) The temperature is assumed to be uniform in any given cross-section inside the loop and is dependent only on the axial direction;
- 3) The fluid is Newtonian, incompressible, and in single-phase;
- 4) The flow is steady;
- 5) The flow is laminar;
- 6) The fluid properties are assumed constant, and evaluated at a mean loop temperature, T_m , except in the evaluation of the buoyancy term, where the mean density is assumed to vary linearly with temperature: This corresponds to the well-known Boussinesq

approximation;

- 7) Curvature effects and form losses are neglected;
- 8) Heat conduction in the pipe and axial conduction in the fluid are neglected;
- 9) Viscous dissipation and pressure work are neglected.

Some of these assumptions require further comments. The first two assumptions are invoked in the majority of traditional one-dimensional analyses found in the literature (Mertol [1980], Damereell and Schoenhals [1979]). The first one implies that changes in the velocity profiles due to fluid heating and cooling are neglected, while the second indicates that radial and circumferential temperature variations are neglected.

Next, consider the steady-state assumption. As mentioned in Chapter 1, the flow inside some closed-loop thermosyphon geometries, such as in a toroidal thermosyphon with heating from below and cooling from above, can experience unstable, oscillatory motions. Huang and Zelaya [1987b] performed a stability analysis for a closed-loop thermosyphon geometry similar to the one used in this study. Based on their analysis, the flow becomes unstable for parameter ranges which are well outside those investigated in the present study.

The laminar flow assumption is certainly valid in the insulated portions of the loop, considering that the buoyancy effects are negligible in this region and that the maximum Re encountered in this study was ≈ 200 . In the heated and cooled sections, however, buoyancy effects could make the flow "non-laminar" (Hallman [1958], Scheele et al.

[1960]) even for Re well below 2000. As reported in the literature review, the general consensus on this issue seems to indicate that a transition to a "non-laminar" flow can be expected downstream of a point of inflexion in the velocity profile. Hallman [1958], based on experimental observations, has proposed a correlation for predicting such "non-laminar" occurrences for the case of an upward flow in a vertically heated pipe. All the results presented in this thesis were verified against the correlation of Hallman [1958] to ensure that conditions were laminar. So, for this work, the assumption of laminar flow in the heated and cooled section is believed to be valid.

The assumption of constant fluid properties, in the context of the Boussinesq approximation, is valid provided that the fluid properties are evaluated at an appropriate mean temperature and that the difference between the minimum and maximum temperatures in the loop is small. In this work, water was used as the heat transfer fluid and the maximum temperature difference was of the order of 10 K.

Unless otherwise stated, the thermophysical properties of water were evaluated, at the appropriate temperature, using the relationships presented in Appendix A. Based on these relationships, it can be shown that variations in the value of the specific heat and density are negligible (well below 1%) over a 10 K range at temperatures near 300 K and, therefore, the assumptions of constant specific heat and density are valid. Of course, the density variation responsible for the buoyancy term has to be retained, because it drives the flow in the thermosyphon. As for variations of thermal conductivity and dynamic viscosity for water, they are significant ($> 1\%$) in the range of temperatures just

mentioned. But, as will be shown later in Chapter 7, the use of constant thermal conductivity and dynamic viscosity in the proposed model does not significantly affect the results when these properties are evaluated at the mean loop temperature, T_m , which is defined as the arithmetic mean of the inlet and outlet temperatures in the heated section. For purposes of comparison between results of different models, it is often desirable to use a common reference temperature to evaluate fluid properties. In these cases, \bar{T}_w is chosen as the reference temperature.

Form losses in the piping, such as the ones associated with the 180° bends, are neglected at this stage of the analysis. They will be incorporated later on, into the specific proposed model of the experimental apparatus, in terms of an equivalent length of pipe.

In the context of a toroidal thermosyphon operating in steady-state, Mertol [1980] has shown that fluid axial conduction is essentially insignificant for fluids such as water. Axial heat conduction in the pipe, as will be shown later, is also negligible for the range of flows investigated in the present study.

Bau and Torrance [1983] have shown that for free convection loops, viscous dissipation and pressure work are important only in exceptional cases where body force fields are relatively strong and where length scales of geophysical dimensions are encountered. Considering the physical dimensions of the loop studied here and the gravitational field, the assumption of negligible viscous dissipation and pressure work is justified.

2.2.2 Derivation of the General One-Dimensional Momentum Equation

In the derivation of the general one-dimensional momentum equation, use is made of the elemental control volume depicted in Fig. 2.2. The location of the control volume with respect to the horizontal is given by the angle θ . The flow is assumed to be in the direction of increasing θ , thus, in the clockwise direction. Application of the principle of conservation of momentum, under the preceding assumptions, yields the following balance between the pressure force, the shear force on the pipe wall, and the gravitational force in the elemental control volume:

$$-(P + \frac{dP}{ds} \Delta s)(\pi r_i^2) - 2\pi r_i \tau_w \Delta s - \rho g \cos \theta (\pi r_i^2) \Delta s + P(\pi r_i^2) = 0 \quad (2.1)$$

where P is the pressure, r_i is the internal radius of the pipe, τ_w is the wall shear stress, ρ is the fluid density, and g is the gravitational acceleration. It is worth mentioning that the inertia term $(d(\rho u)/ds)$ is excluded from this equation due to assumptions 1) and 6). Two terms in Eq. 2.1 cancel out and it can be reduced to:

$$\frac{dP}{ds} + \frac{2\tau_w}{r_i} + \rho g \cos \theta = 0 \quad (2.2)$$

In order to get an overall balance, this equation is integrated around the closed-loop, along path s (Fig. 2.1). This integration leads to:

$$\oint \frac{2 \tau_w}{r_i} ds = -g \oint \rho \cos \theta ds \quad (2.3)$$

where the integral sign, \oint , indicates an integration around the loop. The pressure term disappears, as P is a continuous function of s . Similarly, had the inertia term been included in the analysis, it would have vanished upon integration around the loop. Following the Boussinesq approximation, the density, ρ , can be expressed as:

$$\rho = \rho_m [1 - \beta(T - T_m)] \quad (2.4)$$

where ρ_m is the reference density (evaluated at T_m), T is the fluid temperature in the cross-section of interest, and β is the volumetric coefficient of thermal expansion of the fluid, evaluated at T_m .

The Fanning friction factor is defined as follows:

$$f = \frac{\tau_w}{\rho_m V^2 / 2} \quad (2.5)$$

where V is the average velocity inside the loop. Using Eqs. 2.4 and 2.5 in Eq. 2.3, the following result is obtained:

$$V^2 \oint f(s) ds = r_i g \beta \oint T(s) \cos \theta ds \quad (2.6)$$

Equation 2.6 is the general one-dimensional momentum equation for the type of closed-loop thermosyphons considered in this work. The task now is to evaluate or estimate the values of $f(s)$ and $T(s)$ at all loca-

tions around the loop in order to solve Eq. 2.6.

Equation 2.6 can also be written in a slightly different form:

$$V = \frac{2\rho_m r_i^2 g \beta \oint T(s) \cos \theta \, ds}{\mu \oint f(s) Re \, ds} \quad (2.7)$$

The right hand side of Eq. 2.7 can be considered to represent the ratio of "total buoyancy" over "total friction" (Lavine [1984]). This is a useful concept which will be used in Chapter 7.

2.2.3 Determination of the Friction Factor, $f(s)$

In the traditional approach, the flow is assumed to be fully developed throughout the loop so that $f(s) = 16/Re = \text{constant}$. With this assumption, Eq. 2.6 reduces to:

$$V = \frac{\rho_m r_i^2 g \beta}{8\mu L} \oint T(s) \cos \theta \, ds \quad (2.8)$$

where L is the total length of the loop and μ is the dynamic viscosity of the fluid.

2.2.4 Determination of the Temperature Distribution, $T(s)$

In Eq. 2.8, the temperature distribution around the loop, $T(s)$, is determined by deriving and solving the one-dimensional energy equation.

2.2.4.1 Derivation of the energy equation

With the aid of the elemental control volume of Fig. 2.3, a one-dimensional energy balance gives:

$$\rho_m VA \frac{di}{ds} = 2\pi r_i q \quad (2.9)$$

where i is the enthalpy, A is the cross-sectional area of the pipe, and q is the rate of heat input per unit area. In the context of the assumptions given in section 2.2.1, Eq. 2.9 may be written as:

$$\rho_m VAC_p \frac{dT}{ds} = 2\pi r_i q \quad (2.10)$$

where C_p is the specific heat. Equation 2.10 represents the general one-dimensional energy equation for the closed-loop thermosyphons considered in this thesis. The value of q will change within the loop depending on the imposed thermal boundary conditions.

2.2.4.2 Thermal boundary conditions

In the traditional approach, two sets of thermal boundary conditions, which are identified as Case (1) and Case (2), will be examined:

For Case (1), the thermal boundary conditions are:

- Constant heat flux in the heated section;
- Constant cooling flux in the cooled section;
- Adiabatic condition elsewhere.

Even though the constant cooling flux boundary condition is not physically achievable, it is used here as it simplifies the solution and gives good results except in certain cases, which will be addressed shortly.

For Case (2), the thermal boundary conditions are:

- Constant heat flux in the heated section;
- Constant wall temperature cooling section with a thermally fully developed condition ($Nu = 3.66$);
- Adiabatic conditions elsewhere.

2.2.4.3 Solution of the energy equation

For Case (1) and with respect to the nomenclature presented in Fig. 2.1, the energy equation and the corresponding axial temperature variations are:

In the heated section ($s_3 \leq s \leq s_4$):

$$\rho_m V A C_p \frac{dT}{ds} = P_w / L_3 \quad \text{and} \quad T = T_3 + \frac{(s-s_3)}{\rho_m V A C_p} \frac{P_w}{L_3} \quad (2.11 \text{ a, b})$$

In the cooled section ($s_8 \leq s \leq s_9$):

$$\rho_m VAC_p \frac{dT}{ds} = -P_w/L_8 \quad \text{and} \quad T = T_8 - \frac{(s-s_8) P_w}{\rho_m VAC_p L_8} \quad (2.12 \text{ a,b})$$

In the adiabatic sections:

$$\rho_m VAC_p \frac{dT}{ds} = 0 \quad \left[\begin{array}{l} (s_4 < s < s_8) \\ T = \text{const.} = T_4 \quad \text{and} \quad T_5 = T_6 = T_7 = T_8 = T_4 \\ \\ (s_9 < s < s_3) \\ T = \text{const.} = T_9 \quad \text{and} \quad T_{10} = T_{11} = T_1 = T_2 = T_3 = T_9 \end{array} \right] \quad (2.13 \text{ a,b,c})$$

where P_w is the power input, T_4 and T_9 are the temperatures at s_4 and s_9 , respectively, and L_3 and L_8 are the lengths of the heated and cooled sections, respectively. Temperatures $T_1 \dots T_{11}$, evaluated at their corresponding axial locations, $s_1 \dots s_{11}$, will now be referred to as nodal temperatures.

For Case (2), the equations in the heated and adiabatic sections are unmodified. In the cooled section, the energy equation and the corresponding temperature distribution are:

In the cooled section ($s_8 \leq s \leq s_9$):

$$\rho_m VAC_p \frac{dT}{ds} = -h2\pi r_i (T - \bar{T}_w) \quad \text{and} \quad T = (T_8 - \bar{T}_w) e^{-X(s-s_8)} + \bar{T}_w \quad (2.14 \text{ a,b})$$

$$\text{where } X = \frac{h2\pi r_i}{\rho_m VAC_p} = \frac{\pi k_f Nu}{\rho_m VAC_p}, \quad Nu = 3.66,$$

h is the heat transfer coefficient in the cooled section, k_f is the thermal conductivity of the fluid, and \bar{T}_w is the constant wall temperature in the cooled section.

2.2.5 Solution of the Traditional Model

Equation 2.8 can now be solved using the temperature distributions determined in the previous section. Details of the solution can be found in Appendix B. The end result, in its most general form, which includes Cases (1) and (2), is:

$$V = \left[\frac{P_w \beta g}{8\pi \mu C_p L} (\Delta Z + \epsilon) \right]^{1/2} \quad (2.15)$$

where,

$$\epsilon = 0 \quad \text{for Case (1),}$$

$$\epsilon = \frac{L_8}{2} - \frac{1}{X} + \frac{e^{-XL_8}}{1 - e^{-XL_8}} L_8 \quad \text{for Case (2),}$$

and ΔZ is the height difference between the middle of the heated section and the middle of the cooled section, as shown in Fig. 2.1. Fluid properties are evaluated at \bar{T}_w .

Once the average velocity has been determined, Eqs. 2.11b and 2.14b are used to calculate the temperature distribution in the loop for Case 2. For Case (1), however, the temperatures inside the loop are not related to any boundary temperatures as in Case (2) and, therefore,

only the temperature rise (or drop) in the heated (or cooled) section can be predicted by Eqs. 2.11 and 2.12.

2.2.6 Discussion

Case 1 ($\epsilon=0$)

Equation 2.15 reveals that the average velocity is proportional to the $1/2$ power of P_w , ΔZ , β , and g but inversely proportional to the $1/2$ power of L , C_p and μ . It also indicates that V is independent of r_i . This is an unexpected result and to the knowledge of this author, it is the first time that this independency has been explicitly identified.

Case 2 ($\epsilon \neq 0$)

In Case (2), the first thing to note is that Eq. 2.15 becomes transcendental as V is present in both sides of the equation (on the right hand side, X is dependent on V). The influence of ϵ on the resulting velocity will now be examined.

The value of ϵ is dependent on X and L_g . It can be shown that ϵ is always positive and decreases for decreasing values of X (or, alternatively, increasing values of V), independently of the value of L_g . Therefore, when ΔZ is increased (everything else remaining the same) the average velocity, V , increases but ϵ decreases. Conversely, when ΔZ is decreased, ϵ increases. The difference in magnitude between ϵ and ΔZ , which is problem dependent, will determine whether or not ϵ is negligible. One thing is apparent though, ϵ will have more chances of being negligible for large values of ΔZ than for small ones,

and when this is true Cases (1) and (2) will give essentially identical solutions. The same line of reasoning can be extended to an increase in P_w which also increases V and decreases the importance of ϵ versus ΔZ . This is an interesting result as it implies that, for large values of ΔZ and P_w , values of Nu and \bar{T}_w are not needed to obtain V . For small values of ΔZ and P_w , ϵ becomes important and the solutions given by Cases (1) and (2) will differ. The importance of ϵ versus ΔZ will be quantified in Chapter 7 for a specific geometry.

Another factor has to be taken into consideration when ΔZ is small and/or when P_w is high. When ΔZ is small, the average velocity inside the loop is small, which also implies that Re is small. When P_w is large, the Grashof number (Gr_q) becomes large. In turn, the combined effect of these two factors increases the likelihood of having a mixed-convection situation in both the heated and cooled sections as the ratio Gr_q/Re^2 becomes non-negligible. As noted earlier, this situation will significantly alter the velocity and temperature profiles from their laminar forced convection fully-developed shapes. Therefore, the assumption of fully developed flow which lead, for Case (2), to the assumption of a constant Nu in the cooled section and of a constant f throughout the loop, may not be valid when ΔZ is small or when P_w is high.

Related Studies

It is appropriate at this stage to review the works of other researchers in relation to the foregoing analysis. The experimental work of Huang and Zelaya [1988] will be examined first. Their geometry,

which has been presented in Fig. 1.3, consists of a closed-loop thermosiphon with vertical heat transfer passages, similar to the one considered in this study. By assuming a constant cooling flux (Case 1) and neglecting heat losses, their one-dimensional analysis leads to the following:

$$Re^2 = \frac{WY}{8} \quad (2.16)$$

where,

$$Y = \frac{\Delta Z L_h}{L_{eq} 2r_i} \quad (\text{dimensionless geometric parameter})$$

$$W = \frac{P_w}{2\pi r_i L_h} \frac{\rho_m^2 \beta g (2r_i)^4}{\mu^3 C_p} \quad (\text{dimensionless parameter related to the power input})$$

L_h is the length of the heated section, and L_{eq} is an equivalent length of pipe which accounts for the sum of the total frictional losses and of the form losses associated with four abrupt 90° bends and a valve. Equation 2.16 represents the dimensionless form of Eq. 2.15. It is worth noting, parenthetically, that Eq. 2.16 does not show directly the independency of V with respect to r_i as Eq. 2.15 did.

The experimental results of Huang and Zelaya [1988] agree very well with the predictions given by Eq. 2.16. However, it should be mentioned that, in their case, form losses are greater than frictional losses (8 times as much in one particular case). Thus, any deviation of $f(s)$ and $T(s)$ from their fully developed value, caused by mixed-convection effects, may have been blurred by overwhelming form losses.

In an attempt to improve the accuracy of traditional one-dimensional models, researchers (for example Durig and Shadday [1986]) have used two-dimensional numerical simulations of mixed-convection flow to obtain estimates of average friction factors and average heat transfer coefficients in the heated and cooled sections of closed-loop thermosyphons. These average values, when substituted into the traditional one-dimensional model, yielded improved velocity predictions. These averaged values, however, do not account for the local nature of the flow along the length of both the heated and cooled sections. Furthermore, since the numerical simulations are decoupled from the solution to the traditional one-dimensional model, these average values have to be known beforehand, which is a problem in itself since the velocity is unknown. Thus, numerous simulations have to be performed to get a general correlation for the values of $f(s)$ and $T(s)$ for a broad range of conditions.

Another way to improve the velocity predictions is to get the "exact" solution to the problem by solving numerically the three-dimensional governing equations. Lavine [1984] has explored this avenue by solving the three-dimensional flow in a toroidal thermosyphon. Her results, albeit for a geometry different from the one studied here, indicates that the computational cost (storage and CPU time) involved in such a calculation is considerable.

The proposed model, which is presented in the next section, involves an iterative coupling procedure between the local results of two-dimensional numerical simulations performed in the heated and cooled sections and a traditional one-dimensional model. Of particular interest to this study are the cases where the flow is by mixed-convection

in the heated and cooled sections of a closed-loop thermosyphon.

2.3 THE PROPOSED MODEL

2.3.1 Background

In this section, the governing equations of the proposed model are presented and a brief overview of the coupling procedure is described. Since the coupling procedure involves the input of numerical simulations results, the complete solution procedure is deferred to Chapter 4, following the formulation of the numerical methods, presented in Chapter 3.

The general one-dimensional momentum equation, Eq. 2.6, has been derived in section 2.2, and is repeated here for convenience.

$$v^2 \oint f(s) ds = r_1 g \beta \oint T(s) \cos \theta ds \quad (2.6)$$

In the proposed model, values of $f(s)$ and $T(s)$ around the loop, except in the heated and cooled sections, are determined as follows. The flow is assumed to be fully developed, therefore $f(s) = 16/Re$. As for the axial temperature variation, $T(s)$, it can no longer be assumed axially invariant with "s", as was the case in the traditional model, due to the presence of heat losses (gains). Instead, $T(s)$ is calculated using the one-dimensional energy equation. Values of $f(s)$ and $T(s)$ in the heated and cooled sections of the closed-loop are determined by solving numerically the two-dimensional governing equations of mixed-convection flow.

The calculation domain as well as boundary conditions, for the heated and cooled sections, are presented in Figs. 2.4 a,b. As shown on both figures, the calculation domains are not restricted only to the heated or cooled sections, but include sections downstream of the heated and cooled sections. These sections will be referred to as post-heated and post-cooled sections, while the term extended sections will be used to denote the combined heated and post-heated sections or the cooled and post-cooled sections. These "post" sections are included in the calculation domain because both the velocity and the temperature profiles remain distorted, from their fully developed values, for some distance after the heated or cooled sections. Thus, numerical simulations in these "post" sections ensure that accurate values of $f(s)$ and $T(s)$ are inputted into Eq. 2.6 not only for the heated (or cooled) section but also for these "post" sections. With these considerations and with reference to Figs. 2.4 a,b, the governing one-dimensional momentum equation (Eq. 2.6) takes the following form:

$$v^2 \left[\frac{16}{Re} \int_{s_{10}}^{s_3} ds + \int_{s_3}^{s_5} f_{hs}(s) ds + \frac{16}{Re} \int_{s_5}^{s_8} ds + \int_{s_8}^{s_{10}} f_{cs}(s) ds \right] =$$

(2.17)

$$r_i g \beta \left[\int_{s_{10}}^{s_3} T(s) \cos \theta ds + \int_{s_3}^{s_5} T_{hs}(s) \cos \theta ds + \int_{s_5}^{s_8} T(s) \cos \theta ds + \int_{s_8}^{s_{10}} T_{cs}(s) \cos \theta ds \right]$$

where $f_{hs}(s)$, $f_{cs}(s)$, $T_{hs}(s)$, and $T_{cs}(s)$ refer to friction factors and temperatures obtained from two-dimensional numerical simulations in the heated and cooled sections. Mathematically, they can be expressed by:

$$f_{hs}(s) \text{ or } f_{cs}(s) = \frac{\mu \left. \frac{\partial u}{\partial r} \right|_{r=r_i}}{\rho_m V^2 / 2} \quad (2.18)$$

$$T_{hs}(s) \text{ or } T_{cs}(s) = \frac{\int_A T(r,s) \, dA}{A} \quad (2.19)$$

where A denotes the cross-sectional area. In the extended heated and cooled sections, fluid flow and heat transfer is governed by the Navier-Stokes equations, the continuity equation, and the energy equation, all in cylindrical coordinates. In this work, both the parabolic and elliptic forms of the governing equations have been employed, depending on the problem of interest. These equations will now be presented.

2.3.2 Two-Dimensional Governing Equations and Boundary Conditions in the Heated and Cooled Sections

2.3.2.1 Elliptic forms of the governing equations

Assumptions

- 1) Fluid flow and heat transfer is assumed to be two-dimensional and axisymmetric;
- 2) The flow is assumed to be incompressible, laminar and in steady-

- state;
- 3) Viscous dissipation and pressure work terms are neglected;
 - 4) The specific heat and the density of the fluid are assumed constant and are evaluated at the mean loop temperature, T_m . In the evaluation of the buoyancy term, the Boussinesq approximation is used and mean density is assumed to vary linearly with temperature;
 - 5) At the entrance to the heated and cooled sections, the flow is fully developed (Poiseuille parabola) and the temperature is uniform;
 - 6) Conjugate heat conduction in the pipe is neglected. Modifications needed to include conjugate heat conduction are presented later in this thesis.

After invoking these assumptions, the elliptic set of the governing equations is:

Continuity equation

$$\frac{1}{r} \frac{\partial(rv)}{\partial r} + \frac{\partial u}{\partial z} = 0 \quad (2.20)$$

r-momentum equation

$$\rho_m \left[v \frac{\partial v}{\partial r} + u \frac{\partial v}{\partial z} \right] = - \frac{\partial p}{\partial r} + \frac{1}{r} \frac{\partial}{\partial r} \left[r \mu \frac{\partial v}{\partial r} \right] - \frac{\mu v}{r^2} + \frac{\partial}{\partial z} \left[\mu \frac{\partial v}{\partial z} \right] \quad (2.21)$$

z-momentum equation

$$\rho_m \left[v \frac{\partial u}{\partial r} + u \frac{\partial u}{\partial z} \right] = + \xi \rho_m g - \xi \beta \rho_m g (T - T_m) - \frac{\partial p}{\partial z} + \frac{1}{r} \frac{\partial}{\partial r} \left[r \mu \frac{\partial u}{\partial r} \right] + \frac{\partial}{\partial z} \left[\mu \frac{\partial u}{\partial z} \right] \quad (2.22)$$

where; $\xi=1$ for the cooling in downflow case,
 $\xi=-1$ for the heating in upflow case

Energy equation

$$\rho_m C_p \left[v \frac{\partial T}{\partial r} + u \frac{\partial T}{\partial z} \right] = \frac{1}{r} \frac{\partial}{\partial r} \left[r k_f \frac{\partial T}{\partial r} \right] + \frac{\partial}{\partial z} \left[k_f \frac{\partial T}{\partial z} \right] \quad (2.23)$$

where u and v are the axial and radial velocities, respectively. Equations 2.21 to 2.23 are presented in a general form allowing for variable μ and k_f . However, in the momentum equations, terms such as $[(\partial\mu/\partial z)(\partial u/\partial r)]$, which are usually present when μ is not assumed constant, have been dropped. Preliminary simulations indicated that these terms were negligible and had no perceptible influence on the results.

2.3.2.2 Parabolic forms of the governing equations

Assumptions

In addition to the assumptions given in section 2.3.2.1, the following standard boundary-layer assumptions are necessary to reduce the governing equations to a parabolic set:

- 1) Axial diffusion in the fluid is neglected;
- 2) Cross-stream pressure gradients are neglected.

With these additional assumptions, the governing equations reduce to:

Continuity equation:

$$\frac{1}{r} \frac{\partial(rv)}{\partial r} + \frac{\partial u}{\partial z} = 0 \quad (2.24)$$

r-momentum equation

$$\frac{\partial p}{\partial r} = 0 \quad ; \quad \text{thus } p = p(z) \quad (2.25)$$

z-momentum equation

$$\rho_m \left[v \frac{\partial u}{\partial r} + u \frac{\partial u}{\partial z} \right] = + \xi \rho_m g - \xi \beta \rho_m g (T - T_m) - \frac{dp}{dz} + \frac{1}{r} \frac{\partial}{\partial r} \left[r \mu \frac{\partial u}{\partial r} \right] \quad (2.26)$$

where; $\xi=1$ for the cooling in downflow case,
 $\xi=-1$ for the heating in upflow case

Energy equation

$$\rho_m C_p \left[v \frac{\partial T}{\partial r} + u \frac{\partial T}{\partial z} \right] = \frac{1}{r} \frac{\partial}{\partial r} \left[r k_f \frac{\partial T}{\partial r} \right] \quad (2.27)$$

In addition to the governing equations, boundary conditions are needed to complete the mathematical model.

2.3.2.3 Boundary conditions

With reference to Fig. 2.4, the boundary conditions are:

a) Inlet boundary conditions

For heating in upflow

For cooling in downflow

$s = s_3$ $z = 0$	$s = s_8$ $z = 0$
$u = 2V[1 - (r/r_i)^2]$ $T = T_3$	$u = 2V[1 - (r/r_i)^2]$ $T = T_8$

b) Boundary conditions in the heated and cooled sections:

For heating in upflow

For cooling in downflow

$s_3 < s \leq s_4$ $0 < z \leq L_3$	$s_8 < s \leq s_9$ $0 < z \leq L_8$
at $r=r_i$ $\left[\begin{array}{l} k_f \frac{\partial T}{\partial r} = q = \frac{P_w}{2\pi r_i L_3} \\ u = 0, v = 0 \end{array} \right.$	$T = \bar{T}_w$ $u = 0, v = 0$
at $r=0$ $\left[\begin{array}{l} \frac{\partial T}{\partial r} = 0 \\ \frac{\partial u}{\partial r} = 0, \frac{\partial v}{\partial r} = 0 \end{array} \right.$	$\frac{\partial T}{\partial r} = 0$ $\frac{\partial u}{\partial r} = 0, \frac{\partial v}{\partial r} = 0$

c) Boundary conditions in the post-heated and post-cooled sections:

For heating in upflow

For cooling in downflow

$s_4 < s \leq s_5$ $L_3 < z \leq L_3 + L_4$	$s_9 < s \leq s_{10}$ $L_8 < z \leq L_8 + L_9$
at $r=r_i$ $\left[\begin{array}{l} (2\pi r_i) k_f \frac{\partial T}{\partial r} = -U(T - T_a) \\ u=0, v=0 \end{array} \right.$	
at $r=0$ $\left[\begin{array}{l} \frac{\partial T}{\partial r} = 0 \\ \frac{\partial u}{\partial r} = 0, \frac{\partial v}{\partial r} = 0 \end{array} \right.$	

d) Outlet boundary conditions:

For heating in upflow

For cooling in downflow

$s = s_5$ $z = L_3 + L_4$	$s = s_{10}$ $z = L_8 + L_9$
$\frac{\partial u}{\partial z} = 0, v = 0$ $\frac{\partial T}{\partial z} = 0$	

where U is an overall heat loss coefficient (in W/m^2C) and T_a is the ambient temperature.

2.3.2.4 Energy equation and temperature distribution in regions outside the extended heated and cooled sections

In regions outside the extended heated and cooled sections, the heat rate per unit length to the fluid is:

$$2\pi r_i q = -U(T - T_a) \quad (s_5 < s < s_8) \text{ and } (s_{10} < s < s_3) \quad (2.28)$$

The governing one-dimensional energy equation in these sections is then given by:

$$\rho_m V A C_p \frac{dT}{ds} = -U(T - T_a) \quad (2.29)$$

The overall heat loss coefficient, U , is assumed constant throughout the loop for all V 's. This is a valid assumption provided that the level of insulation is the same everywhere and that the insulation constitutes the dominant thermal resistance. Using the section from s_5 to s_6 as an example, the corresponding temperature distribution can be expressed as:

$$T = (T_5 - T_a)e^{-\Omega(s-s_5)} + T_a \quad (s_5 < s < s_6) \quad (2.30)$$

$$\text{where } \Omega = \frac{U}{\rho_m V A C_p}$$

2.3.2.5 Non-dimensionalization of the governing equations

The details of the non-dimensionalization of the governing equations and boundary conditions are given in Appendix C. For a given closed-loop thermosyphon geometry, five independent dimensionless parameters emerge from this non-dimensionalization:

$$Gr_m = \frac{D^3 g \beta q}{\nu V_{ref} k_f} \quad (\text{modified Grashof number});$$

$$St_m = \frac{U D}{\rho_m V_{ref} A C_p} \quad (\text{modified Stanton number});$$

$$Re_{ref} = \frac{V_{ref} D}{\nu} \quad (\text{reference Reynolds number});$$

$$Pr = \frac{\mu C_p}{k_f} \quad (\text{Prandtl number});$$

$$\phi_\infty = \frac{T_a - \bar{T}_w}{qD/k_f} \quad (\text{dimensionless ambient temperature}).$$

where the reference velocity, V_{ref} , is the velocity obtained in Case (1) of the traditional model, Eq. 2.15:

$$V_{ref} = \left[\frac{P_w \beta g \Delta Z}{8\pi \mu C_p L} \right]^{1/2} \quad (2.31)$$

It should be noted that additional non-dimensional parameters are involved when conjugate heat conduction in the pipe wall is accounted for. These are introduced and discussed in Chapter 3.

2.3.3 Overview of the Solution of the Proposed Model

Equation 2.17 represents the governing momentum equation of the proposed model. In order to solve this equation for V , the average velocity inside the loop, values of $f_{hs}(s)$, $f_{cs}(s)$, $T_{hs}(s)$, $T_{cs}(s)$ are needed. These values are obtained from the numerical solutions to the governing equations in the extended heated and cooled sections. These equations were presented in section 2.3.2, and the numerical solution of these equations is discussed in Chapter 3. The temperature distributions in the insulated sections of the thermosyphon are also required to solve Eq. 2.17, and they can be obtained using the energy equation, as was shown in section 2.3.2.4.

Equation 2.17 and the set of two-dimensional numerical simulations in the extended heated and cooled sections are coupled. This implies that Eq. 2.17 depends on results of the two-dimensional numerical simulations and vice versa. This coupling constitutes the main difficulty in solving Eq. 2.17. A cursory description of the solution procedure will now be given; the complete solution methodology is presented in Chapter 4.

The solution procedure starts with guessed values for the average velocity, V , and for the inlet temperature to the heated and cooled sections, T_3 and T_8 . Then, using V , T_3 and T_8 as inlet conditions,

two-dimensional numerical solutions in the extended heated and cooled sections are obtained.

From these solutions, local values of $f_{hs}(s)$, $f_{cs}(s)$, $T_{hs}(s)$, $T_{cs}(s)$ are determined and inputted into Eq. 2.17 in order to solve for V . This new value of V and the corresponding new values of T_3 and T_8 are then used as new guessed values in the numerical simulations. This process is repeated until a converged value of V is obtained.

2.4 CLOSING REMARKS

The governing equations and boundary conditions associated with the traditional one-dimensional model and the proposed model have been presented in this Chapter. In the next Chapter, the formulation of the numerical methods for simulating mixed-convection flows will be described. The complete solution procedure of the proposed model is given in Chapter 4.

CHAPTER III

NUMERICAL SIMULATION OF MIXED-CONVECTION FLUID FLOW AND HEAT TRANSFER IN VERTICAL PIPES

3.1 INTRODUCTION

The formulation, implementation and testing of a finite-volume based numerical method for the solution of steady, laminar, two-dimensional, axisymmetric mixed-convection in vertical pipes is presented in this Chapter. This method has the capability of solving the conjugate heat transfer problem of mixed-convection in the fluid and conduction in the pipe wall.

The numerical methods developed in this Chapter serve two purposes. Firstly, as shown in Chapter 2, the finite-volume method presented in this Chapter plays a key role in the proposed closed-loop thermosyphon model. Secondly, this Chapter intends to fill the apparent void in the literature on the numerical investigation of conjugate mixed-convection in vertical pipes subjected to a uniform heat flux boundary condition.

As mentioned earlier, the thermosyphon studied in this work experiences mixed-convection situations in both the heated and cooled sections. The heated section is subjected to a uniform heat flux with an upward flow while the cooled section has a constant wall temperature boundary condition with a downward flow.

In this Chapter, however, attention is focussed exclusively on conjugate mixed-convection for upward flow in a vertical pipe subjected to a uniform heat flux. Conjugate mixed-convection for downward flow in a constant wall temperature pipe is not specifically addressed here. A numerical method for the solution of this problem would, in essence, be the same as that used to solve the uniform heat flux case just mentioned. Only very small differences in the formulation and implementation are required to handle these two different boundary conditions.

The numerical methods presented in this Chapter are largely based on the works of Patankar [1978, 1980] and Van Doormaal and Raithby [1984]. Therefore, only succinct descriptions of the key ideas will be presented.

The problem under consideration is solved here by using either the parabolic or the elliptic forms of the governing equations. The use of a parabolic scheme is attractive as it significantly reduces computer storage and execution time. However, when flow reversals occur and/or when axial conduction in the pipe wall is significant, giving rise to conjugate conduction and mixed-convection heat transfer, the use of the elliptic equations is necessary.

The remainder of this Chapter is divided into three main parts. Firstly, the governing equations and their associated boundary conditions, as well as the governing non-dimensional parameters, are described in the next section. Secondly, the integral form of a general conservation equation, the domain discretization, and the derivation and solution of the discretization equations are presented, successively, in sections 3.3 to 3.6. Thirdly, the results of the numerical code valida-

tions, performed for selected test problems, are discussed in section 3.7. The presentation of detailed numerical results is deferred to Chapter 6, where they will also be compared with experimental results.

3.2 GOVERNING EQUATIONS AND BOUNDARY CONDITIONS

Conjugate mixed-convection fluid flow and heat transfer in vertical pipes is governed by the Navier-Stokes equations, the continuity equation, and the energy equation. These equations have been presented earlier in Chapter 2, with the exception of the energy equation in the pipe, and they are repeated here for convenience. Schematic drawings of the problem of interest are presented in Figs. 3.1 and 3.2.

3.2.1 Elliptic Forms of the Governing Equations

3.2.1.1 Assumptions

The assumptions used in the derivation of the elliptic forms of the governing equations are the same as the ones presented in section 2.3.2.1, except that heat conduction in the pipe is not neglected here. As can be seen in Fig. 3.1, downstream and upstream sections have been appended to the heated section. This is to allow for the possible presence of streamwise flow reversals, and to account for axial conduction in the pipe, which preclude the study of the heated section on a stand alone basis. Furthermore, as mentioned in Chapter 2, the velocity and temperature profiles remain distorted from their fully developed forced convection shapes for some distance after the heated section, and the inclusion of a downstream section in the calculation domain is intended to allow predictions of these phenomena.

Two additional assumptions are made. Firstly, the downstream and upstream sections, including the ends of the pipe, are assumed to be perfectly insulated, thus adiabatic. Secondly, the uniform heat flux, q , is applied at the external surface of the pipe of the heated section, as shown in Fig. 3.1. It should be noted, however, that the elliptic code developed for this study has the capability of handling non-adiabatic downstream and upstream sections, and heat generation within the pipe of the heated section.

3.2.1.2 Governing equations

With reference to the nomenclature presented in Fig. 3.1, the governing equations are:

Continuity equation

$$\frac{1}{r} \frac{\partial(rv)}{\partial r} + \frac{\partial u}{\partial z} = 0 \quad (3.1)$$

r-momentum equation

$$\rho_o \left[v \frac{\partial v}{\partial r} + u \frac{\partial v}{\partial z} \right] = - \frac{\partial p}{\partial r} + \frac{1}{r} \frac{\partial}{\partial r} \left[r \mu \frac{\partial v}{\partial r} \right] - \frac{\mu v}{r^2} + \frac{\partial}{\partial z} \left[\mu \frac{\partial v}{\partial z} \right] \quad (3.2)$$

z-momentum equation

$$\rho_o \left[v \frac{\partial u}{\partial r} + u \frac{\partial u}{\partial z} \right] = - \rho_o g + \beta \rho_o g (T - T_o) - \frac{\partial p}{\partial z} + \frac{1}{r} \frac{\partial}{\partial r} \left[r \mu \frac{\partial u}{\partial r} \right] + \frac{\partial}{\partial z} \left[\mu \frac{\partial u}{\partial z} \right] \quad (3.3)$$

Energy equation in the fluid ($0 \leq r \leq r_i$)

$$\rho_o C_p \left[v \frac{\partial T}{\partial r} + u \frac{\partial T}{\partial z} \right] = \frac{1}{r} \frac{\partial}{\partial r} \left[r k_f \frac{\partial T}{\partial r} \right] + \frac{\partial}{\partial z} \left[k_f \frac{\partial T}{\partial z} \right] \quad (3.4)$$

Energy equation in the solid ($r_i \leq r \leq r_i + \delta$)

$$\frac{1}{r} \frac{\partial}{\partial r} \left[r k_s \frac{\partial T}{\partial r} \right] + \frac{\partial}{\partial z} \left[k_s \frac{\partial T}{\partial z} \right] = 0 \quad (3.5)$$

where k_f and k_s are the thermal conductivities of the fluid and of the solid, respectively, and ρ_o is the mean density of the fluid evaluated at T_o , the inlet temperature.

3.2.1.3 Boundary conditions

Inlet: $z = 0$

$0 \leq r \leq r_i$	$r_i \leq r \leq r_i + \delta$
$u = 2V[1 - (r/r_i)^2]$ $v = 0$ $T = T_o$	$u = 0$ $v = 0$ $T = T_o$

Upstream and downstream: $0 < z < L_u$ and $L_u + L_h < z < L_u + L_h + L_d$
sections

$r = 0$	$r = r_i$	$r = r_i + \delta$
$\frac{\partial u}{\partial r} = 0, v = 0, \frac{\partial T}{\partial r} = 0$	$u = 0, v = 0$	$\frac{\partial T}{\partial r} = 0$

Heated section: $L_u \leq z \leq L_h + L_d$

$r = 0$	$r = r_i$	$r = r_i + \delta$
$\frac{\partial u}{\partial r} = 0, v = 0, \frac{\partial T}{\partial r} = 0$	$u = 0, v = 0$	$k_s \frac{\partial T}{\partial r} = q$

Outlet: $z = L_u + L_h + L_d$

$0 \leq r \leq r_i$	$r_i \leq r \leq r_i + \delta$
$\frac{\partial u}{\partial z} = 0, \frac{\partial v}{\partial z} = 0, \frac{\partial T}{\partial z} = 0$	$u = 0, v = 0, \frac{\partial T}{\partial z} = 0$

3.2.2 Parabolic Forms of the Governing Equations

3.2.2.1 Assumptions

The assumptions used in the development of the parabolic forms of the governing equations have been presented in section 2.3.2.2. The fluid properties are assumed constant, except the mass density in the buoyancy term, and evaluated at the inlet temperature. Furthermore, axial heat conduction in the pipe wall is assumed to be negligible. As shown in Fig. 3.2, a downstream pipe section, which is assumed adiabatic, has been appended to the calculation domain to improve the predictions given by the proposed model. However, an upstream section is not needed, and was not added, because of the one-way behavior (Patankar [1980]) of parabolic flows.

As was the case for the elliptic code, the parabolic code can also treat variable viscosity and thermal conductivity, as well as non-adiabatic downstream sections.

3.2.2.2 Governing equations

With respect to Fig. 3.2, the governing parabolic equations are:

Continuity equation

$$\frac{1}{r} \frac{\partial(rv)}{\partial r} + \frac{\partial u}{\partial z} = 0 \quad (3.6)$$

r-momentum equation

$$\frac{\partial p}{\partial r} = 0 \quad ; \text{ thus } p = p(z) \quad (3.7)$$

z-momentum equation

$$\rho_o \left[v \frac{\partial u}{\partial r} + u \frac{\partial u}{\partial z} \right] = - \rho_o g + \beta \rho_o g (T - T_o) - \frac{dp}{dz} + \frac{1}{r} \frac{\partial}{\partial r} \left[r \mu \frac{\partial u}{\partial r} \right] \quad (3.8)$$

Energy equation

$$\rho_o C_p \left[v \frac{\partial T}{\partial r} + u \frac{\partial T}{\partial z} \right] = \frac{1}{r} \frac{\partial}{\partial r} \left[r k_f \frac{\partial T}{\partial r} \right] \quad (3.9)$$

Overall Continuity

$$\dot{m} = \int_A \rho_o u \, dA \quad (3.10)$$

where A is the cross-sectional area of the pipe and \dot{m} is the mass flowrate.

3.2.2.3 Boundary conditions

Inlet: $z = 0, 0 \leq r \leq r_i$

$u = 2V[1-(r/r_i)^2]$	$T = T_0$
-----------------------	-----------

Heated section: $0 < z \leq L_h$

$r = 0$	$r = r_i$
$\frac{\partial u}{\partial r} = 0, v = 0, \frac{\partial T}{\partial r} = 0$	$u = 0, v = 0, k_f \frac{\partial T}{\partial r} = q$

Downstream section: $L_h < z < L_h + L_d$

$r = 0$	$r = r_i$
$\frac{\partial u}{\partial r} = 0, v = 0, \frac{\partial T}{\partial r} = 0$	$u = 0, v = 0, \frac{\partial T}{\partial r} = 0$

Outlet: $z = L_h + L_d, 0 \leq r \leq r_i$

$\frac{\partial u}{\partial z} = 0, \frac{\partial v}{\partial z} = 0, \frac{\partial T}{\partial z} = 0$

The elliptic forms of the governing equations, Eqs. 3.1 to 3.5, and the parabolic forms of the governing equations, Eqs. 3.6 to 3.10, constitute sets of non-linear and coupled partial differential equations. The task is now to solve these equations numerically. Before doing this, the elliptic forms of the governing equations are non-dimensionalized to obtain the governing dimensionless parameters. In

this non-dimensionalization, the fluid properties are assumed constant.

3.2.3 Non-Dimensionalization of the Elliptic Equations

The elliptic governing equations are non-dimensionalized using the following dimensionless variables:

$$u^* = \frac{u}{V} ; \quad v^* = \frac{v}{V} ; \quad r^* = \frac{r}{D} ; \quad z^* = \frac{z}{D} ;$$

$$L_u^* = L_u/D ; \quad L_h^* = L_h/D ; \quad L_d^* = L_d/D ;$$

$$\theta = \frac{T - T_o}{qD/k_f} ; \quad \text{and} \quad P = \frac{p + \rho_o gz}{\rho_o V^2} \quad (D = 2r_i)$$

The resulting non-dimensional governing equations are:

Continuity equation

$$\frac{1}{r^*} \frac{\partial(r^* v^*)}{\partial r^*} + \frac{\partial u^*}{\partial z^*} = 0 \quad (3.11)$$

r-momentum equation

$$v^* \frac{\partial v^*}{\partial r^*} + u^* \frac{\partial v^*}{\partial z^*} = - \frac{\partial P}{\partial r^*} + \frac{1}{Re} \left[\frac{1}{r^*} \frac{\partial}{\partial r^*} \left[r^* \frac{\partial v^*}{\partial r^*} \right] - \frac{v^*}{r^{*2}} + \frac{\partial^2 v^*}{\partial z^{*2}} \right] \quad (3.12)$$

z-momentum equation

$$v^* \frac{\partial u^*}{\partial r^*} + u^* \frac{\partial u^*}{\partial z^*} = \frac{Gr_q}{Re^2} \theta - \frac{\partial P}{\partial z^*} + \frac{1}{Re} \left[\frac{1}{r^*} \frac{\partial}{\partial r^*} \left[r^* \frac{\partial u^*}{\partial r^*} \right] + \frac{\partial^2 u^*}{\partial z^{*2}} \right] \quad (3.13)$$

Energy equation in the fluid ($0 \leq r^* \leq 1/2$)

$$v^* \frac{\partial \theta}{\partial r^*} + u^* \frac{\partial \theta}{\partial z^*} = \frac{1}{Pe} \left[\frac{\partial}{\partial r^*} \left[r^* \frac{\partial \theta}{\partial r^*} \right] + \frac{\partial^2 \theta}{\partial z^{*2}} \right] \quad (3.14)$$

Energy equation in the solid ($1/2 \leq r^* \leq 1/2 + \Delta$)

$$K \frac{\partial}{\partial r^*} \left[r^* \frac{\partial \theta}{\partial r^*} \right] + K \frac{\partial^2 \theta}{\partial z^{*2}} = 0 \quad (3.15)$$

The non-dimensional boundary conditions are:

Inlet: $z^* = 0$

$0 \leq r^* \leq 1/2$	$1/2 \leq r^* \leq 1/2 + \Delta$
$u^* = 2[1 - (2r^*)^2]$ $v^* = 0$ $\theta = 0$	$u^* = 0$ $v^* = 0$ $\theta = 0$

Upstream and downstream: $0 < z^* < L_u^*$ and $L_u^* + L_h^* < z^* < L_u^* + L_h^* + L_d^*$
sections

$r^* = 0$	$r^* = 1/2$	$r^* = 1/2 + \Delta$
$\frac{\partial u^*}{\partial r^*} = 0, v^* = 0, \frac{\partial \theta}{\partial r^*} = 0$	$u^* = 0, v^* = 0$	$\frac{\partial \theta}{\partial r^*} = 0$

Heated section: $L_u^* \leq z^* \leq L_h^* + L_d^*$

$r^* = 0$	$r^* = 1/2$	$r^* = 1/2 + \Delta$
$\frac{\partial u^*}{\partial r^*} = 0, v^* = 0, \frac{\partial \theta}{\partial r^*} = 0$	$u^* = 0, v^* = 0$	$K \frac{\partial \theta}{\partial r^*} = 1$

Outlet: $z^* = L_u^* + L_h^* + L_d^*$

$0 < r^* < 1/2$	$1/2 < r^* < 1/2 + \Delta$
$\frac{\partial u^*}{\partial z^*} = 0, \frac{\partial \theta}{\partial z^*} = 0, \frac{\partial v^*}{\partial z^*} = 0$	$u^* = 0, v^* = 0, \frac{\partial \theta}{\partial z^*} = 0$

As shown by this non-dimensionalization, the governing parameters for conjugate conduction and mixed-convection heat transfer in a vertical pipe subjected to a uniform heat flux are:

$$Re = \frac{V D}{\nu} \quad (\text{Reynolds number})$$

$$Gr_q = \frac{g \beta q D^4}{\nu^2 k_f} \quad (\text{Grashof number based on heat flux})$$

$$Pe = Re \cdot Pr = \frac{\rho_0 V D C_p}{k_f} \quad (\text{Péclet number})$$

$$K = k_s / k_f \quad (\text{solid to fluid thermal conductivity ratio})$$

$$\Delta = \delta / D \quad (\text{thickness to pipe diameter ratio})$$

3.3 INTEGRAL FORM OF THE CONSERVATION EQUATIONS

The governing non-linear and coupled partial differential equations presented in the last section can be cast into the following general, conservative, form (Patankar [1980]):

$$\tilde{\nabla} \cdot \tilde{J} = S \quad (3.16)$$

where \tilde{J} is given by:

$$\tilde{J} = \rho \tilde{V} \phi - \Gamma \tilde{\nabla} \phi \quad (3.17)$$

In these equations, \tilde{J} represents the combined convection-diffusion flux of ϕ , S is the volumetric source term, ρ is the mass density, \tilde{V} is the velocity vector, Γ is the diffusion coefficient, and ϕ is a general scalar dependent variable.

The discretization equation for a scalar quantity ϕ is obtained by deriving a suitable algebraic approximation to the appropriate integral conservation principle applied to a control volume V , which is fixed in space. The integral form of Eq. 3.16 is:

$$\int_{\partial A} \tilde{J} \cdot \tilde{n} \, ds = \int_V S \, dV \quad (3.18)$$

where ∂A is the surface of the control volume, and \tilde{n} is the outward unit vector normal to the differential surface element ds . Details of the computational domain discretization will now be outlined.

3.4 DOMAIN DISCRETIZATION

In this section, the strategy used to divide the computational domain into discrete control volumes is presented. The numerical solution of the two-dimensional axisymmetric problem of interest involves finite-volume calculations over control volumes with dimensions of Δz , Δr and $\Delta \theta$, where $\Delta \theta$ is simply taken equal to 1 radian.

3.4.1 Elliptic Case

When the elliptic governing equations are used, the grid points are arranged according to the type-B practice of Patankar [1980]. Figure 3.3 shows a cross-section of the computational domain where, for reasons of clarity, a coarse grid arrangement is presented. In this figure, the dashed lines represent control volume faces and dots are main grid points.

In the type-B practice, the control volume faces are located first, then the main grid points are placed at the geometric centers of the control volumes. As shown in Fig. 3.3, this practice facilitates the location of control volume faces at discontinuities, such as the fluid/solid interface, thus allowing full advantage of the harmonic mean practice of Patankar [1978] for the interpolation of the diffusion coefficient Γ .

The grid distribution utilized in this work was non-uniform in both the z and r directions. The grid points were concentrated where the largest temperature and velocity gradients occurred: at the inlet of the

pipe; at the interface between the heated section and its downstream and upstream sections; and at the fluid/solid interface. The degree of non-uniformity used was problem dependent: it was usually chosen after a few exploratory runs were made with coarse grids.

In Fig. 3.3, the main grid point of interest is denoted by the letter P and neighbour points are identified by W, E, N, and S, with their corresponding control volume faces marked by the letters w, e, n, and s. Typically, the W and E grid points are, respectively, on the left-hand-side and right-hand-side of the calculation domain. Here, for convenience these positions have been interchanged.

Values of temperature and pressure are calculated at main grid points, while the velocity components are evaluated at staggered locations with respect to the main grid points, as shown in Fig. 3.4a,b, for reasons to be explained shortly.

3.4.2 Parabolic Case

The parabolic equations permit the use of a marching-type procedure, whereby converged values of all dependent variables are obtained at a particular axial station based solely on upstream values and boundary conditions, before moving to the next downstream station.

The domain discretization is constructed as shown in Fig. 3.5. As can be seen, a type-A grid configuration (Patankar [1980]), where control volume faces are located midway between grid points, is used in the radial direction. In the axial direction, control volume faces go from

an upstream node to the next downstream node.

Values of temperature and axial velocity are evaluated at the main grid points, while radial velocities are staggered, as shown in Fig. 3.5. The grid configuration is generated in a manner similar to the one presented above for the elliptic case, with high grid concentration at the entrance of the pipe and near the wall.

This completes the description of the domain discretization. In the next section, suitable profile assumptions between grid points are made in order to derive the discretization equations.

3.5 DISCRETIZATION EQUATIONS

In this section, the task is to derive an algebraic approximation to the general convection-diffusion equation, Eq. 3.18, for the scalar quantity ϕ . A procedure to handle the coupling between the velocity fields and pressure is also presented.

3.5.1 Elliptic Case

3.5.1.1 General convection-diffusion equation

For a known flow field, the problem reduces to a so-called convection-diffusion problem. For such a situation, the left-hand-side of Eq. 3.18 is approximated by the following:

$$\int_{\partial A} \tilde{J} \cdot \tilde{n} \, ds \approx J_e A_e - J_w A_w + J_n A_n - J_s A_s \quad (3.19)$$

where the A terms are the areas of the control volume faces, and the J terms represent total convection-diffusion fluxes across each area. In this thesis, the J terms are approximated using the hybrid difference scheme which makes use of the relative strengths of the convection and diffusion processes, expressed by the grid Péclet number (Patankar [1980]), to determine the type of interpolation function. If the absolute value of the grid Péclet number, $|Pe|$, is smaller than 2, convection and diffusion processes are properly accounted for by using the so-called central-difference scheme. If $|Pe| > 2$, then an upwind-scheme is used. Accurate solutions could be obtained with this scheme, without excessively fine grids. Thus more sophisticated schemes, such as the skew upwind schemes of Raithby [1976], were deemed unnecessary.

The source term on the right-hand-side of Eq. 3.18 is approximated by:

$$\int_V S \, dV \approx \bar{S} \Delta V \quad (3.20)$$

In order that the resulting discretization equations remain nominally linear, \bar{S} is linearized using the technique described by Patankar [1980]:

$$\bar{S} = S_c + S_p \phi_p \quad (3.21)$$

where ϕ_p is the value of the scalar quantity ϕ at grid-point P ,

S_p is the coefficient of ϕ_p , and S_c is the part of \bar{S} that does not depend explicitly on ϕ_p .

With these considerations, the general discretization equation has the following form:

$$a_p \phi_p = a_E \phi_E + a_W \phi_W + a_N \phi_N + a_S \phi_S + b \quad (3.22)$$

where, with the hybrid scheme, the coefficients are given by (with reference to the notation in Fig. 3.3):

$$a_E = \left| -F_e, D_e - F_e/2, 0 \right|_{\max} \quad (3.23)$$

$$a_W = \left| F_w, D_w + F_w/2, 0 \right|_{\max} \quad (3.24)$$

$$a_N = \left| -F_n, D_n - F_n/2, 0 \right|_{\max} \quad (3.25)$$

$$a_S = \left| F_s, D_s + F_s/2, 0 \right|_{\max} \quad (3.26)$$

$$a_p = a_N + a_S + a_W + a_E - S_p \Delta V \quad (3.27)$$

$$b = S_c \Delta V \quad (3.28)$$

The terms a_E , a_W , a_N , and a_S are the coefficients of the E, W, N, and S neighbouring values of ϕ , respectively, F 's ($F = \rho uA$) represent the mass flowrate across a control volume face, and D 's ($D = \Gamma A/\delta x$) are diffusion conductances. The diffusion conductances are calculated according to the harmonic mean practice of Patankar [1978]. With

respect to the nomenclature of Fig. 3.6 and taking D_n as an example, the appropriate expression for the diffusion conductance is:

$$D_n = \left[\frac{(\delta x)_{n-}}{\Gamma_p} + \frac{(\delta x)_{n+}}{\Gamma_N} \right]^{-1} A_n \quad (3.29)$$

Equation 3.22 can be written more compactly as:

$$a_p \phi_p = \sum a_{nb} \phi_{nb} + b \quad (3.30)$$

where the subscript "nb" stands for neighbour and the summation is to be taken over all neighbours.

Using Eq. 3.30, the discretization equations for the whole calculation domain and for every scalar dependent variable can be constructed. However, some special considerations have to be given to the treatment of the fluid flow.

3.5.1.2 Fluid flow equation

The difficulty in the evaluation of the flow field is the unknown pressure field. Examination of the governing momentum equations reveals the presence of a pressure gradient term. In these equations, unless the correct pressure field is employed, the resulting velocity field will not satisfy the continuity equation.

In this thesis, the discretized momentum equations are first solved based on guessed velocity, temperature, and pressure fields. Then the

SIMPLEC procedure of Van Doormaal and Raithby [1984] is used to correct the guessed pressure and calculated velocity fields so as to satisfy the continuity requirements. Then the discretized energy equations are solved. This procedure is then repeated iteratively, until convergence.

Staggered grid geometry

Patankar [1980] has shown that if the velocity components and pressure are calculated at the same grid-point location, physically unrealistic situations may arise. To avoid such problems, Patankar [1980] suggests to calculate pressure and all other variables, except the velocity components, at the main grid points, and to evaluate the u- and v-velocity components at staggered locations with respect to the main grid point P, as shown in Fig. 3.4.

Discretized momentum equation

With respect to the u control volume of Fig. 3.4b, the discretized form of the z-momentum equation, which can be derived in a manner similar to the one used to obtain Eq. 3.30, has the following form:

$$a_n u_n = \sum a_{nb} u_{nb} + b + A_n (p_p - p_N) \quad (3.31)$$

where, the last term reflects the integration of $\partial p / \partial x$ over the control volume, and A_n is the area on which the pressure difference acts. The expressions for a_{nb} , a_n , and b are calculated using the same approach that was used to obtain the corresponding expressions in Eqs. 3.23 to 3.28, by properly accounting for the staggered-grid

geometry when calculating the D and F terms.

Pressure correction equation

Using a guessed pressure field, denoted by $p^\#$, the resulting velocities, $u^\#$, obtained by solving the z-momentum equation, Eq. 3.31, are:

$$a_n u_n^\# = \sum a_{nb} u_{nb}^\# + b + A_n (p_p^\# - p_N^\#) \quad (3.32)$$

The $v^\#$ velocities field can also be obtained in a similar manner.

The calculated $u^\#$ and $v^\#$ fields will generally violate the continuity requirement, because of the incorrect guessed pressure field. A pressure correction, p' , is proposed to correct this estimated pressure field:

$$p = p^\# + p' \quad (3.33)$$

The resulting velocity corrections, u' and v' , are used to correct the $u^\#$ and $v^\#$ fields:

$$u = u^\# + u' \quad (3.34)$$

$$v = v^\# + v' \quad (3.35)$$

By subtracting Eq. 3.32 from Eq. 3.31 and using Eqs. 3.34 and 3.35, the following equation is obtained:

$$a_n u_n' = \sum a_{nb} u_{nb}' + A_n (p_p' - p_N') \quad (3.36)$$

The term $\sum a_{nb} u'_n$ is subtracted from both sides of this equation, and the term $\sum a_{nb} (u'_{nb} - u'_n)$ is neglected, following the SIMPLEC procedure of Van Doormal and Raithby [1984]. Then

$$u_n = u_n^* + d_n (p'_p - p'_n) \quad (3.37)$$

with

$$d_n = \frac{A_n}{(a_n - \sum a_{nb})} \quad (3.38)$$

Correction equations for the v velocity components can be derived using the same approach.

The p' equation can then be obtained by substituting the velocity correction equations, such as Eq. 3.37, into the discretized continuity equation. With respect to a main grid point P and its associated control volume, the pressure correction equation is:

$$a_p p'_p = a_E p'_E + a_W p'_W + a_N p'_N + a_S p'_S + b' \quad (3.39)$$

where,

$$a_E = \rho A_e d_e \quad (3.40)$$

$$a_W = \rho A_w d_w \quad (3.41)$$

$$a_N = \rho A_n d_n \quad (3.42)$$

$$a_S = \rho A_s d_s \quad (3.43)$$

$$a_p = a_E + a_W + a_N + a_S \quad (3.44)$$

$$b' = \rho v_w^* A_w - \rho v_e^* A_e + \rho u_s^* A_s - \rho u_n^* A_n \quad (3.45)$$

The b' term in Eq. 3.39 represents an apparent mass source resulting from the fact that the calculated velocity fields, $u^{\#}$ and $v^{\#}$, do not necessarily satisfy continuity requirements. Using velocity correction equations, such as Eq. 3.37, the calculated velocity fields are corrected using the p' field obtained by solving the equation set given by Eq. 3.39. This process eliminates, after some iterations, the apparent mass source term.

All the tools necessary to obtain the flow field have now been described. The various steps in the solution process, which uses the SIMPLEC procedure, are as follows:

Synopsis of the SIMPLEC procedure

1. Start with guessed values for the dependent variables: $u^{\#}$, $v^{\#}$, $p^{\#}$, and $T^{\#}$.
2. Evaluate the coefficients of the discretized momentum equations, such as Eq. 3.32, and solve to obtain updated values of $u^{\#}$ and $v^{\#}$.
3. Calculate the coefficients of the p' equation (Eq. 3.39) and solve to obtain the p' field.
4. Correct the velocity and pressure fields (Eqs. 3.33 to 3.35), using the values of p' calculated in step 3.
5. Solve for temperature, using Eq. 3.30, and update fluid properties, if necessary.
6. Treat the freshly calculated, and corrected, values of the dependent variables as new guessed values, and return to step 2. Repeat this sequence of steps until convergence is achieved.

3.5.1.3 Finishing touches

Source terms

In the development of the general convection-diffusion equation, Eq. 3.30, the source term ($\bar{S} = S_c + S_p \phi_p$) may be used to account for expressions that can not be cast into the general form of the partial differential equations given by Eqs. 3.16 and 3.17. Two occurrences of such expressions and their incorporation in the source term will now be briefly presented.

In the r-momentum equation (Eq. 3.2), the $-\mu v/r^2$ term was incorporated in the source term. In accordance with the rules established by Patankar [1980], the two components of the source term have been set equal to:

$$S_c = 0 \quad \text{and} \quad S_p = -\mu/r^2 \quad (3.46)$$

The buoyancy term in the z-momentum equation (Eq. 3.3) was also included in the source term as follows:

$$S_c = \beta \rho_0 g (T - T_0) \quad \text{and} \quad S_p = 0 \quad (3.47)$$

Treatment of the solid region

In this thesis, the discretization equations of all dependent variables are established over the whole calculation domain, including the solid region. In the solid region, the u and v velocities are set to

zero by overwriting the coefficients of the corresponding discretized equations. In Eq. 3.31, the a_{nb} coefficients and the $[b + A_n(p_p - p_n)]$ term are overwritten to zero, and the a_n coefficient is set equal to unity. As well, the d_n term, in Eq. 3.38, is set to zero.

Since the calculation domain includes both the fluid and solid regions, the calculation procedure must properly account for the internal fluid/solid interface. This is handled here by placing a control volume face at the interface and by using the harmonic mean practice of Patankar [1980], given by Eq. 3.29.

For fluid flow, the dynamic viscosity in the solid is set to a large value, typically $\mu \approx 10^{30}$, so that the fluid region will experience the correct boundary condition at the interface (Patankar [1980]). As for the temperature field, no special treatment is necessary. The true conductivities are used in both the fluid and solid regions, and the harmonic mean practice is used to evaluate the interface heat flux.

3.5.2 Parabolic Case

In this thesis, the parabolic discretization equations are obtained by using a fully implicit scheme. As shown by Patankar [1980], the fully implicit formulation ensures that the coefficients of the discretization equations remain positive, thereby avoiding physically unrealistic results.

3.5.2.1 Convection-diffusion equation

With respect to the nomenclature presented in Fig. 3.5, where the shaded area represents the control volume of interest, the general convection-diffusion equation can be written as:

$$a_p \phi_p = a_E \phi_E + a_W \phi_W + a_p^0 \phi_p^0 + b \quad (3.48)$$

where ϕ_p^0 refers to a converged value of ϕ obtained at the preceding axial station $(i-1)$.

There is no downstream $(i+1)$ neighbour, due to the one-way nature of parabolic flows. The hybrid difference scheme was used in the radial direction to obtain the interpolation function. Thus, the a_E and a_W coefficients are given by equations similar to Eqs. 3.23 and 3.24, respectively. In the z direction, due to the assumption of negligible axial diffusion, the a_p^0 coefficient is simply given by:

$$a_p^0 = \rho A_p u_p^0 \quad (3.49)$$

where A_p is the control surface area associated with the velocity u_p . With respect to the nomenclature given in Fig. 3.5, A_p is equal to $(1/2)(r_E^2 - r_W^2)$. The a_p coefficient and the b term are given by:

$$a_p = a_W + a_E + a_p^0 - S_p \Delta V \quad (3.50)$$

$$b = S_c \Delta V \quad (3.51)$$

With the fully implicit formulation, all dependent variables at station 'i' are assumed to prevail over the whole axial distance from P^0 to P, Δz in Fig. 3.5.

3.5.2.2 Fluid flow equation

With reference to Fig. 3.5, the discretized form of the z-momentum equation is given by:

$$a_p u_p = a_E u_E + a_W u_W + a_p^0 u_p^0 + b + (-dp/dz)\Delta V \quad (3.52)$$

where u_p^0 is the converged u-velocity component obtained at the previous axial station, and ΔV represents the volume of the control volume. The a_E , a_W , a_p^0 , and a_p coefficients are obtained using the corresponding expressions in Eqs. 3.23, 3.24, 3.49, and 3.50. The buoyancy term in the governing equation is included into the source term as shown in Eq. 3.47. Generally, the u-velocity field obtained by solving Eq. 3.52 will not satisfy the overall continuity equation, unless the correct pressure field is employed. Therefore, a correction procedure, similar to the one used for the elliptic case, is needed. A pressure gradient correction, $(-dp/dz)'$, is proposed to correct the estimated pressure gradient field, $(-dp/dz)^\#$, such that:

$$(-dp/dz) = (-dp/dz)^\# + (-dp/dz)' \quad (3.53)$$

the resulting u-velocity correction, u' , is used to correct the calculated velocity field, $u^\#$:

$$u = u^{\#} + u' \quad (3.54)$$

Using a methodology similar to SIMPLEC described in section 3.5.1.2, the corrected equation for the u-velocity component is then:

$$u_p = u_p^{\#} + d_p (-dp/dz)' \quad (3.55)$$

where,

$$d_p = \frac{\Delta V}{(a_p - a_w - a_e)} \quad (3.56)$$

The $(-dp/dz)'$ equation is obtained using the overall continuity equation (Eq. 3.10), which can be written as:

$$\dot{m} = \int_0^{r_i} \rho u r dr \quad (3.57)$$

where \dot{m} , the mass flowrate per radian of cross-section, is known from the inlet boundary condition. Numerically, Eq. 3.57 is given by:

$$\dot{m} = \sum \rho u_p A_p \quad (3.58)$$

where the summation is to be taken over all grid points in the radial direction. Substituting Eq. 3.55 into Eq. 3.58 yields:

$$\dot{m} = \sum \rho u_p^{\#} A_p + \sum \rho A_p d_p (-dp/dz)' \quad (3.59)$$

The pressure gradient correction equation is then given by:

$$(-dp/dz)' = \frac{\dot{m} - \sum \rho u_p^* A_p}{\sum \rho A_p d_p} \quad (3.60)$$

Once the corrected u-velocity field has been determined, the equation of continuity is used to get the v-velocity components. With respect to the control volume shown in Fig. 3.5, the discretized local continuity equation is:

$$\rho A_p u_p - \rho A_p u_p^0 = \rho A_w v_w - \rho A_e v_e \quad (3.61)$$

where,

$$A_e = r_e \Delta z, \text{ and } A_w = r_w \Delta z$$

With the discretization equations in hand, a solution procedure akin to a marching SIMPLEC procedure can be used. At each z location of interest, this procedure is as follows:

1. Start with guessed values for the dependent variables: $u^{\#}$, $v^{\#}$, $(-dp/dz)^{\#}$, and $T^{\#}$.
2. Evaluate the coefficients of the discretized z-momentum equations (Eq. 3.52) and solve to obtain updated values of $u^{\#}$.
3. Solve the $(-dp/dz)'$ equation (Eq. 3.60).
4. Correct the pressure gradient and the u-velocity field (Eqs. 3.53 and 3.55) using the value of $(-dp/dz)'$.
5. Evaluate the v velocities using local continuity (Eq. 3.61).
6. Solve for temperature, using Eq. 3.48, and update fluid properties, if necessary.
7. Treat the freshly calculated values of the dependent variables as new guessed values and return to step 1. Repeat this sequence of calculations until convergence is achieved.

3.6 SOLUTION OF THE NOMINALLY-LINEAR DECOUPLED SETS OF DISCRETIZATION EQUATIONS

The proposed finite-volume method leads to the formulation of nominally-linear and decoupled algebraic equations at each grid point for each dependent variable ϕ . This section describes how these equations were solved.

For the elliptic case, a line-by-line iterative method is used to solve the discretized equations. In this method, the equations for a given ϕ are solved simultaneously along a particular grid line, using the TriDiagonal Matrix Algorithm (TDMA), as shown by Patankar [1980]. The latest values of ϕ at grid points on neighbouring lines are used whenever needed. The calculation domain is then "swept" line by line in order to visit all grid lines. In all, four different sweeps, performed in alternating directions, constitute one step of this line-by-line iterative procedure. Typically, in this work, the maximum number of such steps for any dependent variable was set to 5. Evaluation of all ϕ variables using this technique constitutes one iteration of the elliptic code.

For the parabolic case, converged values of all dependent variables are obtained along a particular grid line normal to the main flow direction, before moving to the next grid line. The equations for all dependent variables, except the v velocity component, are solved using a TDMA. The v velocity component is obtained by solving Eq. 3.61 at each radial location, starting from $r = 0$. Once all dependent variables have been calculated in this manner, one step of the overall iteration

of the parabolic code at that particular axial location is said to be complete.

In order to avoid divergence in the iterative process, the changes in the dependent variables are moderated, in both the elliptic and parabolic codes, by using the implicit under-relaxation procedure of Patankar [1980]:

$$\phi_p = \phi_p^o + \alpha \left[\frac{\sum a_{nb} \phi_{nb} + b}{a_p} - \phi_p^o \right] \quad (3.62)$$

where ϕ_p^o is the value of ϕ_p obtained from the previous iteration, and α is the relaxation factor. In effect, the use of α damps the change in ϕ_p , which is represented by the contents of the bracket in Eq. 3.62. In this thesis, the following values of α were used:

Elliptic case

$$\alpha_u = 0.5$$

$$\alpha_v = 0.5$$

$$\alpha_p = 1.0$$

$$\alpha_T = 1.0$$

Parabolic Case

$$\alpha_u = 0.5$$

$$\alpha_{dp/dz} = 1.0$$

$$\alpha_T = 1.0$$

The overall convergence of the SIMPLEC procedure was determined by monitoring, at the end of each iteration, the changes in u and T at each grid point in the calculation domain. When the absolute values of the relative changes in u and T between two successive iterations were all below a certain tolerance, typically set at 10^{-4} , the solution was con-

sidered to have converged. In the case of the u velocity component, the changes are normalized using the average velocity V . Thus, in mathematical terms, a solution is considered to have converged when the following conditions are met:

$$\left| \frac{u_p^i - u_p^{i-1}}{V} \right| < 10^{-4} , \quad \left| \frac{T_p^i - T_p^{i-1}}{T_p^{i-1}} \right| < 10^{-4} \quad (\text{for all grid points})$$

where the superscript "i" represents the current iteration.

3.7 COMPUTER CODE IMPLEMENTATION AND VALIDATION

The numerical techniques presented in this Chapter were implemented in computer codes. The elliptic and parabolic codes were developed on a Hewlett-Packard Vectra personal computer (AT-compatible) using the Lahey FORTRAN77 (Version 2.20) compiler. In their final versions, both codes could run on a personal computer. However, because of the storage and speed limitations of the personal computers used in this work, whenever the grid size was higher than $\approx 120 \times 30$, the elliptic code was run on an IBM 3090-180E/VF computer using a Fujitsu FORTRAN77 compiler.

During the development stage, the codes were validated against several test problems. The results of four relevant tests will now be presented.

3.7.1 Laminar Mixed-Convection in a Vertical Pipe Subjected to a Uniform Heat Flux Boundary Condition

The objective of this test was to duplicate the experimental results obtained by Hallman [1958] on laminar mixed-convection flows in a vertical pipe subjected to a uniform heat flux. The average operating conditions are presented on Fig. 3.7, which shows the results of a comparison between the numerically calculated Nusselt numbers (Nu) and the experimentally determined Nu of Hallman [1958] as a function of a non-dimensional axial distance. Hallman [1958] calculated his dimensionless parameters using fluid properties evaluated at the local film temperature. The numerical calculations were also performed, for both the elliptic and parabolic codes, with variable viscosity and thermal conductivity, evaluated at the local film temperature. The specific heat and the mass density, except in the buoyancy term, were taken as constant. As shown in Fig. 3.7, the agreement is very good, indicating that both codes were adequately implemented and that the assumptions of constant specific heat and mass density, which are reported in this Chapter and in Chapter 2, are more than adequate. Not reported on Fig. 3.7, are grid independence checks that were performed for these conditions. These grid checks indicated that the numerical simulations were essentially grid independent, in so far as the Nusselt number is concerned, for a grid size of 70×15 . A further discussion on grid independence checks for cases of mixed-convection in vertical pipes is provided in section 6.2.3.

3.7.2 Sudden Expansion in a Pipe

Macagno and Hung [1967] conducted a complementary numerical and experimental study of flow through an axisymmetric sudden expansion in a isothermal pipe. This problem was numerically simulated using the elliptic code, and the results are shown in Fig. 3.8. As indicated in Fig. 3.8, both the upstream to downstream diameter ratio and the length to downstream diameter ratio were equal to 2. The flow at the entrance of the small diameter pipe was assumed to correspond to that of fully developed Poiseuille flow with $Re = 40$. Numerical calculations were performed over the whole calculation domain, and the region shown as a shaded area in Fig. 3.8 was treated as a solid region using the concepts presented in section 3.5.1.3. The numerically generated streamlines presented in Fig. 3.8 are indistinguishable from the streamlines of Macagno and Hung [1967] and, therefore, the agreement can be considered excellent.

3.7.3 Mixed-Convection in a Vertical Pipe Subjected to a Constant Wall Temperature Boundary Condition

Even though the numerical formulation presented in this Chapter was concerned primarily with the uniform heat flux boundary condition, the proposed model requires numerical simulations in the constant wall temperature section of the closed-loop thermosyphon. Therefore, it was necessary to test the implementation of the constant wall temperature boundary condition in the computer codes. This was done using the numerical data of Marner and McMillan [1970] on mixed-convection flows in constant wall temperature vertical pipes in which the inlet velocity

was assumed to correspond to that of fully developed Poiseuille flow.

The results of this test are shown in Fig. 3.9, where axial velocities, normalized with the average velocity, are plotted against the non-dimensional radial distance for two particular values of the $(z/r_1)/Pe$ parameter, and for values of $Gr/Re = 120$ and $Pr = 1$. The parabolic code was run with a grid size of 200×20 and the elliptic code with a grid size of 130×20 . It can be seen that there is very good agreement between results of the present numerical codes and the data of Marner and McMillan [1970].

3.7.4 Conjugate heat transfer in axisymmetric pipe flows

The coupling of heat conduction in the wall and convection in the fluid, also referred to as conjugate heat transfer, is also of prime importance in this study. In order to verify the computer implementation of this coupling, the elliptic code was tested against the numerical data of Fithen and Anand [1988], with a grid size of 155×17 .

Fithen and Anand [1988] studied conjugate heat transfer in a pipe subjected to an external uniform heat flux boundary condition. The flow was assumed to correspond to that of fully developed Poiseuille flow over the whole calculation domain, which included pre-heated and post-heated sections. Some of their results are shown in Fig. 3.10 along with results generated with the present elliptic code. The values of the governing non-dimensional parameters are $Pe = 50$, $K = 50$, and $\Delta = 0.05$. In this figure, q_i/q represents the ratio of the local heat flux at the inner surface to the applied uniform heat flux at the outer

surface (normalized with the internal radius). As can be seen in Fig. 3.10, the results given by the elliptic code are in excellent agreement with the results of Fithen and Anand [1988].

3.8 CLOSING REMARKS

The numerical methods used to simulate conjugate conduction and mixed-convection in vertical pipes have been presented in this Chapter. As will be shown in the next Chapter and in Chapter 7, these numerical methods constitute an important component of the proposed model of closed-loop thermosyphons. In addition, numerical results on conjugate conduction and mixed-convection fluid flow and heat transfer in vertical pipes, without the closed-loop interaction, are presented in Chapter 6.

CHAPTER IV

SOLUTION OF THE PROPOSED MODEL

4.1 INTRODUCTION

The proposed model involves the iterative coupling of local results of two-dimensional numerical simulations performed in the heated and cooled sections with a traditional one-dimensional analysis. Attention is focussed on cases where ΔZ is small and where the flow is by mixed-convection in the heated and cooled sections of the thermosyphon. The mathematical concepts of the proposed model were presented in Chapter 2 and the formulation and implementation of the two-dimensional finite-volume numerical methods were described in Chapter 3. In this Chapter, the complete solution methodology of the proposed model is presented.

An overview of the proposed model is presented in the next section. This is then followed, in section 4.3, by a step-by-step description of the solution methodology. Section 4.4 presents the specific model pertaining to the present experimental apparatus.

4.2 OVERVIEW OF THE PROPOSED MODEL

4.2.1 One-Dimensional Momentum Equation

With reference to the nomenclature presented in Fig. 2.1, it was shown, in Chapter 2, that the governing one-dimensional momentum equa-

tion of the proposed model is :

$$\begin{aligned}
 v^2 \left[\frac{16}{Re} \int_{s_{10}}^{s_3} ds + \int_{s_3}^{s_5} f_{hs}(s) ds + \frac{16}{Re} \int_{s_5}^{s_8} ds + \int_{s_8}^{s_{10}} f_{cs}(s) ds \right] = \\
 r_i g \beta \left[\int_{s_{10}}^{s_3} T(s) \cos \theta ds + \int_{s_3}^{s_5} T_{hs}(s) \cos \theta ds + \int_{s_5}^{s_8} T(s) \cos \theta ds + \int_{s_8}^{s_{10}} T_{cs}(s) \cos \theta ds \right]
 \end{aligned}
 \tag{2.17}$$

In the proposed model, the values of $f_{hs}(s)$, $f_{cs}(s)$, $T_{hs}(s)$, and $T_{cs}(s)$ are numerically determined using two-dimensional simulations in the extended heated and cooled sections of the closed-loop thermosyphon.

The task in this Chapter is to solve Eq. 2.17, in conjunction with the two-dimensional numerical simulations in the extended heated and cooled sections, in order to obtain V and the temperature distribution around the loop.

4.2.2 Incorporation of Two-dimensional Numerical Inputs

Since the values of $f_{hs}(s)$, $f_{cs}(s)$, $T_{hs}(s)$, and $T_{cs}(s)$ are determined numerically, they are discrete values prevailing over certain finite distances, Δs . With these considerations, the integrals in the extended heated and cooled sections of the thermosyphon are replaced by

summations in Eq. 2.17:

$$\begin{aligned}
 v^2 \left[\frac{16}{\text{Re}} \int_{s_{10}}^{s_3} ds + \sum_{i=1}^{i=L1} f_{hs,i} \Delta s_i^u + \frac{16}{\text{Re}} \int_{s_5}^{s_8} ds + \sum_{i=1}^{i=L1} f_{cs,i} \Delta s_i^u \right] = \\
 r_i g \beta \left[\int_{s_{10}}^{s_3} T(s) \cos \theta \, ds + \sum_{i=1}^{i=L1} T_{hs,i} \cos \theta \, \Delta s_i^T + \int_{s_5}^{s_8} T(s) \cos \theta \, ds + \right. \\
 \left. + \sum_{i=1}^{i=L1} T_{cs,i} \cos \theta \, \Delta s_i^T \right] \quad (4.1)
 \end{aligned}$$

where, as shown in Fig. 3.3, the subscript "i" refers to a particular grid location and L1 represents the total number of grid points in the axial direction. The superscripts T and u refer to temperature and axial velocities, respectively.

The Fanning friction factors, $f_{cs,i}$ and $f_{hs,i}$, and the mean cross-sectional temperatures, $T_{hs,i}$ and $T_{cs,i}$, are obtained by using suitable numerical approximations of Eqs. 2.18 and 2.19. As mentioned in Chapter 3, when the elliptic set of the governing equations is used, temperatures are evaluated at main grid points and axial velocities are calculated at staggered locations to the main grid points. Thus, $f_{hs,i}$ and $f_{cs,i}$ prevail over the distance between two main grid points, denoted by Δs_i^u in Fig. 3.4b and in Eq. 4.1, while $T_{hs,i}$ and $T_{cs,i}$ prevail over the distance between main-grid control volume faces, indicated by Δs_i^T in Fig. 3.3 and in Eq. 4.1.

In the case where the parabolic set of the governing equations is employed, temperature and axial velocities are calculated at main grid points. Because of the fully implicit formulation, which was discussed in Chapter 3, the velocities and, consequently, $f_{hs,i}$ and $f_{cs,i}$, as well as $T_{hs,i}$ and $T_{cs,i}$, are assumed to prevail over the whole distance between two successive grid points in the main flow direction. This distance is identified as Δs_i^T and Δs_i^U in Fig. 3.5 and in Eq. 4.1. The final form of the one-dimensional momentum equation, after incorporation of the two-dimensional numerical inputs, can now be obtained by solving the remaining integrals in Eq. 4.1:

$$\begin{aligned}
 v^2 \left[\frac{16}{Re} (L_{10} + L_1 + L_2 + L_5 + L_7 + 2\pi R) + \sum_{i=1}^{i=L1} f_{hs,i} \Delta s_i^U \right. \\
 \left. + \sum_{i=1}^{i=L1} f_{cs,i} \Delta s_i^U \right] = r_i g \beta \left[- \frac{(T_{10} - T_a)}{\Omega} (1 - e^{-\Omega L_{10}}) - T_a L_{10} \right. \\
 + \frac{(T_1 - T_a)}{\Omega} (1 - e^{-\Omega L_1}) + T_a L_1 + \frac{(T_2 - T_a)}{\Omega} (1 - e^{-\Omega L_2}) + T_a L_2 \\
 + \sum_{i=1}^{i=L1} T_{hs,i} \Delta s_i^T + \frac{(T_5 - T_a)}{\Omega} (1 - e^{-\Omega L_5}) + T_a L_5 - \frac{(T_7 - T_a)}{\Omega} (1 - e^{-\Omega L_7}) \\
 \left. - T_a L_7 - \sum_{i=1}^{i=L1} T_{cs,i} \Delta s_i^T + \frac{\Omega R^2 (e^{-\pi R \Omega} + 1)}{(\Omega^2 R^2 + 1)} (T_6 - T_{11}) \right] \quad (4.2)
 \end{aligned}$$

where the modified heat loss coefficient, Ω , was defined in Chapter 2 as $\Omega = U/\rho_m VAC_p$. When heat losses are negligible,

it can be shown that Eq. 4.2 reduces to:

$$\begin{aligned}
 V^2 & \left[\frac{16}{Re} (L_{10} + L_1 + L_2 + L_5 + L_7 + 2\pi R) + \sum_{i=1}^{i=L_1} f_{hs,i} \Delta s_i^u + \sum_{i=1}^{i=L_1} f_{cs,i} \Delta s_i^u \right] \\
 & = r_i g \beta \left[T_{10} (L_1 + L_2 - L_{10}) + T_5 (L_5 - L_7) + \sum_{i=1}^{i=L_1} T_{hs,i} \Delta s_i^T - \sum_{i=1}^{i=L_1} T_{cs,i} \Delta s_i^T \right] \quad (4.3)
 \end{aligned}$$

4.3 SOLUTION OF THE PROPOSED COUPLED 1-D/2-D MODEL

4.3.1 Preliminary Considerations

The solution of Eq. 4.2 presents two difficulties. Firstly, it can be seen that Eq. 4.2 is a transcendental equation since V is involved on both sides of the equation. This means that root finding techniques, such as the secant method, will have to be appropriately used to obtain V . Secondly, and more importantly, the solution of Eq. 4.2 requires the inputs of two-dimensional numerical simulations which themselves depend on V . In this work, Eq. 4.2 and the two-dimensional numerical simulations in the extended heated and cooled sections are carefully decoupled and solved iteratively to obtain V and the temperature distribution around the loop.

The dimensionless parameters of the proposed model were identified in Chapter 2 and in Appendix C. However, for convenience, the dimensional forms of the equations will be used here. Examination of the dimensionless parameters indicates that the solution for a given set of these parameters can be uniquely determined when suitable values of the

following dimensional values are specified: P_w , \bar{T}_w , r_i , U , T_a , R , and the lengths of the various sections of the loop. The following step-by-step solution procedure is performed for a given set of these fixed values.

It should be recalled that the two-dimensional numerical simulations can be accomplished using either the parabolic or the elliptic set of the governing equations of mixed-convection flows. The simulations are performed according to the numerical formulation given in Chapter 3. The parabolic code has the advantage of being less computer intensive than the elliptic code, but, unlike the elliptic code, it can not handle streamwise flow reversals that may occur in the heated or cooled sections of the closed-loop. The solution methodology is essentially the same in both cases; differences will be noted below.

The solution procedure has been coded in FORTRAN77 and executed, for the most part, on a 80386-based personal computer running at 25 MHz and using the Lahey FORTRAN77 Version 2.20 compiler. Occasionally, for fine grids, the code was compiled using the Fujitsu FORTRAN77 compiler and run on McGill's IBM 3090-180E/VF computer.

4.3.2 Solution Methodology

4.3.2.1 Step 1: Choice of starting conditions

The solution process starts by selecting a guessed average velocity, V_g . The value of V_g has to be reasonably close to the final result, otherwise the solution process may not converge. In this investigation, experience has shown that the velocity obtained for Case 1 of the traditional model (Eq. 2.15) constituted a good guess to initiate the solution of the proposed model. Thus, V_g is set equal to:

$$V_g = \left[\frac{P_w g \beta \Delta Z}{8\pi C_p \mu L} \right]^{1/2} \quad (2.15)$$

The lengths of the "post" sections, L_4 and L_9 , are then determined based on preliminary simulations where various lengths of the "post" sections are examined. The final lengths of the "post" sections are determined when the Fanning friction factors are within 20 % of their fully developed value, $16/Re$. The lengths of both "post" sections are then set and remain unchanged throughout the remainder of the procedure. This appeared, although no optimization studies were undertaken, to be a reasonable compromise between the accuracy of the model and computational cost. Typically, the lengths of these "post" sections were approximately the same as the lengths of the heated and cooled sections.

Preliminary simulations were also used to determine which grid spacing, in the two-dimensional numerical simulations, provided an essentially grid independent solution. Grid independence results as well as the determination of the lengths of the post sections are dependent on

the geometry of the closed-loop; these matters will be further discussed in Chapter 7 in conjunction with the presentation of results.

The nodal temperatures around the loop, T_1, T_2, \dots, T_{11} (Fig. 2.1), are then calculated based on the value of V_g and using the procedure described in Appendix D.

In the following presentation of the methodology, two subscripts are used, namely, m and n . The former one (m) refers to the number of coupling cycles between Eq. 4.2 and the two-dimensional numerical simulations, and the latter one (n) to the number of iterations within the secant method used to solve Eq. 4.2 with given numerical inputs. Execution of Steps 2 to 6 described in the following sub-sections constitutes one coupling cycle.

4.3.2.2 Step 2: Numerical simulations in the extended heated and cooled sections

The latest calculated values of V_g, T_3, T_8 and of the dependent variables in the extended heated and cooled sections $T(i,j), u(i,j), v(i,j)$, and $p(i,j)$, are used to initiate the numerical simulations. Depending on whether the parabolic or the elliptic code is used, the numerical simulations are performed differently.

Elliptic case

In this case it is unnecessary, considering the relatively high computational cost involved with the elliptic code, to obtain a converged

solution in each overall coupling cycle, when it is expected that values of V_g , T_3 , and T_8 will change at the beginning of the next cycle. Typically, in the present study, 50 numerical iterations, as defined in Chapter 3, were performed within each coupling cycle and in both extended sections. However, in the case of the first cycle ($m = 1$) and for the range of conditions experienced in this work, approximately 100 iterations were necessary for the temperature and velocity profiles to take shape. If fewer iterations are performed in the first cycle, erroneous temperatures and friction factors will be inputted into Eq. 4.2, resulting in a possible divergence when solving for V . As the number of overall coupling cycles (m) increases, and the values of V_g , T_3 , and T_8 approach convergence, the 50 numerical iterations performed in each overall cycle were found to produce adequately converged two-dimensional solutions.

Parabolic code

In this case, the numerical computations are relatively inexpensive and calculations are performed, in each overall cycle, until numerical convergence is attained.

Final calculations in Step 2

After completion of the numerical simulations, the values of all dependent variables, at each grid point, are stored for latter retrieval. These values are used as starting values for the next set of iterations at the beginning of the next cycle. The following local values are also calculated and stored: $T_{hs,i,m}$, $T_{cs,i,m}$, $f_{hs,i,m}$, $f_{cs,i,m}$,

and the average Nusselt number in the cooled section, \overline{Nu} , which is defined in the nomenclature. As noted earlier, the subscripts "i" and "m" refer to the axial grid location and to the cycle number, respectively.

4.3.2.3 Step 3: Determination of correction ratios

In this step, axial temperature distributions are first calculated, for each Δs_i^T , using the most recent values of V_g , T_3 , and T_8 , and assuming fully developed forced convection. These temperature distributions are:

In the heated section ($s_3 \leq s_i \leq s_4$):

$$T_{hs,i,m}^{fc} = T_3 + \frac{(s_i - s_3)}{\rho_m V_g A C_p} \frac{P_w}{L_3} \quad (4.4)$$

In the post-heated section ($s_4 < s_i \leq s_5$):

$$T_{hs,i,m}^{fc} = (T_4 - T_a) e^{-\Omega(s_i - s_4)} + T_a \quad (4.5)$$

In the cooled section ($s_8 \leq s_i \leq s_9$):

$$T_{cs,i,m}^{fc} = (T_8 - \overline{T}_w) e^{-X(s_i - s_8)} + \overline{T}_w \quad (4.6)$$

In the post-cooled section ($s_9 < s_i \leq s_{10}$):

$$T_{cs,i,m}^{fc} = (T_9 - T_a) e^{-\Omega(s_i - s_9)} + T_a \quad (4.7)$$

where the superscript "fc" refers to a fully developed forced convection flow and Ω is based on V_g . Then, the following correction ratios, denoted by the letter C, are calculated for each Δs_i^T :

$$C_{hs,i,m} = T_{hs,i,m} / T_{hs,i,m}^{fc} \quad (4.8)$$

$$C_{cs,i,m} = T_{cs,i,m} / T_{cs,i,m}^{fc} \quad (4.9)$$

Since the flows investigated here are not fully developed, these ratios are different from unity. In effect, these ratios can be regarded as indicators of the distortion of the fully developed temperature profiles due to superimposed natural convection effects in the heated and cooled section and to heat losses effects in the post sections. These ratios are used in the next step.

4.3.2.4 Step 4: Solution of Eq 4.2 using the secant method

At this point, all the necessary information is available to solve Eq. 4.2: Nodal temperatures, $T_1 \dots T_{11}$, have been evaluated in Step 1 and $f_{hs,i,m}$, $f_{cs,i,m}$, $T_{hs,i,m}$, and $T_{cs,i,m}$ have been calculated in Step 2. Equation 4.2 is conveniently cast into the following form:

$$F(V) = r_i g \beta \frac{A}{B} - V^2 \quad (4.10)$$

where A and B refer to the content of the left hand side and right hand side brackets of Eq. 4.2, respectively. The objective is to find the root of this equation or, in other words, find what value of V will make $F(V) = 0$. This is done here using the secant method (Dahlquist and Bjorck, [1974]). As with any root finding methods, a judicious choice of initial guesses can speed up the convergence of the calculations. For the secant method, two initial guesses are required. In this work, the first guessed value is set equal to V_g as $T_{hs,i,m}$, $T_{cs,i,m}$, $f_{hs,i,m}$, and $f_{cs,i,m}$ have all been obtained based on this velocity. This can be

written as:

$$V_{m,n=1} = V_g \quad (4.11)$$

where the subscript "n" refers to the iteration number in the secant method. The second guessed value of V is simply set to 90 % of V_g :

$$V_{m,n=2} = 0.9 V_g \quad (4.12)$$

Subsequent guessed values of $V_{m,n}$ are given by the following recursive formula of the secant method (Dahlquist and Bjorck [1974]):

$$V_{m,n} = V_{m,n-1} - F(V_{m,n-1}) \frac{V_{m,n-1} - V_{m,n-2}}{F(V_{m,n-1}) - F(V_{m,n-2})} \quad (4.13)$$

This process is repeated until the absolute value of the relative change in V for two consecutive iterations of the secant method is less than a given tolerance, usually set at 10^{-4} . Mathematically, this can be expressed by:

$$\left| \frac{V_{m,n} - V_{m,n-1}}{V_{m,n-1}} \right| < 10^{-4} \quad (4.14)$$

In the evaluation of $F(V_{m,n})$, for $n \geq 2$, a problem arises. Since the values of $T_{hs,i,m}$, $T_{cs,i,m}$, $f_{hs,i,m}$, and $f_{cs,i,m}$ have been evaluated based on V_g and the corresponding values of T_3 and T_8 , their insertion into Eq. 4.10 to evaluate $F(V)$ for a $V \neq V_g$ could lead to erroneous results and eventually, in some cases, to divergence in the secant method. In order to resolve this problem, values of $f_{hs,i,m}$, $f_{cs,i,m}$, $T_{hs,i,m}$, and $T_{cs,i,m}$ are corrected prior to their introduction into

Eq. 4.10.

Correction procedure for $T_{hs,i,m}$ and $T_{cs,i,m}$

The values of $T_{hs,i,m}$ and $T_{cs,i,m}$, determined in Step 2, are corrected using the correction ratios calculated in Step 3. Specifically, the correction procedure is as follows. Using the most recent values of $V_{m,n}$, the values of T_3 and T_8 are evaluated using the techniques described in Appendix D. Then, assuming fully developed forced convection, axial temperature distributions, $T_{hs,i,m,n}^{fc}$ and $T_{cs,i,m,n}^{fc}$, are calculated for each Δs_i^T , in both extended sections. The subscript "n" is added to indicate that these values are for a given iteration in the secant method. These temperature distributions are given by Eqs. 4.4 to 4.7, where V_g is replaced by $V_{m,n}$ and Nu (included in X in Eq. 4.6) is the latest value of \overline{Nu} , determined in Step 3. The corrected values, for a particular iteration of the secant method, $T_{hs,i,m,n}$ and $T_{cs,i,m,n}$, are then evaluated:

$$T_{hs,i,m,n} = C_{hs,i,m} * T_{hs,i,m,n}^{fc} \quad (4.15)$$

$$T_{cs,i,m,n} = C_{cs,i,m} * T_{cs,i,m,n}^{fc} \quad (4.16)$$

The use of the C ratios modifies the temperature profile to take into account superimposed natural convection and heat losses effects that occurred during the last numerical simulations.

Correction procedure for $f_{hs,i,m}$ and $f_{cs,i,m}$

The correction procedure for the friction factors is based on the fact that f 's are inversely proportional to Re . Thus, the friction factors determined in Step 2, $f_{hs,i,m}$ and $f_{cs,i,m}$, are corrected to obtain the friction factors for a given iteration of the secant method, denoted by $f_{hs,i,m,n}$ and $f_{cs,i,m,n}$, according to:

$$f_{hs,i,m,n} = f_{hs,i,m} \frac{V_g}{V_{m,n}} \quad (4.17)$$

$$f_{cs,i,m,n} = f_{cs,i,m} \frac{V_g}{V_{m,n}} \quad (4.18)$$

4.3.2.5 Step 5: Monitoring of the convergence of V from cycle to cycle

At this stage, the cycle is complete and convergence in the secant method has been reached (Eq. 4.14). Before moving to the next cycle, the new value of V_m (subscript "n" is dropped as the calculations are now outside of the secant method) is compared to the value of V obtained from the previous cycle, V_{m-1} . If the absolute value of the relative change in V from two consecutive cycles is less than 10^{-4} , then the solution is said to have converged. Thus, if

$$\left| \frac{V_m - V_{m-1}}{V_{m-1}} \right| < 10^{-4} \quad (4.19)$$

the calculations are stopped and the solution to Eq. 4.2 is complete.

4.3.2.6 Step 6: Return to the next cycle

If Eq. 4.19 is not satisfied, then iterations have to be performed over another cycle. Before returning to the beginning of the next cycle, the fluid properties are updated, if necessary, using the relationships found in Appendix A, according to the latest mean loop temperature. The new values of the average velocity, V_m , and of the nodal temperatures are then returned to Step 2 and used as the latest calculated values of V_g and $T_1 \dots T_{11}$.

4.4 SPECIFIC MODEL FOR THE EXPERIMENTAL APPARATUS

Due to experimental constraints, which will be described in Chapter 5, the experimental loop has two slightly different internal radii. From s_2 to s_6 the internal radius, designated by r_x , is equal to 0.009 m. Elsewhere around the loop, from s_6 to s_2 , the internal radius, r_i , is equal to 0.0095 m. Even though the difference in the value of the radii is small, it has to be considered in order to obtain an accurate determination of V . It can be shown that Eq. 4.2 takes the following form when these two different radii are accounted for.

$$\begin{aligned}
V_x^2 \left[\frac{16 r_x^4}{Re_i r_i^5} (L_{10} + L_1 + L_7 + [2\pi R + L_{eq}]) + \frac{1}{r_x} \sum_{i=1}^{i=L1} f_{hs,i} \Delta s_i^u \right. \\
\left. - \frac{16}{Re_x r_x} (L_2 + L_5) + \frac{r_x^4}{r_i^5} \sum_{i=1}^{i=L1} f_{cs,i} \Delta s_i^u \right] = \\
g\beta \left[- \frac{(T_{10} - T_a)}{\Omega} (1 - e^{-\Omega L_{10}}) + \frac{\Omega R^2 (e^{-\pi R \Omega} + 1)}{(\Omega^2 R^2 + 1)} (T_6 - T_{11}) \right. \\
+ \frac{T_1 - T_a}{\Omega} (1 - e^{-\Omega L_1}) + \frac{(T_2 - T_a)}{\Omega} (1 - e^{-\Omega L_2}) + \sum_{i=1}^{i=L1} T_{hs,i} \Delta s_i^T \\
+ \frac{(T_5 - T_a)}{\Omega} (1 - e^{-\Omega L_5}) - \frac{(T_7 - T_a)}{\Omega} (1 - e^{-\Omega L_7}) - \sum_{i=1}^{i=L1} T_{cs,i} \Delta s_i^T \\
\left. - T_a (L_{10} - L_1 - L_2 - L_5 + L_7) \right] \quad (4.20)
\end{aligned}$$

where $\Omega = \frac{U}{\rho_m V_x A_x C_p} = \frac{U}{\rho_m V_i A_i C_p}$. The subscripts i and x refer to values in sections from s_6 to s_2 and from s_2 to s_6 , respectively.

The form losses associated with the 180° bends are handled by introducing, as shown in Eq. 4.20, an equivalent length of pipe, L_{eq} . The technique to convert the empirically determined loss coefficient of Blevins [1984] into an equivalent length of pipe is shown in Appendix E. Equation 4.20 is solved to obtain V_x using the technique given in section 4.3.

4.5 CLOSING REMARKS

In this Chapter, a procedure to handle the coupling of two-dimensional numerical simulations performed in the extended heated and cooled sections with a traditional one-dimensional analysis has been presented. The outputs of the solution include the average velocity in the closed-loop, the nodal temperatures around the loop, and the detailed two-dimensional velocity and temperature fields in the extended sections. Some of these outputs will be compared to experimental results in Chapter 6, following the description of the experimental apparatus which is the subject of the next Chapter.

CHAPTER V

EXPERIMENTAL APPARATUS AND PROCEDURES

5.1 INTRODUCTION

A closed-loop thermosyphon with vertical heat transfer passages was specially designed and constructed for the present investigation. One of the key elements of this experimental facility is the heated section. It uses a thin semi-transparent gold-film, glued on the inner surface of a Plexiglass pipe, to provide the power input to the closed-loop. Wall temperature measurements and flow visualization in this heated section provide useful physical insights on the heat transfer and fluid flow phenomena. Furthermore, with these measurements, the numerical simulations of mixed-convection flow in vertical pipes can be verified quantitatively and qualitatively.

This Chapter is organized as follows. In the next section, each element of this newly built apparatus is described. Section 5.3 is devoted to the design and construction of the heated section. Temperature, power and average velocity measurements as well as the real-time data acquisition system used in this study are described in section 5.4. This is followed by a description of a typical test in section 5.5. Flow visualization instrumentation and procedures are outlined in section 5.6.

Experimental results shall be examined in detail in Chapters 6 and 7 where they will be compared with the predictions of the proposed model and numerical simulations performed in the heated section.

5.2 EXPERIMENTAL CLOSED-LOOP THERMOSYPHON

5.2.1 Overall Design

The experimental closed-loop thermosyphon used in this study is presented schematically in Fig. 5.1 and photographically in Fig. 5.2. It consists of two sets of vertical Plexiglass pipe sections joined together by two circular 180° bends. As indicated in Fig. 5.1, the lengths of the heated and cooled sections are 0.664 m and 0.612 m, respectively, and the distance between the centers of these two sections, ΔZ , is 0.294 m. The total circulation length of the closed-loop is 6.2 m. The nominal internal and external diameters of the pipes are 19.05 mm and 25.4 mm, respectively, except in the sections incorporating a gold-film on the interior surface where, as will be shown shortly, the internal diameter is equal to 18 mm.

Water is used as the heat transfer fluid and the loop has a volumetric capacity of about 1.75 liters. The loop is open to the atmosphere at the top, via a small expansion chamber, shown in Fig. 5.1. Thus, the pressure inside the loop is essentially hydrostatic. As can be seen in Fig. 5.2, the apparatus is attached to a modular framing system (Uni-strut, model P1000 channels) which consists of robust steel channels and fittings that can be easily assembled. The channels are anchored to a foundation wall to minimize vibrations.

The whole assembly, except the cooled section, was insulated with 6 cm of foamed plastic pipe insulation (Armaflex, manufactured by Armstrong, $k = 0.04 \text{ W/m}^\circ\text{C}$), shown in black in Fig. 5.2. The pipe insula-

tion was cut into two in the longitudinal direction to facilitate its installation and removal. It was held in place by using a removable cloth tape (DRG Sellotape, model 5803).

5.2.2 Elements of the Closed-Loop Thermosyphon

Using Fig. 5.1 as a guide, each item comprising the loop will now be described starting from the exit of the post-heated section and going clockwise.

The top circular 180° bend, which is shown without its insulation in Fig. 5.3a, is composed of two flexible quarter-circle pipe sections. Each section is made of braided clear Tygon tubing (Fisher, #14-169-20E) glued to square flanges at both extremities. The two sections are joined together by placing a spacer between two flanges. This spacer has an opening on top to permit the junction to a transparent expansion chamber.

The flange-spacer-flange arrangement shown in Fig. 5.3a is typical of every pipe junction in the closed-loop and will now be briefly described. The arrangement consists of two Plexiglass square flanges (75 mm x 75 mm x 9 mm thick) glued at the ends of the pipes to be joined. Each flange has a machined groove to accept an O-ring (PRP seals, model 135). The O-rings are black and can be seen in Fig. 5.3a. The Plexiglass spacer is also square (75 mm x 75 mm) with a thickness varying from 3 mm to 50 mm. The spacer has a center hole of the same diameter as the internal diameter of the adjoining pipes. Both flanges and the spacer are held together using four stainless-steel screws.

Two bulk temperature measurement sections are used. One, labelled as the inlet bulk temperature measurement section is located at the left end of the bottom 180° bend, as in Fig. 5.1. The other is located at the right end of the upper 180° bend, and labelled as the outlet bulk temperature measurement section, as in Fig. 5.1. Both sections have the same design, which is shown in Fig. 5.3b. Each section consists of a Plexiglass spacer with five very fine Type-E thermocouples (Omega Engineering Inc. # 5TC-TT-E-36) aligned along the pipe diameter. Each thermocouple measures the temperature of the fluid flowing inside the loop at that particular location. The thermocouples are located in the center of three equal cross-sectional areas. They are held in place by inserting their bead into a tightly stretched fishing rod wire having a diameter of 0.2 mm. The thermocouples and fishing rod wires are inserted into grooves made in the Plexiglass spacer and cemented in place with epoxy glue (Devcon, 2-Ton clear epoxy). Typically, the Reynolds number, based on the diameters of the wires, was of the order of one. Therefore, the bulk temperature measurement section should affect the flow pattern only in the immediate vicinity of the wires.

More details on the inlet and outlet bulk temperature measurements will be given in section 5.4.1.1. It should be noted that these two measurements along with the net power input measurement are used, as will be shown in section 5.4.2, to obtain the average velocity inside the closed-loop.

A straight Plexiglass pipe, with a length of 44 cm, follows the outlet bulk temperature measurement. This pipe is used to let the flow reach a fully developed condition at the entrance of the cooled section.

This is required to allow the experimental conditions to correspond with the fully developed velocity profile assumption used in the proposed model.

A close-up view of the cooled section is shown in Fig 5.3c. It consists of a double-pipe heat exchanger, designed to provide an essentially constant and uniform wall temperature condition on the inner pipe. The inner pipe is made of copper, with an internal diameter of 19.05 mm, a thickness of 1.6 mm, and a length of 0.612 m. The outer Plexiglass pipe is also 0.612 m long with an internal diameter of 38 mm and a thickness of 3.2 mm. The resulting annulus formed by this double-pipe assembly is approximately 8 mm wide. Both pipes are glued to flanges, located at each extremity, using epoxy (Devcon, 2-Ton clear epoxy) and a bead of silicone adhesive sealant (CGE, model RTV-108). The annulus is filled with plastic scrooge wool, shown in yellow in Fig. 5.3c, to promote water mixing.

Cooling water, supplied by a 20-liter constant temperature bath (Neslab, model RTE-220A) which can be seen in the lower left corner of Fig. 5.1 and Fig. 5.2, was circulated in the annulus of the cooled section at a flowrate much greater than the flowrate inside the closed-loop in order to approximate the uniform wall temperature condition on the inner pipe. During the preliminary tests and the final runs, the inner-pipe wall temperature uniformity was continuously monitored using three Type-E thermocouples (Omega Engineering Inc. #TT-E-30) glued to the copper pipe using an epoxy-based high thermal conductivity glue (Omega Engineering Inc., # OB-101-2). As shown in Fig. 5.3c, one of the thermocouples is located in the middle of the cooled section, while the

other two are located near the inlet and outlet pipe connections. Typically, in all runs, the temperatures measured by the 3 thermocouples were all within 1 °C of each other.

Two Plexiglass pipes are encountered after the cooled section. These two pipes along with the pipe preceding the cooled section could be interchanged to modify the value of ΔZ , but this feature was not used in the present study. Following this, the flow changes direction in a 180° bend, which is nominally identical to the top 180° bend described earlier. A drain valve, located at the lowest point of the bend is used to fill and empty the loop. Following the 180° bend, is the inlet bulk temperature measurement section. As was stated earlier, this section is identical to the outlet bulk temperature measurement section described above.

Coming next, following a short Plexiglass pipe, are the pre-heated, heated and post-heated sections. These three sections are nominally identical in length and internal diameters. Each section is composed of a Plexiglass pipe, with an internal diameter of 19.05 mm and an external diameter of 25.4 mm, in which a thin semi-transparent gold-film has been glued on the inner surface. The resulting internal diameter of these gold-film sections is 18 mm.

The heated section is the only one energized during a test, and it is instrumented with thermocouples to measure wall temperatures. The pre-heated and post-heated sections were built to ensure that the internal pipe diameters upstream and downstream of the heated section would be identical to the internal diameter of the heated section. In addi-

tion, a straight pre-heated section was necessary so that the flow could be assumed to be fully developed at the entrance of the heated section.

The design and construction of the gold-film sections will now be described.

5.3 DESIGN AND CONSTRUCTION OF THE GOLD-FILM SECTIONS

5.3.1 Introduction

Recall that one of the objectives of the present investigation is to have a transparent (or essentially transparent) pipe section in which a uniform heat flux is applied to the fluid circulating in the closed-loop. This is accomplished here by using a thin semi-transparent and flexible gold-film.

As was mentioned in the literature review of Chapter 1, the thin gold-film technique has been successfully used in a number of heat transfer experiments involving flow visualization and local heat transfer measurements. However, in these experiments, the gold-film was either fixed on the exterior surface of a test object, as was done by Neill [1989], or internally in a pipe with a relatively large diameter, such as the 9.5 cm diameter pipe used by Baughn et al. [1985]. The main challenge involved in the construction of the present gold-film sections was to fix the gold-film on the inner surface of a relatively small pipe, having an internal diameter of 19.05 mm and to provide appropriate electrical connections to the heating surface. This required the testing of several prototypes before the selection and construction of the

final design.

The various techniques used the construction of the gold-film sections will now be described, but first a brief description of the characteristics of the gold-film is in order.

5.3.2 Characteristics of the Gold-Film

The thin semi-transparent gold-film used in this study is commercially available in flat sheets of various sizes, thicknesses and resistances. It is manufactured by the Sierracin Corporation (Sylmar, CA) under the brand name Intrex. It consists of a thin transparent polyester film on which a coat of gold has been applied by means of vacuum deposition. The gold layer is overcoated with a proprietary ceramic coating to protect the gold from abrasion. The main characteristics of the film used in this study are:

1- Overall thickness:

0.13 mm (0.005 inches).

2- Gold coating thickness:

Estimated at approximately 20 Angstroms.

3- Maximum sustained operating temperature:

100 °C at the coating interface.

4- Transparency to light:

80% \pm 10%.

5- Resistivity:

13.54 Ω /sq. \pm 6.2%, Neill [1989].

6- Thermal conductivity of the polyester film:

0.28 W/m°C, Maeda [1989].

5.3.3 Construction Procedures

5.3.3.1 Preliminary considerations

A total of four gold-film sections were built for this study and, to differentiate them, they will be referred to as heated section no.1, heated section no.2, flow visualization section no.1, and flow visualization section no.2. During any particular test, only three of these sections were used. They all had the same nominal length, and they could, therefore, be interchanged in the loop to act as the pre-heated, heated or post-heated section.

One of the early design decisions was to fix the gold-film on the interior surface of a Plexiglass pipe. This was done for two reasons. Firstly, had the gold-film been fixed on the exterior surface of the pipe, it would not have been in direct contact with the circulating fluid, so it could become overheated under the operating conditions of interest in this study. Secondly, and more importantly, with the gold-film on the exterior of the pipe, a uniform heat flux applied at the surface of the gold film would not necessarily result in a uniform heat flux at the inner surface, of the pipe, due to heat conduction in the pipe wall.

A preliminary prototype was built by gluing the polyester side of the film to the inner surface of a Plexiglass pipe. Thus, in this arrangement, the gold surface of the film is in direct contact with the

fluid. This prototype was energized and water was allowed to circulate inside the pipe. Unfortunately, it was found that the resistance of the prototype almost doubled over a time period of one hour indicating that the gold-film was deteriorating rapidly. This problem is believed to be due to an erosion and/or corrosion processes as a visual inspection of the gold-film at the end of this test indicated that patches of gold had been removed from the film. Based on this experience, it was decided to protect the gold coating by gluing the gold side of the film to the Plexiglass pipe, thus leaving the polyester side of the film in contact with the circulating water.

The disadvantage of this latter technique is that, unlike the case where the gold-coating is touching the fluid, there is a thermal resistance between the gold-film and the fluid due to the presence of the polyester film. This thermal resistance has to be properly taken into account to correct the measured wall temperatures in order to obtain the true inner wall temperatures; the correction procedure is discussed in section 5.4.1.3 and in Appendix G.

In other early experiments, attempts were made at fixing the gold-film inside the pipe by using the method devised by Baughn et al. [1985]. This technique consists of sliding the gold-film into a pipe and then inflating a rubber hose to press the film against the pipe while gluing it to the wall. This technique did not work as, unlike the pipe used by Baughn et al. [1985], the pipe used in this study has a relatively small diameter (19.05 mm), and it was very difficult to slide the film into the pipe for more than ~ 15 cm. Considering that the final length of the gold-film sections had to be ~ 70 cm, this technique

was abandoned.

Instead, it was decided to build the gold-film sections using two half sections. This so-called split design consisted of five major steps: (i) cutting of the Plexiglass pipes in the longitudinal direction so as to form two half sections; (ii) cutting, painting, bending and gluing of the gold-film in each of these half sections; (iii) mating and sealing of two half sections so as to form a circular pipe; (iv) providing electrical connections from the gold-film to the power supply; and (v) gluing of thermocouples in the Plexiglass wall, in the case of heated sections no.1 and no.2.

The details involved in each of these steps will now be presented. To facilitate the description, a number of photographs are presented in Figs. 5.4 a-f and Figs. 5.5 a-f, and a cross-section of one of the extremities of these sections is shown in Fig. 5.6.

5.3.3.2 Cutting of the Plexiglass pipe

As shown in Fig. 5.4a., Plexiglass pipes, with an internal diameter of 19.05 mm and an external diameter of 25.4 mm, were cut in the longitudinal direction to obtain half sections. The blade of the milling machine was adjusted so that one of the two resulting cut sections had the required half height of 12.7 mm. The other cut section was discarded.

After the cutting operations, the half sections were carefully deburred. As indicated in Fig. 5.6, a groove with a width of ~ 0.8 mm

and a depth of ~ 0.4 mm was cut in the flat edge of one of the two half sections used to construct the split pipe. The half section with this groove will now be referred to as the female half section. A sealing gasket (Cole-Palmer, micro-tubing # J-6418-01) was inserted in this groove.

5.3.3.3 Cutting, painting, bending and gluing of the gold-film

The gold-film used in this study is very fragile, thus the four procedures described in this section had to be undertaken with great care. In order to detect any abnormalities or damage to the gold-film, the resistance of each of the various gold-film strips was monitored from the initial cutting stages to the final electrode assembly. These resistance measurements have been summarized in Table 5-1 and will be referred to in the following paragraphs.

Cutting

The film used in this work was taken from a sample roll 30 cm wide and 15.2 m long. Two samples, denoted by the letters A and B in Table 5.1, with a width of 30 cm and a length of 70 cm were cut from this roll. Then, both sides of the film were immediately covered with a removable transparent tape (3M, Scotch Brand MagicPlus) to protect the film. Neill [1989] has found that the application and removal of this tape did not affect the gold-film. Furthermore, as an extra protection, the gold-film samples were always handled with clean surgical gloves.

Each sample was cut to form 8 strips, approximately 33 mm wide and

70 cm long. Although the value of the width itself is not critical at this stage, each strip has to have the same width over its entire length in order to make meaningful resistance measurements. Therefore, the cutting technique had to be quite precise and it was accomplished with the gold-film cutter conceived and constructed by Neill [1989]. Briefly, this cutter consists of a knife blade holder sliding along a pair of carefully machined parallel steel rails. It is estimated that, using this cutter, the width of each strip is within 0.1 mm over its entire length.

The strips were cut wider than the half internal circumference of the Plexiglass pipe. This facilitated, as will be shown shortly, the gluing of the film inside the pipe. The excess width is cut off at a later stage of construction. Using an Exacto knife, the strips were cut in lengths of 68.25 cm, making sure that the resulting extremities of the strips were parallel to each other.

Painting

Following the cutting operation described above, the removable tape was taken off at both extremities of each strip so as to have an uncovered region, 33 mm wide and 9.5 mm long. This region was then painted with a silver-loaded paint (Sunshine Scientific Instruments, Part No. C-24), as shown in Fig. 5.4b. As will be shown later, this paint provides the electrical contact between the gold-film and the copper electrodes. Neill [1989] has shown that the electrical resistance of the paint is negligible in comparison to the resistance of the gold-film. Therefore, as indicated in Fig. 5.6, ohmic heating takes place only in

the region bounded by the silver painted extremities. After the paint was allowed to dry for at least 24 hours, as recommended by Neill [1989], the electrical resistance of each strip was measured by a multimeter (Hewlett Packard, model 3478A, see specifications in Table 5.2) using the 4-wire technique. These initial resistance measurements are reported in the second column of Table 5-1, and it can be seen that the maximum difference between the average resistance and any single resistance is + 4%. This seems to indicate a slightly better resistance uniformity than the value of $\pm 6.2\%$ quoted by Neill [1989], for the same gold-film roll. This can be explained by the fact that the resistance uniformity reported by Neill [1989] was based on 25.4 mm x 25.4 mm strips. In the present case, local non-uniformities tend to get averaged over the full length, while local non-uniformities are more apparent in the experiments of Neill [1989], because of the small size of the strips.

The gold-film strips glued to the two half sections of the split Plexiglass pipe were ultimately electrically connected in parallel to copper electrodes. This parallel arrangement meant that the resistances of the gold-film strips in the two half sections had to be closely matched in order for the current to be the same in both half sections. The third column in Table 5-1 indicates which strips were matched to form a particular section.

Bending and gluing

To the knowledge of this author, there is no discussion, in the published literature, on the bending of this type of gold-film into a

radius of curvature of 9.5 mm, such as the one used in this study. Therefore, at the initiation of this experimental investigation, tests were performed to measure the variation in resistance of a gold-film bent into such a small radius of curvature. The results of these tests indicated that the change in resistance due to bending was of the order of $\pm 1\%$. Therefore, bending effects were considered to be negligible.

Attachment of the gold-film to the inner surface of the Plexiglass pipe required the use of a suitable adhesive. This adhesive had to have the following properties: (i) bind the film firmly to the Plexiglass pipe; (ii) be transparent; and (iii) not cause deterioration of the gold-film when placed in contact with it. After unsuccessful attempts with transparent silicon sealant (CGE, RTV-108) and double-sided tape (3M, Scotch Brand Tape, No. Y9473) it was found that a two-part epoxy glue (Devcon, 2-Ton clear epoxy) fulfilled the three requirements just-mentioned. With the aid of Figs. 5.4c-f and Figs. 5.5a, the bending-gluing sequence will now be described.

After removing the protective tape on the gold side of the film, equal amounts of part A and B of the epoxy glue are thoroughly mixed in a clean beaker to obtain approximately 40 ml of glue. Then, this mixture is poured on the gold side of the strip, as shown in Fig. 5.4c. Once the strip is fully wetted by the glue, it is inserted into the half section of Plexiglass pipe. Then, as demonstrated in Fig. 5.4d, it is pressed against the pipe using a brass rod, with a diameter of 18.5 mm.

Following this, specially machined aluminum blocks are placed on top of the brass rod and are slowly screwed down to the bottom blocks as

shown in Fig. 5.4e. A close-up view is shown in Fig. 5.4f where, for photographic purposes, the gold-film has been replaced by an unglued piece of white cardboard. In this last figure, the protruding excess width of the strip can be clearly seen. This excess width is necessary to divert the overflow of glue away from the brass rod. The excess width is cut, as shown in Fig. 5.5a, by using an Exacto blade. The blade was carefully positioned on the flat portion of the Plexiglass pipe half-section, so as to cut the gold-film exactly at the inner edge of the flat portion.

Once the glue had dried for at least 24 hours, the aluminum blocks were unscrewed and the brass rod was delicately removed. If necessary, the flat portions of the Plexiglass pipe half-section were sanded to remove any excess glue.

After the bending-gluing process had been completed, the resistances of the half sections were measured again, and the results are presented in the fourth column of Table 5-1. The resistances presented earlier in the second column are different from the ones of the fourth column because the width of the gold-film has been reduced. As shown in the fourth column, the resistances of the paired half sections are still closely matched.

5.3.3.4 Mating and sealing of the two half sections

In order to form a complete gold-film section, two half sections needed to be assembled and sealed together. The assembly is started by inserting the sealing gasket into the female half section and carefully

aligning the male half section with its female counterpart. Then, approximately twenty hose clamps (Tridon, model #012) are used to squeeze these two half sections together as demonstrated in Fig. 5.5b. This was a delicate procedure in which the hose clamps had to be tightened gradually and sequentially to avoid any stress point that might lead to pipe cracking. Also shown in Fig. 5.5b are the sealing gaskets which extend beyond the extremity of the gold-film section.

The tightening process was stopped when measurements, taken at three locations on the pipe, indicated that the external diameter of the newly formed pipe was within ± 0.08 mm of the original 25.4 mm external diameter of the Plexiglass pipe. Then, a few drops of Krazy glue were applied along the entire length of both seams.

After the glue had dried for at least an hour, the hose clamps were removed. The external diameter was re-measured and found to be within the same tolerance as the one indicated in the previous paragraph. The mating-sealing technique just described provided a good leak-proof seal for the range of pressures encountered in this work.

5.3.3.5 Electrode construction

The final electrode design is shown in Fig. 5.5c and Fig. 5.6. Copper plates with a thickness of 3.2 mm were used to connect both extremities of the gold-film to the external power leads. Each copper plate was tightly screwed against a Plexiglass flange, with four flat head stainless-steel machine screws. This assembly was then carefully inserted into the gold-film section until the silver-painted extremity

of the gold-film was flush with the external surface of the copper plate. Then, the flanges are glued to the Plexiglass pipe using epoxy glue (Devcon, 2-Ton epoxy glue), as shown in Fig. 5.6. In this last operation, both electrodes are carefully aligned so that they are parallel to each other and perpendicular to the axis of the pipe.

In this position, the silver-painted extremities of the gold-film touch the copper plate but this does not provide a reliable electrical contact. A more permanent electrical connection was achieved by joining the copper plates and the silver-painted extremities with three coats of silver-loaded paint (Sunshine Scientific Instruments, Part No. C-24) along the circumference of a specially machined groove at the center of the copper plate. The three coats of paint are represented by a dark triangle in the insert of Fig. 5.6. Each coat was allowed to dry for at least 24 hours. The remaining space in the groove was then filled with epoxy glue so as to seal the paint from the outside environment.

Resistance measurements were taken after both electrodes had been constructed. The results are presented in the last column of Table 5-1. These resistance measurements correspond very closely to the theoretical resistance (shown in bracket) obtained by connecting, in parallel, the two corresponding resistances of the fourth column. This agreement indicates that: (i) the mating and sealing of the two half sections did not affect the gold-film; and (ii) the additional electrical resistances, due to the three coats of paint and to the copper plates, are negligible.

The construction of the gold-film sections is now complete and the

final result can be seen in Fig. 5.5e. It should be noted that the length of the heated portion of each gold-film section is 0.664 m while the overall lengths of the gold-film sections, between the external faces of the copper plates, vary from 0.680 to 0.683 m (Table 5.3).

5.3.3.6 Gluing of thermocouples in heated sections no.1 and no.2

During the construction of heated section no.1, holes were drilled through the Plexiglass walls of both half sections to accommodate thermocouples for wall temperature measurements. Dowell pins were inserted into these holes during the gold-film gluing process to prevent the holes from being filled with glue. The dowell pins can actually be seen in Fig. 5.4c, where they are shown on the bottom of the Plexiglass pipe. After the glue was allowed to dry, the dowell pins were removed, leaving an unobstructed hole leading to the thin coat of glue behind the gold surface of the film. Thermocouples were inserted into these holes until the bead touched the thin coat of glue. The thermocouples were epoxied (Devcon, 5-minute epoxy) in place as shown in Figs. 5.5d,f. Unfortunately, heated section no.1 started to malfunction at the initiation of the final test runs and, therefore, it could no longer be used.

Instead of rebuilding another gold-film section, complete with holes through the Plexiglass, it was decided to use an already built gold-film section, which will now be called heated section no.2, and to carefully drill holes in the Plexiglass pipe. As indicated in Fig. 5.6 and Fig. 5.7, these holes have a diameter of 3.0 mm. The depth was set at 1.6 mm, half the thickness of the wall of the Plexiglass pipe, to avoid drilling too close to the gold-film. Thus, when inserted and cemented

into the holes, the thermocouples were further away from the gold-film than in the case of heated section no.1. But this was not a major drawback, because, as is shown in Appendix G, the temperature corrections to obtain the true inner wall temperatures are only marginally dependent on the location of the thermocouple inside the wall of the Plexiglass pipe.

5.3.4 Determination of the Average Internal Diameter of the Gold-Film Sections

It was not possible to measure directly the internal diameter of the gold-film sections, except near the immediate vicinity of the inlet and outlet. Thus an indirect method of measurement was used to obtain the average internal diameter. The method basically consists of measuring the mass of the gold-film sections before and after it has been filled with distilled water. Then, by precisely measuring the length of the pipe, and using the known density of the distilled water, the average internal diameter can be determined. The mass measurements were done using a triple-beam balance (Cole-Palmer model J-1020-00) with an uncertainty of ± 0.1 g. The results of these measurements are reported in Table 5-3, where it can be seen that the nominal internal diameter of the four gold-film sections is 18 mm. Considering that the film is 0.13 mm thick, the thickness of the glue is then approximately equal to 0.40 mm.

5.4 SUPPORTING EQUIPMENT AND INSTRUMENTATION

5.4.1 Temperature Measurements

A total of sixty chromel-constantan thermocouples (Type-E) were used in the final stage of this study. Ten ready-made miniature 36-gauge thermocouples (Omega Engineering Inc., 5TC-TT-E-36), were used in both the inlet and outlet bulk temperature measurements sections. The other fifty thermocouples were fabricated in-house, using the technique described by Neill [1989], using 30-gauge thermocouple wires (Omega Engineering Inc., TT-E-30). Out of these fifty thermocouples, forty-six were inserted into heated section no.2, three were glued to the wall of the cooled section, and the last one was used to measure ambient temperature.

The thermocouple wires were connected, via rugged extension wires (Omega Engineering Inc., EXPP-E-20), to a data acquisition unit (Hewlett-Packard, model 3497A). This unit contains three hardware-compensated relay multiplexers (Option 020), each having a capacity of twenty thermocouples. Hardware compensation is provided internally, using the voltage output of the reference junction transducer which reads the temperature of the isothermal block. The multiplexers are linked to a 5 1/2 digit voltmeter with a resolution of 1 μ V and an accuracy of $\pm 3 \mu$ V in the 0-0.10 Volts range. The specifications of the voltmeter are given in Table 5.2.

All thermocouples were individually calibrated, except the three thermocouples located in the cooled section, against a calibrated quartz

thermometer (Hewlett-Packard, model 2804A). Appendix F describes the thermocouple calibration procedure and results. Based on these results, the uncertainty in the temperatures measured with the calibrated thermocouples is estimated at ± 0.05 °C; the uncertainty on the temperature measurements in the cooled section is estimated at ± 0.1 °C.

5.4.1.1 Inlet and outlet bulk temperature measurements, T_{in} and T_{out}

The inlet and outlet bulk temperature measurements are used to obtain the temperature difference across the heated section, which in turn is used, as will be shown in section 5.4.2, to determine the average velocity in the closed-loop. As was mentioned earlier and as shown in Fig. 5.3b, the inlet and outlet bulk temperature measurement sections are composed of five thermocouples. Each thermocouple is located in the center of three equal cross-sectional areas.

For pipe flow, the bulk temperature, T_b , at a particular cross-section is given by:

$$T_b = \frac{\int_A \rho C_p T(r) u(r) dA}{\int_A \rho C_p u(r) dA} \quad (5.1)$$

where A is the cross-sectional area of the pipe, and $T(r)$ and $u(r)$ are, respectively, the cross-sectional temperature and velocity profiles.

As shown by Eq. 5.1, the fluid temperature, density, and velocity

profiles are needed to determine the bulk temperature. However, if the temperature is uniform at a given cross-section then the bulk temperature is simply equal to that temperature without the need to measure the velocity profile. In this work, the temperature uniformity in the inlet and outlet bulk temperature measurement sections was continuously monitored during a test and typically, as shown in Appendix K, all five thermocouples were well within 0.3°C of each other. With such a small difference among the temperature measurements the temperature uniformity was quite good and the inlet and outlet bulk temperatures were assumed equal to the arithmetic average of the five thermocouple measurements. Based on the uncertainty of $\pm 0.05^{\circ}\text{C}$ on the individual temperature measurements, the overall uncertainty on T_{in} and T_{out} , is estimated, based on the propagation of uncertainty technique of Kline and McClintock [1953], at $\pm 0.11^{\circ}\text{C}$ ($[5\{0.05\}^2]^{0.5}$).

As shown in Fig. 5.1, the inlet and outlet bulk temperature measurements were not made immediately at the inlet and outlet of the heated section. This was done for two reasons: Firstly, had the inlet bulk temperature measurement been made at the inlet of the heated section, the immersed thermocouple wires could have affected the inlet velocity profile. Secondly, because the temperature profile at the outlet of the heated section is distorted, an outlet bulk temperature measurement at that location would have required, based on the foregoing discussion, a knowledge of the velocity profile. Instead, the outlet temperature measurement was located away from the outlet of the heated section and after the top 180° bend so as to get a more uniform fluid temperature over the cross-section of the pipe.

As for the bulk temperature difference, it was simply obtained as the difference between the outlet and inlet bulk temperature measurements. Based on the $\pm 0.11^\circ\text{C}$ uncertainty on T_{in} and T_{out} , the uncertainty on this temperature difference is, conservatively, set at $\pm 0.2^\circ\text{C}$ ($[2\{0.11\}^2]^{0.5} \approx \pm 0.2^\circ\text{C}$).

5.4.1.2 Ambient temperature measurement, T_a

The ambient temperature was measured using a thermocouple located at the mid-height of the closed-loop. In order to reduce radiation errors, the thermocouple was shielded by inserting it into a 6 mm brass tube.

5.4.1.3 Wall temperature measurements in heated section no.2

Final wall temperature measurements were taken with forty-six thermocouples glued, as discussed in section 5.3.3.6, inside the Plexiglass pipe of heated section no.2.

The axial location of each thermocouple is shown in Fig. 5.5f and tabulated in Table 5.4. As shown in Table 5.4 and in the pipe cross-section in Fig. 5.6, two thermocouples were positioned at each axial measuring point; one in the male half section and one in the female half section. The uncertainty in the axial and radial positioning of the thermocouples are estimated at ± 0.5 mm and ± 0.1 mm, respectively. In order to assess the asymmetry of the wall temperatures, six thermocouples were positioned in a cross-section at 60° intervals, located at a distance of 0.2320 m from the inlet.

As mentioned earlier, the temperature readings given by the thermocouples have to be corrected in order to get the true inner wall temperature. This correction procedure is presented in Appendix G.

5.4.2 Average Velocity Measurements

Classic methods of flowrate measurements could not be used in this study. Devices such as orifice plates and turbine flowmeters introduce unacceptable flow restrictions while noninvasive measurement techniques such as ultrasonic flowmeters require, as mentioned by Fanney and Dougherty [1987], fluid velocities greater than the ones normally encountered in thermosyphons.

In this work, the average velocity inside the closed-loop was not directly measured. Instead, the mass flowrate was first evaluated. Then the average velocity was determined from a knowledge of the cross-sectional area of the pipe and the density of the water.

The mass flowrate, \dot{m} , is determined by measuring the net power input between the locations of inlet and outlet bulk temperature measurement sections. Mathematically, and with reference to Fig. 5.8, this can be expressed by:

$$\dot{m} = \frac{P_w - (Q_x + Q_y + Q_z)}{C_p(T_{out} - T_{in})} \quad (5.2)$$

where P_w is the power input to the heated section, Q_x , Q_y , and Q_z are the heat losses in the regions indicated in Fig. 5.8, C_p is the specific heat of the water, and $T_{out} - T_{in}$ is the difference between the outlet and inlet bulk temperatures. The average velocity, V , can then be obtained as follows:

$$V = \frac{\dot{m}}{\rho A} \quad (5.3)$$

where ρ is the density of the water and A is the cross-sectional area of the pipe. The heat losses, Q_x , Q_y , and Q_z are obtained using the following relationship (Fig. 5.8):

$$Q_i = U L_i (T_{m,i} - T_a) \quad (5.4)$$

where U is an overall heat loss coefficient (W/m^2C), L_i is the length of section i , $T_{m,i}$ is the mean bulk temperature inside section i , and T_a is the ambient temperature. The value of U was determined experimentally, using the technique described in Appendices H and I, and is equal to $0.18 W/m^2C \pm 20 \%$.

Typically, during a closed-loop thermosyphon test, the sum of $Q_x + Q_y + Q_z$ amounts to less than 10 % of P_w . Therefore, even though the uncertainty on U , and correspondingly on $Q_x + Q_y + Q_z$, is $\pm 20 \%$, its impact on the $P_w - (Q_x + Q_y + Q_z)$ measurement is less than $\pm 2 \%$.

Since one of the main criteria of comparison between the proposed model and the experimental results is the average velocity, a thorough

in-situ calibration of the average velocity measurements was undertaken. The details of this calibration can be found in Appendix J, where it is shown that the uncertainty on the average velocity measurement is $\pm 5\%$.

5.4.3 Current, Voltage, Resistance and Power measurements

A schematic representation of the electrical circuit of the heated section is shown in Fig. 5.9. As was mentioned earlier, the heated section is composed of two resistances connected in parallel and is represented as such in Fig. 5.9. Electrical power was provided to the heated section by a DC power supply (Sorensen, model DCR300-3B). Current was measured using a multimeter (Hewlett-Packard, model HP3478A). Voltage measurements across the heated section were obtained using a separate multimeter (Keithley, model 195A). Table 5.2 lists the specifications of both multimeters and of the power supply.

Both multimeters are equipped with HP-IB links (IEEE-488) which permitted transmission of current and voltage measurements to a real-time data acquisition system, which will be described shortly. During a test, the electrical power input, P_w , and the resistance of the heated section, Ω , were evaluated, within a custom written data acquisition computer program, using the above-mentioned voltage, V , and current, I , measurements:

$$P_w = V \cdot I \quad (5.5)$$

$$\Omega = V/I \quad (5.6)$$

Based on the accuracy specifications listed in Table 5.2, it can be

shown, using the combination of uncertainty technique of Kline and McClintock [1953], that, in the worst case, the uncertainties on the P_w and Ω measurements are less than $\pm 0.5 \%$.

5.4.4 Real-Time Data Acquisition System

The foundation of the real-time data acquisition system is a data acquisition and thermocouple multiplexer unit (Hewlett Packard, Model 3497A) controlled, via an HP-IB (IEEE-488) interface, by a BASIC language processor card (Hewlett-Packard, Model 82300A) incorporated into a personal computer (Hewlett-Packard Vectra, AT compatible). This card acted as a stand-alone computer and was internally linked to the personal computer, which made it possible to transfer data and programs between the two computers. The card was also connected, using the HP-IB link, to both multimeters.

A general-purpose computer program was written in the BASIC language to acquire, process, monitor and store measurements taken by these instruments.

Data acquisition

The above-mentioned computer program was used to acquire, at a user-specified time interval, the readings of the measuring instruments. During a typical data acquisition sequence, a total of 62 raw measurements were taken: 60 thermocouple voltage readings as well as current and voltage measurements in the heated section.

Data processing

Individual thermocouple voltage measurements were converted to temperatures, using their respective polynomial calibration curve, and wall temperature measurements were corrected according to the procedure given in Appendix G. The electrical power input and the resistance of the gold-film in the heated section were calculated, as discussed in section 5.4.3. The inlet and outlet bulk temperature were evaluated using the method described in section 5.4.1. The mass flowrate and the corresponding average velocity were determined using the technique discussed in section 5.4.2.

Data monitoring

Once the raw measurements were processed, they were all displayed on the monitor of the computer, as can be seen in Fig 5.2. The image of the monitor can also be transferred, if necessary, to a printer (Hewlett-Packard, LaserJet series II). Figure 5.10 presents the result of such a transfer.

The display of processed data provided an instant picture of all the measurements at their respective locations in the closed-loop. The long vertical rectangle located on the left of Fig 5.10 represents the heated section. The flow enters at the bottom, and adjoining numbers indicate wall temperatures at those particular axial locations. The two circles in the middle of Fig. 5.10 symbolize the inlet and outlet bulk temperature measurement sections. The temperatures on the top right-hand side of both circles represent the bulk temperatures given by the five ther-

thermocouples shown inside the circles. The three wall temperature measurements in the cooled section are shown on the right of the closed-loop, beside the ambient temperature measurement and above the average velocity measurement. Also shown, in the bottom right corner of Fig. 5.10, are the measurements related to the electrical power input and to the resistance of the heated section.

Data Storage

The computer program stores, in internal memory, the last 10 readings of every measurement. The program has the capability of providing a time history plot of these last 10 readings. This allowed a rapid visual inspection of the stability of any measurement in the closed-loop. Permanent data storage is done on floppy disk files for later retrieval and analysis.

5.5 SYNOPSIS OF THE EXPERIMENTAL PROCEDURE

The following step-by-step procedure was used during a typical closed-loop thermosyphon test.

1. All instruments were powered-up for a 24 hour warm-up period.
2. The vertical orientation of the loop was checked, in both planes, using a spirit level.
3. The closed-loop thermosyphon was then filled with distilled water. A filling bottle, shown in Fig. 5.1, was positioned above the highest

point of the loop and connected to the drain valve at the bottom of the loop; water was allowed to fill the loop from the bottom to the top.

4. Electrical power to the heated section was gradually increased up to the desired level. The temperature of the water bath, and consequently, the wall temperature in the cooled section, were adjusted to the desired conditions. Typically, step 4 would take two to three hours.
5. Using the real-time data acquisition system, the average velocity inside the loop was monitored every 60 seconds. Conditions were considered to be steady when the measured average velocity did not vary by more than $\pm 1\%$ over a time period equivalent to at least twice the time required for a packet of fluid, travelling at the average velocity, to complete one revolution around the loop.
6. Once the steady-state criteria stipulated in step 5 had been met, all measurements were monitored and then permanently stored on disks for future analysis.
7. Return to step 4 with the next set of power input and wall temperature in the cooled section.

5.6 FLOW VISUALIZATION INSTRUMENTATION AND PROCEDURE

5.6.1 Introduction

Flow visualization studies were undertaken to obtain qualitative observations of two phenomena occurring in mixed-convection upward flow in vertical circular pipes subjected to a uniform heat flux boundary condition.

The first phenomenon pertains to the presence of recirculation cells. Although these cells have been numerically predicted, they have, apparently, never been visually observed due to the fact that previous experiments relied on ohmic heating of opaque walls. In this work, the walls of the flow visualization section do not suffer from this limitation as heating is provided by a thin semi-transparent gold-film.

The transparency of the heated section also permitted to examine the second phenomenon of interest, namely, the laminar-turbulent transition in mixed-convection flows. As stated earlier in Chapter 1, a number of researchers have discovered that such transitional flows can exist in mixed-convection situations, even if the Reynolds number is well below 2000.

As reported by Macagno [1969], a number of methods are available for flow visualization in liquids. The most prominent ones are: (i) the hydrogen-bubble method (Mueller, [1983]); (ii) small particle injection (Merzkirch, [1974]); (iii) electrolytic dye production (Baker, [1966]); and (iv) dye injection (Merzkirch, [1974]).

In the present study, the dye injection method was used to visualize the flow as the other three methods were found to be inadequate. Methods (i) and (ii) are inappropriate in the present case, where buoyancy effects are important, because it is very difficult to obtain neutrally buoyant particles or bubbles. The method proposed by Baker [1966] involves the preparation of an acidic solution which changes color in the vicinity of energized electrodes. This method was also rejected in order to avoid possible degradation of the gold-film by the acidic solution. The dye injection method did not suffer from these difficulties. Another advantage of the dye injection method was that the same set-up could be used to study both above-mentioned phenomena.

The following sections describe the dye injection instrumentation and the flow visualization procedure.

5.6.2 Dye Injection Instrumentation

The flow was best visualized by using a fluorescent dye (fluorescein sodium salt, Sargent-Welch #SC12184). Non-fluorescent dyes, such as milk and food colorants, were tried but they did not provide the sharp contrast obtained with the fluorescent dye.

The dye was prepared by completely dissolving approximately 2 grams of dye powder with 1 liter of distilled water. Being essentially composed of water, the dye solution was considered to be neutrally buoyant. This dye had another advantage in that it had a small molecular diffusion rate which made it well-suited for visualization of filament lines.

The key elements of the dye injection set-up are presented in Fig. 5.11a-c. These figures present, respectively, a special Plexiglass spacer incorporating a small injection tube, an air-pressurized dye reservoir, and the flow visualization section along with illuminating lights.

As shown in Fig. 5.11a, the dye injection tube is made of brass and is part of a special spacer which is inserted immediately upstream of the inlet of the heated section (Fig. 5.1). The center hole of the spacer was carefully machined so as to be of the same diameter as the adjoining pipes, in order to avoid any abrupt pipe transition. The internal and external diameters of the brass tube are 0.8 mm and 1.6 mm, respectively, and the tube is 25 mm long in the flow direction. The injection tube is bent at a 90° angle and positioned at the geometric center of the hole using the special Plexiglass positioning plate shown in Fig. 5.11a. The length and diameter of the brass tube provided, when needed, a relatively large volume of dye at the local inlet temperature without significantly disturbing the main flow.

The brass tube was linked to the dye reservoir, which is shown in Fig. 5.11b, using a Tygon tube. Typically, the 200 cm³ reservoir was filled with 80 ml of dye and air-pressurized up to 0.4 MPa. A valve located at the outlet of the reservoir permitted to regulate the flow from a trickle to a flooding condition.

During a flow visualization test, the dye was illuminated using two 15 Watts long-wave black lights (Panasonic Blacklight Blue - F15

T8/BL-B). As shown in Fig 5.11c, the lights were fastened to telescopic tripods and positioned on each side of the flow visualization section. A ruler, located near the flow visualization section, indicated distances from the inlet of the section.

The best photographic results were obtained when the laboratory was in total darkness and when a black felt was placed behind the flow visualization section. Photographs were taken using either a Canon AE-1 or a Pentax SP-500 camera. A number of different films were tried and the best photographs were obtained using either an Agfachrome slide film (ASA 1000, with a typical camera setting of 1/30 sec. and f1.8) or a Kodacolor Gold color print film (ASA 400, 1/15 sec. and f1.8).

5.6.3 Flow Visualization Procedures

The following procedure was used during the final flow visualization tests.

1. The closed-loop thermosyphon was modified to make it an open-loop.

This open-loop configuration, which is shown in Fig. 5.12 and described in Appendix I, was used, instead of the closed-loop configuration, for two reasons: Firstly, it is easier to obtain the desired flowrate from a constant-head tank than from the natural circulation of a closed-loop. Secondly, dye-infested water can be easily evacuated from the loop.

2. The heated section and its covering insulation was removed and replaced by a flow visualization section. The vertical orientation

of the flow visualization section was checked with a spirit level.

3. The whole open-loop, including the constant-head tank and the constant-temperature bath, was filled with distilled water.
4. The bath temperature was set such that the inlet temperature to the flow visualization section was within $\pm 1^\circ\text{C}$ of the ambient temperature. This minimizes heat losses (gains) from the flow visualization section. The flowrate was adjusted to the desired condition. Conditions were monitored and considered to be stable when the inlet temperature and flowrate variations were less than $\pm 0.1^\circ\text{C}$ and $\pm 1\%$, respectively.
5. Once the inlet temperature and flowrate had reached their stability criteria, electrical power to the flow visualization section was gradually increased up to the desired level. This was followed by a 30 minute settling period. Dye was then injected into the flow field using one of the two following methods.

6A. Observations of recirculation cells

For these cases, the flow field was flooded using a method similar to the one described by Scheele and Hanratty [1962]. This technique consisted of injecting a large quantity of dye for a short period of time (typically 1 second). The dye was then washed out from the main flow by the water flowing in the flow visualization section, while dye remained trapped in the recirculation cell for a longer period of time. This washing out process would typically last for 10 minutes

before the contours of the cell could be clearly distinguished and photographed. The dye contained in the cell would eventually disappear due to molecular diffusion of the dye. Although this injection technique was primarily used for the study of recirculation cells, it was also successfully applied to the study of transitional flows as will be shown in Chapter 6.

6B. Observations of transitional flows

Transitional flows were mainly observed by injecting a dye filament at the inlet of the flow visualization section.

The injection of a dye filament, in a flow where natural convection effects are important, is at best difficult. The difficulties lie in matching the temperature and velocity of the dye, respectively, with the temperature and the relatively small velocity of the main flow. The temperature of the dye has to be equal to the temperature of the fluid at the exit of the injection tube, otherwise the dye sinks down or rises abnormally. This problem was circumvented by letting the dye settle in the brass tube before each injection. As for the flow-rate of the injected dye, it has to be high enough to have a visible dye filament and low enough to minimize disturbances to the main flow.

5.7 CLOSING REMARKS

The experimental apparatus and its related instrumentation as well as the design and construction of heated sections with gold-film heaters were described in this Chapter. The results of the closed-loop thermosyphon tests and the flow visualization experiments are presented in the next two chapters. The full set of experimental data is presented in Appendix K.

CHAPTER VI

RESULTS:

CONJUGATE CONDUCTION AND LAMINAR MIXED-CONVECTION IN VERTICAL PIPES FOR UPWARD FLOW AND UNIFORM WALL HEAT FLUX

6.1 INTRODUCTION

One of the objectives of this work was to study conjugate conduction and laminar mixed-convection in vertical pipes. Attention was focussed on the problem presented in Fig. 3.1, where the flow is in the upward direction and the inlet velocity is assumed to correspond to the fully developed Poiseuille parabola. A uniform heat flux is applied on the outside surface of the heated pipe, and the upstream and downstream sections of the pipe are considered adiabatic.

This Chapter presents the results of numerical simulations and flow visualization studies on mixed-convection flows. In the next two sections, numerical results on conjugate conduction and mixed-convection flows are presented. Then, in section 6.4, experimental observations of recirculation cells and of laminar-turbulent transitions, encountered in mixed-convection flows are reported.

It should be noted that local wall temperature measurements in mixed-convection flows were undertaken during the course of this study, and these are reported in Chapter 7 in conjunction with the results of the proposed closed-loop thermosyphon model.

6.2 PRELIMINARY CONSIDERATIONS

6.2.1 Introduction

The elliptic forms of the governing equations, as well as the boundary conditions of conjugate conduction and mixed-convection flows in vertical pipes, have been presented in Chapter 3. These equations were non-dimensionalized and it was shown that the governing non-dimensional parameters are: Gr_q/Re^2 , the Grashof number over the Reynolds number squared; Re , the Reynolds number; Pe , the Péclet number; K , the ratio of the thermal conductivity of the wall to the thermal conductivity of the fluid; and Δ , the ratio of wall thickness to pipe diameter. In addition and with reference to Fig. 3.1, the problem of interest is also dependent on the following non dimensional lengths: L_u/D , L_h/D , and L_d/D .

The governing equations were solved numerically using the finite-volume approach of Patankar [1980], as was described in Chapter 3. The results presented in the next two sub-sections were obtained by assuming that the thermophysical properties of the fluid and pipe were constant. The effects of variable fluid viscosity and thermal conductivity are discussed in Chapter 7.

6.2.2 Selection of Non-Dimensional Parameters

Due to the large number of independent non-dimensional parameters in this problem, a parametric study of all these individual parameters would have generated an enormous set of results. Thus, it was decided

to fix the values of certain non-dimensional parameters, so as to keep the analysis at a manageable level.

The Prandtl number was set equal to 5, thus, the fluid can be considered to be water. The value of the Grashof number was fixed at 5000, and two values of the Reynolds number were studied: 1 and 10. Thus, the corresponding Gr_q/Re^2 ratios were 5000 and 50, respectively, while the Péclet numbers were 5 and 50, respectively. The last two Pe values are representative of cases where axial conduction in the fluid is significant, for $Pe = 5$, and negligible, in the case where $Pe = 50$. To summarize, two mixed-convection cases will be examined. They will be referred to as the low Re and the high Re cases:

Low Re case

$$Pr = 5$$

$$Gr_q = 5000$$

$$Re = 1$$

$$Gr_q/Re^2 = 5000$$

$$Pe = 5$$

High Re case

$$Pr = 5$$

$$Gr_q = 5000$$

$$Re = 10$$

$$Gr_q/Re^2 = 50$$

$$Pe = 50$$

The value of the non-dimensional heated section length, L_h/D , was set equal to 10. This length was sufficiently long to study the development of the flow and short enough to keep the computational effort reasonable. The non-dimensional upstream section length was determined based on the results of preliminary simulations, which indicated that wall axial conduction effects may extend, in some cases, as much as 30 radii upstream of the inlet of the heated section. Based on this, L_u/D

was set equal to 30. The non-dimensional downstream section length, L_d/D , was fixed at 10. This distance was long enough to account for downstream wall conduction and to ensure that the outlet boundary conditions ($\partial u/\partial z = 0$ and $\partial T/\partial z = 0$) were satisfied.

Four different values of K were selected: 0.5, 5, 50 and 500. Since the Prandtl number selected corresponds to that of water, the thermal conductivity of the fluid, k_f , is approximately equal to 0.6 W/m•K (Baumeister et al. [1978]). Thus, the four corresponding values of the thermal conductivity of the pipe wall, k_s , are 0.3, 3, 30, and 300 W/m•K, respectively. These values are representative of the following common pipe materials: Plexiglass, stainless steel, brass, and copper (Baumeister et al. [1978]). Three values of Δ , the wall thickness to pipe diameter ratio, were chosen: 0.01, 0.05, and 0.25. These values fall within the range representative of commercially available pipes.

6.2.3 Grid Independence Checks

The purpose of this sub-section is to find which grid spacing provides a grid-independent solution to conjugate conduction and mixed-convection flows for the range of parameters mentioned above. As was mentioned in Chapter 3, the grid spacing was non-uniform in both the radial and axial directions, with a greater concentration of grid points near the fluid-solid interface and at the inlet and outlet of the heated section.

The number of grid points in the solid in the radial direction was fixed at 4 for all the simulations presented in this Chapter. Prelimi-

nary simulations indicated that a higher number of grid points in the solid in the radial direction did not change the results significantly.

To check whether the results were independent of the grid size, the computations were carried out for $Gr_q/Re^2 = 50$, $Re = 10$, $Pe = 50$, $K = 500$, and $\Delta = 0.05$. These conditions are believed to represent the most demanding conditions that the computer code had to handle due, as will be shown shortly, to the extent of upstream and downstream heating. The results were analyzed by examining: (i) the normalized radial velocities, u/V , at half the heated section length ($z/D = 5$); (ii) the axial variation of the non-dimensional bulk and wall temperature, θ_b and θ_w ; (iii) the axial variation of the fRe product; and (iv) the axial variation of the ratio of local heat flux, at the inner surface, to the applied uniform heat flux on the external surface of the pipe, q_i/q .

The axial variation of fRe turned out to be the most strict criteria to verify the grid independence and, therefore, only these checks will be presented. The variations of fRe as a function of the non-dimensional axial length, z/D , are presented in Figs. 6.1a,b. Figure 6.1a shows the effect of grid refinement in the z direction for a fixed radial discretization, while Fig. 6.1b compares the results of three different grid sizes in the radial direction with a fixed axial discretization. As can be seen in these figures, the grid size in the axial direction was divided in three parts, given by the 3 numbers listed under 'z', representing the number of grid points in the upstream, heated, and downstream sections, respectively. In the r -direction, two numbers are presented under 'r', the first number repre-

sents the grid points in the fluid and the second is the number of grid points in the solid, which, as previously mentioned, was fixed at 4 for all simulations reported here. It should also be recalled that the values $z/D = 0$ and $z/D = 10$ represent the location of the inlet and outlet of the heated section, respectively.

As shown in Fig. 6.1a, the differences in fRe for the 25,30,15 x 16,4 and 35,50,20 x 16,4 grids are small and those between the 35,50,20 x 16,4 and 40,76,24 x 16,4 grids are barely noticeable. Therefore, an axial grid size of 140 (40,76,24) was considered to give grid independent results. As for grid refinement in the radial direction, Fig. 6.1b shows that the results for the 40,76,24 x 10,4 grid differ somewhat from the results obtained with the finer grids, 40,76,24 x 13,4 and 40,76,24 x 16,4. The simulations performed with the finer grids, 40,76,24 x 13,4 and 40,76,24 x 16,4 yielded nearly identical results. Thus, the solution was considered to be grid independent in the radial direction when a total of 20 grid points (16 in the fluid and 4 in the solid) were used. Hence, all subsequent computations reported in this Chapter were performed with a 140 x 20 grid.

As a final remark on Fig. 6.1, it should be noted that the sudden increase in the value of fRe for $z/D = 10$ is due to a sudden increase in the calculated velocity gradient at the wall. This numerical result is unusual, as one would expect fRe to decrease smoothly when a decrease in the velocity gradient at the wall is caused by a decrease in wall heating at that location. As will be shown in Chapter 7, an increase in the number of grid points in the axial direction improves the smoothness of the transition but does not eliminate the 'kink' completely. Consider-

ing that the value of fRe is essentially grid independent everywhere else in the calculation domain, and that other results such as θ_b , θ_w , q_i/q , and u/V did not exhibit such a behavior, it was decided to use a 140×20 grid size, keeping in mind the limitations of such a grid near $z/D = 10$.

6.3 RESULTS AND DISCUSSION

6.3.1 Introduction

The results of the numerical simulations will now be presented. The axial variations of q_i/q , θ_b , θ_w , u/V , and fRe will be examined for various values of K and Δ . Even though calculations were performed from $z/D = -30$ to $z/D = 20$, the results will be plotted only from $z/D = -10$ to $z/D = 20$, as little is gained in studying the results between $z/D = -10$ and $z/D = -30$. Recall that $z/D = 0$ corresponds to the inlet of the heated section. Extreme cases, such as the $Re = 1$ and $K = 500$ and the $Re = 10$ and $K = 0.05$ combinations, will not be examined here. In the former case the calculation domain would have had to be stretched much further than $z/D = -30$, while in the later case, axial wall conduction is negligible.

6.3.2 Normalized Interface Heat Flux, q_i/q

The axial variation of the normalized interface heat flux, q_i/q , for the low and high Re cases are shown in Figs. 6.2 and 6.3, respectively, for different values of K and Δ . The non-dimensional variable q_i/q represents the ratio of the convective heat flux, normalized

to the outside diameter, at the inner surface wall to the applied uniform heat flux on the outside diameter. A ratio of unity indicates that the applied heat flux goes directly to the fluid without any axial conduction in the wall.

As shown in Figs. 6.2 and 6.3, a significant portion of the applied heat flux on the outside surface of the heated section is redistributed by axial conduction within the heated, upstream, and downstream sections of the pipe. This results in a bell-shaped curve where q_i/q is lower than unity in the heated section and tends towards zero in the upstream and downstream sections. It is interesting to note that the two tails of the bell are not symmetrical, as the wall temperature variation in the upstream region is greater than that in the downstream one.

An examination of Figs. 6.2 and 6.3 reveals that the magnitude and the extent of upstream and downstream heating increases monotonically with an increase of K and/or Δ . This is to be expected because an increase in K and Δ , which increases the cross-sectional area of the pipe wall, both contribute to make the wall a more attractive axial heat flow path for the applied heat flux.

As K and/or Δ decrease, the ratio q_i/q tends to be equal to 1 in the heated section and zero elsewhere, indicating that axial wall conduction tends to be negligible for low values of K and Δ . For example, in Fig. 6.2c, axial wall conduction is almost negligible for $\Delta = 0.01$ and $K = 0.5$ and, in Fig. 6.3c, axial wall conduction subsides to an insignificant level for $K = 5$ and $\Delta = 0.01$.

As indicated in Figs. 6.2 and 6.3, upstream axial conduction is generally more significant than downstream axial conduction, especially when K and Δ are high and when Re is low. In order to explain this, the q_i/q ratio has been plotted, in Fig. 6.4, for the low and high Re cases and for the same values of K and Δ .

In the upstream section, for the same ρ , D , and μ , the higher velocities associated with the high Re case imply that there is higher convective heat transfer at the wall than for the low Re case. In other words, the thermal resistance at the fluid-solid interface will be lower for the high Re case than for the low Re case. Thus, in the low Re case, the applied uniform heat flux at the outer surface of the pipe gets redistributed further upstream: because of a higher thermal resistance at the fluid-solid interface, there is greater heat conduction in the pipe wall.

The peak in the curve near $z/D = 0$ for $Re = 1$ is somewhat unexpected as one would think that q_i/q would not approach unity at that location because of the just-mentioned upstream redistribution of the heat flux. This behavior is believed to be due to a highly distorted velocity profile near $z/D = 0$ for $Re = 1$. This will be further explained in section 6.3.4 where velocity distributions are presented.

In the heated section and for $Re = 1$, the q_i/q ratio drops off steadily, while for $Re = 10$, q_i/q reaches a plateau near 1 and then drops suddenly towards zero near the outlet of the heated section. The steady drop of q_i/q for $Re = 1$ can be explained by the fact that so much of the imposed heat flux has been redistributed upstream that, from an

energy balance standpoint, there is much less heat to exchange near the heated and downstream sections.

6.3.3 Distributions of Dimensionless Bulk and Wall Temperatures, θ_b and θ_w

The axial variation of the dimensionless bulk and wall temperatures are presented in Figs. 6.5 and 6.6 for the low and high Re cases, respectively. The values of K and Δ correspond to those considered in Figs. 6.2 and 6.3. As indicated by the horizontal arrows on Figs. 6.4 and 6.5, the left-hand axis correspond to values of the dimensionless wall temperature, whereas the right-hand axis refers to values of the dimensionless bulk temperatures. It should also be noted that the scale of the y-axis in Fig. 6.5 is 10 times the scale of the y-axis in Fig. 6.6. This is simply due to the fact that for the same amount of power input (same Gr_q), the temperature rise for $Re = 1$ is 10 times higher than that for $Re = 10$.

An examination of Fig. 6.5, the low Re case, reveals that $\theta_b > 0$ and $\theta_w > 0$ at the entrance of the heated section, confirming that the wall and the fluid get pre-heated prior to the start of the heated section. As was mentioned above, the extent of this pre-heating increases with an increase in K and/or Δ . In the heated section, the bulk and wall temperature variations become linear as the flow reaches a fully developed state. Near the outlet of the heated section, both θ_b and θ_w tend towards the same value, which they reach after a small distance downstream of the heated section. This is to be expected as q_i/q reaches zero soon after the exit of the heated section.

As shown in Fig. 6.6, the axial variations of θ_b and θ_w for the high Re case indicate that wall and fluid pre-heating increases with an increase in K and/or Δ . But for the same K and Δ , the extent of the pre-heating is less for this high Re case than for the low Re case, for reasons which were discussed in section 6.3.2. In the heated section, both θ_b and θ_w reach a fully developed state, except where wall conduction effects are strong, e.g. for $K = 500$ and $\Delta = 0.05$.

The low Re case corresponds also to a low Péclet number situation, $Pe = 5$, for which fluid axial conduction is important. Figure 6.7 illustrates the axial variation of the bulk temperature for cases where axial wall conduction is strong, $K = 50$ and $\Delta = 0.05$, and where it is nonexistent, $\Delta = 0$. The importance of fluid axial conduction compared to wall axial conduction should increase as K and Δ are decreased. This expected behavior is evident in Fig. 6.7.

6.3.4 Velocity Distribution, u/V

Velocity distributions at various axial locations have been plotted in Fig. 6.8 for $K = 50$ and $\Delta = 0.05$. In Fig. 6.8a, the $Re = 1$ case is presented, whereas Fig. 6.8b is devoted to the $Re = 10$ case. In each of these figures, five axial locations are examined: the inlet and outlet of the calculation domain, $z/D = -30$ and $z/D = 20$, respectively; and the inlet, outlet and mid-point of the heated section, $z/D = 0$, $z/D = 10$, and $z/D = 5$, respectively.

The first thing to note is that the velocity profiles are more dis-

torted for the low Re case than for the high Re case. This can be explained by looking at the Gr_q/Re^2 ratio, which is proportional to the buoyancy forces over the inertia forces. For the low Re case, $Gr_q/Re^2 = 5000$, the buoyancy forces become important and the flow tends to accelerate, in the region of the highest temperatures (in the vicinity of the wall). Since the mass flowrate is constant, the centerline velocity shows a corresponding decrease. For the high Re case, the acceleration of the fluid near the wall amounts to relatively smaller distortions of the velocity profiles.

Attention will first be focussed on Fig 6.8a. At $z/D = -30$, the inlet velocity profile is parabolic as imposed by the inlet boundary condition. At the entrance of the heated section, $z/D = 0$, the velocity profile has already been distorted to a point where, due to the above-mentioned buoyancy forces, the centerline velocity is negative. This underscores once more the significance of upstream pre-heating caused by axial wall conduction. Flow reversals in mixed-convection flows will be examined more closely in the flow visualization section of this Chapter. Furthermore, for $z/D = 0$, at the wall, the velocity gradient, and the associated heat transfer coefficient are high. Thus, at $z/D = 0$, the resistance to convective heat transfer is relatively low and this explains why the value of q_i/q is near unity in Fig. 6.4.

From $z/D = 0$ to $z/D = 5$, the value of q_i/q is close to one (Fig. 6.4) and, therefore, the buoyancy forces are high in the vicinity of the wall, and the velocity profile continues to be distorted. From $z/D = 5$ to $z/D = 10$, q_i/q decreases towards zero, so the temperature variation in a cross-section is not too steep in the wall region.

Thus the buoyancy forces in this region decrease and viscous forces start to dominate. So the flow decelerates in the wall region with a corresponding increase in the centerline velocity as is indicated by the $z/D = 10$ curve in Fig. 6.8a. Finally, ten diameters downstream of the heated section, at $z/D = 20$, a fully developed parabolic velocity profile is re-established.

The velocity profile for the high Re case will now be examined, Fig. 6.8b. At the entrance of the heated section, the velocity profile is slightly distorted, from its incoming parabolic shape, due to upstream wall conduction. In relative terms, however, this distortion is much less than that experienced by the low Re case.

Downstream of the inlet of the heated section, the value of q_1/q is essentially constant, Fig. 6.4. Therefore, the "local" value of Gr_q/Re^2 does not change appreciably. This implies that the buoyancy, viscous, and pressure forces balance each other, soon after the entrance to the heated section, establishing a fully developed state. Indeed, as will be shown shortly with the fRe curves, the velocity profile reaches a fully developed state soon after $z/D = 0$. The velocity profile at $z/D = 5$ is representative of this fully developed profile. At $z/D = 10$, q_1/q decreases from its constant value and, as illustrated in Fig. 6.8b, the profile is slowly distorted back to its original parabolic shape, which is reached at $z/D = 20$.

6.3.5 Fanning Friction Factor-Re Product, fRe

In order to complement the analysis of section 6.3.4, Fanning fric-

tion factor-Reynolds number products are presented in Fig. 6.9 for $K = 50$ and $\Delta = 0.05$ and for $Re = 1$ and 10 . As was discussed in section 6.3.4, the velocity gradients at the wall for $Re = 1$ are higher than that for $Re = 10$ as also evidenced by the larger values of fRe for $Re = 1$. Furthermore, in contrast to the high Re case, fRe for $Re = 1$ never reaches a constant value, indicating that the velocity profile constantly changes with axial distance in the heated section due to the heat flux redistribution caused by axial wall conduction.

6.4 FLOW VISUALIZATION STUDIES ON MIXED-CONVECTION FLOWS

6.4.1 Introduction

Flow visualization studies were undertaken to check the corresponding numerically predicted recirculation cells, and also to experimentally establish the laminar-turbulent transition which occurs in mixed-convection flows. The objective was not to do an exhaustive study, but rather to demonstrate the ability of the semi-transparent gold-film heated sections to provide a uniform heat flux while enabling experimental observations of these two phenomena.

During the flow visualization studies, the open-loop configuration of the closed-loop thermosyphon was used. This configuration, which is described in Appendix G and presented schematically in Fig. 5.12, permitted better control of the inlet mass flowrate and inlet temperature than would have been possible with the natural circulation of the closed-loop thermosyphon.

Flow visualization section no.2, which is shown in Figs. 5.5e and 5.11c, was used for the tests reported in this Chapter. The internal diameter is 0.0183 m and the heated length is 0.664 m, giving an L/D ratio of 36.3. As shown in Fig. 5.12, the flow visualization section is preceded by a straight length of insulated pipe, with an L/D of 48, to ensure that the flow is essentially fully developed at the entrance of the heated section. The insulation covering the heated section in Fig. 5.12 was removed during the flow visualization tests.

Care was taken to ensure that the inlet water temperature was always within 1 °C of the ambient temperature so as to minimize heat losses from the insulation-free flow visualization section. As for the dye injection instrumentation and procedure used to observe the flow field, the reader is referred to section 5.6 for a complete description. Finally, as will be shown in Chapter 7, axial wall conduction in the present flow visualization section is negligible as Δ approaches zero ($< 10^{-2}$) and values of Re are relatively high.

6.4.2 Recirculation Cells

6.4.2.1 Introduction

During the course of this study, the presence of recirculation cells were experimentally observed for a number of cases representative of mixed-convection situations. One such case is presented below for the following conditions: $V = 0.417$ cm/s, $P_w = 19.43$ W, $T_o = 25.6$ °C, and $T_a = 26.3$ °C. The corresponding non-dimensional parameters, which were evaluated at the mean fluid temperature in the heated section, are:

$$Re = 90$$

$$Gr_q = 0.33 \times 10^6; (Gr_q/Re^2 = 40.7)$$

$$Pr = 5.6; (Pe = 504)$$

A photograph of the resulting recirculation cell is presented in Fig. 6.10a. The corresponding streamline plot of the numerical simulation, which was drawn at the same scale, is presented in Fig. 6.10b. As indicated by the ruler on the right of Fig. 6.10a, the experimentally observed recirculation region covers approximately 1/3 of the heated section, up to a distance of 20 cm ($L/D = 11$) from the inlet. For completeness, the numerically predicted streamlines over the full calculation domain, including the upstream and downstream sections, are shown in Fig. 6.11. In Figs. 6.10a, 6.10b, and 6.11, the main flow is from the bottom to the top of the page. In Fig. 6.11, for reasons of clarity, the scale in the radial direction has been drawn to 10 times the scale in the z -direction. In this last figure, starting from the pipe wall and going towards the centerline, the streamlines plotted are for $\psi = 1.5 \times 10^{-4}, 1.3 \times 10^{-4}, \dots, 0.3 \times 10^{-5}, 0.2 \times 10^{-5}, 0.1 \times 10^{-5}, 0.5 \times 10^{-6}, 0.1 \times 10^{-6}, 0, -1 \times 10^{-7}, \dots, -5 \times 10^{-7}$. In Fig. 6.10b, only the streamlines encompassing the recirculation cell have been plotted and they correspond to values of $\psi = 0, -1 \times 10^{-7}, -2 \times 10^{-7}, -3 \times 10^{-7}, -4 \times 10^{-7}, -5 \times 10^{-7}$. The dimensional streamfunctions were evaluated using the results obtained for the velocity components according to the usual definition of the streamfunction: $\partial\psi/\partial r = \rho u$; $\partial\psi/\partial z = -\rho v$. In this formulation, the difference between two streamlines represent the mass flowrate between these two streamlines.

The numerical simulations were performed over a 1 meter length ($L/D = 55$), which included 0.05 m for the upstream section, 0.664 m for the heated section itself, and 0.286 m for the downstream section. The calculations were performed using variable (temperature dependent) viscosity and thermal conductivity in the fluid, and the outside boundary of the Plexiglass pipe was assumed to be adiabatic. This last assumption is fairly good considering that: (i) the inlet fluid temperature is within 1 °C of the ambient temperature; and (ii) the Plexiglass pipe has a low value of thermal conductivity, 0.19 W/m (Commercial Plastics, [1985]). In the fluid, 100 and 20 grid points were used in the axial and radial directions, respectively.

6.4.2.2 Observations

Physically, the existence of these recirculation cells can be explained as follows. The fluid enters the upstream section with a fully developed parabolic velocity profile and a uniform temperature. Due to the relatively large Pe and the absence of any significant axial heat conduction in the wall, the flow field is not disturbed until it enters the heated section. At the entrance of the heated section, the fluid near the wall is heated and its density becomes lower than the one associated with the fluid further from the wall. This density difference, in conjunction with the gravitational force field, leads to a buoyancy force, that causes the fluid to accelerate in the region next to the wall. To satisfy mass conservation, the increase in fluid velocity, and associated mass flowrate, in the vicinity of the wall is fed by fluid drawn from the pipe centerline region. In turn, this moves the point of maximum axial velocity towards the wall. This also progres-

sively depletes the fluid near the center of the pipe up to a point where the axial velocity at the centerline of the pipe is zero. The start of the recirculation cell corresponds to that point: it can be seen at $z \approx 14$ cm in Fig. 6.11.

Beyond the start of the recirculation cell, the fluid near the wall continues to accelerate and to fulfill the mass conservation requirements, the fluid near the centerline of the pipe must flow in the opposite direction to the main (or overall) flow. This establishes a closed zone where the fluid recirculates, with part of the fluid moving in the direction of the main flow and an equal amount of fluid flowing in the opposite direction.

Further down from the entrance and up to the end of the heated section, the streamlines are essentially parallel to one another. This indicates that the flow has reached a fully developed condition, whereby the velocity profile does not change with axial distance. In this fully developed region, the buoyancy, pressure, and viscous forces balance each other.

At the exit of the heated section, there is a sudden decrease in the level of the buoyancy forces, and the viscous forces, which now dominate, cause the fluid near the wall to decelerate. The excess fluid is directed towards the centerline, where the axial velocity becomes positive. Finally, at the end of the upstream section, the shapes of the streamlines are almost identical to those at the inlet of the calculation domain. This indicates that the parabolic velocity profile has been re-established at the outlet.

A comparison between Fig. 6.10a and Fig. 6.10b indicates that the location and size of the numerically-predicted recirculation zone agree fairly well with the experimental observations. Indeed, the cell starts at $z \approx 11.5$ cm in the experiment and at $z \approx 14$ cm in Fig. 6.10b. Assuming that the numerical simulations are accurate, this difference could be due to three factors.

Firstly, near the start of the cell, the axial velocities are very small, so that the dye is advected away very slowly with the main flow. It is, therefore, possible that the apex of the cell shown in Fig. 6.10a represents a zone of slow upward-moving fluid and not the exact start of the recirculation zone. However, this phenomenon is not believed to be that significant in this particular example as the observed apex remained stationary, within the reading accuracy of the ruler (± 1 mm) for approximately 10 minutes. The second factor is that in the regions of low flow velocity, such as the start of the recirculation cell, there could be some upstream (with respect to the main flow) diffusion of the dye.

The third possible source of discrepancy, which is believed to be the most significant of the three mentioned, is due to a heat flux greater than average at the entrance of the heated section. As will be shown and discussed in section 7.3.1.4, the two gold-film sections, which were instrumented with thermocouples, experienced unusually high wall temperatures at the entrance of the heated section. This indicated that the heat flux in this region was significantly greater than the average measured heat flux over the length of the heated section. The

flow visualization section used for this study was not equipped with thermocouples, so that unusual wall temperatures could not be recorded. But it is conceivable, since all gold-film sections were assembled the same way, that the present flow visualization section has the same generic "defect". If that is the case, then the fluid would get heated with a greater-than-average heat flux near the inlet. Thus, the buoyancy effects, which are responsible for the initiation of the cell, would be greater and, therefore, the recirculation zone would start sooner.

As a final point regarding Fig. 6.10a, it is interesting to note that the fully developed nature of the flow is clearly observable as the width of the recirculation zone remains essentially constant downstream of the beginning of the cell.

To summarize, the use of a semi-transparent gold-film section enabled the experimental visualization and verification of numerically-predicted recirculation cells. To the knowledge of this author, experimental observations of such cells for a uniform heat flux boundary condition have not been reported in the published literature.

6.4.3 Laminar-Turbulent Transition

6.4.3.1 Introduction

Several cases of laminar-turbulent transitions in mixed-convection flows were observed during the course of the flow visualization studies. Two such cases are presented in Figs. 6.12 and 6.13 and discussed in the next sub-section. Transition to an unstable flow is defined here as the

conditions for which an injected dye-tracer deviates from its streamline motion to form a somewhat unsteady wave-like motion.

6.4.3.2 Observations

Attention will first be focussed on Fig. 6.12, where transition was observed by injecting a continuous stream of dye in the center of the pipe at the entrance of the flow visualization section. The operating conditions were such that $Re = 72$ and $Gr_q = 0.7 \times 10^5$. The fluid used was water with $Pr = 6.0$. The "x" on the right of Fig. 6.12 indicates where the unsteady wave started to be discernible: it is located ≈ 46 cm ($L/D = 25.5$) from the inlet of the heated section.

The second observation of a laminar-turbulent transition flow, which is presented in Fig. 6.13, was obtained for the following conditions: $Re = 48$, $Gr_q = 0.95 \times 10^5$, and $Pr = 6.0$. In this experiment, the flow field was flooded with dye in a manner similar to the one used to observe recirculation cells. As shown in Fig. 6.13, the injected dye was carried away by the main flow except in a slow-moving flow region near the centerline of the pipe. This region has the appearance of a recirculation cell but careful monitoring of the location of the lower tip of this region indicated that it was moving upward at a velocity of ≈ 3 mm/min. The absence of a recirculation cell was later confirmed by numerical simulations. The laminar-turbulent transition was observed at a distance of ≈ 50 cm ($L/D = 28$) from the inlet.

As reported in the literature review of Chapter 1, the existence of a transition zone in low-Reynolds number (< 2000) mixed-convection

flows, is believed to be due to the presence of an inflexion point in the flow field which destabilizes the flow. This hypothesis is confirmed here, as numerical simulations performed for the above-mentioned conditions indicates the presence of inflexion points for both cases. For the conditions of Figs. 6.12 and 6.13, the presence of inflexion points were predicted at $L/D \approx 4$ and at $L/D \approx 6$, respectively.

As can be seen by comparing the location of the numerically predicted inflexion points and the start of the transition region, the disturbances needed some distance to grow before they became noticeable. This is in agreement with the findings of Hallman [1958] and Schaele et al. [1960]. It appears, though, that the semi-transparent gold-film heater and flow visualization techniques used in this study are better suited for an experimental investigation of this transition phenomenon in mixed-convection flows, subjected to a uniform heat flux, than the techniques used by Hallman [1958] and Schaele et al. [1960].

As was mentioned in Chapter 1, Hallman [1958] relied on wall temperature fluctuations to determine transition, as he could not observe the flow through his opaque heating tubes. Schaele et al. [1960] determined transition by observing the behavior of their injected dye filament at the exit of an opaque heating tube. The major advantage of the semi-transparent gold-film sections developed for this study is that, unlike the studies of Hallman [1958] and Schaele et al. [1960], the injected dye, and consequently the flow field, can be visualized over the full length of the heated section.

6.5 CLOSING REMARKS

To summarize, axial wall conduction can significantly affect the temperature and velocity fields of mixed-convection flows, when there is substantial redistribution of the applied heat flux. For water and for $Gr_q = 5000$, axial wall conduction was shown to be more pronounced when K and Δ were high and when Re was low.

The advantage offered by the flow visualization capability of the semi-transparent gold-film heated section, developed for this study, was demonstrated by observing the presence of recirculation regions and laminar-turbulent transitions which occur in mixed-convection flows. These experimental observations were compared with corresponding numerical predictions.

The results pertaining to the proposed closed-loop thermosyphon model are presented in the next Chapter.

CHAPTER VII

RESULTS: THE PROPOSED MODEL

7.1 INTRODUCTION

The proposed closed-loop thermosyphon model couples the local results of two-dimensional numerical simulations performed in the extended heated and cooled sections with a one-dimensional analysis of the entire loop. The mathematical formulation of this model has been presented in Chapter 2; the complete solution methodology was given in Chapter 4; and the governing non-dimensional parameters were identified in Appendix C. This Chapter presents the results obtained using this proposed model.

The results for two different geometries are presented in section 7.3. First, in order to validate the proposed model by comparing its results with the present experimental data, which are presented in Appendix K, the geometry used in the experimental portion of this thesis is considered. A second geometry is used to study the effects of heat losses and to compare the results given by the traditional one-dimensional models with the ones obtained with the proposed model. Before presenting these results, a few preliminary considerations are in order.

7.2 PRELIMINARY CONSIDERATIONS

This section is divided into four sub-sections. First, the two geometries considered in this Chapter are presented. The results of grid independence checks performed on one of these two geometries are discussed next. Then, consideration is given to the determination of appropriate lengths of the post-heated and post-cooled sections. Finally, the effects of axial wall conduction and heat losses from the heated section of the experimental closed-loop thermosyphon are discussed.

7.2.1 Presentation of the Two Geometries

A schematic representation of the geometries and the nomenclature used in the proposed model are given in Fig. 2.1. With reference to this figure, the dimensional and non-dimensional lengths of the two geometries considered in this Chapter are given in Table 7.1. As was discussed in Chapter 4 (Eq. 4.1), the proposed model relies on the inputs of local mean temperatures, $T_{hs,1}$ and $T_{cs,1}$, and friction factors, $f_{hs,1}$ and $f_{cs,1}$, provided by two-dimensional numerical simulations of mixed-convection flow in the extended heated and cooled sections. These extended sections include post-heated and post-cooled sections, as illustrated in Fig. 2.4a,b.

In geometry #1, which corresponds to the experimental apparatus, the cooled section is composed of a copper pipe ($\Delta = 0.084$) maintained at a constant temperature, \bar{T}_w , on its outside boundary. The post-

cooled section is made of a Plexiglass pipe and is insulated from the ambient fluid with a plastic foam insulation. The extended heated section arrangement of geometry #1 is somewhat more complex; a cross-section of this arrangement is shown in Fig. 5.7. As indicated in Chapter 5, the heat input was provided by passing electric current through a thin gold-film glued on the inner surface of a Plexiglass pipe. The numerical simulations performed in the proposed model had to account for these and other particularities of both these extended sections.

In the extended heated section, a total of 10 grid points were used in the solid region of the calculation domain, from r_x to r_6 in Fig. 5.7: 3 grid points were used in the polyester film, with one of these grid points essentially located at r_x (9.000127 mm) to obtain the wall temperature, T_w ; 1 grid point in the gold coating; 3 grid points in the combined Plexiglass pipe and glue region, with one of these located at the thermocouple location, r_4 ; and 3 grid points in the covering insulation. Control volume faces were positioned at the interface between each material, so as to ensure proper application of the harmonic mean practice for interpolating diffusion coefficients, as described in sub-section 3.5.1.3. The power input to the heated section was converted to a constant volumetric heat source, S_c in Eq. 3.21. This S_c was assumed to prevail over the whole control volume encompassing the gold coating, from r_2 to r_3 in Fig. 5.7. In the post-heated section, S_c was set equal to zero. The boundary condition on the outside surface was one of prescribed constant heat transfer coefficient and ambient fluid temperature, h_o and T_a , respectively, in Fig. 5.7. As stated earlier, h_o was set equal to 10 W/m°C.

In the extended cooled section of geometry # 1 a total of 3 grid points were used in the solid region. In the cooled section, the boundary condition on the outside surface was one of constant temperature, \bar{T}_w . In the post-cooled section, the thickness of the Plexiglass pipe was assumed to be the same as the thickness of the copper pipe and an "effective" h_o was used as the external boundary condition. This h_o was set equal to $2.5 \text{ W/m}^2\text{C}$, which takes into account the thermal resistance of the outside insulation.

All numerical simulations relevant to geometry #1 were performed with the elliptic set of the governing equations. This allows the inclusion of the wall regions in the calculation domain and accounts for the presence of possible flow reversals in the extended sections.

In the case of geometry #2, the thickness of the pipe wall in both extended sections is assumed to be negligible. Thus, numerical calculations are performed only in the fluid. Furthermore, because of a relatively high ΔZ in geometry #2, flow reversals in the heated and cooled sections occur only for cases of high heating (high Gr_m). Thus many of the simulations pertaining to this geometry could be undertaken with the less computer intensive parabolic set of the governing equations.

7.2.2 Grid Independence Checks

Many preliminary numerical simulations were undertaken to determine what grid spacing would provide grid independent results with the proposed model. These grid checks were performed in the extended heated and cooled sections of both geometries but only the results pertaining

to the extended heated section of geometry #1 will now be presented; the results obtained in the extended cooled section of both geometries and in the extended heated section of geometry #2 show similar trends. The conditions used for these checks were the same as those of experimental run # 8 (Appendix K) which represented the highest power input and thus the most demanding conditions.

As was mentioned in Chapter 3, the grid spacing was non-uniform in both the radial and axial directions, with a greater concentration of grid points near steep gradients.

It was found that the radial distribution of the grid points in the solid regions of geometry # 1, as discussed in the previous subsections, provided excellent grid independence. Further refinements of the radial grid in the solid regions changed the results by amounts which for all practical purposes were negligible. Thus the aforementioned radial distribution of grid points in the solid regions of geometry #1 was adopted for all further simulations with the proposed model. Attention in this section will therefore be focussed on the sensitivity of the results to the radial distribution of the grid points in the region occupied by the fluid and on the axial grid point distribution.

As was the case for the grid checks presented in Chapter 6, the axial variation of fRe was the most strict criteria to verify grid independence. The results of these grid checks are presented in Figs. 7.1a,b,c, where $z/D = 0$ and $z/D = 36.9$ correspond to the inlet and outlet of the heated section, respectively, and $z/D = 73.8$ to the outlet of the post-heated section. These grid checks were performed

with a short upstream section which extended from $z/D = -4.61$ to $z/D = 0$. The grid sizes quoted in Figs. 7.1a,b,c are composed of three numbers: the first two, under the heading "z", refer to the number of grid points in the axial direction in the heated and post-heated sections, respectively, and the third number, under the heading "r", represents the number of grid points in the fluid in the r-direction. The number of grid points in the solid region, which were discussed in the previous sub-section, are not reported in these figures. Figures 7.1a and 7.1b compare grid refinements in the axial and radial directions, respectively. In these two figures, numerical simulations were performed with variable viscosity and thermal conductivity in the fluid, with Re evaluated at the local film temperature, $(T_w + T_b)/2$.

As shown in Fig. 7.1a, the differences in the values of fRe obtained with the three axial grid spacings is barely noticeable, except in the region near the outlet of the heated section, which will be further examined shortly in Fig. 7.1c. Based on the results shown in this figure, a grid spacing of 40,30 was considered to give grid independent results in the axial direction, and all subsequent computations related to the extended heated and cooled sections of geometry #1 were performed with such a grid spacing. Figure 7.1b shows the effects of refining the grid in the radial direction. It is seen that a grid spacing of 10 in the radial direction gives an essentially grid independent solution. Therefore, 10 grid points were used in the radial direction for all following calculations in both extended sections.

It has already been mentioned in Chapter 6 that the numerically calculated value of fRe has an unexpected "kink" near the outlet of the

heated section. As is seen in Figs. 7.1a and 7.1b, this behavior is also present here for geometry #1. The existence of this "kink" is believed to be due to the abrupt decrease in wall heating at $z/D = 36.9$. As illustrated in Fig. 7.1c, which was obtained based on constant property calculations, an increase in the number of grid points in the axial direction diminishes this kink in the value of fRe at the outlet of the heated section. But this has been achieved with a substantial increase in the number of grid points; almost 3 times as many grid points as those in the other calculations have been utilized. The distance over which fRe displays this kink is small compared to the overall length of the loop. Thus, the $\Sigma f\Delta s$ terms in Eq. 7.1 remain practically unchanged, and the net effect of this kink on the determination of the average velocity in the loop is negligible. With these considerations in mind, it was decided that the grid with an axial distribution of 40,30 points and a radial distribution of 10 points in the region occupied by the fluid provided the optimum balance between accuracy of results and the computational costs.

With geometry # 2, for which the majority of simulations were done using the parabolic set of equations, it was found that in order to get an essentially grid independent solution, 70 and 55 grid points were necessary in the axial direction in the heated and post-heated sections, respectively. In the radial direction, 15 grid points provided a grid independent solution. For cases where the elliptic set of equations was used, the axial grid sizes in the heated and post-heated sections were identical to those use in the parabolic set, but, due to computer storage limitations, only 10 grid points were used in the fluid. It will be shown later that the average velocity determined with this last grid

spacing agrees within 1% with the average velocity prediction given by the 70,55 x 15 grid size of the parabolic set of equations.

7.2.3 Determination of the Lengths of the Post-Heated and Post-Cooled Sections

As noted in Chapter 2, the velocity and temperature profiles remain distorted, with respect to their fully developed forced convection distributions, for some distance beyond the heated and cooled sections. For this reason, post-heated and post-cooled sections were added to the calculation domain in the two-dimensional numerical calculations. This made it possible to supply the proposed model with accurate values of $f(s)$ and $T(s)$ in these sections.

Suitable lengths of the post-heated and post-cooled sections for geometry #1 were determined based on simulations performed with the same conditions as those used for the grid independence checks. As shown in Figs. 7.1a,b,c, near the end of the extended heated section, the calculated values of fRe tend, asymptotically, towards the fully developed laminar pipe flow value of 16. At $z/D = 73.8$, the value of fRe is within approximately 20% of $fRe = 16$. This value of z/D corresponds to a post-heated section length of 0.664 m, which is the same length as the heated section itself. Similarly, it can be shown that a post-cooled section length equal to the length of the cooled section, 0.612 m, was sufficient for the calculated value of fRe to be within approximately 20 % of $fRe = 16$.

As for geometry #2, it was observed that post-heated and post-cooled sections lengths of 1.5 m were required for the value of fRe to be within approximately 20% of $fRe = 16$. Therefore, all simulations performed with geometry #2 were done with post sections that were 1.5 m long.

7.2.4 Axial Wall Conduction and Heat Losses in the Heated Section of Geometry # 1

Simulations were undertaken to assess the significance of axial wall conduction and heat losses for the heated section of geometry #1. A cross-section of this arrangement is shown in Fig. 5.7. The deployment of grid points for this geometry was discussed in section 7.2.1, for the solid region, and in section 7.2.2, for the region occupied by the fluid. Figure 7.2 presents the axial variation of q_i/q for the conditions of experimental run # 8 ($P_w = 74.58$ W, $T_{i,n} = 17.01$ °C, and $T_a = 27.73$ °C): q_i represents the calculated heat flux at the fluid-solid interface, and q is the applied uniform heat flux normalized to the internal diameter ($q = P_w / 2\pi r_x L_3$). As indicated in Fig. 7.2, the combined effects of axial wall conduction and heat losses are small as the value of q_i/q is well within 1% of unity over the full length of the heated section. This was to be expected considering the very small thickness of the gold coating (20 \AA), the relatively high value of the Péclet number (≈ 1000), and the relatively high level of insulation on the outside surface of the plexiglass tube.

7.3 RESULTS AND DISCUSSION

7.3.1 Comparison Between Results of the Proposed Model and the Present Experimental Data

7.3.1.1 Introduction

As was mentioned in Chapter 2, traditional one-dimensional models of closed-loop thermosyphons are less accurate when the distance between the heated and cooled sections, ΔZ in Fig. 2.1, is small and/or when the power input, P_w , is high. This is because of the increased importance of mixed-convection effects and the associated distortions of the velocity and temperature fields from their fully developed forced convection distributions. The proposed model is designed to account for these effects. In order to test this new model, it was decided to compare its results against experimental data for operating conditions which produce strong mixed-convection effects including, for all runs considered here, flow reversals in the heated and cooled sections.

In the experiments, the power input was varied from 9.8 to 74.6 Watts ($Gr_m = 2181$ to 5078). The average wall temperature in the cooled section, \bar{T}_w , varied from 13.3°C to 26.9°C and was adjusted so that the mean closed-loop temperature would be relatively close to the ambient temperature, T_a , thereby limiting the amount of heat losses. In addition, using the correlation of Hallman [1958], conditions were carefully selected so as to avoid the laminar-turbulent transition often found in mixed-convection flows.

The model equation specialized for simulating flow and heat transfer

in the experimental apparatus, Eq. 4.20, was solved using the corresponding experimental conditions. Four inputs were needed: P_w , T_a , U , and \bar{T}_w . With these inputs, the proposed model was used to generate overall and local results which will now be compared to the experimental results.

7.3.1.2 Average velocity in the heated section

Figure 7.3 presents a comparison between the experimentally determined average velocity in the heated section of the closed-loop thermosyphon and the corresponding predictions of the proposed model. Both sets of data are also presented in Table 7.2. The diagonal on Fig. 7.3 represents a line of perfect agreement between the results of the proposed model and the experimental measurements. The error bars are the uncertainties on the measured average velocity ($\pm 5\%$) and are based on a calibration of the average velocity measurement, which is reported in Appendix J. The results of the proposed model presented in Fig. 7.3 were obtained by assuming constant fluid properties, evaluated at the mean loop temperature, T_m .

As illustrated in Fig. 7.3, the agreement between the proposed model and the experiments is very good. The line of perfect agreement lies totally within the experimental uncertainty.

As expected, the results in Table 7.2 indicate that the average velocity in the heated section increases with an increase in power input. However, the rate of increase in the average velocity is much

less than the one predicted by traditional one-dimensional models. For example, according to Case 1 of the traditional one-dimensional model, Eq. 2.15, and assuming that the thermophysical properties are constant, the average velocity in the thermosyphon should vary as the square root of the power input. Thus, over the range of power input conditions presented in Table 7.2, the average velocity should have increased by a factor of $(74.6/9.8)^{1/2} = 2.76$. As shown in Fig. 7.3 and in Table 7.2, the measured average velocity increases by a factor of only 1.85. This represents a 33% difference.

Notwithstanding the facts that the pipe radius in geometry #1 takes on two slightly different values, that heat losses could not be completely eliminated, and that form losses in the 180° bends are not accounted for in the traditional model, the disagreement between the traditional one-dimensional model and the observed results is important. It underscores the inability of traditional one-dimensional models to predict average velocities in the presence of strong mixed-convection effects in the extended heated and cooled sections. This is simply because, as will be shown in more detail in section 7.3.2.1, some of the assumptions used in the derivation of the traditional one-dimensional model are markedly incorrect in the presence of strong mixed-convection effects. Indeed, the invalidity of the $fRe = 16$ assumption can be clearly noticed in Fig. 7.1 where fRe is significantly higher than 16 over most of the heated section.

7.3.1.3 Axial wall temperature variations in the heated section

The local variations of the wall temperatures in the heated section are presented in Fig. 7.4a,b,c for run # 2, 4, and 8, respectively. The dots represent the average of the readings taken by thermocouples located in the female and male half sections at the same axial location. As indicated in Appendix G, the uncertainty on the wall temperatures was estimated at ± 0.05 °C. The uncertainty associated with the positioning of the thermocouples was ± 0.5 mm. Both of these uncertainty values are well within the diameter of the dots presented in Fig. 7.4. The solid lines plotted in Fig. 7.4a,b,c refer to the local wall temperatures predicted by the proposed model and were obtained by assuming constant fluid properties evaluated at T_m . The dashed line in Fig. 7.4c is for a variable property calculation and will be reviewed in section 7.3.1.5.

As can be seen, the agreement between the local predictions of the proposed model and the experimental measurements is quite good at low power levels, run # 2 and run # 4, but there is a deterioration in the level of agreement at high power, run # 8. In all three cases, the measured wall temperatures are higher than the numerical predictions in the entrance region of the heated section, at $z/D \approx 0$. Another point to note is that the last experimental wall temperatures measured near the outlet at $z/D \approx 35$ are all higher than their corresponding upstream neighbors. Furthermore, as illustrated in Fig. 7.5, the difference in the wall temperature measurements performed in the male and female half sections, at the same axial location, are important. These discrepancies can not be attributed solely to the ± 6.2 % heat flux uniformity of

the gold-film reported by Neill [1989] for this gold-film. The experimental results are, in all probability, also affected by some other defects in the gold-film sections. This point is elaborated in the next sub-section.

7.3.1.4 Problems encountered with the gold-film sections

Four gold-film sections were built during the course of this work. Two of these were instrumented with thermocouples. All of these sections eventually failed. This behavior is believed to be due to a gradual deterioration of the electrical connection between the copper electrodes and the gold-film.

Recall that the electrical connection between the gold-film and the copper electrode is provided by a thin coat of silver-loaded paint applied at both extremities of the gold-film section, as shown in the insert of Fig. 5.6. As mentioned in Chapter 5, the electrical resistance of the gold-film sections was carefully monitored from the initial cutting stage to the final electrode assembly. As indicated in Table 5.1, no abnormalities in the resistance of the gold-film sections were detected. It is only when the gold-film sections were supplied with electric power in the loop that problems were first noticed.

It is believed that, under the conditions of thermal expansion and contraction experienced by the gold film sections, the electrical link between the gold-film and the copper electrodes weakened with time, causing a local increase in the value of the electrical resistance at the electrode-film interface. This created a greater-than-average heat

flux and higher-than-normal wall temperatures, as seen in Figs. 7.4 and 7.5, in the vicinity of those locations. Furthermore, a 10 % increase in the value of the electrical resistance across heated section no.2 was observed from the initial test to the last test just before failure. It should also be noted that the preliminary temperature measurements obtained with heated section no.1 showed similar higher-than-normal temperatures in the vicinity of the electrodes, indicating that this defect is probably common to the four gold-film sections built for this study, including flow visualization sections no.1 and no.2.

As illustrated in Fig. 7.5, the measured wall temperatures near $z/D = 0$ are quite different depending on whether they are located inside the male or female half sections. This indicates that the aforementioned deterioration in the electrical contact between the film and the copper electrodes was not occurring at the same rate in the two half sections. Indeed, the two half sections did not fail at the same time. As the power input was increased to ≈ 100 Watts, the electrical link on one of the two half sections failed, creating an open circuit, while the other half section was still functional.

As indicated in Fig. 7.5, there are other regions where the measured temperatures are higher than expected, notably in the male section at $z/D = 12.9$ and $z/D = 18.5$. This is probably due to a manufacturing defect in the gold-film, causing a higher-than-average resistance. Unfortunately, these defects could only be observed using temperature measurements during the actual operation of the gold-film section; they could not be detected with the electrode-to-electrode resistance measurements performed during the construction phase.

These higher-than-average heat fluxes in the heated section must have affected the local values of the friction factors and of the mean temperatures. But these latter effects seem to have had only a small impact on the resulting average velocity in the thermosyphon: Thus the results of the proposed model, which were obtained by assuming a uniform heat flux in the heated section, agree, within the experimental uncertainty, with the experimental observations.

Furthermore, as was shown in section 6.4, despite these defects, the gold-film sections provided good qualitative flow visualization results on mixed-convection flows.

7.3.1.5 Effects of variable properties

The results described thus far in this Chapter were obtained by assuming that the thermophysical properties of the fluid were constant. The effects of variable properties on the overall and local results of the proposed model will now be examined.

The variable-property calculations were performed as follows. In the extended heated and cooled sections, where the changes in the physical properties of the fluid were the most significant and important, the thermal conductivity and the dynamic viscosity of the fluid were evaluated at each grid point based on the fluid temperature prevailing at that grid point. Elsewhere, around the loop, the fluid properties were evaluated at T_m .

As can be seen in Table 7.2, the average velocity obtained with the

proposed model using the variable property simulations are in good agreement with the constant-property calculations. The maximum difference occurs for the highest power input, run # 8, and is of the order of 1.5%. It can also be seen in Fig. 7.4c, which is also for run #8, that the wall temperatures are marginally affected by a variable-property calculation. Thus, for the conditions experienced in this work with geometry #1, the constant property assumption can be considered to be valid.

However, as indicated in Table 7.2, the difference in the values of the average velocity produced by variable- and constant-property calculations increase as the power input increases. This is due to the fact that as the power input increases, the temperature rise (or drop) increases in the heated (or cooled) sections. Thus, as the power input is augmented, there is an increase in the differences between local fluid properties and properties evaluated at T_m . Moreover, at the entrance of the cooled section, the fluid temperature decays more rapidly, because of the constant wall temperature boundary condition, than the corresponding increase in the heated section. Therefore, the viscosity of the fluid increases more rapidly in the cooled section than the corresponding decrease in the heated section. Accordingly, for a given flowrate in the loop, the frictional resistance in the cooled section increases more rapidly than the corresponding decrease of frictional resistance in the heated section. This implies, as shown in Table 7.2, that the overall frictional resistance and the average velocity will be, respectively, higher and lower for a variable-property calculation than for a constant-property calculation. Furthermore, the difference in V produced by constant- and variable-property calculations will increase

as the power input increases.

7.3.2 Results for Geometry #2

Since geometry #1 had two slightly different internal radii, only an approximate comparison with the results of the traditional one-dimensional analyses could be made. Furthermore, geometry #1 required the use of the elliptic set of the governing equations because of the presence of flow reversals in the extended sections. This implied that a detailed analysis of heat losses from thermosyphons corresponding to geometry #1 would have been computationally expensive. Geometry #2 does not suffer from these two drawbacks: the radius is the same all around the loop and ΔZ is high enough to avoid, for the most part, flow reversals in the heat transfer sections so that the parabolic set of equations could be used.

All results related to geometry #2 were done with $\bar{T}_w = 20.3^\circ\text{C}$. The fluid properties were evaluated at that temperature giving a $Pr = 7.0$. The desired Gr_m was obtained by varying the heat flux, q . Notice that $Gr_m (D^3 g \beta q / \nu V_{ref} k_f)$ is only proportional to the square root of q as V_{ref} is also proportional to $q^{1/2}$. For a fixed Gr_m , different values of $St_m (UD / \rho V_{ref} AC_p)$ were obtained by changing U . The non-dimensional ambient temperature, $\phi_\infty ([T_a - \bar{T}_w] / [qD / k_f])$, was varied, for fixed values of Gr_m and St_m , by changing T_a . Form losses in the 180° bends were neglected. The relevant equation to be solved with geometry #2 is Eq. 4.2. When heat losses are neglected, as will be the case in the next sub-section, Eq. 4.2 reduces to Eq. 4.3.

7.3.2.1 Comparison between the results of the proposed model and those of Cases 1 and 2 of the traditional one-dimensional model

Average velocity results

Figure 7.6 presents the results of a comparison between Cases 1 and 2 of the traditional one-dimensional model and the proposed model. Non-dimensional average velocities, $V^* = V/V_{ref}$, are plotted against Gr_m . The modified Stanton number, St_m , was set to zero, thereby eliminating heat loss effects from this comparison. It is worth noting, parenthetically, that once the value of St_m has been set to zero, the value of the non-dimensional ambient temperature, ϕ_∞ , is inconsequential since St_m multiplies ϕ_∞ in the governing non-dimensional equations and boundary conditions (see Appendix C). The predictions of the proposed model are for several different specified values of Gr_m ; as shown in Fig. 7.6, the resulting values of V^* were joined by straight piecewise lines. Also, for $Gr_m \geq 2000$, the use of the elliptic set of the governing equations was required due to the appearance of reversed flow in the extended heated and cooled sections.

For $Gr_m = 600$, both the parabolic and the elliptic set of equations were used in separate simulations. As can be seen in Fig. 7.6 and as stated earlier in section 7.2.2, the agreement between the resulting V^* is very good, with a difference of less than 1%. It is interesting to note that the CPU time required to run the proposed model with the parabolic set of equations was approximately 6 minutes, while the elliptic set of equations needed approximately 120 minutes of CPU time. Both simulations were done on the same 80386-based personal

computer running at 25 MHz. This comparison, albeit for different grids, illustrates the substantial computer time savings that can be obtained by using the parabolic set of equations, for cases where they are applicable, instead of the elliptic set in the proposed model.

As indicated in Fig. 7.6, for Case 1 of the traditional one-dimensional model, V^* is independent of Gr_m and is equal to unity. This reflects the fact that V_{ref} is, by definition, equal to the average velocity obtained using Case 1 of the traditional one-dimensional model. It can also be seen that for large values of Gr_m , the values of V^* for Case 2 reach, asymptotically, the value of V^* given by Case 1. For small Gr_m , the average velocity predictions of the proposed model are in good agreement with Case 2 of the traditional one-dimensional model, while the agreement with Case 1 is not as good. As Gr_m is increased, the discrepancy between the proposed model and the traditional one-dimensional model increases significantly. For $Gr_m = 4000$, the average velocity given by the proposed model is 28 % lower than the predictions given by Cases 1 and 2 of the traditional one-dimensional model.

In order to understand these differences between the proposed model and the traditional one-dimensional model, attention in the following sub-sections will be focussed on local results in the extended heated and cooled sections for a small and a large value of Gr_m . For convenience in the following discussion, Eq. 4.3, is written below in a slightly different form:

$$V = \frac{2r_i^2 g \beta \left[\begin{array}{c} \text{I} \quad \text{II} \quad \text{III} \quad \text{IV} \quad \text{V} \quad \text{VI} \quad \text{VII} \\ - T_{10}L_{10} + T_{10}L_1 + T_{10}L_2 + \sum_{i=1}^{i=L1} T_{hs,i} \Delta s_i^T + T_5L_5 - T_7L_7 - \sum_{i=1}^{i=L1} T_{cs,i} \Delta s_i^T \end{array} \right]}{\nu \left[\begin{array}{c} \text{IX} \quad \text{X} \quad \text{XI} \\ 16 (L_{10} + L_1 + L_2 + L_5 + L_7 + 2\pi R) + \sum_{i=1}^{i=L1} f_{hs,i} \text{Re} \Delta s_i^u + \sum_{i=1}^{i=L1} f_{cs,i} \text{Re} \Delta s_i^u \end{array} \right]} \quad (7.1)$$

As was mentioned in relation with Eq. 2.7, the numerator and denominator of Eq. 7.1 represent the "total buoyancy" and "total friction", respectively. Each of these expressions depends on V . They are composed of various terms identified by the letters I to XI. The dimensional form of this equation has been preferred to the non-dimensional form, Eq. C.1. This is because the relation between \bar{T}_w and the temperature levels in the loop is relatively easier to understand and discuss, from one Gr_m to another, than the corresponding relations among the non-dimensional temperatures, $\phi ([T - \bar{T}_w]/[qD/k_f])$, which depend on q .

Local results in the extended sections for $Gr_m = 300$

Figures 7.7a,b present local results in both heated and cooled extended sections for $Gr_m = 300$. The values of fRe are given in Fig. 7.7a; in the traditional models, fRe is set equal to 16. Distributions of the area-weighted mean temperature, T , and of the bulk temperature, T_b , are reported in Fig. 7.7b. The corresponding Nusselt number variations in the cooled section are depicted in Fig. 7.9.

As can be seen in Fig. 7.7a, because of mixed-convection effects, the fRe value in the heated and cooled sections can change significantly

from the value of 16 assumed in the traditional one-dimensional models.

Figure 7.7b shows the axial variation of the area-weighted mean cross-sectional temperature predicted by the proposed model and the axial temperature variations predicted by Cases 1 and 2 of the traditional one-dimensional model. As noted in Chapter 2, the results of Case 1 do not give the level of the absolute temperature in the loop; only the temperature rise (or drop) in the heated (or cooled) section can be predicted. However, in this work, for comparison purposes, it is assumed that the temperature at the outlet of the cooled section for Case 1 is the same as the one obtained using Case 2. For the proposed model, both the cross-sectional mean and bulk temperature predictions are presented. Recall that the former one is an area-weighted mean temperature while the later is a velocity-weighted temperature. For Cases 1 and 2 of the traditional one-dimensional model, these temperatures are equal. Also, as noted in Fig. 7.7b, and with reference to Fig. 2.1, the temperature at the inlet of the extended cooled section is equal to the temperature at the outlet of the extended heated section, T_5 , because heat losses are zero. Similarly, the temperature at the inlet of the extended heated section is equal to the temperature at the outlet of the extended cooled section, T_{10} .

As shown in Fig. 7.7b, the temperature distribution in the cooled section is linear for Case 1 and exponential for Case 2. For the proposed model, the mean temperature variation in the cooled section has an exponential-like shape, with a rapid decay at the entrance. The bulk temperature variation follows the same trend except that the values of T_b are slightly higher than the corresponding values of T . This is

because the rapid temperature changes that occur near the wall are not reflected as strongly in the bulk temperature due to the small velocities prevailing in the near-wall region.

In the heated section, the axial temperature variation is linear for Cases 1 and 2 and for the bulk temperature of the proposed model. Near the entrance, the area-weighted mean temperature variation predicted by the proposed model increases sharply due to the rapid temperature changes that occur near the wall. Further downstream along this section, the cross-sectional temperature profile reaches a fully developed condition, and the axial variation of the area-weighted mean temperature, T , becomes linear.

In the post-heated and post-cooled sections, the bulk temperature is the same as the one prevailing at the outlets of the heated and cooled sections, respectively. The area-weighted mean temperature predicted by the proposed model reaches, after a short distance, the same value as the bulk temperature. This last behavior is to be expected as the temperature profile become more and more uniform, within the cross-section of the pipe, as the fluid moves downstream of the heated (or cooled) section.

The differences in the values of fRe and T predicted by the different models influence the corresponding values of V^* . Perhaps the best way to explain these differences is to examine the various terms composing the "total buoyancy" and the "total friction" in Eq. 7.1. By adding terms II, III, IV, and V and then dividing them by the corresponding sum of the lengths, an average "hot" side temperature, T_{hot} , can be deter-

mined:

$$T_{hot} = \frac{T_{10}L_1 + T_{10}L_2 + \sum_{i=1}^{i=L1} T_{hs,i} \Delta s_i^T + T_5L_5}{L_1 + L_2 + L_3 + L_4 + L_5} \quad (7.2)$$

Similarly, an average "cold" side temperature, T_{cold} , can be evaluated:

$$T_{cold} = \frac{T_{10}L_{10} + T_7 L_7 + \sum_{i=1}^{i=L1} T_{cs,i} \Delta s_i^T}{L_7 + L_8 + L_9 + L_{10}} \quad (7.3)$$

It is the difference between T_{hot} and T_{cold} which drives the flow in the thermosyphon. As $T_{hot} - T_{cold}$ increases, total buoyancy increases. Opposing this total buoyancy is the total friction, the denominator of Eq. 7.1. This total friction can be divided by the total length of the the loop to give an average value for the frictional resistance, \overline{fRe} :

$$\overline{fRe} = \frac{16(L_{10} + L_1 + L_2 + L_5 + L_7 + 2\pi R) + \sum_{i=1}^{i=L1} f_{hs,i} Re \Delta s_i^u + \sum_{i=1}^{i=L1} f_{cs,i} Re \Delta s_i^u}{L_1 + L_2 + L_3 + L_4 + L_5 + L_7 + L_8 + L_9 + L_{10} + 2\pi R} \quad (7.4)$$

Table 7.3 presents the values of T_{hot} , T_{cold} , and \overline{fRe} predicted by the proposed model and both Cases of the traditional one-dimensional model. A comparison between Cases 1 and 2 indicates that the average cold side temperature is lower for Case 2. The main reason for this is that the term $\sum_{i=1}^{i=L1} T_{cs,i} \Delta s_i^T$ is lower for Case 2 than for Case 1, due to the exponential decay of temperature in the cooled section for Case 2. This increases total buoyancy and the corresponding average velocity. On the other hand, the increased average velocity for Case 2 decreases the tem-

perature rise across the heated section and, consequently, T_{hot} is slightly higher for Case 1 than for Case 2. But overall, the temperature difference, $T_{hot} - T_{cold}$, is higher in Case 2 than in Case 1, 0.201 versus 0.193. This represents a 4.1% difference. Since $\overline{fRe} = 16$ in both cases, the difference in V^* is also 4.1% as is seen in Table 7.3.

It is interesting to make a similar comparison using the simple equation for Case 2 developed in Chapter 2:

$$V = \left[\frac{P_w \beta g}{8\pi\mu C_p L} (\Delta Z + \epsilon) \right]^{1/2} \quad (2.15)$$

where,

$$\epsilon = 0 \quad \text{for Case 1,}$$

$$\epsilon = \frac{L_8}{2} - \frac{1}{X} + \frac{e^{-XL_8}}{1 - e^{-XL_8}} L_8 \quad \text{for Case 2,}$$

$$\text{and } X = \frac{\pi k Nu}{\rho_m V A C_p}, \text{ with } Nu = 3.66$$

Equation 2.15, much akin to Eq. 7.1, represents the ratio of total buoyancy over total friction in the loop. In that respect, the value of ϵ can be considered to be a correction factor applied to the total buoyancy to account for the exponential variation of temperature in the cooled section for Case 2, as opposed to the linear variation in Case 1. In the case being discussed here, $\epsilon = 0.16$ and $\Delta Z = 2.00$ m, which leads to $V^* = 1.041$.

The local results of the proposed model for $Gr_m = 300$ will now be considered. As illustrated in Fig. 7.7b, the area-weighted mean temperature at the inlet of the cooled section decreases quite rapidly. This is due to high heat transfer coefficients in the inlet region. Indeed, as indicated in Fig. 7.9, the Nusselt number in the inlet region is much higher than the value of 3.66 assumed in Case 2 of the traditional one-dimensional model. Due to this rapid decay in temperature in the entrance region of the cooled section, the term $\sum_{i=1}^{I=L1} T_{cs,i} \Delta s_i$ is lower for the proposed model than for Cases 1 and 2. Thus, as indicated in Table 7.3, T_{cold} is lower for the proposed model than for Cases 1 and 2. This increases total buoyancy and the corresponding average velocity. As was mentioned above, this increase in average velocity decreases the overall temperature rise in the heated section, which decreases T_{hot} . However, the decrease in T_{cold} is higher than the decrease in T_{hot} and total buoyancy for the proposed model is 12.4 % higher than for Case 1. However, the average frictional resistance, \overline{fRe} , predicted by the proposed model is only 6.9% higher than that for Cases 1 and 2. Thus, relative to Case 1, the combined effects of these increases in total buoyancy and total friction lead to a 5.5 % increase in V^* , as indicated in Table 7.3.

Local results in the extended sections for $Gr_m = 3000$

As can be seen in Fig. 7.8a, mixed-convection effects are very significant in both the extended heated and cooled sections for $Gr_m = 3000$. In fact, flow reversals were identified in both extended sections. The fRe product reaches values that are approximately four times greater than the value of 16 associated with fully developed flow.

The striking feature of Fig. 7.8b is the difference in the temperature levels predicted by Cases 1 and 2 of the traditional one-dimensional model and by the proposed model. The proposed model predicts a mean loop temperature of around 28.5°C whereas the traditional model predicts that $T_m \approx 42.5^{\circ}\text{C}$. This is mainly due to the following reason. As shown in Fig. 7.9, the Nusselt number predicted by the proposed model for $Gr_m = 3000$ is much higher than the value of $Nu = 3.66$ assumed for Case 2 of the traditional one-dimensional model. Indeed, the mean Nusselt number obtained with the proposed model is equal to 9.44 for $Gr_m = 3000$. This implies that fluid cooling will be more rapid with the proposed model than for Case 2. Consequently, the overall temperature levels will be lower for the proposed model.

Figure 7.8b also shows that the area-weighted mean and bulk temperatures predicted by the proposed model are quite different. The bulk temperature variations in the heated and cooled sections follow the expected trends, while the mean temperature variations are somewhat more complicated due to strong mixed-convection effects. Furthermore, because of the drastic change in thermal boundary conditions that occurs at the outlets of the heated and cooled sections, there is a sudden decrease in the value of T at $z/D = 50$. In the post-sections, the mean temperature tends towards the value of T_b , as the cross-sectional temperatures become more and more uniform.

As shown in Table 7.4, the resulting values of T_{hot} and T_{cold} , predicted by the traditional one-dimensional model and the proposed model, are quite different. It is also seen that the average value of

the frictional resistance, \overline{fRe} , predicted by the proposed model is significantly higher than the value of 16 used in the traditional model. This leads to a decrease in V . In turn, this increases the temperature rise (drop) in the heated (cooled) sections, which translates into a greater difference between T_{hot} and T_{cold} . So, in effect, an increase in total friction contributes to an increase in total buoyancy. However, as shown in Table 7.4, relative to Cases 1 and 2, the predictions of the proposed model indicate that the increase in total friction is greater than the increase in total buoyancy. Consequently, V^* predicted by the proposed model is lower than 1, and equal to 0.799.

Also of interest in Fig. 7.8b is the fact that the temperature predictions given by Cases 1 and 2 are nearly identical, while they were quite different for $Gr_m = 300$. This can be explained with reference to Eq. 2.14b. When Gr_m is increased from 300 to 3000, V increases by a factor of 10. Accordingly, X in Eq. 2.14b, decreases by a factor of 10. When multiplied by $(s - s_g)$, the exponent of the exponential function varies from 0 to X since $(s_g - s_g) = 1$ for geometry #2. Thus, for $Gr_m = 3000$, the range of variations of the exponent is 10 times less than that for $Gr_m = 300$. Over this reduced range, the exponential function gives an almost linear temperature variation, as shown in Fig. 7.8b. Since Case 1 is based on the assumption of a linear temperature variation, it is not surprising to see a very good agreement between Cases 1 and 2, as is also shown in Table 7.4. This explanation is also consistent with observations made earlier in connection with Fig. 7.6, that the velocity predictions for Case 2 reach, asymptotically, the values given by Case 1 as Gr_m increases.

In addition, since the temperature variation in the cooled section for Case 2 is almost linear, ϵ in Eq. 2.15 should be negligible in comparison to ΔZ . Indeed, for $Gr_m = 3000$, $\epsilon = 0.02$ for $\Delta Z = 2.00$.

7.3.2.2 Effects of heat losses (gains) from thermosyphons

The effects of heat losses on V^* predicted by the proposed model are presented in Fig. 7.10 for geometry #2. Values of V^* are plotted against a non-dimensional ambient temperature, $\phi_\infty = (T_a - \bar{T}_w)/(qD/k_f)$, for three different values of St_m and for $Gr_m = 500$. The values of V^* were obtained by solving Eq. 4.2. It should be recalled that the level of insulation is inversely proportional to St_m . At the limit when $St_m = 0$, the thermosyphon is perfectly insulated. For completeness, the value of V^* corresponding to a perfectly insulated loop, $V^* = 1.030$, is presented in Fig. 7.10.

As is seen in Fig. 7.10, the impact of heat losses (gains) on V^* can be significant. For example, for $St_m = 1 \times 10^{-4}$ and $\phi_\infty = -10$, V^* is equal to 0.571. This corresponds to a 45% decrease in comparison with the value of V^* obtained for $St_m = 0$. At the other extreme, a 28% increase in the value of V^* is noted for $St_m = 1 \times 10^{-4}$ and $\phi_\infty = 10$.

In order to explain this behavior, the concept of hot and cold side temperatures will be used again. Equation 4.2 can be written in a form similar to Eq. 7.1:

$$V = \frac{2r_i^2 g \beta \left[\begin{array}{l} \text{I} \quad \text{II} \\ - \frac{(T_{10} - T_a)}{\Omega} (1 - e^{-\Omega L_{10}}) - T_a L_{10} + \frac{(T_1 - T_a)}{\Omega} (1 - e^{-\Omega L_1}) + T_a L_1 \\ \\ \text{III} \quad \text{IV} \quad \text{V} \\ + \frac{(T_2 - T_a)}{\Omega} (1 - e^{-\Omega L_2}) + T_a L_2 + \sum_{i=1}^{L_1} T_{hs,i} \Delta s_i^T + \frac{(T_5 - T_a)}{\Omega} (1 - e^{-\Omega L_5}) + T_a L_5 \\ \\ \text{VI} \quad \text{VII} \quad \text{VIII} \\ - \frac{(T_7 - T_a)}{\Omega} (1 - e^{-\Omega L_7}) - T_a L_7 - \sum_{i=1}^{L_1} T_{cs,i} \Delta s_i^T + \frac{\Omega R^2 (e^{-\pi R \Omega} + 1)}{(\Omega^2 R^2 + 1)} (T_6 - T_{11}) \end{array} \right]}{\nu \left[\begin{array}{l} \text{IX} \quad \text{X} \quad \text{XI} \\ 16 (L_{10} + L_1 + L_2 + L_5 + L_7 + 2\pi R) + \sum_{i=1}^{L_1} f_{hs,i} \text{Re} \Delta s_i^u + \sum_{i=1}^{L_1} f_{cs,i} \text{Re} \Delta s_i^u \end{array} \right]} \quad (7.5)$$

When compared to Eq. 7.1, the numerator of Eq. 7.5 contains an extra term, term VIII, which accounts for heat losses (gains) in the 180° bends. It can be shown, however, that the impact of this extra term on total buoyancy is insignificant and can be neglected. So, hot and cold side temperatures can be defined in a manner similar to the one used in sub-section 7.3.2.1, and the corresponding terms of Eq. 7.5. The value of total friction is the same as the one determined for the case where heat losses are zero, Eq. 7.4.

The first thing to note here is that the amount of heat loss is not

the same in the various sections of the loop. In each section, the amount of heat losses (gains) is proportional to the overall heat loss coefficient, U ($\text{W/m}^2\text{C}$), to the length of the section, and to the difference between the average temperature of the fluid inside the loop and the ambient fluid temperature. For example, consider the post-heated and post-cooled sections. Since the lengths of these two sections are equal and U is the same around the loop, the difference between the average temperature of the fluid inside the loop and the ambient fluid temperature will determine the difference in heat losses (gains) between the two sections. If the temperature at the outlet of the cooled section, T_9 , is lower than T_a , heat gains in the post-cooled section will be higher than in the post-heated section. In fact, there may even be cases where T_4 will be greater than T_a while T_9 is smaller than T_a . This would create a situation where there would be heat losses in the post-heated section while the post-cooled section would experience heat gains. Such imbalances between heat losses (gains) in various sections of the loop imply that the average hot and cold side temperatures do not increase (or decrease) at the same rate. In turn, these influence total buoyancy and the average velocity.

Yet another factor which explains the variation of the average velocity with heat losses (gains) is the fact that the amount of heat removed in the cooled section is greatly influenced by the cumulative amount of heat losses (gains) around the loop. This is illustrated in Table 7.5 where the two extreme cases mentioned above are examined, along with the case of the perfectly insulated loop.

In Table 7.5, Q_L/P_w represents the ratio of heat losses around

the loop and the power input in the heated section. The first thing to note in this table is that \overline{fRe} is approximately equal to the fully developed value of 16 in all three cases. This indicates that the velocity profiles are only mildly affected by mixed-convection effects and the total friction does not change significantly from one case to the other. However, the variation in total buoyancy (or $T_{hot} - T_{cold}$) is much greater.

For the case where $\phi_{\infty} = +10$, it can be seen that the total amount of heat gain around the loop, excluding the heated and cooled sections, is greater than the power input to the loop. In order to satisfy the overall energy balance in the closed-loop, the amount of heat removed in the cooled section has to be 2.23 times the power input supplied in the heated section. Thus, the overall temperature drop across the cooled section has to be higher than the overall temperature rise in the heated section. Consequently, the difference $T_{hot} - T_{cold}$ increases when compared to the case where $St_m = 0$. The corresponding total buoyancy and average velocity also increase as indicated in Table 7.5.

As for the case where $\phi_{\infty} = -10$, an interesting situation occurs. For this particular condition, the ratio of Q_L/P_w is negative and greater than 1. This implies that heat losses around the loop, excluding the heated and cooled sections, exceed the power input to the loop. Consequently, because of the overall energy balance requirements, heat is supplied (and not removed) in the cooled section. As shown in Table 7.5, this profoundly affects T_{hot} and T_{cold} and the resulting average velocity.

As indicated in Fig. 7.10, for a given ϕ_{∞} , the magnitude of the difference between the values of V^* obtained with a specified St_m and for a perfectly insulated loop increases as St_m is increased. This reflects the fact that the above-mentioned phenomena are amplified when the insulation level is decreased or, alternatively, when St_m is increased.

Of course, the analysis of the effects of heat losses on V^* presented in this sub-section is specific to geometry #2. Nonetheless, the results presented here indicate that the average velocity inside a closed-loop thermosyphon can be markedly affected by heat gains (or losses) in the insulated portion of the thermosyphon.

7.4 CLOSING REMARKS

In this Chapter, it was established that the proposed model can successfully predict the average velocity measured experimentally in the closed-loop thermosyphon of interest. Using the proposed model, it was also shown that traditional one-dimensional models can significantly overpredict the average velocity in thermosyphons when strong mixed-convection effects are present. This is because traditional one-dimensional models do not account for the local nature of the flow in the extended heated and cooled sections of the thermosyphon. Also, the proposed model revealed that heat losses (gains) from thermosyphons can significantly affect the average velocity.

This concludes the presentation of results obtained during the course of this study.

C H A P T E R V I I I

CONCLUSION

8.1 REVIEW OF THE THESIS

Complementary analytical, numerical, and experimental investigations of fluid flow and heat transfer in closed-loop thermosyphons with vertical heated and cooled sections were presented in this thesis. Attention was focussed on the geometry shown in Fig. 1.1. Of particular interest to this study, were the cases where conditions similar to mixed-convection prevailed in both the heated and cooled sections.

Analytically, the traditional one-dimensional approach to the modeling of closed-loop thermosyphon was reviewed in Chapter 2. Using this approach, it was shown that the average velocity in the thermosyphon is equal to: $V = \left[\frac{P_w \beta g}{8\pi \mu C_p L} (\Delta Z + \epsilon) \right]^{1/2}$ (Eq. 2.15). When V is high, the temperature drop in the cooled section can be assumed to be linear. In this case, ϵ , which accounts for the exponential variation of temperature in the cooled section, is negligible when compared to ΔZ . In turn, V becomes independent of r_1 , Nu , and \bar{T}_w . However, when ΔZ is small and/or when P_w is high, the ratio Gr_q/Re^2 could take on values which lead to mixed-convection conditions in the heated and cooled sections of the loop. For those cases, the assumption of fully developed forced convection conditions, used in traditional one-dimensional model, is incorrect and Eq. 2.15 can not be used to accurately predict the average velocity inside the loop.

A new model has been proposed to alleviate these deficiencies. The proposed model, which has been described in Chapter 2, involves the coupling of local results of two-dimensional numerical simulations of mixed-convection in the heated and cooled sections with a traditional one-dimensional analysis. Also, unlike the traditional one-dimensional models, the proposed model allows the analysis of heat gains (or losses) from sections of the thermosyphons other than the heated and cooled sections. The proposed model enables the determination of the average velocity inside the loop, and provides detailed temperature and velocity profiles in the heat transfer passages of the loop.

Numerically, the work reported in Chapter 3 included the formulation, implementation and testing of a finite-volume based method for the solution of steady, laminar, two-dimensional, axisymmetric mixed-convection in vertical pipes. The computer code based on these methods was used as part of the proposed model and was also used to study conjugate conduction and mixed-convection in vertical pipes.

The methodology for the solution of the general momentum equation of the proposed model, Eq. 4.2, has been described in Chapter 4. The methodology requires the inputs of two-dimensional numerical simulations, which themselves depend on the results of Eq. 4.2. This coupling is handled by the use of an iterative procedure.

Experimentally, as reported in Chapter 5, a closed-loop thermosyphon was specially designed and constructed for this study in order to validate the proposed model. One of the key elements of this experimental facility is the heated section. It uses a thin semi-transparent gold-film, glued on the inner surface of a Plexiglass pipe. Power input to the closed-loop thermosyphon is provided by passing electric current through this gold-film. This heated section was instrumented with thermocouples to obtain local wall temperature measurements. Furthermore, the flow visualization capability offered by the semi-transparent heated section enabled observations of recirculation cells and laminar-turbulent transitions which occurred in the heated section.

8.2 SUMMARY OF RESULTS AND MAJOR CONTRIBUTIONS

Mixed-convection flows

The computer code developed for this study was used to fill an apparent void in the literature on the treatment of conjugate conduction and laminar mixed-convection in vertical pipes for upward flow and uniform wall heat flux. Using this code, it was found that significant portions of the applied heat flux on the outside surface of the heated section could be redistributed by axial conduction within the heated, upstream, and downstream sections of the pipe. The magnitude and the extent of upstream and downstream heating increases monotonically with an increase of K (solid to fluid thermal conductivity ratio) and/or Δ (pipe thickness to diameter ratio). In turn, this heat flux redistribution could significantly affect the temperature and velocity fields inside the fluid. For example, in one particular case, it was found

that upstream axial wall conduction distorted the parabolic velocity profile at the entrance of the upstream section to a point where the centerline velocity was negative at the entrance of the heated section.

The existence of recirculation cells for upward mixed-convection flows in vertical pipes subjected to a uniform wall heat flux had been established by a number of researchers and was confirmed with the present numerical investigation. In this work, for the first time, these cells were experimentally observed using the flow visualization capability of the gold-film heater.

Laminar-turbulent transitions which are often encountered in mixed-convection flows even for low Re (< 2000) were also observed experimentally. In this case, the major advantage of the semi-transparent gold-film heater is that the injected dye, and consequently the flow field, can be visualized over the full length of the heated section. Earlier experimental studies of such mixed-convection flows (Hallman [1958], Scheele et al. [1960]) did not have such a facility, and laminar-transitions were inferred indirectly either through thermocouple measurements (Hallman [1958]) or by flow visualization at the end of the heated section (Scheele et al. [1960]). The present experimental approach is superior to these earlier investigations.

Proposed model

The proposed model successfully predicted the average velocity measured in the closed-loop thermosyphon over the range of power inputs studied experimentally in this work, from 10 to 75 Watts ($Gr_m \approx 2200$ to

5100). Predictions made with this model indicate that the rate of increase of V with increasing power input, P_w , is much lower than the $V \sim (P_w)^{1/2}$ relationship predicted by the traditional one-dimensional model, Eq. 2.15.

In addition, the proposed model was able to predict fairly well, specially at low power levels, local wall temperature measurements made in the heated section of the closed-loop thermosyphon. At high power levels, the agreement was not so good. This may be due to an unforeseen deterioration of the electrodes of the gold-film heater section.

A second geometry, which is somewhat simpler than that used in the experiments, was used to examine the differences between the traditional one-dimensional and the proposed models. For the case where there are no heat losses, $St_m = 0$, it was shown that traditional one-dimensional models can significantly overpredict the average velocity in thermosyphons for high Gr_m . In one particular case, for $Gr_m = 4000$, the average velocity given by the traditional one-dimensional model was 28 % higher than the predictions of the proposed model. This is because traditional one-dimensional models do not account for the distortion of the velocity and temperature profiles from fully developed forced convection shapes. Such distortions occur due to mixed-convection effects, especially for high values of Gr_m .

Using the proposed model, heat losses (and gains), from sections of the thermosyphon other than the heated and cooled portions, were studied, seemingly for the first time. For $Gr_m = 500$, it was shown that such heat losses (or gains) can significantly alter the average velocity

in the thermosyphon when compared to that in a perfectly insulated loop, $St_m = 0$. For example, for $St_m = 1 \times 10^{-4}$ and $\phi_\infty = -10$, V is about 45 % lower than for the case where $St_m = 0$.

8.3 PROPOSED EXTENSIONS OF THIS WORK

The numerical code developed in this work could be extended to examine uninvestigated areas of mixed-convection flows in pipes such as three-dimensional developing mixed-convection flow and heat transfer in inclined pipes.

The results obtained with the gold-film heaters were quite encouraging but more work is required to improve the electrical link between the gold-film heater and the electrode. Once this problem with the electrical connection at the electrode is solved, these semi-transparent heated sections could be very good tools to further enhance the understanding of mixed-convection flows including the laminar-turbulent transition phenomenon.

As for the proposed model, a number of extensions can be envisioned. The modelling of turbulent mixed-convection flows would be a logical addition to the proposed model. Also, the inclusion of a transient capability into the proposed model could be a useful extension. For example, it could be used to study the behavior of the loop at start-up.

In conjunction with control volume finite element methods (CVFEM) (Baliga, [1988]), the proposed model could be used to simulate thermosyphons with irregular-shaped heated (or cooled) sections, such as rod

bundle geometries with axial flow in the interstices between heated rods.

The experimental facility built for this study could easily be modified to examine, for example, other values of ΔZ or power inputs. This would broaden the experimental data base initiated with the work presented in this thesis.

REFERENCES

- Acosta, R., Sen, M., Ramos, E., Single-Phase Natural Circulation in a Tilted Square Loop, **Wärme-und Stoffübertragung**, vol. 21, pp. 269-275, 1987.
- Aung, W., Worku, G., Developing Flow and Flow Reversal in a Vertical Channel with Asymmetric Wall Temperatures, **ASME Journal of Heat Transfer**, vol. 108, pp. 299-304, 1986a.
- Aung, W., Worku, G., Theory of Fully Developed, Combined Convection Including Flow Reversal, **ASME Journal of Heat Transfer**, vol. 108, pp. 485-488, 1986b.
- Baker, D.J., A Technique for the Precise Measurement of Small Fluid Particles, **J. Fluid Mech.**, vol. 26, part 3, pp. 573-575, 1966.
- Baliga, B.R., Patankar, S.V., Elliptic Systems: Finite-Element Method II, in Minkowycz, W.J., Sparrow, E.M., Schneider, G.E., Pletcher, R.H., (eds.), **Handbook of Numerical Heat Transfer**, Chap. 11, pp. 421-461, Wiley, New York, 1988.
- Barozzi, G.S., Pagliarini, G., Experimental Investigation of Coupled Conduction and Laminar Convection in a Circular Tube, **Int. J. Heat Mass Transfer**, vol. 27, no. 12, pp. 2321-2329, 1984.
- Barozzi, G.S., Pagliarini, G., A Method to Solve Conjugate Heat Transfer Problems: The Case of Fully Developed Laminar Flow in a Pipe, **ASME Journal of Heat Transfer**, vol. 107, pp. 77-83, 1985.
- Bau, H.H., Torrance, K.E., On the Effects of Viscous Dissipation and Pressure Work in Free Convection Loops, **Int. J. Heat Mass Transfer**, vol. 26, no. 5, pp. 727-734, 1983.
- Baughn, J.W., Takahashi, R.K., Hoffman, M.A., McKillop, A.A., Local Heat Transfer Measurements Using an Electrically Heated Thin Gold-Coated Plastic Sheet, **ASME Journal of Heat Transfer**, vol. 107, pp. 953-959, 1985.
- Baumeister, T., Avallone, E.A., Baumeister III, T., **Marks' Standard Handbook of Mechanical Engineers**, Eight edition, McGraw-Hill, 1978.
- Blevins, R.D., **Applied Fluid Dynamics Handbook**, Van Nostrand Reinhold Company, 1984.
- Campo, A., Schuler, C., Heat Transfer in Laminar Flow Through Circular Tubes Accounting for Two-Dimensional Wall Conduction, **Int. J. Heat Mass Transfer**, vol. 31, no. 11, pp. 2251-2259, 1988.
- Chow, L.C., Husain, S.R., Campo, A., Effects of Free Convection and Axial Conduction On Forced-Convection Heat Transfer Inside a Vertical Channel at Low Péclet Numbers, **ASME Journal of Heat Transfer**, vol. 106, pp. 297-303, 1984.

- Collins, M.W., Combined Convection in Vertical Tubes, **Symposium on Heat and Mass Transfer by Combined Forced and Natural Convection**, The Institution of Mechanical Engineers, paper C155/71, 1971.
- Collins, M.W., Finite Difference Analysis for Developing Laminar Flow in Circular Tubes Applied to Forced and Combined Convection, **Int. J. Numer. Meths. Engrg.**, vol. 15, pp. 381-404, 1980.
- Commercial Plastics & Supply Corp.**, company literature, 1985.
- CRC Handbook of Chemistry and Physics**, edited by Weast, R.C. and Lide, D.R., 70th edition, 1989.
- Creveling, H.F., De Paz, J.F., Baladi, J.Y., Schoenhals, R.J., Stability Characteristics of a Single-Phase Free Convection Loop, **J. Fluid Mech.**, vol. 67, part 1, pp. 65-84, 1975.
- Dalbert, A.M., Penot, F., Peube, J.L., Convection Naturelle Laminaire dans un Canal Chauffé à Flux Constant, **Int. J. Heat Mass Transfer**, vol. 24, no. 9, pp. 1463-1473, 1981.
- Dalbert, A.M., Natural, Mixed and Forced Convection in a Vertical Channel with Asymmetric Uniform Heating, **Proc. 7th Int. Heat Transfer Conf.**, Munich, Federal Republic of Germany, vol. 3, pp. 431-434, 1982.
- Dahlquist, G., Bjorck, A., **Numerical Methods**, Prentice-Hall, Englewood Cliffs, N.J., 1974.
- Damerell, P.S., Flow in a Toroidal Thermosyphon with Angular Displacement of the Heated and Cooled Sections, M.S.M.E. Thesis, Purdue University, 1977.
- Damerell, P.S., Schoenhals, R.J., Flow in a Toroidal Thermosyphon with Angular Displacement of Heated and Cooled Sections, **ASME Journal of Heat Transfer**, vol. 101, pp. 672-676, 1979.
- Davis, E.J., Gill, W.N., The Effects of Axial Conduction in the Wall on Heat Transfer with Laminar Flow, **Int. J. Heat Mass Transfer**, vol. 13, pp. 459-470, 1970.
- Durig, B.R., Shadday, M.A., Flow in a Rectangular Closed-Loop Thermosyphon with Vertical Heat Transfer Passages, ASME paper 86-WA/HT-78, 1986.
- Dyer, J.R., The Development of Laminar Natural-Convective Flow in a Vertical Uniform Heat Flux Duct, **Int. J. Heat Mass Transfer**, vol. 18, pp. 1455-1465, 1975.
- Faghri, M., Sparrow, E.M., Simultaneous Wall and Fluid Axial Conduction in Laminar Pipe-Flow Heat Transfer, **ASME Journal of Heat Transfer**, vol. 102, pp. 58-63, 1980.
- Fanney, A.H., Dougherty, B.P., Measurement of Buoyancy-Induced Flow Using a Self-Heated Thermistor Flowmeter, **ASME Journal of Solar Energy Engineering**, vol. 109, pp. 34-39, 1987.

Fithen, R.M., Anand, N.K., Finite-Element Analysis of Conjugate Heat Transfer in Axisymmetric Pipe Flows, **Numer. Heat Transfer**, vol. 13, pp. 189-203, 1988.

Glen, J.S., Hilborn, J.W., The Canadian Slowpoke Heating Reactor, in Nuclear Heat Application, Proc. of a Technical Committee Meeting and Workshop on Nuclear Heat Application, International Atomic Energy Agency, pp. 129-139, 1984.

Greif, R., Zvirin, Y., Mertol, A., The Transient and Stability Behavior of a Natural Convection Loop, **ASME Journal of Heat Transfer**, vol. 101, pp. 684-688, 1979.

Greif, R., Natural Circulation Loops, **ASME Journal of Heat Transfer** (50th Anniversary Issue), vol. 110, pp. 1243-1258, 1988.

Habchi, S., Acharya, S., Laminar Mixed Convection in Symmetrically or Asymmetrically Heated Vertical Channel, **Numer. Heat Transfer**, vol. 9, pp. 605-618, 1986.

Hallinan, K.P., Heat Transfer From a Vertical Tube Bundle in a Natural Circulation Loop, M.Sc., Purdue University, 1983.

Hallinan, K.P., Viskanta, R., Heat Transfer from a Vertical Tube Bundle Under Natural Circulation Conditions, **Int. J. Heat and Fluid Flow**, vol. 6, no. 4, pp. 256-264, 1985.

Hallman, T.H., Combined Forced and Free Convection in a Vertical Tube, Ph.D. Thesis, Purdue University, 1958.

Hanratty, T.J., Rosen, E.M., Kabel, R.L., Effect of Heat Transfer on Flow Field at Low Reynolds Numbers in Vertical Tubes, **Ind. Eng. Chem.**, vol. 50, no. 5, pp. 815-820, 1958.

Hippensteele, S.A., Russell, L.M., Stepka, F.S., Evaluation of a Method for Heat Transfer Measurements and Thermal Visualization Using a Composite of a Heater Element and Liquid Crystals, **ASME Journal of Heat Transfer**, vol. 105, pp. 184-189, 1983.

Hippensteele, S.A., Russell, L.M., Torres, F.J., Local Heat-Transfer Measurements on a Large Scale-Model Turbine Blade Airfoil Using a Composite of a Heater Element and Liquid Crystals, **ASME Journal of Engineering for Gas Turbines and Power**, vol. 107, pp. 953-960, 1985.

Holman, J.P., Boggs, J.H., Heat Transfer to Freon 12 Near the Critical State in a Natural-Circulation Loop, **ASME Journal of Heat Transfer**, vol. 82, pp. 221-226, 1960.

Huang, B.J., A Combined Convection Correlation for Vertical Downward Cooling Flow in a Natural Circulation Loop, **Int. J. Heat Mass Transfer** vol. 30, no. 7, pp. 1544-1546, 1987a.

Huang, B.J., Zelaya, R., Stability Analysis of a Thermosyphon Loop, ISES Solar World Congress, Hamburg, Federal Republic of Germany, pp. 1091-1096, 1987b.

Huang, B.J., Zelaya, R., Heat Transfer Behavior of a Rectangular Thermosyphon Loop, **ASME Journal of Heat Transfer**, vol. 110, pp. 487-493, 1988.

Iqbal, M., Aggarwala, B.D., Khatry, A.K., On the Conjugate Problem of Laminar Combined Free and Forced Convection Through Vertical Non-Circular Ducts, **ASME Journal of Heat Transfer**, vol. 94, pp. 52-56, 1972.

International Standard Organization, **Mesure de débit des liquides dans les conduites fermées - Méthode par pesée**, Norme Internationale ISO 4185-1980(F), 1980.

Jackson, J.D., Cotton, M.A., Axcell, B.P., Studies of Mixed Convection in Vertical Tubes, **Int. J. Heat and Fluid Flow**, vol. 10, no.1, pp. 2-15, 1989.

Japkise, D., Advances in Thermosyphon Technology, in **Advances in Heat Transfer**, edited by Irvine, T.F. and Hartnett, J.P., vol. 9, pp. 1-111, Academic Press, New York, 1973.

Kakaç, S., Yener, Y., Laminar Forced Convection in the Combined Entrance Region of Ducts, in **Low Reynolds Number Flow Heat Exchangers**, edited by Kakaç, S., Shah, R.K., Bergles, A.E., pp. 165-204, Hemisphere, Washington, D.C., 1983.

Karki, K.C., Patankar, S.V., Cooling of a Vertical Shrouded Array by Natural Convection: A Numerical Study, **Fundamentals of Natural Convection/Electronic Equipment Cooling**, ASME HTD-vol. 32, pp. 33-40, 1984.

Kays, W.M., Perkins, H.C., Forced Convection, Internal Flow in Ducts, in **Handbook of Heat Transfer - section 7**, edited by Rohsenow, W.M. and Hartnett, J.P., McGraw-Hill, 1973.

Keller, J.B., Periodic Oscillations in a Model of Thermal Convection, **J. of Fluid Mech.**, vol. 26, part 3, pp. 599-606, 1966.

Kenemy, G.A., Somers, E.V., Combined Free and Forced-Convective Flow in Vertical Circular Tubes - Experiments with Water and Oil, **ASME Journal of Heat Transfer**, vol. 84, pp. 339-346, 1962.

Kline, S.J., McClintock, F.A., Describing Uncertainties in Single-Sample Experiments, **Mechanical Engineering**, pp. 3-8, January 1953.

Lavine, A.G., A Three-Dimensional Analysis of Natural Convection in a Toroidal Loop, Ph.D. Thesis, U.C. Berkeley, 1984.

Lavine, A.S., Greif, R., Humphrey, J.C., Three-Dimensional Analysis of Natural Convection in a Toroidal Loop: Effect of Tilt Angle, **ASME Journal of Heat Transfer**, vol. 108, pp. 796-805, 1986.

Lavine, A.S., Greif, R., Humphrey, J.C., A Three-Dimensional Analysis of Natural Convection in a Toroidal Loop - The Effect of Grashof number, **Int. J. Heat Mass Transfer**, vol. 30, no. 2, pp. 251-262, 1987.

Lawlor, D., Calibration of One Hewlett-Packard Quartz Thermometer, Model 2804A, Serial No. 2432A01529, NRC Physics Division, Report No. APH2833, 1987.

Lawrence, W.T., Chato, J.C., Heat-Transfer Effects on the Developing Laminar Flow Inside Tubes, **ASME Journal of Heat Transfer**, vol. 88, pp. 214-222, 1966.

Macagno, E.O., Flow Visualization in Liquids, Iowa Institute of Hydraulic Research, Report No. 114, 1969.

Macagno, E.O., Hung, T., Computational and Experimental Study of a Captive Annular Eddy, **J. Fluid Mech.**, vol. 28, part 1, pp. 43-64, 1967.

Maeda, Mr., Toriay Company - Plastic and film division, personal communication, 1989.

Marner, W.J., McMillan, H.K., Combined Free and Forced Laminar Convection in a Vertical Tube with Constant Wall Temperature, **ASME Journal of Heat Transfer**, vol. 92, pp. 559-562, 1970.

Mertol, A., Heat Transfer and Fluid Flow in Thermosyphons, Ph.D. Thesis, U.C. Berkeley, 1980.

Mertol, A., Place, W., Webster, T., Greif, R., Detailed Loop Model (DLM) Analysis of Liquid Solar Thermosyphons with Heat Exchangers, **Solar Energy**, vol. 27, no. 5, pp. 367-386, 1981.

Mertol, A., Greif, R., Zvirin, Y., Two-Dimensional Study of Heat Transfer and Fluid Flow in a Natural Convection Loop, **ASME Journal of Heat Transfer**, vol. 104, pp. 508-514, 1982.

Mertol, A., Greif, R., Giz, A.T., The Transient, Steady State, and Stability Behavior of a Thermosyphon with a Parallel-Flow Heat Exchanger, **ASME Journal of Heat Transfer**, vol. 105, pp. 58-65, 1983.

Mertol, A., Greif, R., A Review of Natural Circulation Loops, in **Natural Convection Fundamentals and Applications**, edited by Kakaç, S., Aung, W., Viskanta, R., Hemisphere, Washington, D.C., 1985.

Merzkirch, W., **Flow Visualization**, Academic Press, New York, 1974.

Metias, B., Criteria for Mixed Convection, HTL Technical Report No. 51, Heat Transfer Laboratory, University of Minnesota, 1963.

Metias, B., Eckert, E.R.G., Forced, Mixed and Free Convection Regimes, **ASME Journal of Heat Transfer**, vol. 86, pp. 295-296, 1964.

Mori, S., Sakakibara, M., Tanimoto, A., Steady Heat Transfer to Laminar Flow in Circular Tube with Conduction in the Tube Wall, **Heat Transfer-Japanese Research**, vol. 3, no. 2, pp. 37-46, 1974.

Morton, B., Ingham, D.B., Kenn, D.J., Heggs, P.J., Recirculating Combined Convection in Laminar Pipe Flow, **ASME Journal of Heat Transfer**, vol. 111, pp. 106-113, 1989.

- Mueller, T.J., Hydrodynamic Flow Visualization, in **Fluid Mechanics Measurements**, edited by Goldstein, R.J., Hemisphere, Washington, D.C., 1983.
- National Bureau of Standards, **Reference Tables for Thermocouples**, NBS Circular 561, Washington D.C., 1955.
- National Bureau of Standards, **Thermocouple Reference Tables**, NBS Monograph 125, Washington D.C., 1979.
- Neill, W.S., Local Natural Convection Heat Transfer Measurements Using a Thin Gold-Film Technique, M. Eng. Thesis, McGill University, 1989.
- Pagliarini, G., Effects of Axial Conduction in the Wall and the Fluid on Conjugate Heat Transfer in Thick-Walled Circular Tubes, **Int. Comm. Heat Mass Transfer**, vol. 15, pp. 581-591, 1988.
- Patankar, S.V., A Numerical Method for Conduction in Composite Materials, Flow in Irregular Geometries and Conjugate Heat Transfer, 6th Int. Heat Transfer Conf., vol. 3, pp. 297-302, 1978.
- Patankar, S.V., **Numerical Heat Transfer and Fluid Flow**, Hemisphere, 1980.
- Penot, F., Dalbert, A.M., Convection Naturelle Mixte et Forcée dans un Thermosyphon Vertical Chauffé à Flux Constant, **Int. J. Heat Mass Transfer**, vol. 26, no. 11, pp. 1639-1647, 1983.
- Raithby, G.D., Skew Upstream Differencing Schemes for Problems Involving Fluid Flow, **Comput. Meths. Appl. Mech. Engrg.**, vol. 9, pp. 153-164, 1976.
- Ronen, A., Zvirin, Y., The Behavior of a Toroidal Thermosyphon at High Graetz (and Grashof) Numbers, **ASME Journal of Heat Transfer**, vol. 107, pp. 254-258, 1985.
- Scheele, G.F., Rosen, E.M., Hanratty, T.J., Effect of Natural Convection on Transition to Turbulence in Vertical Pipes, **Can. J. Chem. Eng.**, pp. 67-73, 1960.
- Scheele, G.F., Hanratty, T.J., Effect of Natural Convection on Stability of Flow in a Vertical Pipe, **J. Fluid Mech.**, vol. 14, pp. 244-256, 1962.
- Scheele, G.F., Hanratty, T.J., Effect of Natural Convection Instabilities on Rates of Heat Transfer at Low Reynolds Numbers, **A.I.Ch.E. Journal**, vol. 9, no. 2, pp. 183-185, 1963.
- Scheele, G.F., Greene, H.L., Laminar-Turbulent Transition for Nonisothermal Pipe Flow, **A.I.Ch.E. Journal**, vol. 12, no. 4, pp. 737-740, 1966.
- Sen, M., Ramos, E., Trevino, C., The Toroidal Thermosyphon With Known Heat Flux, **Int. J. Heat Mass Transfer**, vol. 28, no. 1, pp. 219-233, 1985a.

Sen, M., Ramos, E., Trevino, C., On the Steady-State Velocity of the Inclined Toroidal Thermosyphon, **ASME Journal of Heat Transfer**, vol. 107, pp. 974-977, 1985b.

Shadday, M.A., Combined Forced/Free Convection Through Vertical Tubes at High Grashof Numbers, Proc. of the 8th Int. Heat Transfer Conf., San Francisco, vol. 3, pp. 1433-1437, 1986.

Shah, R.K., London, A.L., **Laminar Flow Forced Convection in Ducts**, Supplement 1 to Advances in Heat Transfer, Academic Press, 1978.

Shah, R.K., Fully Developed Laminar Flow Forced Convection in Channels, in **Low Reynolds Number Flow Heat Exchangers**, ed. by Kakaç, S., Shah, R.K., Bergles, A.E., pp. 75-108, Hemisphere, 1983.

Shirtliffe, C.J., Optimum Polynomials for Representing Temperature-emf Data for Thermocouples over Limited Ranges, NRCC Division of Building Research, Technical Paper No. 355, 1971.

Sparrow, E.M., Chrysler, G.M., Azevedo, L.F., Observed Flow Reversals and Measured-Predicted Nusselt Numbers for Natural Convection in a One-Sided Heated Vertical Channel, **ASME Journal of Heat Transfer**, vol. 106, pp. 325-332, 1984.

Stern, C.H., Greif, R., Humphrey, J.A.C., An Experimental Study of Natural Convection in a Toroidal Loop, **ASME Journal of Heat Transfer**, vol. 110, pp. 877-884, 1988.

Tabor, H., Some Thoughts on Water Heaters for Rural Areas, **Sunworld**, vol. 8, no. 2, pp. 44-46, 1984.

Van Doormaal, J.P., Raithby, G.D., Enhancements of the SIMPLE Method for Predicting Incompressible Fluid Flows, **Numer. Heat Transfer**, vol. 7, pp. 147-163, 1984.

Welander, P., On the Oscillatory Instability of a Differentially Heated Fluid Loop, **J. Fluid Mech.**, vol. 29, part 1, pp. 17-30, 1967.

Yao, L.S., Is a Fully-Developed and Non-Isothermal Flow Possible in a Vertical Pipe?, **Int. J. Heat Mass Transfer**, vol. 30, no. 4, pp. 707-716, 1987.

Zariffah, E.K., Soliman, H.M., Trupp, A.C., The Combined Effects of Wall and Fluid Axial Conduction on Laminar Heat Transfer in Circular Tubes, Proc. 7th Int. Heat Transfer Conf., Munich, Federal Republic of Germany, vol. 4, pp. 131-136, 1982.

Zeldin, B., Schmidt F.W., Developing Flow with Combined Forced-Free Convection in an Isothermal Vertical Tube, **ASME Journal of Heat Transfer**, vol. 94, pp. 211-223, 1972.

Zvirin, Y., Shitzer, A., Bartal-Bornstein, A., On the Stability of the Natural Circulation Solar Heater, Proc. 6th Int. Heat Transfer Conf., Toronto, Canada, vol. 2, pp. 141-145, 1978.

Zvirin, Y., A Review of Natural Circulation Loops in Pressurized Water Reactors and Other Systems, **Nuclear Engineering and Design**, vol. 67, pp. 203-225, 1981a.

Zvirin, Y., Jeuck III, P.R., Sullivan, C.W., Duffey, R.B., Experimental and Analytical Investigation of a Natural Circulation System with Parallel Loops, **ASME Journal of Heat Transfer**, vol. 103, pp. 645-652, 1981b.

APPENDIX A

THERMOPHYSICAL PROPERTIES OF WATER

In this thesis, the thermophysical properties of water were obtained using the correlations presented in this Appendix. The correlations represent least squares fit to the data contained in the CRC Handbook of Physics [1989]. In the following relationships, the temperature T is in $^{\circ}\text{C}$.

Specific Heat: ($\text{J/kg}^{\circ}\text{C}$)

$$C_p = 4179.9 - 0.9233 T + 0.011285 T^2$$

Thermal Conductivity: ($\text{W/m}^{\circ}\text{C}$)

$$k = 0.5586 + 0.002171 T - 9.822 \times 10^{-6} T^2$$

Dynamic Viscosity: (Ns/m^2)

$$\mu = 1.6701 \times 10^{-3} - 4.1734 \times 10^{-5} T + 4.9043 \times 10^{-7} T^2 - 2.1638 \times 10^{-9} T^3$$

Density: (kg/m^3)

$$\rho = 1001.2 - 0.08982 T - 0.003462 T^2$$

Coefficient of Thermal Expansion: (K^{-1})

$$\beta = (0.006924 T + 0.08982) / \rho$$

A P P E N D I X B

SOLUTION OF THE TRADITIONAL MODEL

The governing equations and the boundary conditions of the traditional one-dimensional model have been presented in Chapter 2. In this Appendix, the governing equations of the traditional model are solved for two sets of thermal boundary conditions, which are referred to as Case (1) and Case (2).

Case (1):

For Case (1), the thermal boundary conditions are:

- Constant heat flux in the heated section;
- Constant cooling flux in the cooled section;
- Adiabatic condition elsewhere.

The governing equations are given by:

Momentum equation around the loop:

$$V = \frac{\rho_m r_i^2 g \beta}{8\mu L} \oint T(s) \cos\theta \, ds \quad (2.8)$$

Energy equation:

In the heated section ($s_3 \leq s \leq s_4$):

$$\rho_m V A C_p \frac{dT}{ds} = P_w / L_3 \quad \text{and} \quad T = T_3 + \frac{(s-s_3)}{\rho_m V A C_p} \frac{P_w}{L_3} \quad (2.11 \text{ a,b})$$

In the cooled section ($s_8 \leq s \leq s_9$):

$$\rho_m \text{VAC}_p \frac{dT}{ds} = -P_w/L_8 \quad \text{and} \quad T = T_8 - \frac{(s-s_8)}{\rho_m \text{VAC}_p} \frac{P_w}{L_8} \quad (2.12 \text{ a,b})$$

In the adiabatic sections:

$$\rho_m \text{VAC}_p \frac{dT}{ds} = 0 \quad \left[\begin{array}{l} (s_4 < s < s_8) \\ T = \text{cte} = T_4 \quad \text{and} \quad T_5=T_6=T_7=T_8=T_4 \\ (s_9 < s < s_3) \\ T = \text{cte} = T_9 \quad \text{and} \quad T_{10}=T_{11}=T_1=T_2=T_3=T_9 \end{array} \right] \quad (2.13 \text{ a,b,c})$$

Introducing these temperature distributions into Eq. 2.8 and integrating along path "s", as shown in Fig. 2.1, leads to:

$$\begin{aligned} V = \frac{\rho_m r_i^2 g \beta}{8 \mu L} & \left[\int_{s_1}^{s_3} T_9 \cos \theta \, ds + \int_{s_3}^{s_4} \left(T_3 + \frac{(s-s_3)}{\rho_m \text{VAC}_p} \frac{P_w}{L_3} \right) \cos \theta \, ds + \right. \\ & + \int_{s_4}^{s_6} T_4 \cos \theta \, ds + \int_{s_6}^{s_7} T_4 \cos \theta \, ds + \int_{s_7}^{s_8} T_4 \cos \theta \, ds \\ & \left. + \int_{s_8}^{s_9} \left(T_8 - \frac{(s-s_8)}{\rho_m \text{VAC}_p} \frac{P_w}{L_8} \right) \cos \theta \, ds + \int_{s_9}^{s_{11}} T_9 \cos \theta \, ds + \int_{s_{11}}^{s_1} T_9 \cos \theta \, ds \right] \quad (B.1) \end{aligned}$$

In the 180° bends (from s_6 to s_7 and from s_{11} to s_1), θ varies and the corresponding integrals can not be evaluated directly. Using the transformation $ds = R d\theta$ for these bends and solving, Eq. B.1 reduces to:

$$V = \frac{\rho_m r_i^2 g \beta}{8 \mu L} \left[T_9 (L_1 + L_2) + T_3 L_3 + \frac{P_w L_3}{2 \rho_m V A C_p} + T_4 (L_4 + L_5) + T_4 R \sin \theta \right]_0^\pi$$

$$- T_4 L_7 - T_8 L_8 + \frac{P_w L_8}{2 \rho_m V A C_p} - T_9 (L_9 + L_{10}) - T_9 R \sin \theta \left[\right]_\pi^{2\pi} \quad (B.2)$$

Under the adiabatic assumption, the temperature rise across the heated section is simply given by:

$$(T_4 - T_3) = \frac{P_w}{\rho_m V A C_p} \quad (B.3)$$

Using this relationship, Eq. B.2 reduces to:

$$V = \left[\frac{P_w \beta g \Delta Z}{8 \pi C_p \mu L} \right]^{1/2} \quad (B.4)$$

where ΔZ is the height difference between the middle of the cooled section and the middle of the heated section:

$$\Delta Z = (L_{10} + L_9 + \frac{L_8}{2}) - (L_1 + L_2 + \frac{L_3}{2}) \quad (B.5)$$

Case (2):

For Case (2), the thermal boundary conditions are:

- Constant heat flux in the heated section;
- Constant wall temperature in the cooled section;
- Adiabatic condition elsewhere.

The governing equations are the same as for Case (1) except for the cooled section where:

In the cooled section ($s_8 \leq s \leq s_9$):

$$\rho_m \text{VAC}_p \frac{dT}{ds} = -h2\pi r_i (T - \bar{T}_w) \quad \text{and} \quad T = (T_8 - \bar{T}_w)e^{-X(s-s_8)} + \bar{T}_w \quad (2.14 \text{ a,b})$$

$$\text{where } X = \frac{h2\pi r_i}{\rho_m \text{VAC}_p} = \frac{\pi k \text{Nu}}{\rho_m \text{VAC}_p}, \quad \text{Nu} = 3.66$$

Using this temperature distribution and solving, one obtains:

$$V = -\frac{\rho_m r_i^2 g \beta}{8\mu L} \left[T_9(L_1+L_2) + T_3 L_3 + \frac{P_w L_3}{2\rho_m \text{VAC}_p} + T_4(L_4+L_5) \right. \\ \left. - T_4 L_7 + \frac{1}{X} (T_8 - \bar{T}_w)(e^{-XL_8} - 1) - \bar{T}_w L_8 - T_9(L_9+L_{10}) \right] \quad (B.6)$$

Regrouping terms and simplifying:

$$V^2 = \frac{P_w \beta g}{8\pi C_p \mu L} \left[L_4 + L_5 - L_7 + L_3/2 - \frac{1}{X} + \frac{e^{-XL_8}}{(1-e^{-XL_8})} L_8 \right] \quad (B.7)$$

Adding and subtracting $L_8/2$ in the bracket, Eq. B.7 can then be written as:

$$V^2 = \frac{P_w \beta g}{8\pi C_p \mu L} \left[\underbrace{L_4 + L_5 - L_7 + L_3/2 - L_8/2}_{\Delta Z} + \underbrace{\frac{L_8}{2} - \frac{1}{X} + \frac{e^{-XL_8}}{(1-e^{-XL_8})} L_8}_{\epsilon} \right] \quad (B.8)$$

which is equation 2.15 .

APPENDIX C

NON-DIMENSIONALIZATION OF THE GOVERNING EQUATIONS OF THE PROPOSED MODEL

In this Appendix, the governing equations of the proposed model, without conjugate heat conduction in the pipe wall, will be non-dimensionalized with reference to the problem of interest (Fig. 2.1). For this analysis, the elliptic set of the governing equations and the following dimensionless variables will be used:

$$u^* = \frac{u}{V_{ref}}, \quad v^* = \frac{v}{V_{ref}}, \quad V^* = \frac{V}{V_{ref}}$$

$$r^* = \frac{r}{D}, \quad z^* = \frac{z}{D}, \quad s^* = \frac{s}{D}$$

$$L_1^* = L_1/D, \quad L_2^* = L_2/D, \quad L_3^* = L_3/D, \quad L_4^* = L_4/D, \quad L_5^* = L_5/D$$

$$L_6^* = L_6/D, \quad L_7^* = L_7/D, \quad L_8^* = L_8/D, \quad L_9^* = L_9/D, \quad L_{10}^* = L_{10}/D$$

$$R^* = R/D \quad (D=2r_i)$$

$$\phi = \frac{T - \bar{T}_w}{qD/k_f}, \quad \phi_3 = \frac{T_3 - \bar{T}_w}{qD/k_f}, \quad \phi_8 = \frac{T_8 - \bar{T}_w}{qD/k_f}, \quad \phi_m = \frac{T_m - \bar{T}_w}{qD/k_f}$$

$$P^* = \frac{p - \xi \rho_m g z}{\rho_m V_{ref}^2}$$

where the reference velocity, V_{ref} , is defined as:

$$V_{ref} = \left[\frac{P_w \beta g \Delta Z}{8\pi C_p \mu L} \right]^{1/2}$$

The dimensionless governing equations are the following:

Momentum equation around the loop: (Eq. 2.17)

$$\left[32V^* \int_{s_{10}^*}^{s_3^*} ds^* + 4 \int_{s_3^*}^{s_5^*} \left. \frac{\partial u^*}{\partial r^*} \right|_{r^*=1/2} ds^* + 32V^* \int_{s_5^*}^{s_8^*} ds^* + 4 \int_{s_8^*}^{s_{10}^*} \left. \frac{\partial u^*}{\partial r^*} \right|_{r^*=1/2} ds^* \right] =$$

$$Gr_m \left[\int_{s_{10}^*}^{s_3^*} \phi \cos \theta ds^* + \int_{s_3^*}^{s_5^*} \phi_{hs} \cos \theta ds^* + \int_{s_5^*}^{s_8^*} \phi \cos \theta ds^* + \int_{s_8^*}^{s_{10}^*} \phi_{cs} \cos \theta ds^* \right] \quad (C.1)$$

Energy equation in the insulated sections (Eq. 2.29)

$$V^* d\phi = - St_m (\phi - \phi_\infty) ds^* \quad (C.2)$$

Extended heated and cooled sections

Continuity equation (Eq. 2.20):

$$\frac{1}{r^*} \frac{\partial(r^* v^*)}{\partial r^*} + \frac{\partial u^*}{\partial z^*} = 0 \quad (C.3)$$

r-momentum equation (Eq. 2.21):

$$v^* \frac{\partial v^*}{\partial r^*} + u^* \frac{\partial v^*}{\partial z^*} = - \frac{\partial P^*}{\partial r^*} + \frac{1}{Re_{ref}} \left[\frac{1}{r^*} \frac{\partial}{\partial r^*} \left[r^* \frac{\partial v^*}{\partial r^*} \right] - \frac{v^*}{r^{*2}} + \frac{\partial^2 v^*}{\partial z^{*2}} \right] \quad (C.4)$$

z-momentum equation (Eq. 2.22):

$$v^* \frac{\partial u^*}{\partial r^*} + u^* \frac{\partial u^*}{\partial z^*} = - \xi \frac{Gr_m}{Re_{ref}} (\phi - \phi_m) - \frac{\partial P^*}{\partial z^*} + \frac{1}{Re_{ref}} \left[\frac{1}{r^*} \frac{\partial}{\partial r^*} \left[r^* \frac{\partial u^*}{\partial r^*} \right] + \frac{\partial^2 u^*}{\partial z^{*2}} \right] \quad (C.5)$$

where; $\xi=1$ for downward flow with cooling
 $\xi=-1$ for the case of heating in upflow

Energy equation (Eq. 2.23)

$$v^* \frac{\partial \phi}{\partial r^*} + u^* \frac{\partial \phi}{\partial z^*} = \frac{1}{Pr Re_{ref}} \left[\frac{1}{r^*} \frac{\partial}{\partial r^*} \left[r^* \frac{\partial \phi}{\partial r^*} \right] + \frac{\partial^2 \phi}{\partial z^{*2}} \right] \quad (C.6)$$

Boundary conditions

a) Inlet boundary conditions:

For heating in upflow

For cooling in downflow

$s^* = s_3$ $z^* = 0$	$s^* = s_8$ $z^* = 0$
$u^* = 2V^* [1 - (2r^*)^2]$ $\phi = \phi_3$	$u^* = 2V^* [1 - (2r^*)^2]$ $\phi = \phi_8$

b) Boundary conditions in the heated and cooled sections:

For heating in upflow

For cooling in downflow

$s_3^* < s \leq s_4^*$ $0 < z \leq L_3^*$	$s_8^* < s \leq s_9^*$ $0 < z \leq L_8^*$
at $r^* = \frac{1}{2}$ $\left[\begin{array}{l} \frac{\partial \phi}{\partial r^*} = 1 \\ u^* = 0, v^* = 0 \end{array} \right.$	$\left[\begin{array}{l} \phi = 0 \\ u^* = 0, v^* = 0 \end{array} \right.$
at $r^* = 0$ $\left[\begin{array}{l} \frac{\partial \phi}{\partial r^*} = 0 \\ \frac{\partial u^*}{\partial r^*} = 0, \frac{\partial v^*}{\partial r^*} = 0 \end{array} \right.$	$\left[\begin{array}{l} \frac{\partial \phi}{\partial r^*} = 0 \\ \frac{\partial u^*}{\partial r^*} = 0, \frac{\partial v^*}{\partial r^*} = 0 \end{array} \right.$

c) Boundary conditions in the post-heated and post-cooled sections:

For heating in upflow

For cooling in downflow

$s_4^* < s^* \leq s_5^*$ $L_3^* < z^* \leq L_3^* + L_4^*$	$s_9^* < s^* \leq s_{10}^*$ $L_8^* < z^* \leq L_8^* + L_9^*$
$\text{at } r^* = \frac{1}{2} \left[\begin{array}{l} \frac{\partial \phi}{\partial r^*} = - \frac{St_m Re_{ref} Pr}{4} (\phi - \phi_\infty) \\ u^* = 0, v^* = 0 \end{array} \right.$	
$\text{at } r = 0 \left[\begin{array}{l} \frac{\partial \phi}{\partial r^*} = 0 \\ \frac{\partial u^*}{\partial r^*} = 0, \frac{\partial v^*}{\partial r^*} = 0 \end{array} \right.$	

d) Outlet boundary conditions:

For heating in upflow

For cooling in downflow

$s^* = s_5^*$ $z^* = L_3^* + L_4^*$	$s^* = s_{10}^*$ $z^* = L_8^* + L_9^*$
$\frac{\partial u^*}{\partial z^*} = 0, v^* = 0$ $\frac{\partial \phi}{\partial z^*} = 0$	

From the foregoing analysis it can be seen that the governing non-dimensionalized parameters of this problem are:

$$Gr_m = \frac{D^3 g \beta q}{\nu V_{ref} k_f} \quad (\text{modified Grashof number});$$

$$St_m = \frac{U D}{\rho_m V_{ref} AC_p} \quad (\text{modified Stanton number});$$

$$Re_{ref} = \frac{V_{ref} D}{\nu} \quad (\text{reference Reynolds number});$$

$$Pr = \frac{\mu C_p}{k_f} \quad (\text{Prandtl number});$$

$$\phi_{\infty} = \frac{T_a - \bar{T}_w}{qD/k_f} \quad (\text{dimensionless ambient temperature}).$$

APPENDIX D

DETERMINATION OF THE NODAL TEMPERATURES FOR A GIVEN V

The determination of the average velocity, V , using the proposed model has been described in Chapters 2 and 4. The solution procedure involves the evaluation of V for a given set of conditions. This Appendix presents the procedure to update the value of the nodal temperatures, $T_1 \dots T_{11}$, based on this value of V .

Using the latest values of V , T_8 , and \overline{Nu} (obtained from the two-dimensional numerical simulations), the determination of the nodal temperatures is initiated by relating the temperature at the outlet of the cooled section, T_9 , to the wall temperature in the cooled section, \overline{T}_w . Using Eq. 2.14b, T_9 can be expressed by:

$$T_9 = (T_8 - \overline{T}_w)e^{-XL_8} + \overline{T}_w \quad (D.1)$$

where $X = \frac{\pi k_f \overline{Nu}}{\rho_m V A C_p}$, and L_8 is the length of the cooled section.

Then, from s_9 to s_7 the following calculations, based on Eqs. 2.11b and 2.30, are performed:

$$T_{10} = (T_9 - T_a)e^{-\Omega L_9} + T_a \quad (D.2)$$

$$T_{11} = (T_{10} - T_a)e^{-\Omega L_{10}} + T_a \quad (D.3)$$

$$T_1 = (T_{11} - T_a)e^{-\Omega R} + T_a \quad (D.4)$$

$$T_2 = (T_1 - T_a)e^{-\Omega L_1} + T_a \quad (D.5)$$

$$T_3 = (T_2 - T_a)e^{-\Omega L_2} + T_a \quad (D.6)$$

$$T_4 = T_3 + \frac{P_w}{\rho_m VAC_p} \quad (D.7)$$

$$T_5 = (T_4 - T_a)e^{-\Omega L_4} + T_a \quad (D.8)$$

$$T_6 = (T_5 - T_a)e^{-\Omega L_5} + T_a \quad (D.9)$$

$$T_7 = (T_6 - T_a)e^{-\Omega R} + T_a \quad (D.10)$$

$$\text{where } \Omega = \frac{U}{\rho_m VAC_p}.$$

Then T_8 is updated using:

$$T_8 = (T_7 - T_a)e^{-\Omega L_7} + T_a \quad (D.11)$$

This new updated value of T_8 is then returned to the beginning of the iterative process, Eq. D.1. Iterations are performed until the change in two consecutive values of T_8 is less than 0.01 °C. Typically, less than 5 iterations are necessary.

A P P E N D I X E

DETERMINATION OF L_{eq} DUE TO FORM LOSSES IN THE 180° BENDS

It is well known that fluid flow in curved pipes induces a secondary fluid motion in the pipe. The additional pressure loss associated with this secondary motion has been assessed by Blevins [1984] for laminar flows. His graphical representation of the loss coefficient in curved pipes, K_L , has been curve-fitted to obtain:

$$\log_{10} K_L = 6.11 - 3.98 \log_{10} (Re) + 0.66 \log_{10} (Re^2) \quad (E.1)$$

This relationship is valid for $Re < 2000$, $0.5 < \frac{R}{2r_i} < 11.7$ and a bend angle of 90°. Blevins [1984] recommends to multiply Eq. E.1 by 2 to obtain the loss coefficient for a 180° bend. For the present geometry $\frac{R}{2r_i} = 13.5$. Even though this ratio is not within the limit set by Blevins [1984], it was judged to be close enough to be valid. According to Blevins [1984], errors of the order of 10 % to 20 % can be expected on the value of K_L . By definition, K_L is given by:

$$K_L = \frac{h_m}{v^2/2g} \quad (E.2)$$

where h_m is the head loss in meters of fluid.

For convenience, the loss coefficient is transformed into an equivalent length of pipe, using the Darcy friction factor relationship:

$$h_m = f_D \frac{L_{eq}}{2r_i} \frac{V^2}{2g} = K_L \frac{V^2}{2g} \quad (E.3)$$

which reduces to:

$$L_{eq} = \frac{K_L 2r_i}{f_D} \quad (E.4)$$

where L_{eq} is the equivalent length of pipe due to pressure losses in the bend, and f_D is the Darcy friction factor for fully developed laminar flow, $64/Re$. As shown in Eq. 4.20, L_{eq} is added to the actual length of the bends, $2\pi R$.

A P P E N D I X F

THERMOCOUPLE CALIBRATION PROCEDURE AND RESULTS

F.1 INTRODUCTION

The thermocouple calibration procedure and results are reported in this Appendix. All thermocouples used during the course of this study were individually calibrated, except the three thermocouples used in the cooled section which were installed prior to the calibration. These latter three thermocouples used the technique described by Shirtliffe [1971] to obtain temperatures from thermocouple voltages.

Tables of temperatures as function of thermocouple emf (referenced to the triple point of water) have been published by the National Bureau of Standards [1955, 1979]. Shirtliffe [1971], among others, has curve-fitted the data contained in these tables to produce n^{th} order polynomials over specific temperature ranges. The use of such polynomials is adequate for non-critical temperature measurements, such as in the cooled section of the present work. For critical temperature measurements a thorough calibration is necessary to account for possible thermocouple construction error and hardware compensation inaccuracies.

F.2 THERMOCOUPLE CALIBRATION PROCEDURE

A total of sixty thermocouples could be individually calibrated during a typical calibration test. Thermocouples were calibrated against a

quartz thermometer (Hewlett-Packard, Model 2804A). The resolution of the quartz thermometer was set at 0.001°C . Its accuracy was verified at the Physics Division of National Research Council of Canada (Lawlor, [1987]) against the national platinum resistance thermometer. Based on these results, the accuracy of the quartz thermometer is $\pm 0.005^{\circ}\text{C}$ over the temperature range from 0°C to 95°C .

The thermocouple calibration procedure is similar to the one adopted by Neill [1989]. Briefly, the procedure is as follows:

- (1) The quartz thermometer and the data acquisition and control unit were energized at least 24 hours prior to the calibration test.
- (2) The quartz thermometer probe (Hewlett-Packard, model 18111A) and the uncalibrated thermocouples were inserted into a machined copper block to minimize temperature fluctuations. This copper block was then placed inside a temperature-controlled water bath (Neslab, Model RTE-220A) and covered with approximately 10 cm of distilled water to minimize wire conduction errors.
- (3) The temperature of the bath was allowed to reach the lowest temperature in the calibration range, i.e. 5°C . Typically, the bath temperature was considered to be constant when the temperature indicated by the quartz thermometer would not fluctuate by more than $\pm 0.002^{\circ}\text{C}$ for a least 5 minutes.
- (4) Once the temperature of the bath was constant, the output of the quartz thermometer as well as the individual thermocouple voltages

were read and stored by the data acquisition system in a manner similar to the one described in section 5.4.4. This process was repeated five times at 30 second intervals. Then, the average of these five readings was stored.

(5) Step (3) and (4) were then repeated at approximately 5°C increments up to 70°C.

F.3 THERMOCOUPLE CALIBRATION RESULTS

A fifth-order polynomial equation was then fitted to the quartz temperature-thermocouple voltage data, obtained in step (4) of the calibration procedure, using the least squares method. With this method, the thermocouple temperatures are related to the voltages by the following relationship (Neill [1989]):

$$T_j = \sum_{i=0}^5 [C_{i,j} (V_j)^i] \quad (F.1)$$

where V_j is the voltage reading of thermocouple j , and $C_{i,j}$ are the polynomial coefficients for thermocouple j . Typical calibration results for one particular thermocouple are shown in Table F.1 (next page).

F.4 UNCERTAINTY ON THE TEMPERATURE MEASUREMENTS

As can be seen in Table F.1, thermocouple temperatures obtained using the above-mentioned procedure yield very accurate results that are within $\pm 0.01^\circ\text{C}$ of the quartz thermometer reading. However, these

results should be interpreted with caution for two main reasons.

Firstly, the ambient temperature during a test was not necessarily within the range of ambient temperature experienced during a calibration test. Secondly, as shown in Table 5.2, the accuracy of the voltmeter of the data acquisition and control unit is $\pm 3\mu\text{V}$. For Type-E thermocouples, which have a sensitivity of $\approx 60 \mu\text{V}/^\circ\text{C}$, this corresponds to a temperature accuracy of $\pm 0.05^\circ\text{C}$. Because of these two factors, the uncertainty on the temperature measurements is estimated at $\pm 0.05^\circ\text{C}$.

A 5th order polynomial over the range 0 - 50 $^\circ\text{C}$ was used in the cooled section to obtain temperatures from thermocouple voltages (Shirtliffe [1971]). A comparison between the results obtained with the present polynomials (Eq. F.1) and the ones given by the fifth order polynomials of Shirtliffe [1971] indicated that the uncertainty on the temperature measurements in the cooled section is of the order of $\pm 0.1^\circ\text{C}$.

Temperatures read by the quartz thermometer ($^\circ\text{C}$)	Thermocouple temperatures (obtained using the polynomial coefficients) ($^\circ\text{C}$)
4.943	4.94
9.874	9.88
15.446	15.45
19.795	19.79
25.016	25.02
30.020	30.02
34.906	34.90
40.038	40.03
44.978	44.99
49.940	49.93
54.966	54.96
59.976	59.98
65.002	65.00
69.998	70.00

Table F.1: Calibration results for thermocouple T50. Ambient temperature during calibration was $25^\circ\text{C} \pm 2^\circ\text{C}$.

A P P E N D I X G

WALL TEMPERATURE CORRECTIONS

G.1 INTRODUCTION

As reported in section 5.4.1.3, wall temperature measurements are taken inside the Plexiglass pipe of heated section no.2, thus they are not true inner wall temperatures. The following Appendix presents the procedure used to correct these measured temperatures to obtain inner wall temperatures.

G.2 CORRECTION PROCEDURE

Figure 5.7 represents a cross-section of heated section no.2 with the relevant materials and dimensions reported in the adjoining table. In this figure, T_4 is the temperature read by the thermocouple, while T_w is the inner wall temperature.

Assuming one-dimensional heat flow in the radial direction and with reference to the nomenclature of Fig. 5.7, the heat losses out of the heated section, q_{out} , can be calculated from a knowledge of the measured wall temperature, T_4 :

$$q_{out} = \frac{(T_4 - T_a)}{\frac{\ln(r_5/r_4)}{2\pi k_p L_h} + \frac{\ln(r_6/r_5)}{2\pi k_i L_h} + \frac{1}{2\pi r_6 h_o L_h}} \quad (G.1)$$

where L_h is the length of the heated section. The outside film coefficient, h_o , is assumed equal to $10 \text{ W/m}^2\text{°C}$. The accuracy of h_o is not critical since the second term in the denominator of Eq. G.1, which represent the thermal resistance of the foamed plastic insulation, is much greater than the other term related to h_o . For the same reason, the value of q_{out} , and consequently T_w , is mildly dependent on the position of T_4 , since the first term in the denominator of Eq. G.1 is much smaller than the second term.

Using q_{out} , T_3 can be determined by:

$$T_3 = q_{out} \left[\frac{\ln(r_4/r_3)}{2\pi k_p L_h} \right] + T_4 \quad (G.2)$$

Assuming that the temperature drop in the gold coating is negligible, then $T_2 = T_3$ and the inner wall temperature, T_w , is given by:

$$T_w = - q_{in} \left[\frac{\ln(r_2/r_x)}{2\pi k_f L_h} \right] + T_2 \quad (G.3)$$

where q_{in} , the heat supplied to the fluid, is simply:

$$q_{in} = P_w - q_{out} \quad (G.4)$$

During a test, temperature readings given by the thermocouples were corrected using Eqs. G.1 to G.4. As shown in Appendix K, the value of the temperature correction, $T_4 - T_w$, ranged from $\approx 0.1 \text{ K}$ to 1.0 K .

As was mentioned in section 7.2.1, two-dimensional numerical simulations in the heated section were performed with the same geometry and materials that were used in this Appendix. These simulations revealed that the numerically calculated values of $T_4 - T_w$ were typically within ± 0.01 K of the corresponding value calculated using the approach presented in this thesis. Thus, the one-dimensional heat flow assumption used in the correction procedure was very good.

As was stated in Chapter 5, the uncertainty on the radial positioning of the thermocouples inside the Plexiglass pipe is ± 0.5 mm. Thus, thermocouples may not be located exactly at r_4 as assumed by the correction procedure. However, it can be shown that this positioning uncertainty has a negligible impact on the determination of $T_4 - T_w$ simply because q_{out} is very small. Therefore, when experimental results are compared to the numerical simulations in the heated section, the uncertainty on the experimental value of T_w is equal to the uncertainty obtained from the calibration of the thermocouples: $\pm 0.05^\circ\text{C}$ (Appendix F).

A P P E N D I X H

EXPERIMENTAL DETERMINATION OF THE OVERALL HEAT LOSS COEFFICIENT (U)

H.1 INTRODUCTION

The overall heat loss coefficient, U , of the insulated portions of the closed-loop thermosyphon was evaluated experimentally. The procedure and results of this experiment are presented in this Appendix.

H.2 EVALUATION OF U

The determination of U is simply based on the principle that, without power input to the loop, the amount of heat losses between T_{in} and T_{out} is equal to the enthalpy difference of the fluid between these two points multiplied by the mass flowrate. With reference to Fig. 5.8, U can then be expressed by:

$$U = \frac{\dot{m} C_p (T_{in} - T_{out})}{(L_x + L_y + L_z)(T_a - T_m)} \quad (H.1)$$

where \dot{m} is the mass flowrate, C_p is the specific heat, T_{in} and T_{out} are the measured inlet and outlet bulk temperatures, respectively, L_x is the length of the pipe section preceding the heated section, L_y is the length of the heated section, L_z is the length of the pipe section from the outlet of the heated section to the outlet bulk temperature measurement, T_a is the ambient temperature, and T_m is the mean temper-

ature in the loop between T_{in} and T_{out} .

The value of U was experimentally determined by measuring, under steady-state conditions, the quantities indicated in Eq. H.1. For this test, the open-loop configuration was utilized. This configuration, which is described in Appendix I, provides a steady ($\pm 1\%$) and accurately measurable mass flowrate ($\pm 0.1\%$) as well as a constant inlet temperature ($\pm 0.05^\circ\text{C}$). The values of L_x , L_y , L_z are equal to 0.872 m, 0.664 m, and 1.544 m, respectively (Table 7.1).

H.3 RESULTS

Table H.1 presents the results of the experimental determination of U . As can be seen, measurements were taken over a 10 minute period. Values of $T_{in} - T_{out}$ were taken every minute, while measurements of T_a and T_m were taken at the beginning and at the end of the 10 minute interval. By averaging these measurements and using Eq. H.1, U was found to be equal to $0.18 \text{ W/m}^\circ\text{C}$.

H.4 UNCERTAINTY ON THE VALUE OF U

It can be shown that the largest sources of uncertainties in the determination of U are due to the $T_{in} - T_{out}$ and $T_a - T_m$ measurements. The present evaluation of U was done with a value of $T_a - T_m$ of 12.5 K. Assuming, conservatively, that the uncertainty on the $T_a - T_m$ measurement is of the order of $\pm 0.2 \text{ K}$ then the $T_a - T_m$ measurement has a relative uncertainty of $\pm 1.6\%$. The measured value of $T_{in} - T_{out}$ is almost equal to 1.0 K. As mentioned in section 5.4.1.1, the uncertainty

on the $T_{in}-T_{out}$ measurement is ± 0.2 K. This implies that the relative uncertainty on the $T_{in}-T_{out}$ measurement is of the order of $\pm 20\%$.

From the foregoing analysis it can be concluded that the uncertainty on the $T_{in}-T_{out}$ measurement is the dominant uncertainty. Therefore, the uncertainty on the value of U is simply set at $\pm 20\%$.

Time (min)	$T_{in}-T_{out}$ (K)	\dot{m} (g/s)	T_a (°C)	T_m (°C)
1	0.95	1.585	28.6	17.2
2	0.95	-	-	-
3	0.95	-	-	-
4	0.94	-	-	-
5	0.94	-	-	-
6	0.95	-	-	-
7	0.95	-	-	-
8	0.94	-	-	-
9	0.95	-	-	-
10	0.94	1.580	28.8	17.3
Averages	0.946	1.583	28.7	17.25

Table H.1: Results obtained during the experimental determination of U .

A P P E N D I X I

DESCRIPTION OF THE OPEN-LOOP CONFIGURATION

I.1 INTRODUCTION

During the course of this study, it was necessary to modify the closed-loop thermosyphon to perform the following experiments: (i) evaluation of the overall heat loss coefficient, U ; (ii) calibration of the average velocity measurement; and (iii) flow visualization studies. For these three cases, a steady and accurately measurable water flowrate at a constant temperature was needed at the inlet of the heated section of the loop. This required the use of an open-loop configuration with water supplied from a constant-head tank, with mass flowrates measured by the so-called stopwatch-bucket method.

I.2 GENERAL DESCRIPTION

The open-loop configuration, which is presented schematically in Fig. 5.12, has been built according to the techniques recommended by the International Standard Organization [1980]. The open-loop configuration uses all the components of the closed-loop, except that the cooled section has been removed and replaced by flexible pipes which are connected to a constant-head tank and to a flow diverter. As shown in Fig. 5.12, the open-loop configuration consists of two circuits.

In the primary circuit, water flows by gravity into the loop from a constant-head tank. After travelling around the loop, the water is directed towards a flow diverter. Then, the water flows either into a bucket, when one of the three above-mentioned experiments is performed, or back to a constant-temperature bath. The flowrate is adjusted by using coarse and fine adjustments valves located within the primary circuit. The stability of the flowrate in the primary circuit has been observed to be better than $\pm 1\%$.

The dimensions of the constant-head tank are 40 cm wide x 60 cm long x 40 cm high and the tank is insulated with 25 mm of Styrofoam insulation. The tank contains approximately 100 liters of distilled water and sits on a leveled metal support which is anchored to the ceiling. A smaller inner tank (10 cm x 10 cm x 32 cm high) is located within the constant-head tank.

In the secondary circuit, water is pumped from a 20 liter temperature-controlled water bath (Neslab, model RTE-220A) to the bottom of the constant-head tank. Then, the water moves upward in the tank and "overflows" in the inner tank to finally return to the constant-temperature bath. In order to maintain the water level constant, the flowrate in the secondary circuit is regulated, using a globe valve, so that water overflows into the inner tank at all times.

With this set-up, the temperature of the water in the constant-head tank can be maintained constant to within $\pm 0.05^{\circ}\text{C}$.

1.3 DETERMINATION OF THE MASS FLOWRATE IN THE PRIMARY CIRCUIT

The mass flowrate in the primary circuit is obtained by measuring the mass of water accumulating in a bucket over a certain time interval.

The step-by-step procedure is as follows:

- (1) The initial position of the flow diverter is such that water is directed to the constant-temperature bath. The mass of the empty bucket, $m_{b,i}$, is measured by a weight scale;
- (2) The flow is then diverted to the bucket and a stopwatch is immediately started;
- (3) Once the desired mass of water has accumulated in the bucket, the flow is diverted back to the constant-temperature bath and the stopwatch is immediately stopped;
- (4) The mass of the water-filled bucket, $m_{b,f}$, is measured.

Then, the mass flowrate is simply determined by the following :

$$\dot{m} = \frac{m_{b,f} - m_{b,i}}{\Delta t} \quad (1.1)$$

where Δt is the time interval indicated by the stopwatch.

I.4 UNCERTAINTY ON THE VALUE OF THE MASS FLOWRATE OBTAINED USING THE OPEN-LOOP CONFIGURATION

The uncertainty associated with the mass flowrate, as measured using the techniques described in the preceding section, is dependent on the uncertainty of the mass and time measurements.

The mass of water was measured using a weight scale (Ohaus triple beam balance, Cole-Palmer model J-1012-00). This scale has a capacity of 2610 grams and an in-house calibration revealed that its uncertainty, was ± 0.1 grams in the 50-2000 grams range. Time measurements were done with a stopwatch (CASIO alarm chrono, model no. 248548) and its uncertainty is estimated at ± 0.01 sec. But the uncertainty on the time interval measurement was mainly due to the uncertainty associated with the flow diverter mechanism. This latter uncertainty is estimated at ± 0.1 sec.

Using the propagation of random uncertainty technique of Kline and McClintock [1953], the overall uncertainty on the on the value of \dot{m} , $\omega_{\dot{m}}$, is given by:

$$\omega_{\dot{m}} = \left[\left[\frac{\partial \dot{m}}{\partial m_{b,f}} \omega_{m_{b,f}} \right]^2 + \left[\frac{\partial \dot{m}}{\partial m_{b,i}} \omega_{m_{b,i}} \right]^2 + \left[\frac{\partial \dot{m}}{\partial \Delta t} \omega_{\Delta t} \right]^2 \right]^{1/2} \quad (1.2)$$

where $\omega_{m_{b,f}}$, $\omega_{m_{b,i}}$, $\omega_{\Delta t}$ are the uncertainties on the final and

initial mass measurements and on the time interval measurement, respectively. Solving Eq. 1.2 and simplifying, the relative uncertainty on \dot{m} becomes:

$$\frac{\omega_{\dot{m}}}{\dot{m}} = \left[2 \left[\frac{\omega_{m_{b,f}}}{m_{b,f} - m_{b,i}} \right]^2 + \left[\frac{\omega_{\Delta t}}{\Delta t} \right]^2 \right]^{1/2} \quad (1.3)$$

Equation 1.3 shows that to reduce the uncertainty on the value of \dot{m} , the values of $m_{b,f} - m_{b,i}$ and Δt should be as large as possible.

In this work, during the evaluation of U and the calibration of V , the values of $m_{b,f} - m_{b,i}$ and Δt were chosen so that the resulting relative uncertainty on the value of \dot{m} would always be less than $\pm 0.1 \%$. When flow visualization studies were performed, Δt and $m_{b,f} - m_{b,i}$ had to be relatively small in order to devote all the attention to the dye observations. Nonetheless, for these cases, the relative uncertainty on \dot{m} was still below $\pm 1 \%$.

A P P E N D I X J

CALIBRATION OF THE AVERAGE VELOCITY MEASUREMENT

J.1 INTRODUCTION

This Appendix presents the results of the calibration performed on the average velocity measurement in the closed-loop thermosyphon. As mentioned in Chapter 5, the average velocity inside the closed-loop thermosyphon is obtained using the following relationship (Fig. 5.8):

$$V = \frac{P_w - (Q_x + Q_y + Q_z)}{C_p (T_{out} - T_{in}) \rho A} \quad (J.1)$$

where Eqs. 5.2 and 5.3 have been combined to give Eq. H.1.

J.2 CALIBRATION PROCEDURE

The average velocity measurement was calibrated in-situ by using the open-loop configuration. As shown in Appendix I, the open-loop configuration provides a steady ($\pm 1\%$) and accurately measurable mass flow-rate ($\pm 0.1\%$) as well as a constant temperature ($\pm 0.05^\circ\text{C}$) at the inlet of the heated section.

The calibration procedure consists of comparing, under steady-state conditions, the average velocity obtained using Eq. J.1 with the average velocity given by the stopwatch-bucket method of the open-loop

configuration.

J.3 CALIBRATION RESULTS

Five calibration tests were performed over the range of expected operating conditions. The results are presented in Table J.1.

P_w (Watts)	$Q_x + Q_y + Q_z$ (Watts)	T_{in} (°C)	T_{out} (°C)	T_a (°C)	V^+ (cm/s)	V_{sb}^{++} (cm/s)	Difference ($V - V_{sb}$)/ V_{sb} (%)
10.04	-0.82	24.2	26.7	27.2	0.360	0.350	2.9
25.02	-1.82	21.9	26.0	27.7	0.555	0.534	4.0
39.96	-1.81	20.1	25.4	26.5	0.674	0.649	3.8
54.42	-2.20	20.3	26.1	27.8	0.834	0.793	5.1
24.96	-4.55	16.7	21.6	27.9	0.504	0.501	0.6
$^+ V$ = Average velocity calculated using Eq. J.1 $^{++} V_{sb}$ = Average velocity as measured by the stopwatch-bucket method of the open-loop configuration							

Table J.1: Calibration results on the average velocity measurement in the closed-loop thermosyphon.

Based on the results presented in Table J.1, the uncertainty on the experimental determination of V , using Eqs. 5.2 and 5.3, is estimated at $\pm 5\%$.

A P P E N D I X K**EXPERIMENTAL DATA**

The experimental data obtained during the course of this study are tabulated in this Appendix. Eight experimental runs were performed and each of the following pages contains the results of one particular run.

As was mentioned in Chapter 5, the wall temperature in the cooled section, \bar{T}_w , was equal to the arithmetic average of three measurements, $T_{w,1}$, $T_{w,2}$, $T_{w,3}$. Likewise, the average inlet and outlet bulk temperatures, T_{in} and T_{out} , were evaluated by taking the arithmetic average of five thermocouple measurements. The governing non-dimensional parameters were evaluated at the mean loop temperature and were based on the internal diameter of the heated section. The average velocity in the heated section was measured using the technique described in section 5.4.2 .

The wall temperature measurements in the heated section are given in a four column format. In the first column, the letters F and M refer to thermocouples located in the female and male half sections, respectively. The non-dimensional axial location, z/D , of these thermocouples is also given in the first column. The measured temperatures are reported in the second column, while the corrected wall temperatures, obtained using the correction procedure given in Appendix G, are presented in the third column. Finally, the average of the corrected wall temperatures at each axial location is given in the last column. As was mentioned in Appendix G, the uncertainty on the corrected wall temperatures is ± 0.05 °C.

RUN # 1		Wall temperatures in the heated section			
Measurements in the closed-loop		Location z/D	Measured temp. (°C)	Corrected wall temp. (°C)	Average of corrected temperatures (°C)
$P_w = 9.97 \text{ W}$					
$T_a = 29.20^\circ\text{C}$		F 0.529	28.66	28.53	28.75
		M 0.529	29.10	28.97	
$T_{w,1} = 26.8^\circ\text{C}$ $T_{w,2} = 26.8^\circ\text{C}$ $T_{w,3} = 27.2^\circ\text{C}$ $\left[\bar{T}_w = 26.9^\circ\text{C} \right]$		F 1.23	28.78	28.65	28.84
		M 1.23	29.16	29.04	
		F 1.94	28.76	28.63	28.69
		M 1.94	28.89	28.76	
		F 2.64	28.71	28.58	28.58
		M 2.64	28.72	28.59	
		F 3.71	28.73	28.60	28.59
		M 3.71	28.71	28.58	
$T_{in,1} = 27.35^\circ\text{C}$ $T_{in,2} = 27.32^\circ\text{C}$ $T_{in,3} = 27.35^\circ\text{C}$ $T_{in,4} = 27.28^\circ\text{C}$ $T_{in,5} = 27.25^\circ\text{C}$ $\left[T_{in} = 27.30^\circ\text{C} \right]$		F 5.12	28.80	28.67	28.67
		M 5.12	28.80	28.67	
		F 6.53	28.89	28.76	28.74
		M 6.53	28.85	28.72	
		F 7.94	28.95	28.82	28.86
		M 7.94	29.02	28.89	
		F 9.35	29.02	28.90	28.89
		M 9.35	29.01	28.88	
		F 10.76	29.14	29.02	28.97
		M 10.76	29.04	28.92	
		F 12.88	29.18	29.06	29.10
		M 12.88	29.19	29.07	
		F 12.88	29.11	28.99	
		M 12.88	29.18	29.06	
		F 12.88	29.18	29.06	
		M 12.88	29.46	29.34	
		M 12.88	29.22	29.10	29.19
		F 15.70	29.34	29.22	
		M 15.70	29.27	29.15	29.48
		F 18.52	29.44	29.33	
		M 18.52	29.74	29.63	29.53
		F 21.34	29.68	29.58	
		M 21.34	29.60	29.49	29.61
		F 24.17	29.80	29.70	
		M 24.17	29.62	29.51	29.81
		F 26.99	29.86	29.75	
		M 26.99	29.97	29.87	29.91
		F 29.11	29.96	29.86	
		M 29.11	30.06	29.96	29.92
		F 31.22	29.87	29.77	
		M 31.22	30.17	30.07	30.04
		F 32.63	30.06	29.96	
		M 32.63	30.21	30.11	30.12
		F 34.04	30.16	30.06	
		M 34.04	30.28	30.19	30.38
		F 35.46	30.51	30.42	
		M 35.46	30.42	30.33	
Non-dimensional parameters					
$Gr_m = 2181$					
$Re_{ref} = 85.3$					
$Pr = 5.6$					
$St_m = 0.78 \times 10^{-3}$					
$\phi_\infty = 0.291$					
Average velocity in the heated section					
$V = 0.483 \text{ cm/s}$					

RUN # 2		Wall temperatures in the heated section			
Measurements in the closed-loop		Location z/D	Measured temp. (°C)	Corrected wall temp. (°C)	Average of corrected temperatures (°C)
$P_w = 9.83 \text{ W}$		F 0.529	24.29	24.12	24.32
$T_a = 26.18^\circ\text{C}$		M 0.529	24.68	24.52	
$T_{w,1} = 21.8^\circ\text{C}$ $T_{w,2} = 21.9^\circ\text{C}$ $T_{w,3} = 22.2^\circ\text{C}$ $\left[\bar{T}_w = 22.0^\circ\text{C} \right]$		F 1.23	24.47	24.31	24.46
		M 1.23	24.77	24.62	
		F 1.94	24.49	24.32	24.33
		M 1.94	24.50	24.34	
$T_{in,1} = 22.67^\circ\text{C}$ $T_{in,2} = 22.66^\circ\text{C}$ $T_{in,3} = 22.73^\circ\text{C}$ $T_{in,4} = 22.60^\circ\text{C}$ $T_{in,5} = 22.60^\circ\text{C}$ $\left[T_{in} = 22.64^\circ\text{C} \right]$		F 2.64	24.37	24.20	24.18
		M 2.64	24.32	24.15	
		F 3.71	24.38	24.21	24.19
		M 3.71	24.33	24.16	
$T_{out,1} = 24.79^\circ\text{C}$ $T_{out,2} = 24.88^\circ\text{C}$ $T_{out,3} = 24.89^\circ\text{C}$ $T_{out,4} = 24.89^\circ\text{C}$ $T_{out,5} = 24.90^\circ\text{C}$ $\left[T_{out} = 24.87^\circ\text{C} \right]$		F 5.12	24.46	24.30	24.27
		M 5.12	24.41	24.25	
		F 6.53	24.50	24.34	24.32
		M 6.53	24.45	24.29	
$T_{out,1} = 24.79^\circ\text{C}$ $T_{out,2} = 24.88^\circ\text{C}$ $T_{out,3} = 24.89^\circ\text{C}$ $T_{out,4} = 24.89^\circ\text{C}$ $T_{out,5} = 24.90^\circ\text{C}$ $\left[T_{out} = 24.87^\circ\text{C} \right]$		F 7.94	24.56	24.40	24.43
		M 7.94	24.62	24.46	
		F 9.35	24.64	24.48	24.46
		M 9.35	24.59	24.43	
$T_{out,1} = 24.79^\circ\text{C}$ $T_{out,2} = 24.88^\circ\text{C}$ $T_{out,3} = 24.89^\circ\text{C}$ $T_{out,4} = 24.89^\circ\text{C}$ $T_{out,5} = 24.90^\circ\text{C}$ $\left[T_{out} = 24.87^\circ\text{C} \right]$		F 10.76	24.73	24.57	24.54
		M 10.76	24.66	24.50	
$T_{out,1} = 24.79^\circ\text{C}$ $T_{out,2} = 24.88^\circ\text{C}$ $T_{out,3} = 24.89^\circ\text{C}$ $T_{out,4} = 24.89^\circ\text{C}$ $T_{out,5} = 24.90^\circ\text{C}$ $\left[T_{out} = 24.87^\circ\text{C} \right]$		F 12.88	24.80	24.64	24.68
		M 12.88	24.82	24.67	
		F 12.88	24.70	24.55	
		F 12.88	24.78	24.63	
$T_{out,1} = 24.79^\circ\text{C}$ $T_{out,2} = 24.88^\circ\text{C}$ $T_{out,3} = 24.89^\circ\text{C}$ $T_{out,4} = 24.89^\circ\text{C}$ $T_{out,5} = 24.90^\circ\text{C}$ $\left[T_{out} = 24.87^\circ\text{C} \right]$		M 12.88	25.07	24.93	
		M 12.88	24.84	24.69	
$T_{out,1} = 24.79^\circ\text{C}$ $T_{out,2} = 24.88^\circ\text{C}$ $T_{out,3} = 24.89^\circ\text{C}$ $T_{out,4} = 24.89^\circ\text{C}$ $T_{out,5} = 24.90^\circ\text{C}$ $\left[T_{out} = 24.87^\circ\text{C} \right]$		F 15.70	24.95	24.80	24.79
		M 15.70	24.92	24.77	
$T_{out,1} = 24.79^\circ\text{C}$ $T_{out,2} = 24.88^\circ\text{C}$ $T_{out,3} = 24.89^\circ\text{C}$ $T_{out,4} = 24.89^\circ\text{C}$ $T_{out,5} = 24.90^\circ\text{C}$ $\left[T_{out} = 24.87^\circ\text{C} \right]$		F 18.52	25.09	24.95	25.09
		M 18.52	25.37	25.23	
$T_{out,1} = 24.79^\circ\text{C}$ $T_{out,2} = 24.88^\circ\text{C}$ $T_{out,3} = 24.89^\circ\text{C}$ $T_{out,4} = 24.89^\circ\text{C}$ $T_{out,5} = 24.90^\circ\text{C}$ $\left[T_{out} = 24.87^\circ\text{C} \right]$		F 21.34	25.34	25.20	25.15
		M 21.34	25.24	25.10	
$T_{out,1} = 24.79^\circ\text{C}$ $T_{out,2} = 24.88^\circ\text{C}$ $T_{out,3} = 24.89^\circ\text{C}$ $T_{out,4} = 24.89^\circ\text{C}$ $T_{out,5} = 24.90^\circ\text{C}$ $\left[T_{out} = 24.87^\circ\text{C} \right]$		F 24.17	25.48	25.34	25.24
		M 24.17	25.29	25.15	
$T_{out,1} = 24.79^\circ\text{C}$ $T_{out,2} = 24.88^\circ\text{C}$ $T_{out,3} = 24.89^\circ\text{C}$ $T_{out,4} = 24.89^\circ\text{C}$ $T_{out,5} = 24.90^\circ\text{C}$ $\left[T_{out} = 24.87^\circ\text{C} \right]$		F 26.99	25.48	25.34	25.41
		M 26.99	25.61	25.47	
$T_{out,1} = 24.79^\circ\text{C}$ $T_{out,2} = 24.88^\circ\text{C}$ $T_{out,3} = 24.89^\circ\text{C}$ $T_{out,4} = 24.89^\circ\text{C}$ $T_{out,5} = 24.90^\circ\text{C}$ $\left[T_{out} = 24.87^\circ\text{C} \right]$		F 29.11	25.58	25.45	25.51
		M 29.11	25.70	25.57	
$T_{out,1} = 24.79^\circ\text{C}$ $T_{out,2} = 24.88^\circ\text{C}$ $T_{out,3} = 24.89^\circ\text{C}$ $T_{out,4} = 24.89^\circ\text{C}$ $T_{out,5} = 24.90^\circ\text{C}$ $\left[T_{out} = 24.87^\circ\text{C} \right]$		F 31.22	25.44	25.31	25.48
		M 31.22	25.78	25.65	
$T_{out,1} = 24.79^\circ\text{C}$ $T_{out,2} = 24.88^\circ\text{C}$ $T_{out,3} = 24.89^\circ\text{C}$ $T_{out,4} = 24.89^\circ\text{C}$ $T_{out,5} = 24.90^\circ\text{C}$ $\left[T_{out} = 24.87^\circ\text{C} \right]$		F 32.63	25.65	25.52	25.60
		M 32.63	25.81	25.69	
$T_{out,1} = 24.79^\circ\text{C}$ $T_{out,2} = 24.88^\circ\text{C}$ $T_{out,3} = 24.89^\circ\text{C}$ $T_{out,4} = 24.89^\circ\text{C}$ $T_{out,5} = 24.90^\circ\text{C}$ $\left[T_{out} = 24.87^\circ\text{C} \right]$		F 34.04	25.75	25.62	25.68
		M 34.04	25.87	25.75	
$T_{out,1} = 24.79^\circ\text{C}$ $T_{out,2} = 24.88^\circ\text{C}$ $T_{out,3} = 24.89^\circ\text{C}$ $T_{out,4} = 24.89^\circ\text{C}$ $T_{out,5} = 24.90^\circ\text{C}$ $\left[T_{out} = 24.87^\circ\text{C} \right]$		F 35.46	26.15	26.03	25.97
		M 35.46	26.03	25.91	
Non-dimensional parameters					
$Gr_m = 1957$ $Re_{ref} = 67.6$ $Pr = 6.4$ $St_m = 0.88 \times 10^{-3}$ $\phi_\infty = 0.540$					
Average velocity in the heated section					
$V = 0.457 \text{ cm/s}$					

RUN # 3		Wall temperatures in the heated section			
Measurements in the closed-loop		Location z/D	Measured temp. (°C)	Corrected wall temp. (°C)	Average of corrected temperatures (°C)
$P_w = 25.18 \text{ W}$					
$T_a = 27.60^\circ\text{C}$		F 0.529	25.85	25.50	25.97
		M 0.529	26.76	26.44	
$T_{w,1} = 21.0^\circ\text{C}$ $T_{w,2} = 21.1^\circ\text{C}$ $T_{w,3} = 21.8^\circ\text{C}$ $\left[\bar{T}_w = 21.3^\circ\text{C} \right]$		F 1.23	26.11	25.77	26.14
		M 1.23	26.82	26.50	
		F 1.94	26.06	25.72	25.80
		M 1.94	26.21	25.87	
$T_{in,1} = 22.53^\circ\text{C}$ $T_{in,2} = 22.51^\circ\text{C}$ $T_{in,3} = 22.58^\circ\text{C}$ $T_{in,4} = 22.42^\circ\text{C}$ $T_{in,5} = 22.42^\circ\text{C}$ $\left[T_{in} = 22.48^\circ\text{C} \right]$		F 2.64	25.89	25.55	25.51
		M 2.64	25.81	25.46	
		F 3.71	25.90	25.56	25.52
		M 3.71	25.84	25.49	
		F 5.12	26.04	25.70	25.66
		M 5.12	25.97	25.62	
		F 6.53	26.18	25.84	25.79
		M 6.53	26.09	25.75	
		F 7.94	26.25	25.91	26.00
		M 7.94	26.42	26.09	
$T_{out,1} = 26.29^\circ\text{C}$ $T_{out,2} = 26.44^\circ\text{C}$ $T_{out,3} = 26.46^\circ\text{C}$ $T_{out,4} = 26.47^\circ\text{C}$ $T_{out,5} = 26.47^\circ\text{C}$ $\left[T_{out} = 26.43^\circ\text{C} \right]$		F 9.35	26.41	26.08	26.04
		M 9.35	26.33	26.00	
		F 10.76	26.58	26.25	26.14
		M 10.76	26.36	26.03	
		F 12.88	26.66	26.34	26.44
		M 12.88	26.68	26.35	
		F 12.88	26.51	26.18	
		F 12.88	26.65	26.33	
		M 12.88	27.32	27.01	
		M 12.88	26.77	26.45	26.59
Non-dimensional parameters		F 15.70	26.97	26.65	
		M 15.70	26.85	26.53	27.24
		F 18.52	27.22	26.91	
		M 18.52	27.86	27.56	27.30
		F 21.34	27.74	27.44	
		M 21.34	27.46	27.16	27.49
		F 24.17	28.03	27.74	
		M 24.17	27.55	27.25	27.75
		F 26.99	27.91	27.62	
		M 26.99	28.19	27.90	27.99
Average velocity in the heated section		F 29.11	28.19	27.90	
		M 29.11	28.37	28.08	28.15
		F 31.22	28.03	27.74	
		M 31.22	28.51	28.23	28.26
		F 32.63	28.30	28.01	
		M 32.63	28.56	28.28	28.26
		F 34.04	28.43	28.15	
		M 34.04	28.65	28.37	28.92
		F 35.46	29.34	29.08	
		M 35.46	29.02	28.75	
$V = 0.628 \text{ cm/s}$					

RUN # 4		Wall temperatures in the heated section			
Measurements in the closed-loop		Location z/D	Measured temp. (°C)	Corrected wall temp. (°C)	Average of corrected temperatures (°C)
$P_w = 39.84 \text{ W}$					
$T_a = 27.36^\circ\text{C}$		F 0.529	25.77	25.25	25.89
		M 0.529	27.02	26.53	
		F 1.23	26.08	25.57	26.08
		M 1.23	27.08	26.60	
$T_{w,1} = 18.6^\circ\text{C}$ $T_{w,2} = 18.6^\circ\text{C}$ $T_{w,3} = 19.3^\circ\text{C}$ $\left[\bar{T}_w = 18.9^\circ\text{C} \right]$		F 1.94	25.96	25.45	25.52
		M 1.94	26.11	25.60	
		F 2.64	25.71	25.20	25.11
		M 2.64	25.55	25.03	
		F 3.71	25.71	25.19	25.13
		M 3.71	25.59	25.07	
$T_{in,1} = 20.83^\circ\text{C}$ $T_{in,2} = 20.76^\circ\text{C}$ $T_{in,3} = 20.85^\circ\text{C}$ $T_{in,4} = 20.66^\circ\text{C}$ $T_{in,5} = 20.68^\circ\text{C}$ $\left[T_{in} = 20.74^\circ\text{C} \right]$		F 5.12	25.89	25.38	25.33
		M 5.12	25.80	25.29	
		F 6.53	26.06	25.55	25.49
		M 6.53	25.94	25.43	
		F 7.94	26.15	25.64	25.77
		M 7.94	26.41	25.90	
		F 9.35	26.36	25.86	25.80
		M 9.35	26.25	25.74	
		F 10.76	26.61	26.11	25.94
		M 10.76	26.28	25.78	
$T_{out,1} = 25.94^\circ\text{C}$ $T_{out,2} = 26.15^\circ\text{C}$ $T_{out,3} = 26.15^\circ\text{C}$ $T_{out,4} = 26.16^\circ\text{C}$ $T_{out,5} = 26.15^\circ\text{C}$ $\left[T_{out} = 26.12^\circ\text{C} \right]$		F 12.88	26.70	26.20	26.37
		M 12.88	26.72	26.23	
		F 12.88	26.44	25.94	
		F 12.88	26.68	26.19	
		M 12.88	27.76	27.29	
		M 12.88	26.85	26.36	
		F 15.70	27.08	26.60	26.53
		M 15.70	26.95	26.46	
		F 18.52	27.48	27.01	27.50
		M 18.52	28.45	28.00	
		F 21.34	28.17	27.71	27.51
		M 21.34	27.77	27.31	
		F 24.17	28.65	28.20	27.80
		M 24.17	27.86	27.40	
		F 26.99	28.29	27.84	28.09
		M 26.99	28.80	28.35	
		F 29.11	28.69	28.25	28.44
		M 29.11	29.07	28.63	
		F 31.22	28.45	28.00	28.40
		M 31.22	29.23	28.79	
		F 32.63	28.85	28.41	28.65
		M 32.63	29.31	28.88	
		F 34.04	29.04	28.60	28.79
		M 34.04	29.40	28.97	
		F 35.46	30.39	29.99	29.75
		M 35.46	29.92	29.50	
Non-dimensional parameters					
$Gr_m = 3920$ $Re_{ref} = 134.8$ $Pr = 6.4$ $St_m = 0.44 \times 10^{-3}$ $\phi_\infty = 0.269$					
Average velocity in the heated section					
$V = 0.722 \text{ cm/s}$					

RUN # 5		Wall temperatures in the heated section			
Measurements in the closed-loop		Location z/D	Measured temp. (°C)	Corrected wall temp. (°C)	Average of corrected temperatures (°C)
$P_w = 39.89 \text{ W}$					
$T_a = 27.36^\circ\text{C}$		F 0.529	23.58	23.02	23.64
		M 0.529	24.77	24.25	
		F 1.23	23.96	23.42	23.88
		M 1.23	24.87	24.34	
$T_{w,1} = 15.4^\circ\text{C}$ $T_{w,2} = 15.5^\circ\text{C}$ $T_{w,3} = 16.2^\circ\text{C}$ $\left[\bar{T}_w = 15.7^\circ\text{C} \right]$		F 1.94	23.89	23.34	23.34
		M 1.94	23.89	23.34	
		F 2.64	23.53	22.97	22.85
		M 2.64	23.30	22.73	
		F 3.71	23.47	22.91	22.83
		M 3.71	23.32	22.76	
$T_{in,1} = 18.10^\circ\text{C}$ $T_{in,2} = 18.10^\circ\text{C}$ $T_{in,3} = 18.20^\circ\text{C}$ $T_{in,4} = 17.95^\circ\text{C}$ $T_{in,5} = 17.97^\circ\text{C}$ $\left[\bar{T}_{in} = 18.05^\circ\text{C} \right]$		F 5.12	23.66	23.10	23.04
		M 5.12	23.54	22.98	
		F 6.53	23.83	23.28	23.20
		M 6.53	23.68	23.12	
		F 7.94	23.94	23.39	23.52
		M 7.94	24.19	23.65	
		F 9.35	24.18	23.64	23.58
		M 9.35	24.07	23.52	
		F 10.76	24.45	23.91	23.75
		M 10.76	24.13	23.59	
$T_{out,1} = 23.70^\circ\text{C}$ $T_{out,2} = 23.87^\circ\text{C}$ $T_{out,3} = 23.93^\circ\text{C}$ $T_{out,4} = 23.92^\circ\text{C}$ $T_{out,5} = 23.98^\circ\text{C}$ $\left[\bar{T}_{out} = 23.89^\circ\text{C} \right]$		F 12.88	24.47	23.93	24.09
		M 12.88	24.51	23.97	
		F 12.88	24.18	23.63	
		F 12.88	24.42	23.88	
		M 12.88	25.52	25.01	
		M 12.88	24.62	24.09	
		F 15.70	24.89	24.36	24.28
		M 15.70	24.74	24.21	
Non-dimensional parameters		F 18.52	25.27	24.76	25.24
		M 18.52	26.22	25.73	
$Gr_m = 3679$ $Re_{ref} = 117.3$ $Pr = 6.9$ $St_m = 0.47 \times 10^{-3}$ $\phi_\infty = 0.347$		F 21.34	25.39	25.49	25.27
		M 21.34	25.55	25.04	
		F 24.17	26.43	25.94	25.57
		M 24.17	25.70	25.20	
		F 26.99	26.11	25.62	25.88
		M 26.99	26.62	26.14	
		F 29.11	26.58	26.10	26.28
		M 29.11	26.93	26.46	
		F 31.22	26.36	25.87	26.25
		M 31.22	27.10	26.63	
Average velocity in the heated section		F 32.63	26.73	26.25	26.48
		M 32.63	27.17	26.71	
		F 34.04	26.93	26.46	26.66
		M 34.04	27.33	26.86	
$V = 0.679 \text{ cm/s}$		F 35.46	28.21	27.77	27.55
		M 35.46	27.78	27.33	

RUN # 6		Wall temperatures in the heated section			
Measurements in the closed-loop		Location z/D	Measured temp. (°C)	Corrected wall temp. (°C)	Average of corrected temperatures (°C)
$P_w = 54.83 \text{ W}$					
$T_a = 27.26^\circ\text{C}$		F 0.529	25.47	24.77	25.54
		M 0.529	26.97	26.31	
$T_{w,1} = 15.5^\circ\text{C}$ $T_{w,2} = 15.6^\circ\text{C}$ $T_{w,3} = 16.4^\circ\text{C}$ $\left[\bar{T}_w = 15.8^\circ\text{C} \right]$		F 1.23	25.82	25.12	25.75
		M 1.23	27.03	26.37	
		F 1.94	25.62	24.92	24.97
		M 1.94	25.72	25.02	
$T_{in,1} = 18.68^\circ\text{C}$ $T_{in,2} = 18.63^\circ\text{C}$ $T_{in,3} = 18.72^\circ\text{C}$ $T_{in,4} = 18.47^\circ\text{C}$ $T_{in,5} = 18.49^\circ\text{C}$ $\left[T_{in} = 18.58^\circ\text{C} \right]$		F 2.64	25.24	24.53	24.39
		M 2.64	24.98	24.26	
		F 3.71	25.20	24.49	24.39
		M 3.71	25.00	24.28	
		F 5.12	25.45	24.75	24.66
		M 5.12	25.28	24.57	
		F 6.53	25.65	24.95	24.85
		M 6.53	25.45	24.75	
		F 7.94	25.76	25.06	25.23
		M 7.94	26.08	25.39	
$T_{out,1} = 25.25^\circ\text{C}$ $T_{out,2} = 25.47^\circ\text{C}$ $T_{out,3} = 25.50^\circ\text{C}$ $T_{out,4} = 25.52^\circ\text{C}$ $T_{out,5} = 25.53^\circ\text{C}$ $\left[T_{out} = 25.46^\circ\text{C} \right]$		F 9.35	26.02	25.33	25.25
		M 9.35	25.86	25.16	
		F 10.76	26.36	25.68	25.43
		M 10.76	25.87	25.18	
		F 12.88	26.45	25.77	25.94
		M 12.88	26.43	25.75	
		F 12.88	26.08	25.39	
		F 12.88	26.37	25.69	
		M 12.88	27.76	27.11	
		M 12.88	26.61	25.93	
		F 15.70	26.92	26.25	26.17
		M 15.70	26.75	26.08	
Non-dimensional parameters $Gr_m = 4437$ $Re_{ref} = 146.3$ $Pr = 6.7$ $St_m = 0.39 \times 10^{-3}$ $\phi_\infty = 0.261$		F 18.52	27.42	26.77	27.50
		M 18.52	28.86	28.24	
		F 21.34	28.39	27.77	27.47
		M 21.34	27.81	27.16	
		F 24.17	28.93	28.31	27.79
		M 24.17	27.91	27.27	
		F 26.99	28.44	27.81	28.13
		M 26.99	29.06	28.44	
		F 29.11	28.98	28.37	28.60
		M 29.11	29.43	28.82	
		F 31.22	28.78	28.16	28.59
		M 31.22	29.62	29.02	
Average velocity in the heated section		F 32.63	29.15	28.54	28.81
		M 32.63	29.69	29.09	
		F 34.04	29.33	28.72	28.98
		M 34.04	29.82	29.23	
$V = 0.776 \text{ cm/s}$		F 35.46	31.08	30.52	30.22
		M 35.46	30.50	29.93	

RUN # 7		Wall temperatures in the heated section			
Measurements in the closed-loop		Location z/D	Measured temp. (°C)	Corrected wall temp. (°C)	Average of corrected temperatures (°C)
$P_w = 54.80 \text{ W}$					
$T_a = 27.67^\circ\text{C}$		F 0.529	23.70	22.94	23.60
		M 0.529	24.99	24.26	
$T_{w,1} = 12.9^\circ\text{C}$ $T_{w,2} = 12.9^\circ\text{C}$ $T_{w,3} = 13.8^\circ\text{C}$ $\left[\bar{T}_w = 13.2^\circ\text{C} \right]$		F 1.23	24.15	23.40	23.89
		M 1.23	25.10	24.38	
		F 1.94	23.94	23.19	23.11
		M 1.94	23.78	23.02	
$T_{in,1} = 16.32^\circ\text{C}$ $T_{in,2} = 16.30^\circ\text{C}$ $T_{in,3} = 16.40^\circ\text{C}$ $T_{in,4} = 16.10^\circ\text{C}$ $T_{in,5} = 16.14^\circ\text{C}$ $\left[T_{in} = 16.23^\circ\text{C} \right]$		F 2.64	23.45	22.68	22.46
		M 2.64	23.00	22.23	
		F 3.71	23.36	22.59	22.43
		M 3.71	23.04	22.27	
		F 5.12	23.58	22.81	22.67
		M 5.12	23.29	22.52	
		F 6.53	23.81	23.06	22.90
		M 6.53	23.51	22.75	
		F 7.94	23.91	23.15	23.28
		M 7.94	24.16	23.41	
$T_{out,1} = 23.39^\circ\text{C}$ $T_{out,2} = 23.58^\circ\text{C}$ $T_{out,3} = 23.62^\circ\text{C}$ $T_{out,4} = 23.64^\circ\text{C}$ $T_{out,5} = 23.67^\circ\text{C}$ $\left[T_{out} = 23.59^\circ\text{C} \right]$		F 9.35	24.18	23.43	23.30
		M 9.35	23.92	23.17	
		F 10.76	24.51	23.77	23.50
		M 10.76	23.97	23.22	
		F 12.88	24.60	23.86	24.02
		M 12.88	24.53	23.79	
		F 12.88	24.19	23.45	
		F 12.88	24.50	23.77	
		M 12.88	25.98	25.27	
		M 12.88	24.71	23.97	
		F 15.70	25.08	24.36	24.24
		M 15.70	24.85	24.12	
Non-dimensional parameters $Gr_m = 4206$ $Re_{ref} = 130.4$ $Pr = 7.1$ $St_m = 0.41 \times 10^{-3}$ $\phi_\infty = 0.329$		F 18.52	25.63	24.92	25.67
		M 18.52	27.09	26.42	
		F 21.34	26.56	25.88	25.57
		M 21.34	25.96	25.26	
		F 24.17	27.14	26.47	25.90
		M 24.17	26.03	25.33	
		F 26.99	25.97	25.27	25.95
		M 26.99	27.29	26.63	
		F 29.11	27.20	26.54	26.79
		M 29.11	27.20	27.04	
		F 31.22	27.11	26.44	26.81
		M 31.22	27.84	27.18	
Average velocity in the heated section		F 32.63	27.35	26.69	26.96
		M 32.63	27.89	27.24	
		F 34.04	27.53	26.87	27.14
		M 34.04	28.05	27.40	
$V = 0.739 \text{ cm/s}$		F 35.46	29.35	28.74	28.43
		M 35.46	28.74	28.11	

RUN # 8		Wall temperatures in the heated section			
Measurements in the closed-loop		Location z/D	Measured temp. (°C)	Corrected wall temp. (°C)	Average of corrected temperatures (°C)
$P_w = 74.58 \text{ W}$					
$T_a = 27.73^\circ\text{C}$		F 0.529	26.52	25.59	26.27
		M 0.529	27.84	26.95	
$T_{w,1} = 13.0^\circ\text{C}$ $T_{w,2} = 13.0^\circ\text{C}$ $T_{w,3} = 14.1^\circ\text{C}$ $\left[\begin{array}{l} \bar{T}_w = 13.3^\circ\text{C} \end{array} \right.$		F 1.23	27.00	26.08	26.56
		M 1.23	27.93	27.04	
		F 1.94	26.54	25.61	25.41
		M 1.94	26.14	25.21	
$T_{in,1} = 17.13^\circ\text{C}$ $T_{in,2} = 17.09^\circ\text{C}$ $T_{in,3} = 17.15^\circ\text{C}$ $T_{in,4} = 16.89^\circ\text{C}$ $T_{in,5} = 16.91^\circ\text{C}$ $\left[\begin{array}{l} T_{in} = 17.01^\circ\text{C} \end{array} \right.$		F 2.64	25.91	24.97	24.58
		M 2.64	25.16	24.20	
		F 3.71	25.74	24.79	24.52
		M 3.71	25.20	24.24	
		F 5.12	25.97	25.03	24.79
		M 5.12	25.49	24.54	
		F 6.53	26.27	25.34	25.09
		M 6.53	25.78	24.83	
		F 7.94	26.35	25.42	25.52
		M 7.94	26.54	25.61	
$T_{out,1} = 25.33^\circ\text{C}$ $T_{out,2} = 25.59^\circ\text{C}$ $T_{out,3} = 25.59^\circ\text{C}$ $T_{out,4} = 25.65^\circ\text{C}$ $T_{out,5} = 25.64^\circ\text{C}$ $\left[\begin{array}{l} T_{out} = 25.57^\circ\text{C} \end{array} \right.$		F 9.35	26.69	25.77	25.52
		M 9.35	26.20	25.27	
		F 10.76	27.10	26.19	25.73
		M 10.76	26.20	25.27	
		F 12.88	27.16	26.25	26.41
		M 12.88	26.74	25.82	
		F 12.88	26.64	25.72	
		F 12.88	27.03	26.12	
		M 12.88	29.08	28.22	
		M 12.88	27.25	26.34	26.60
Non-dimensional parameters		F 15.70	27.74	26.84	
		M 15.70	27.26	26.35	28.64
		F 18.52	28.33	27.45	
		M 18.52	30.65	29.83	28.26
		F 21.34	29.50	28.65	
		M 21.34	28.74	27.87	28.64
		F 24.17	30.28	29.45	
		M 24.17	28.71	27.84	28.69
		F 26.99	28.81	27.94	
		M 26.99	30.26	29.43	29.43
Average velocity in the heated section		F 29.11	30.00	29.16	
		M 29.11	30.53	29.71	29.30
		F 31.22	29.74	28.90	
		M 31.22	30.53	29.70	29.36
		F 32.63	29.93	29.09	
		M 32.63	30.45	29.63	29.50
		F 34.04	30.11	29.28	
		M 34.04	30.54	29.71	31.19
		F 35.46	32.56	31.78	
		M 35.46	31.40	30.59	
$V = 0.845 \text{ cm/s}$					

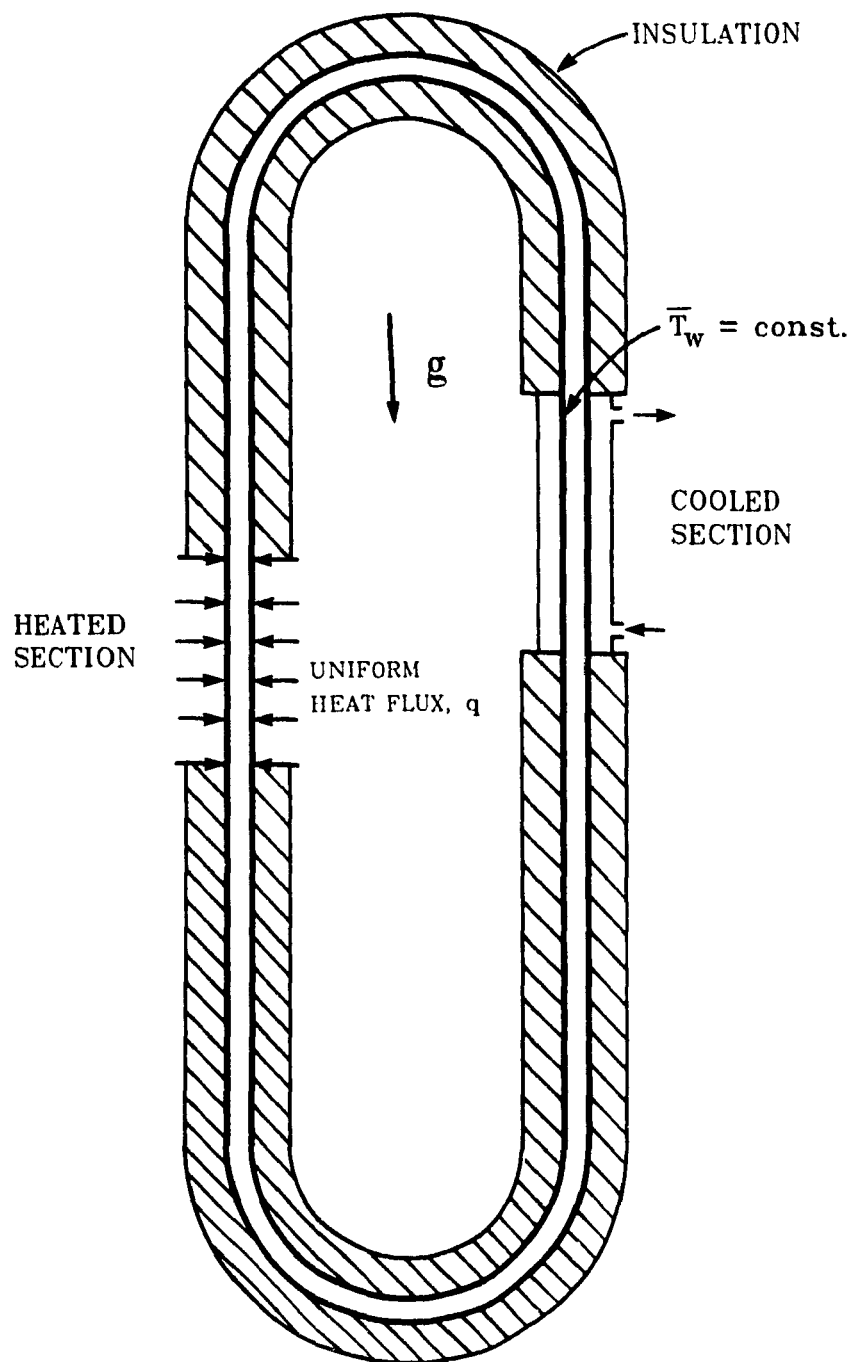


Figure 1.1: Schematic illustration of the closed-loop thermosyphon used in the present study.

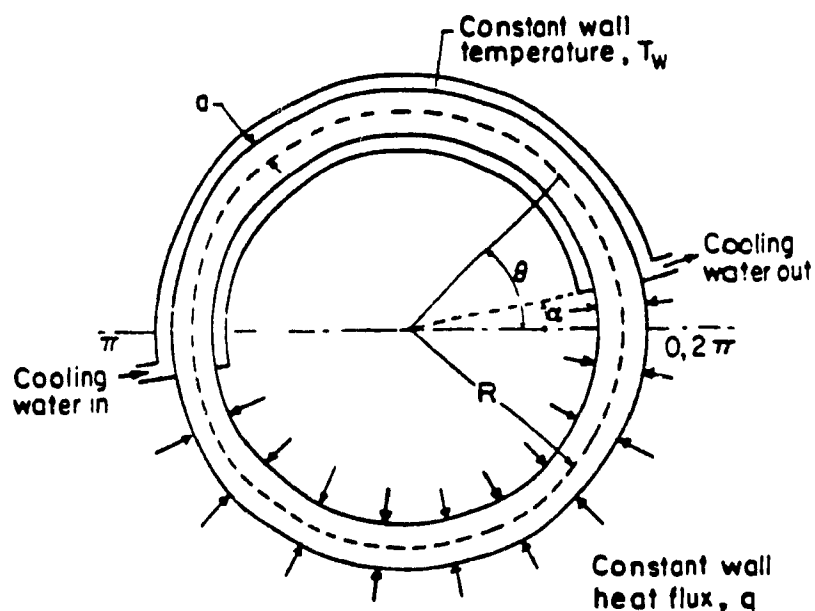


Figure 1.2: Schematic illustration of a toroidal thermosyphon (Lavine, [1984]).

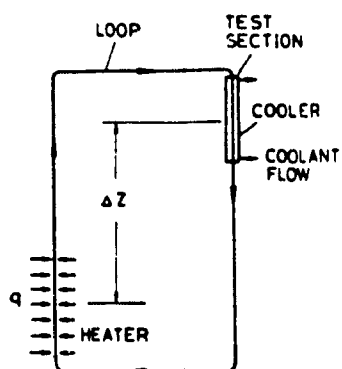


Figure 1.3: Schematic illustration of a closed-loop thermosyphon with vertical heat transfer passages (Huang, [1987]).

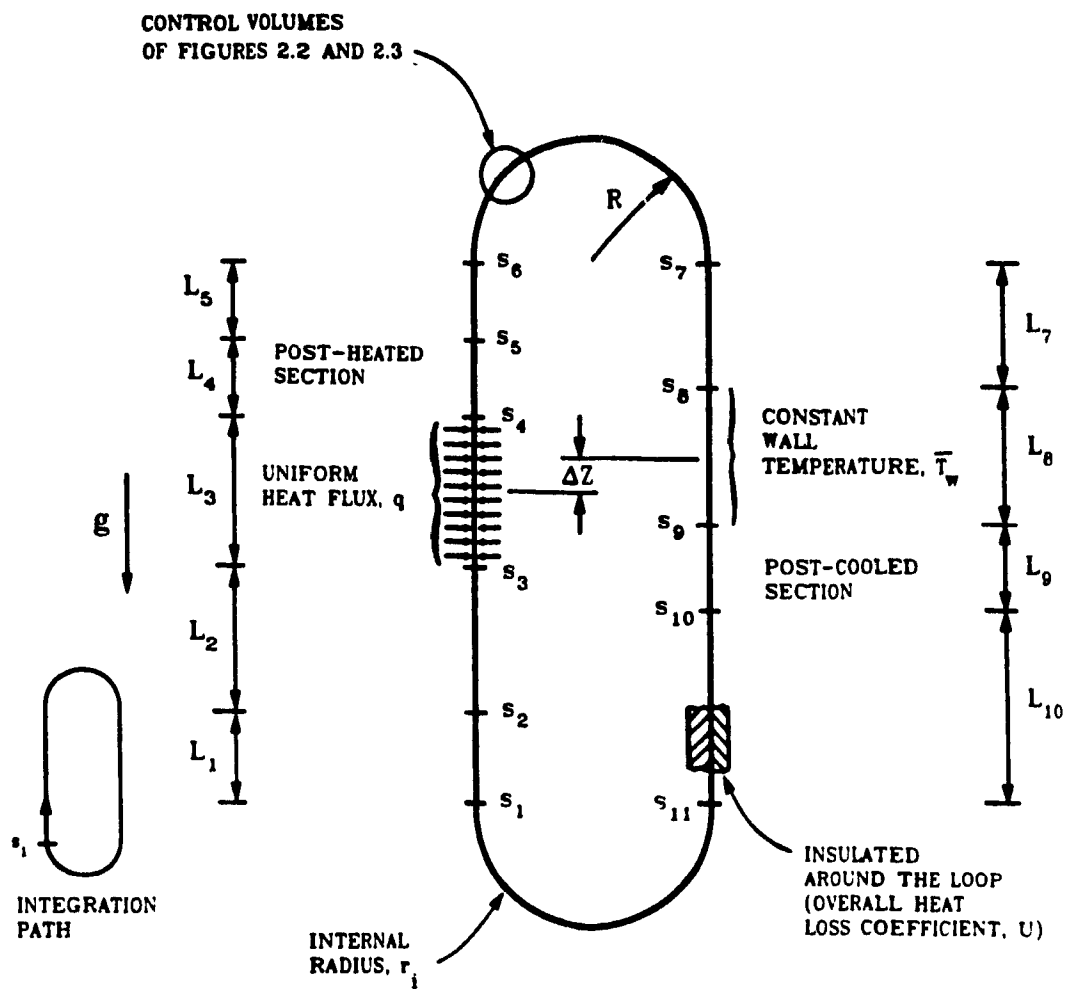


Figure 2.1: Geometric details and nomenclature used in the proposed model.

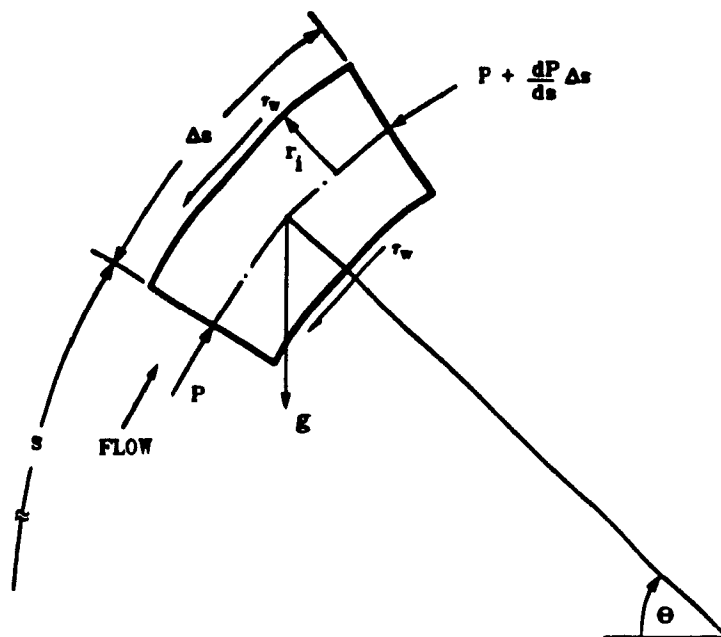


Figure 2.2: Elemental control volume used in the derivation of the general one-dimensional momentum equation.

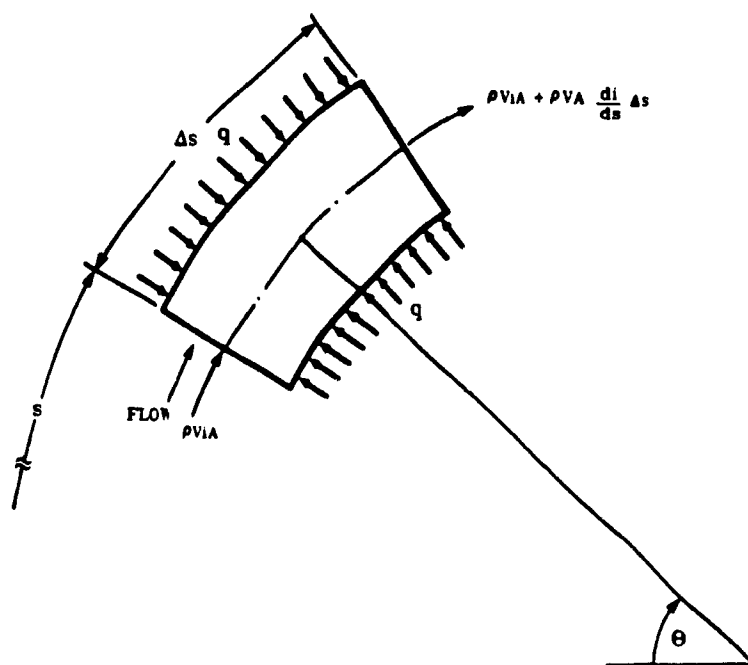


Figure 2.3: Elemental control volume used in the derivation of the general one-dimensional energy equation.

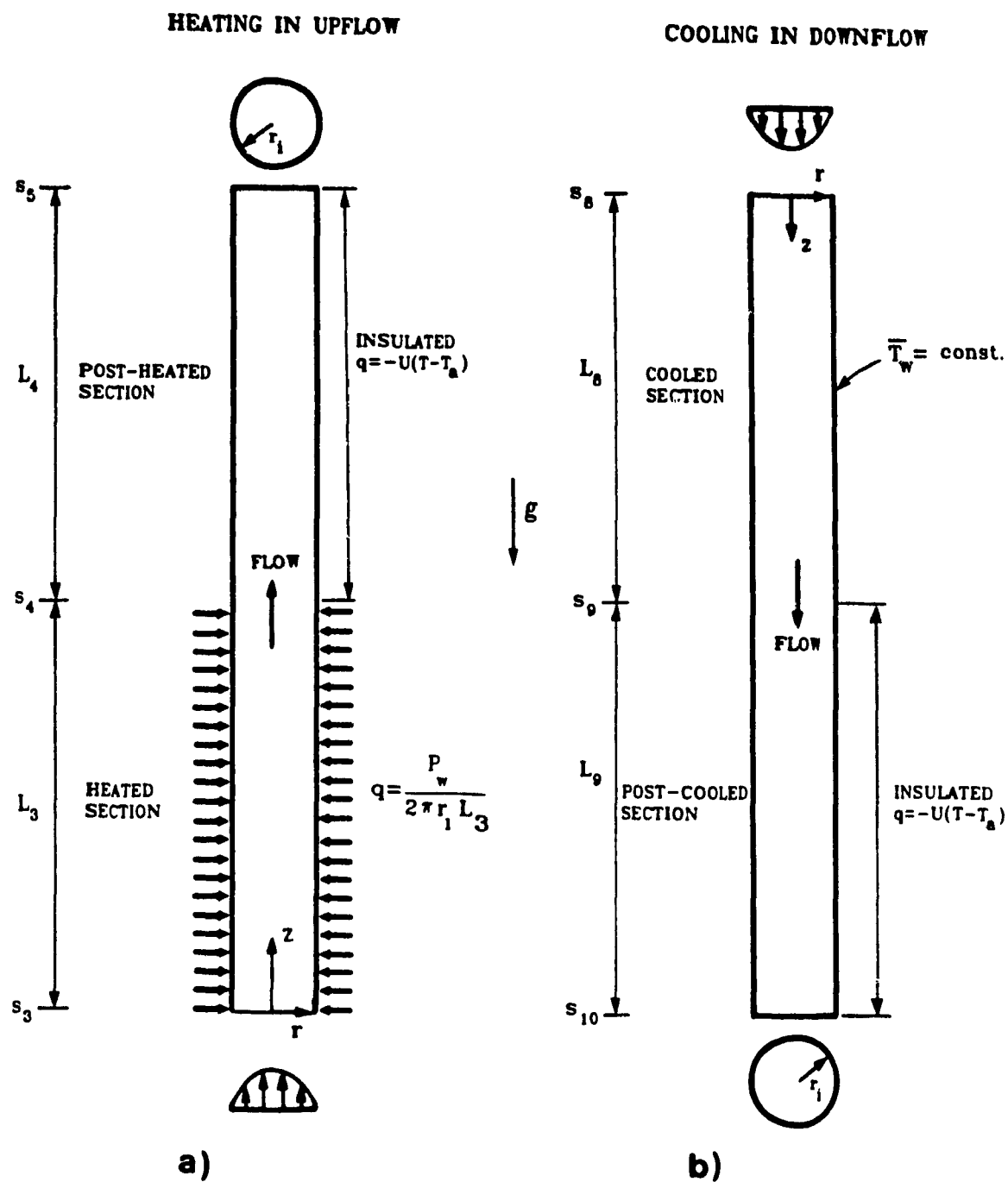


Figure 2.4: Calculation domain and boundary conditions used in the two-dimensional numerical simulations of the proposed model: (a) the extended heated section; and (b) the extended cooled section.

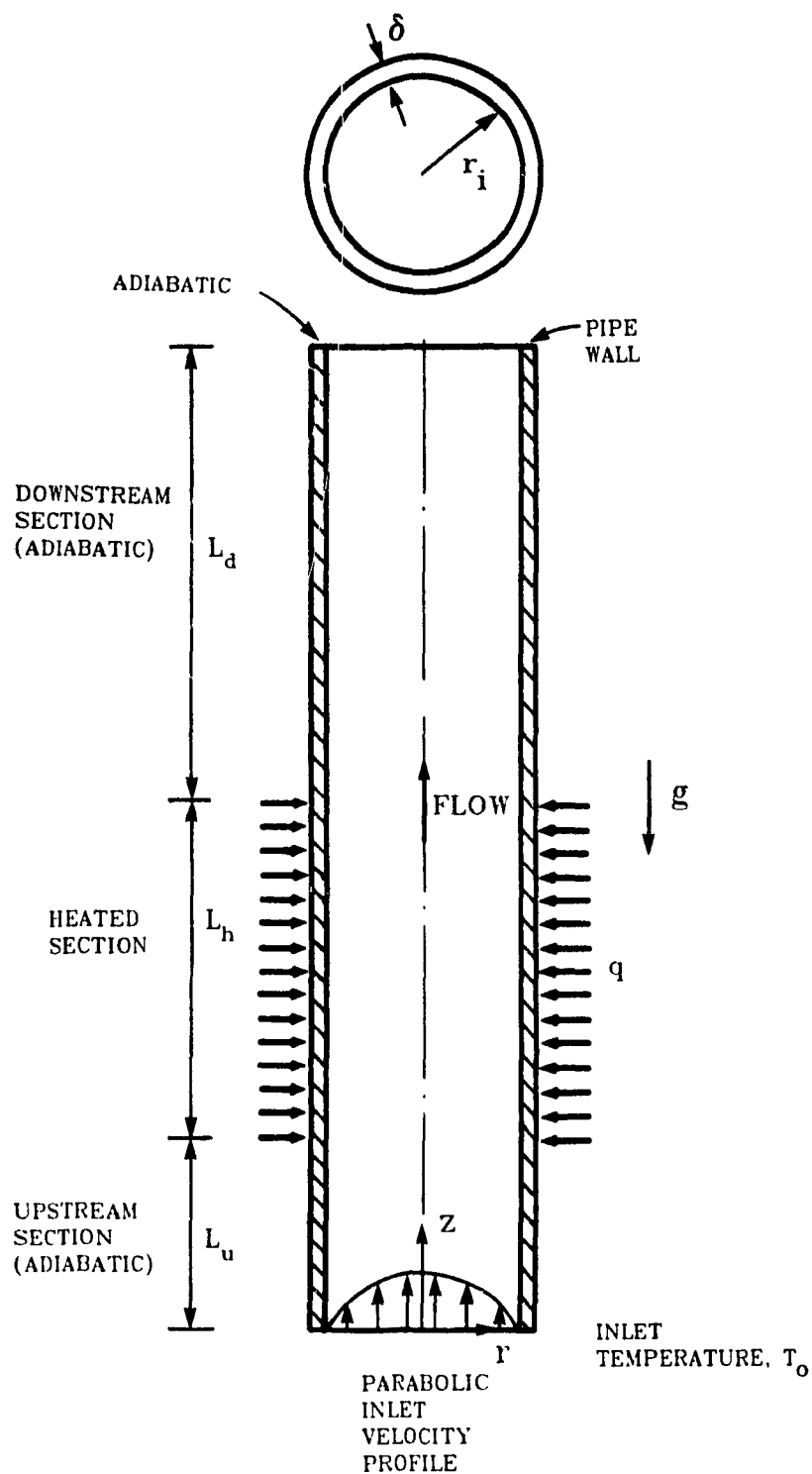


Figure 3.1: Calculation domain and boundary conditions used in the study of conjugate conduction and mixed-convection in a vertical pipes. Case where the elliptic equations are used.

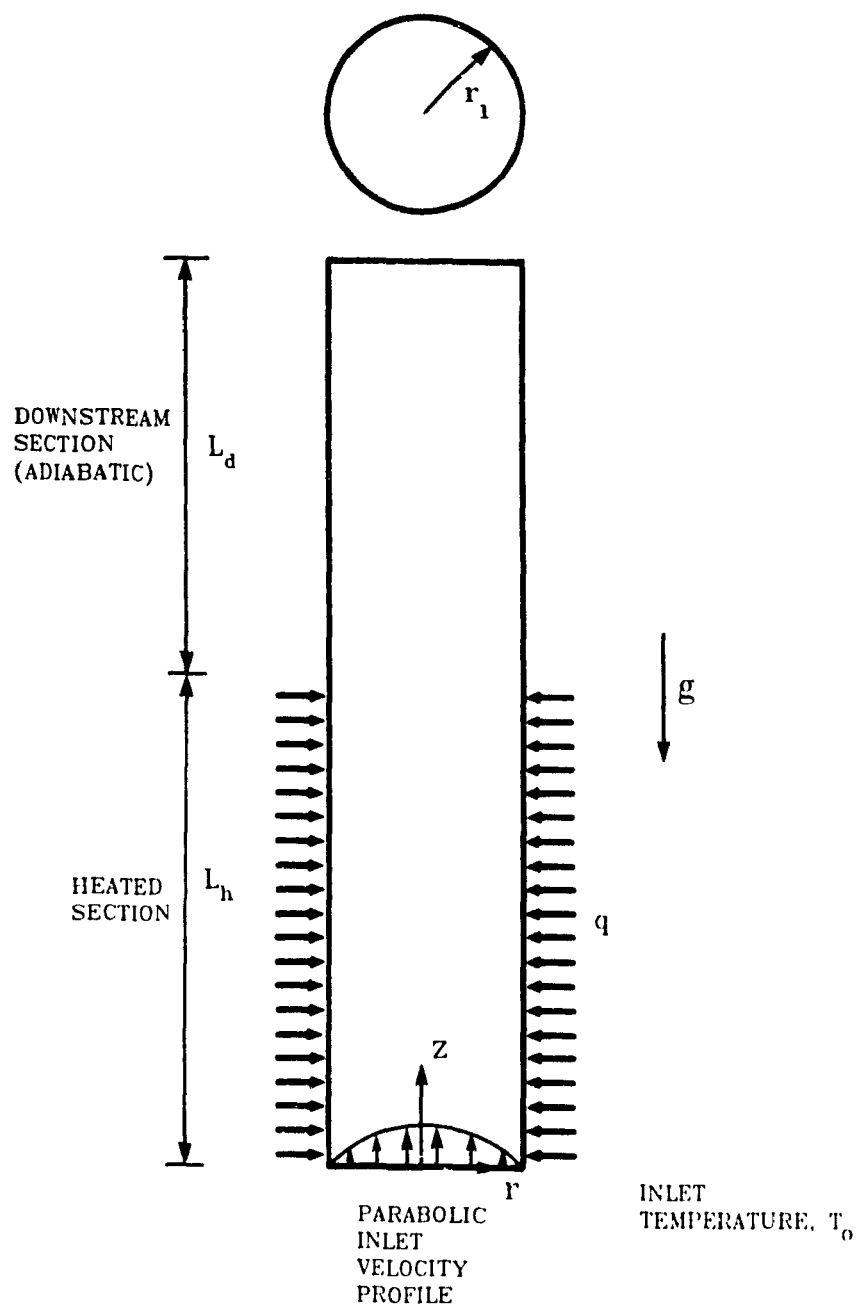


Figure 3.2: Calculation domain and boundary conditions used in the study of mixed-convection in vertical pipes. Case where the parabolic equations are used.

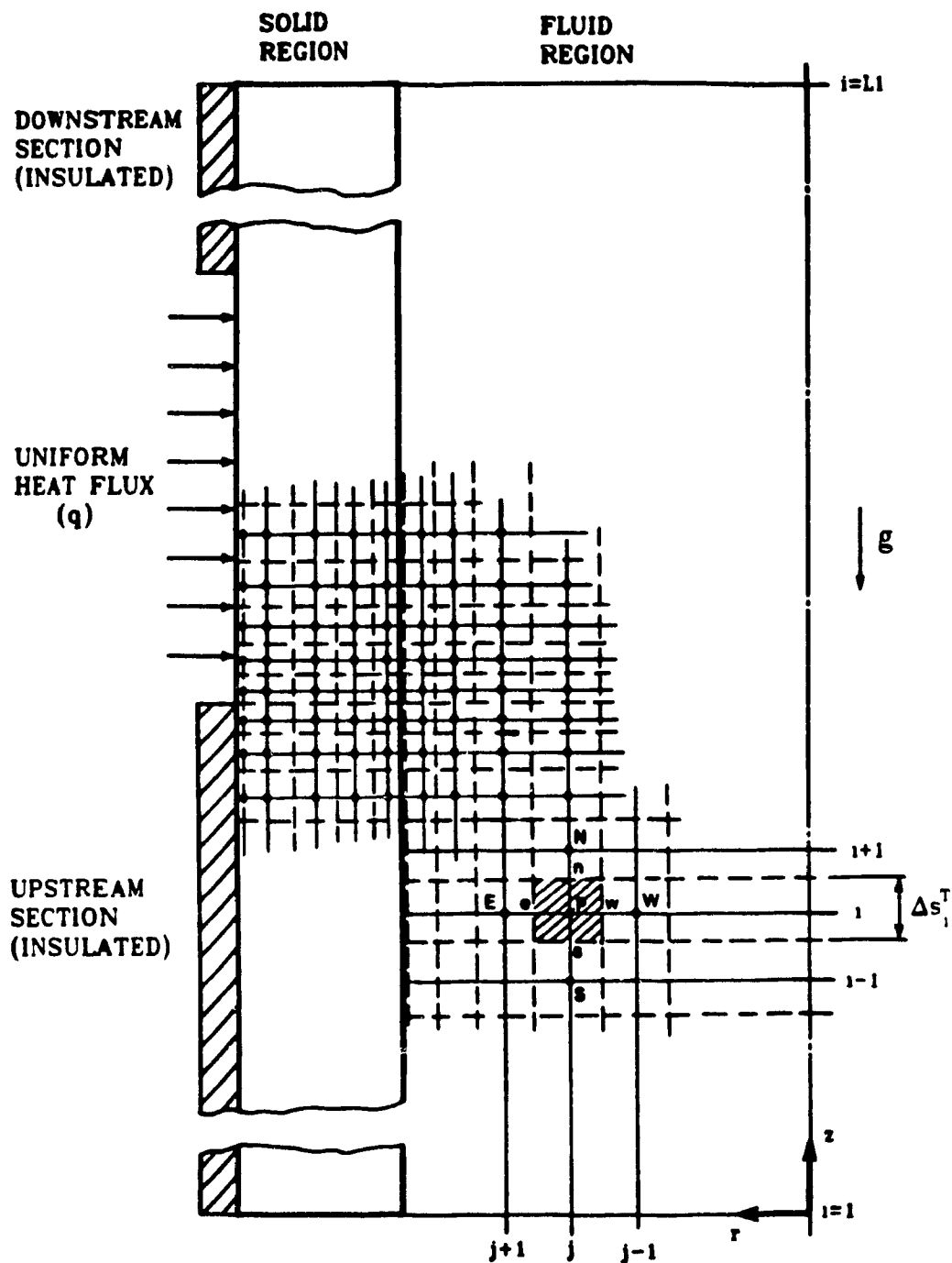


Figure 3.3: Typical grid distribution in the solid and in the fluid for the case where the elliptic equations are used. Also shown is a schematic of the control volume associated with node P along with its corresponding neighbouring nodes.

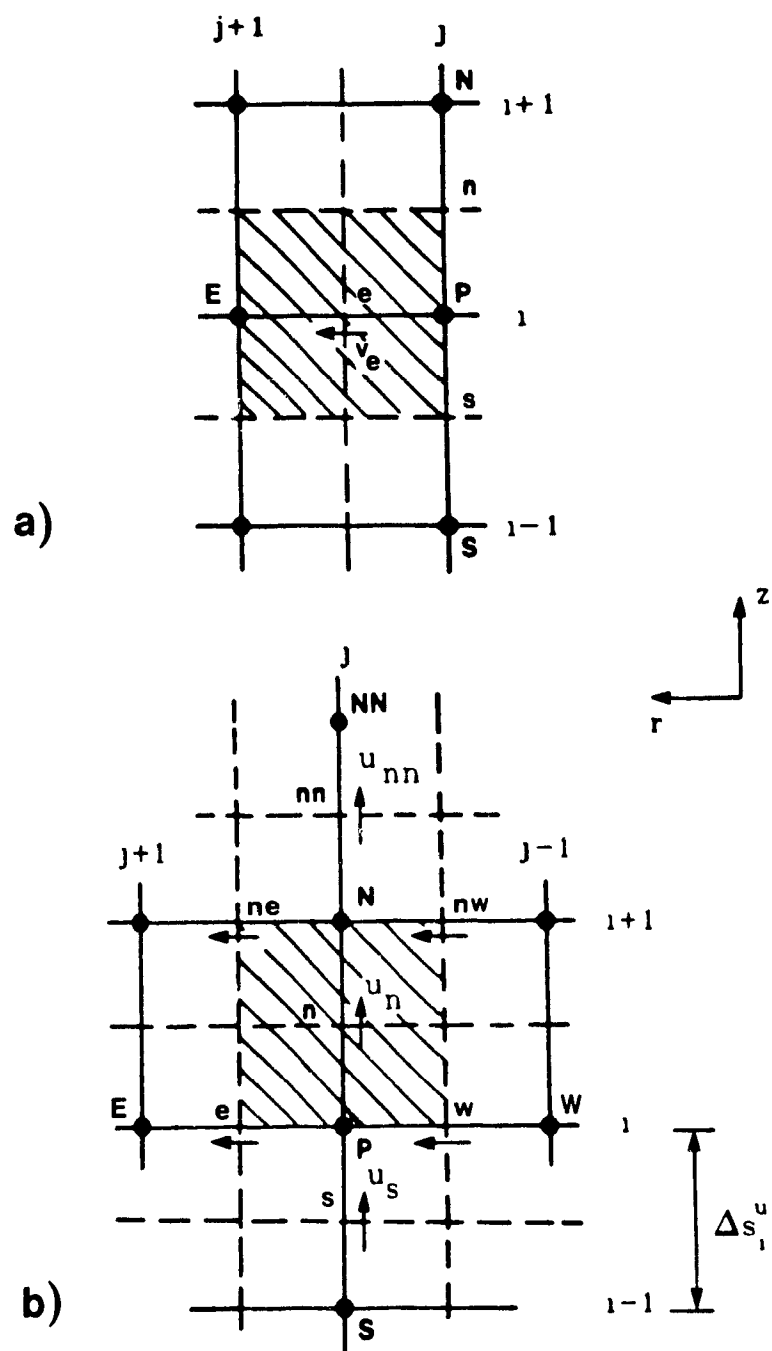


Figure 3.4: Staggered momentum control volumes for: (a) radial velocity; (b) axial velocity.

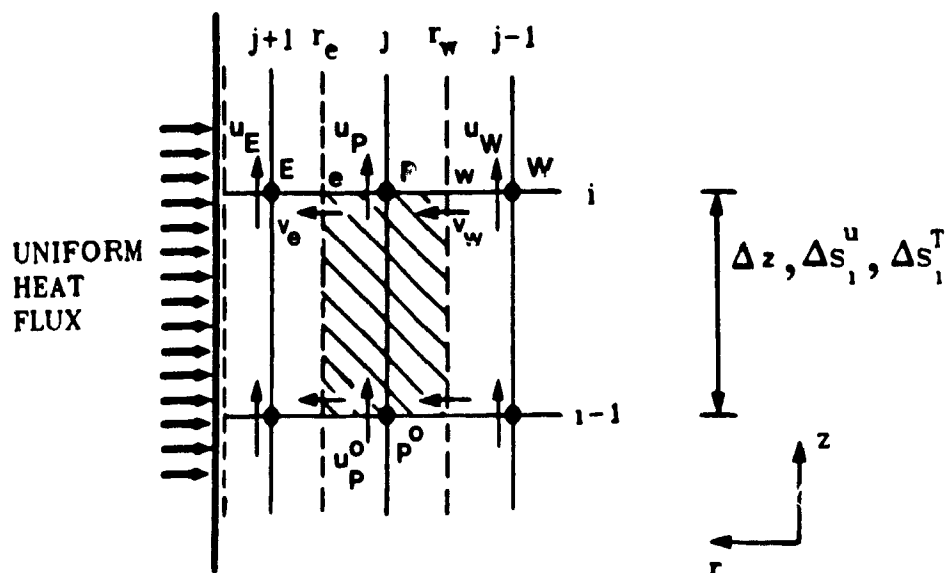


Figure 3.5: Schematic of the control volume associated with node P along with its corresponding neighbouring nodes. Case where the parabolic equations are used.

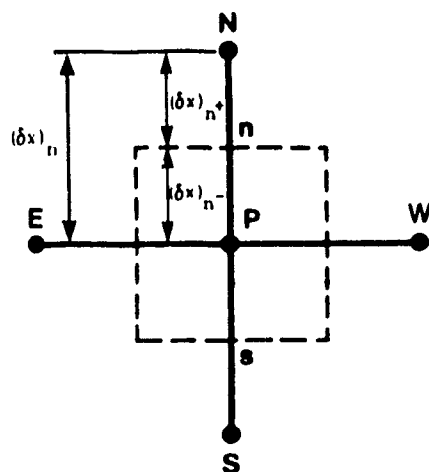


Figure 3.6: Distance between neighbouring nodes and control volume faces.

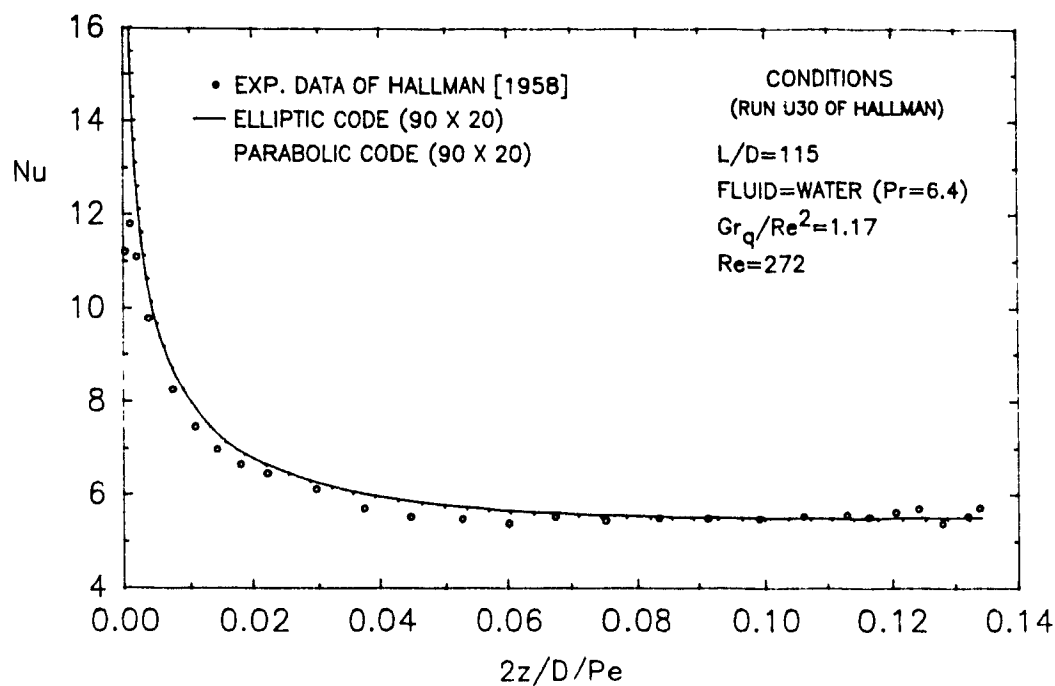


Figure 3.7: Mixed-convection in a vertical pipe subjected to uniform heat flux boundary condition. Results of a Nusselt number comparison among the experimental data of Hallman [1958] and the present numerical codes.

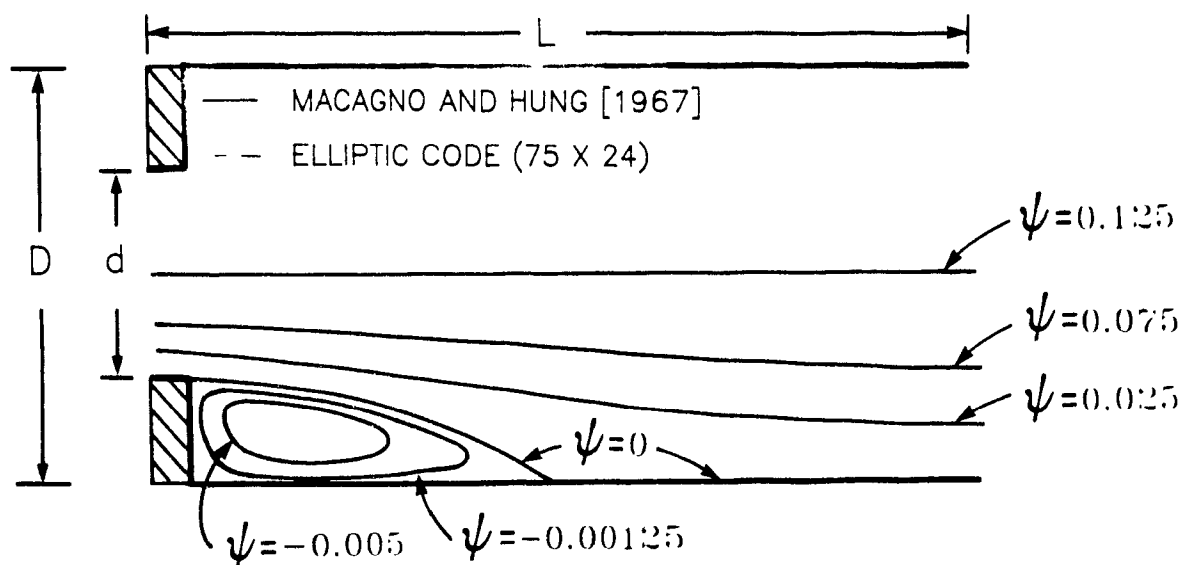


Figure 3.8: Sudden expansion in a pipe. $Re_d = 40$, $D/d = 2$, $L/D = 2$. The streamlines generated by the present elliptic code are indistinguishable from the ones obtained by Macagno and Hung [1967].

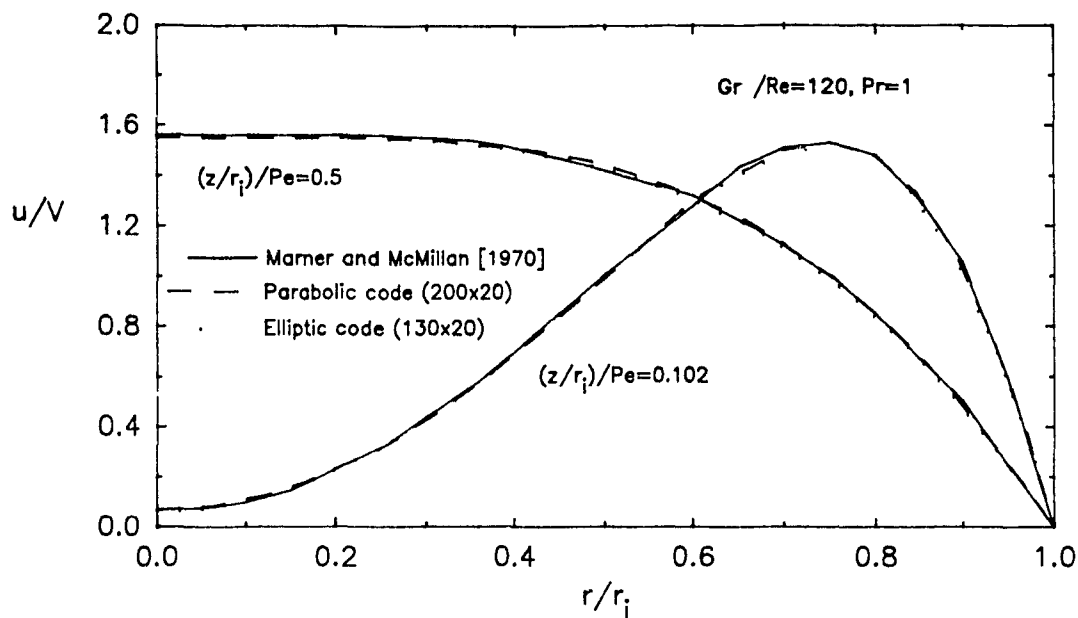


Figure 3.9: Mixed-convection in a vertical pipe subjected to constant wall temperature boundary condition. Results of a velocity profile comparison among the numerical data of Marner and McMillan [1970] and the present numerical codes

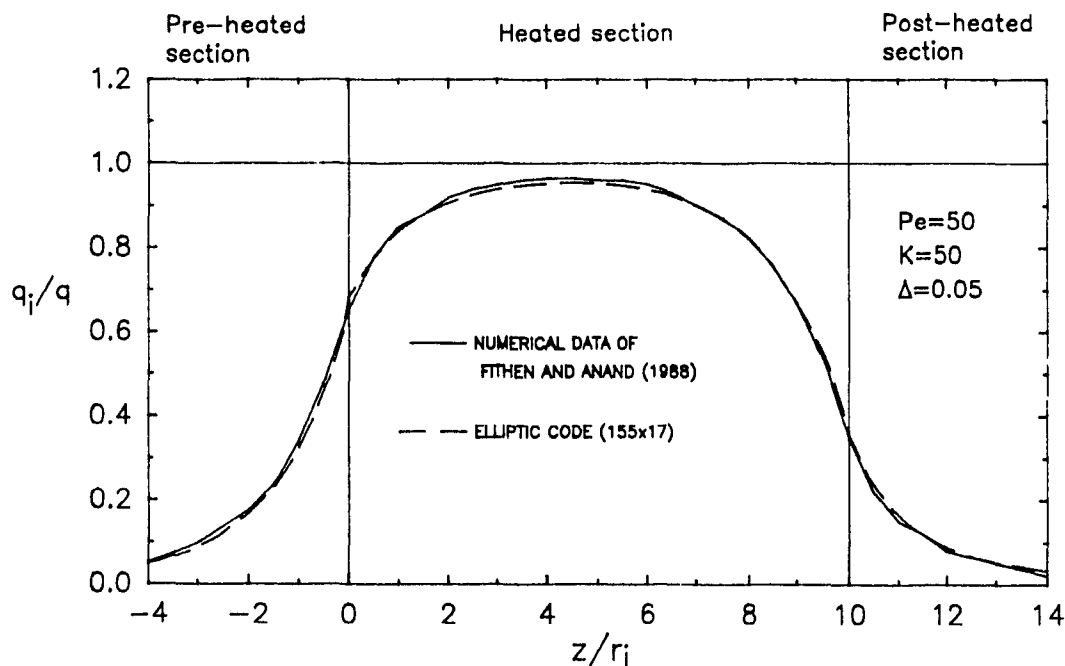


Figure 3.10: Conjugate conduction in the wall for the case where the flow is assumed to be fully developed throughout the calculation domain. Comparison of the ratio of the interface heat flux over the applied heat flux obtained by Fithen and Anand [1988] and the present elliptic code.

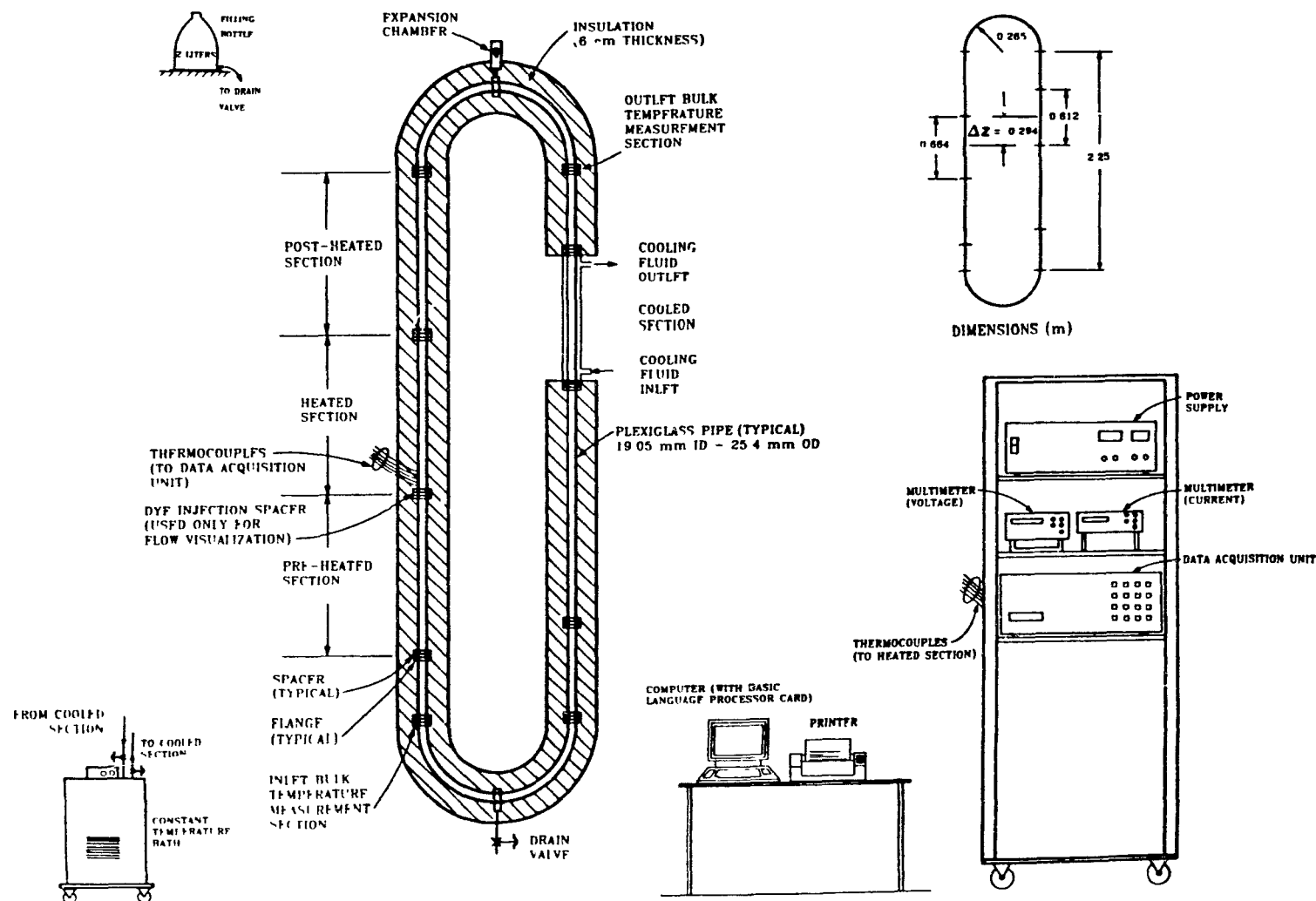


Figure 5.1: Schematic of the experimental closed-loop thermosyphon.



Figure 5.2: Photograph of the experimental closed-loop thermosyphon showing, from left to right: a constant temperature bath; the closed-loop thermosyphon covered with black insulation; a computerized data acquisition system; and an instrument rack holding the power supply, two multimeters, and the data acquisition and control unit.

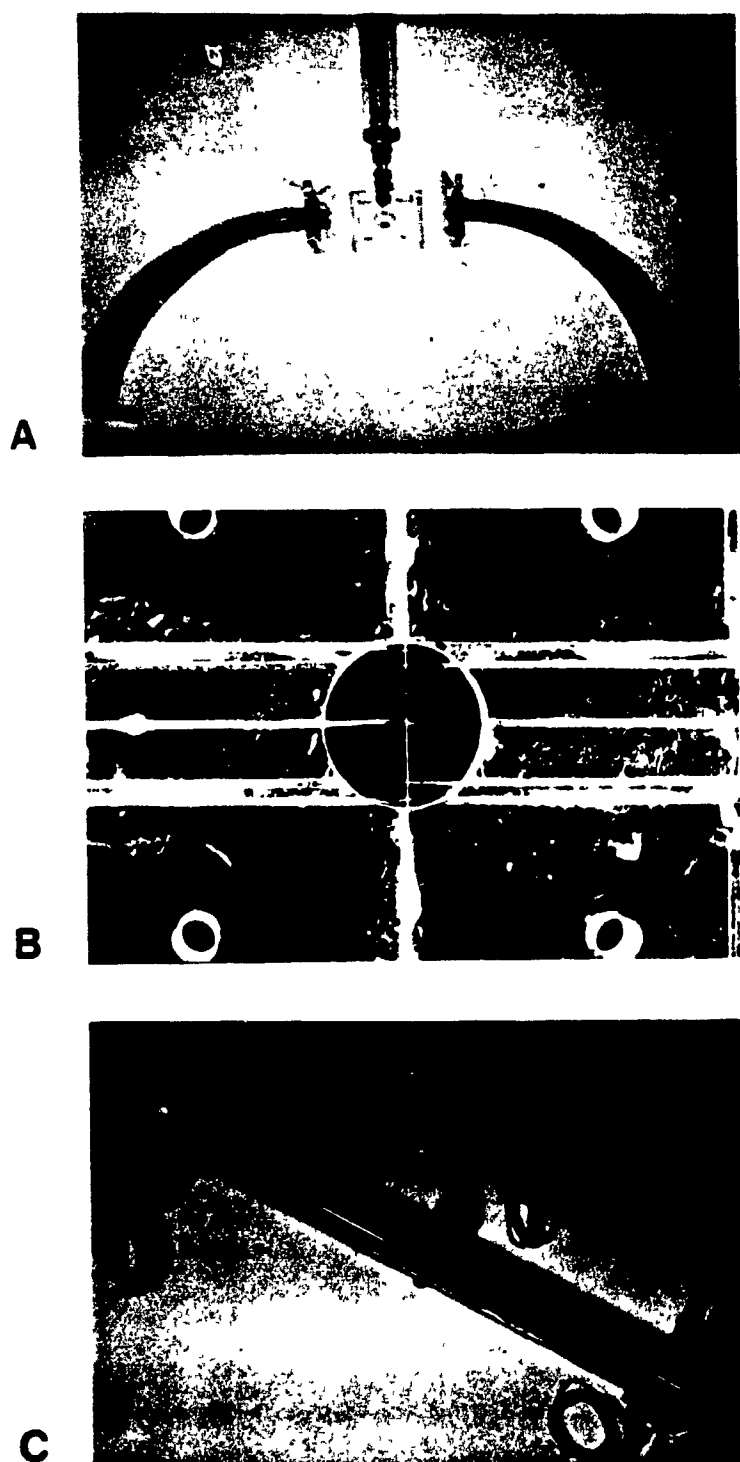


Figure 5.3: Elements of the closed-loop thermosyphon: (a) top circular 180° bend showing the flange-spacer-flange arrangement and the transparent expansion chamber; (b) bulk temperature measurement section; (c) cooled section.



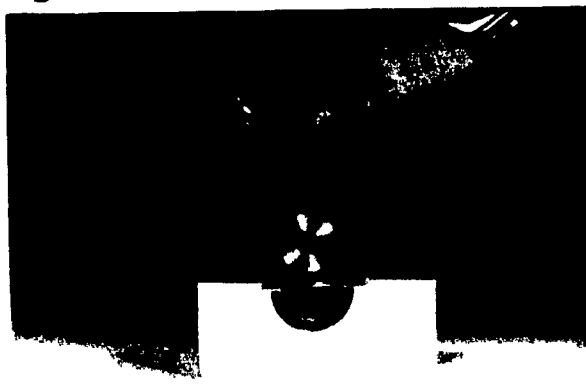
A



B



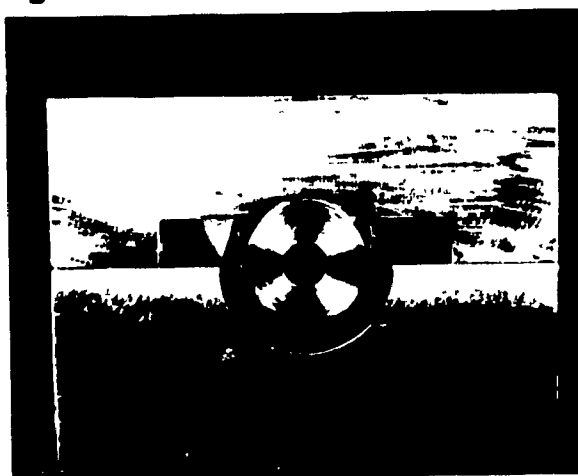
C



D



E



F

Figure 5.4: Construction of the gold-film sections: (a) cutting in half of the Plexiglass pipe; (b) painting of the extremities of a gold-film strip; (c) pouring of the epoxy glue on the gold side of the film; (d) insertion of the gold-film into the Plexiglass pipe using a brass rod; (e) tightening of the top aluminum block; (f) final assembly showing the protruding excess width of the film.

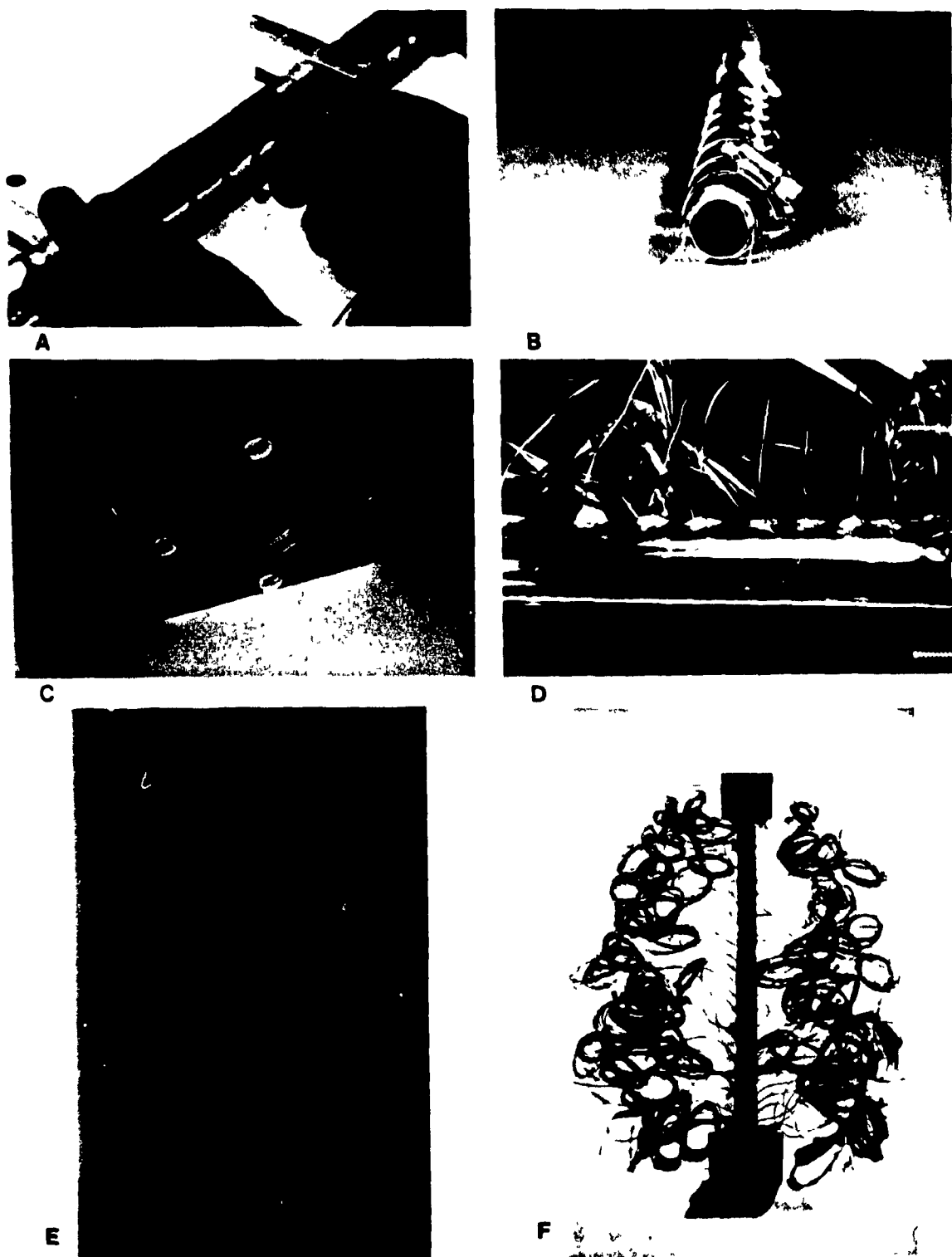


Figure 5.5: Construction of the gold-film sections: (a) cutting of the excess width; (b) mating and sealing of two half sections; (c) junction between the copper electrode and the gold-film; (d) close-up view of the thermocouple wires glued inside the Plexiglass pipe; (e) completed assembly of a flow visualization section; (f) completed assembly of a heated section.

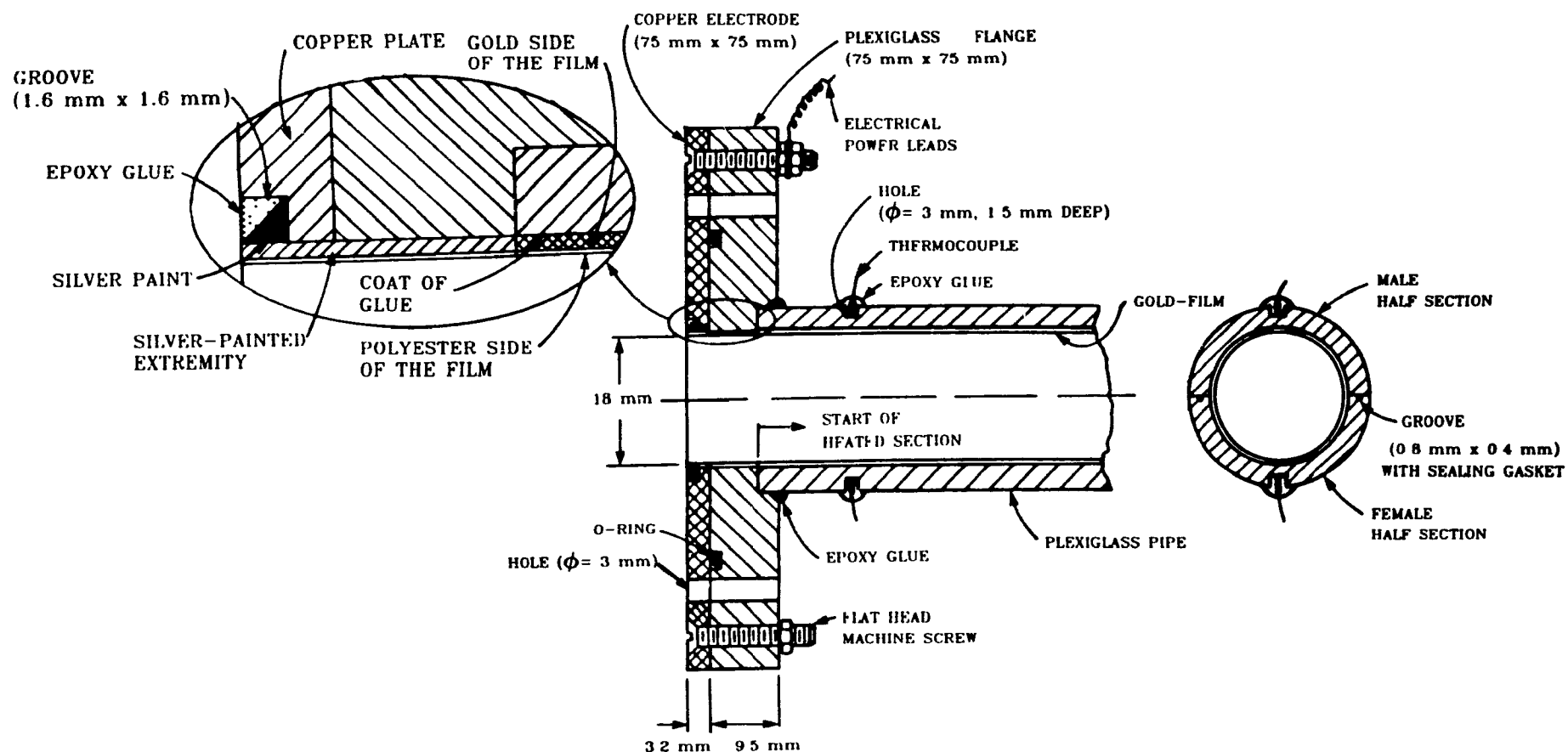


Figure 5.6: Cross-sectional view of one end of heated section no.2 showing the electrical connection between the copper electrode and the gold-film.

Radii (mm)		Thermal Conductivities (W/m°C)
r_x	9.00	$k_f = 0.28$
r_2	9.127	
r_3	$9.127 + 20 \text{ \AA}$	
r_4	11.15	$k_g = 317$
r_5	12.68	$k_p = 0.19$
r_6	69.7	$k_i = 0.04$

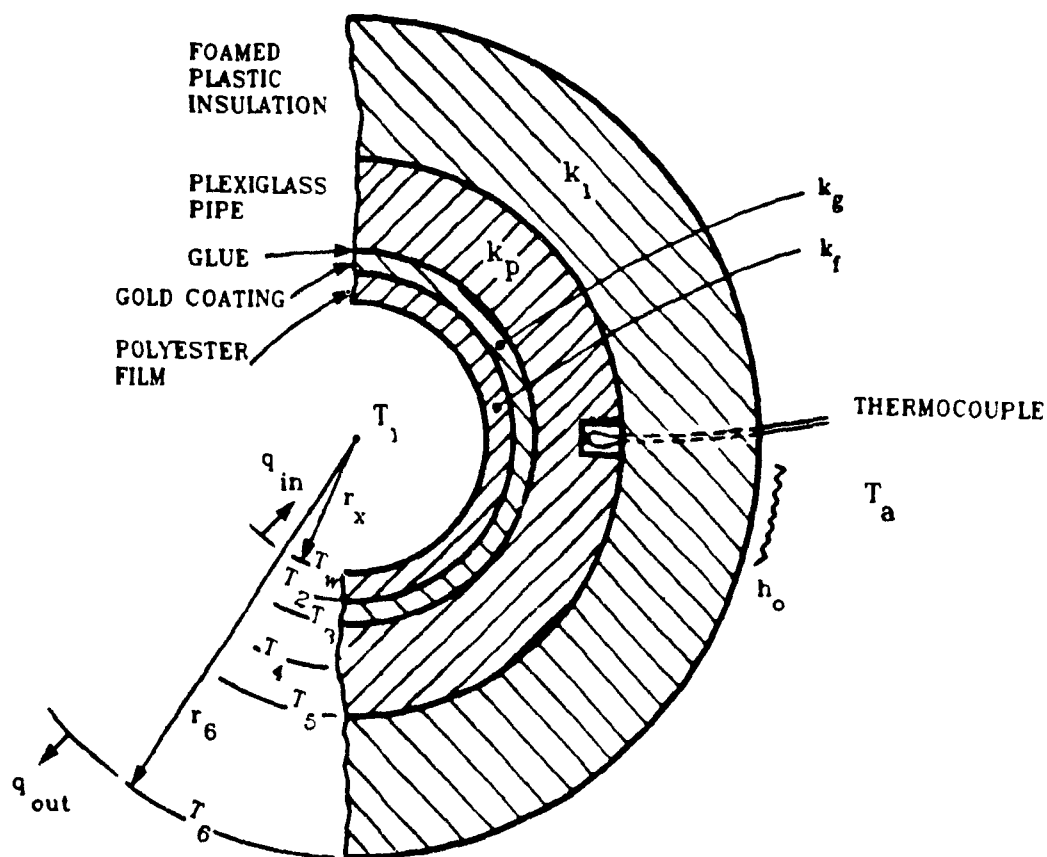


Figure 5.7: Cross-sectional view of heated section no.2 showing the location of the thermocouples inside the Plexiglass pipe and the various relevant materials and dimensions. Note: the figure is not to scale.

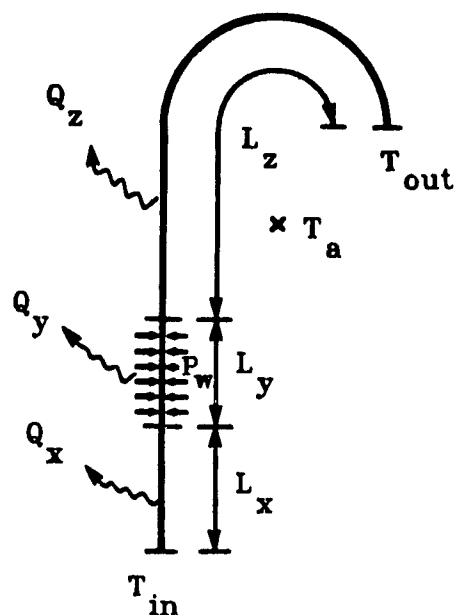


Figure 5.8: Geometric parameters and nomenclature used in the determination of the average velocity inside the closed-loop thermosyphon.

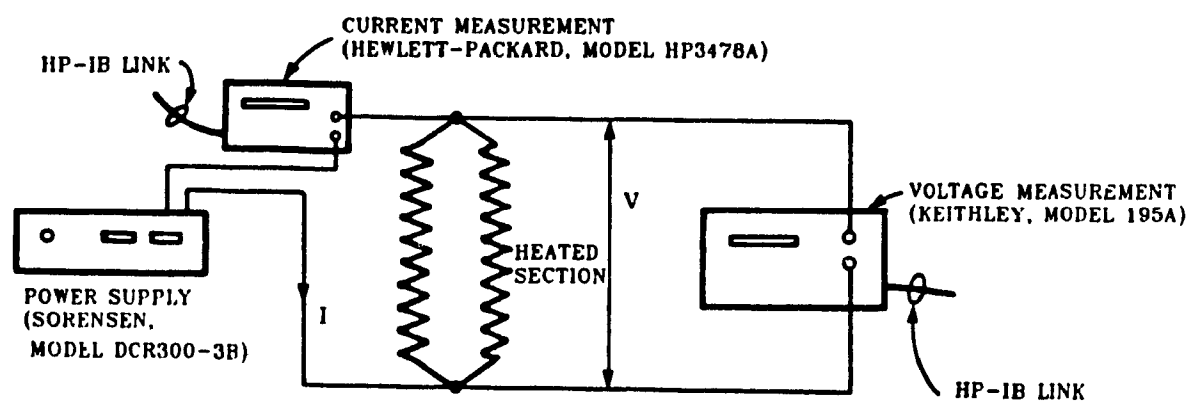


Figure 5.9: Schematic diagram of the electrical circuit.

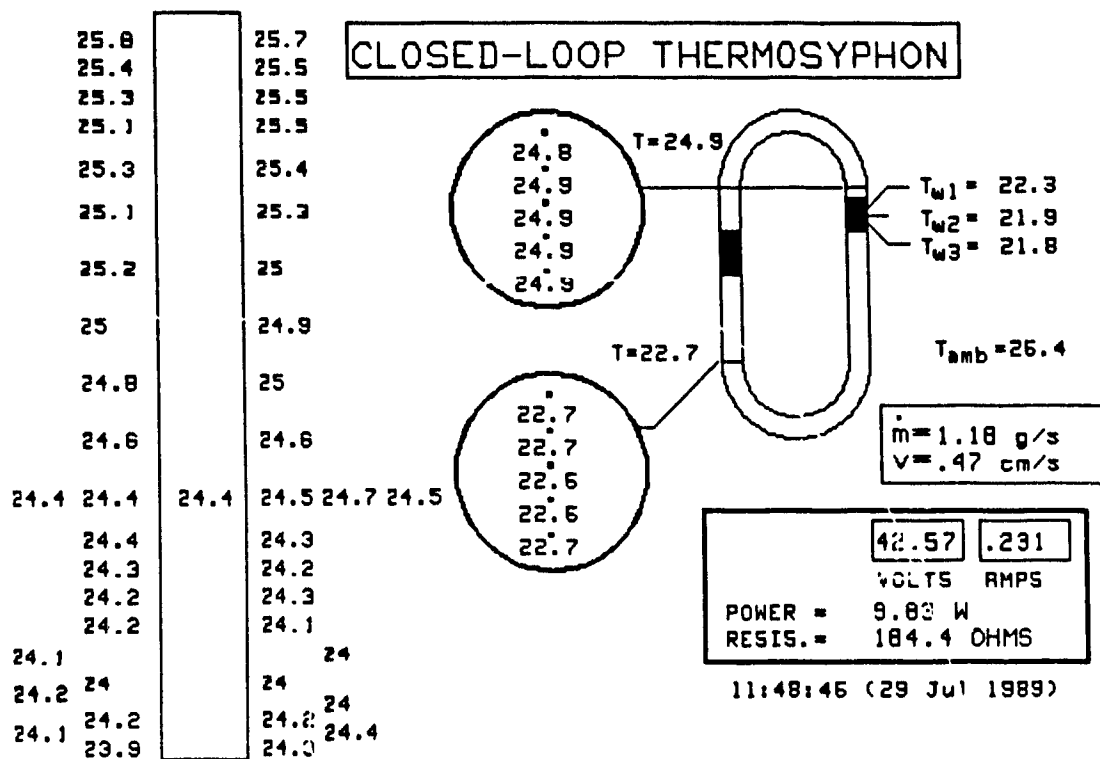
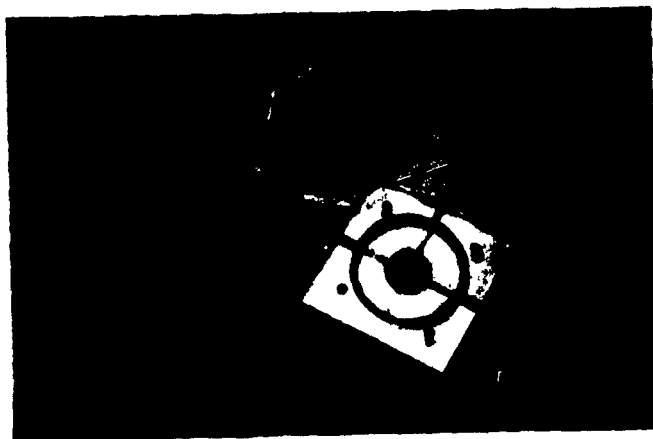
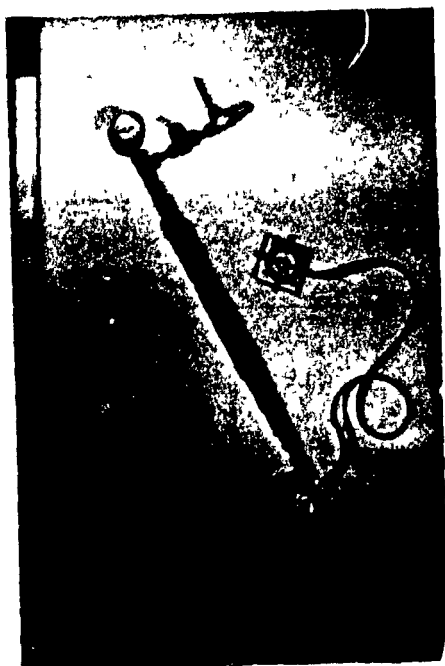


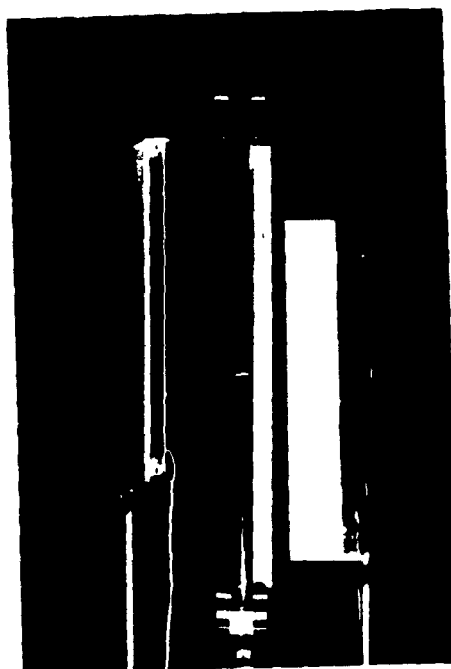
Figure 5.10: Transfer of a computer screen image (also shown in Fig. 5.2) to a printer showing all the measurements taken in the thermosyphon.



A



B



C

Figure 5.11: Instrumentation for flow visualization studies: (a) dye injection tube; (b) pressurized dye reservoir; and (c) flow visualization section, with long-wave black lights on each side.

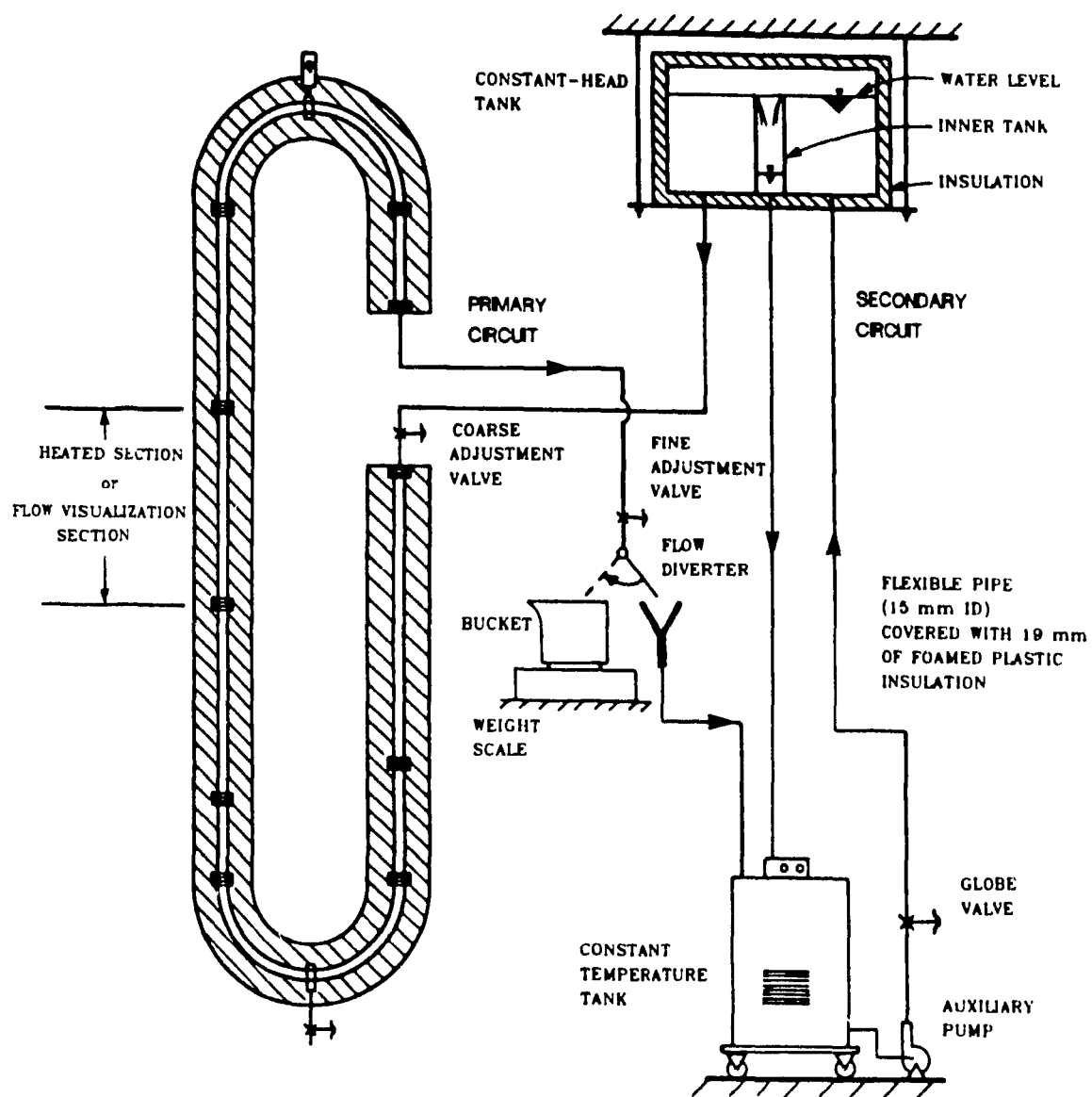


Figure 5.12: Schematic of the open-loop configuration

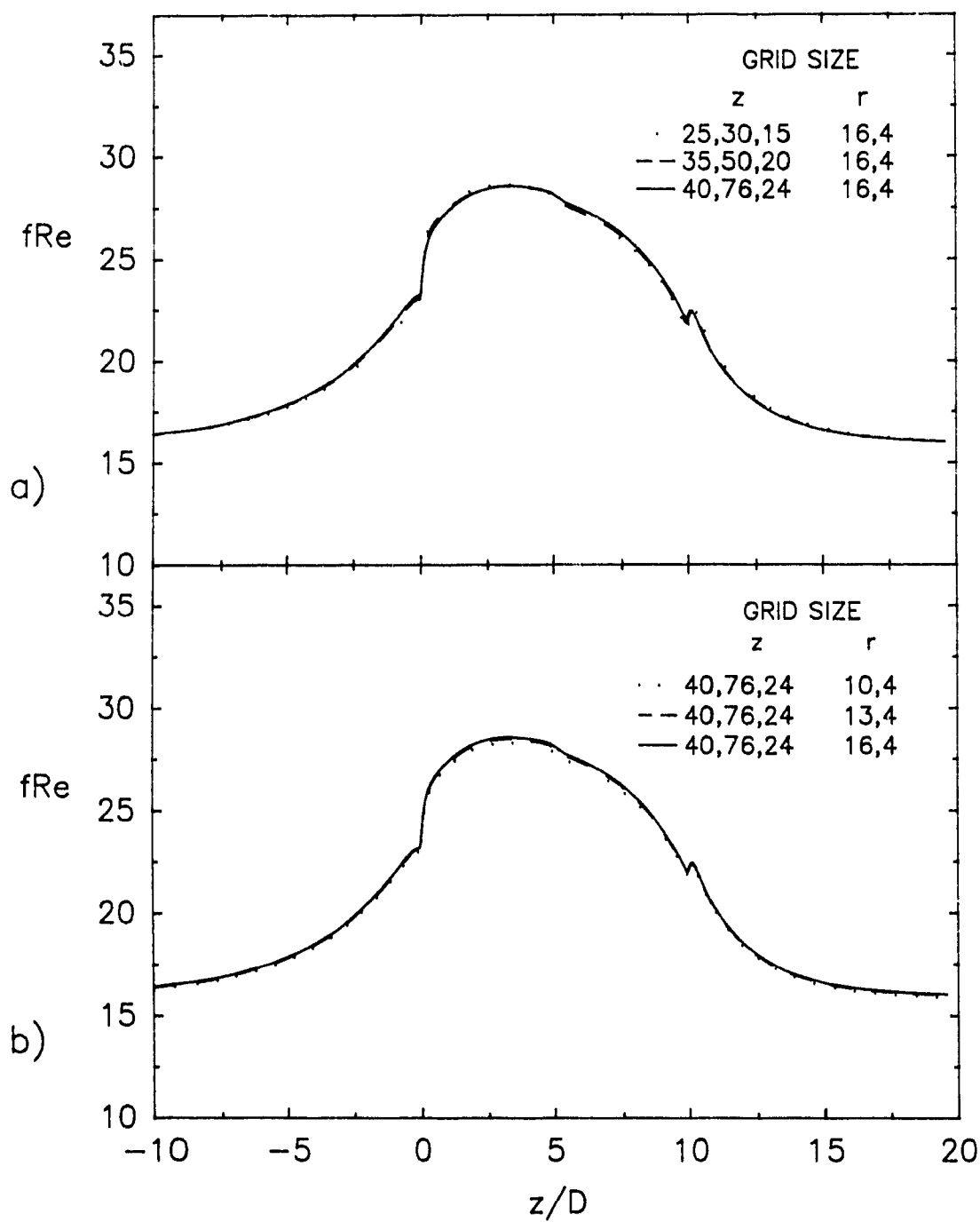


Figure 6.1: Results of grid-independence checks for $Gr_q/Re = 50$, $Re = 10$, $Pe = 50$, $K = 500$, and $\Delta = 0.05$: (a) effects of axial grid refinements; (b) effects of radial grid refinements.

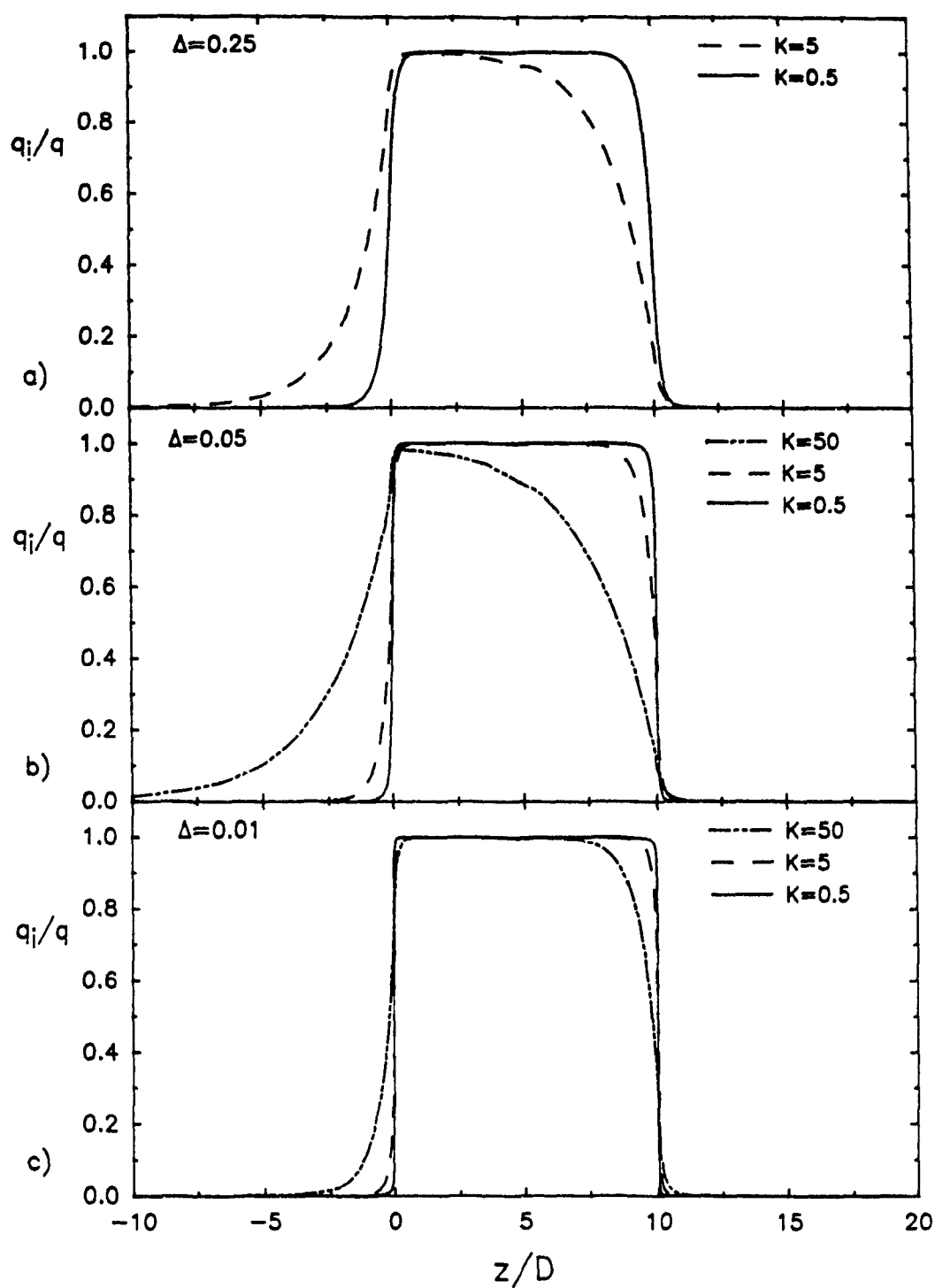


Figure 6.2: Axial variation of the ratio of the heat flux at the fluid-solid interface over the applied heat flux (q_i/q) for $Gr_q/Re^2 = 5000$, $Re = 1$, $Pe = 5$.

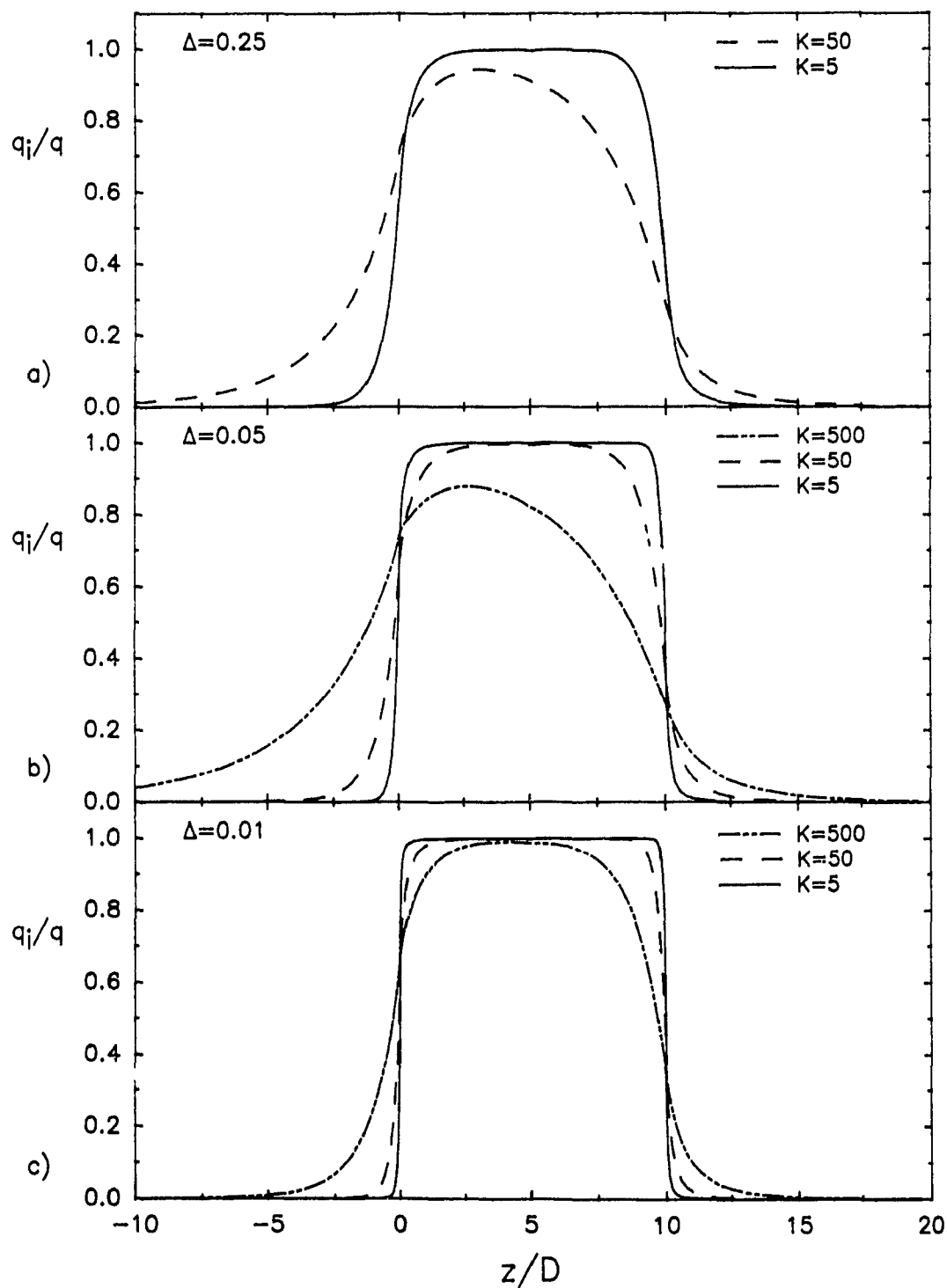


Figure 6.3: Axial variation of the ratio of the heat flux at the fluid-solid interface over the applied heat flux (q_i/q) for $Gr_q/Re^2 = 50$, $Re = 10$, $Pe = 50$.

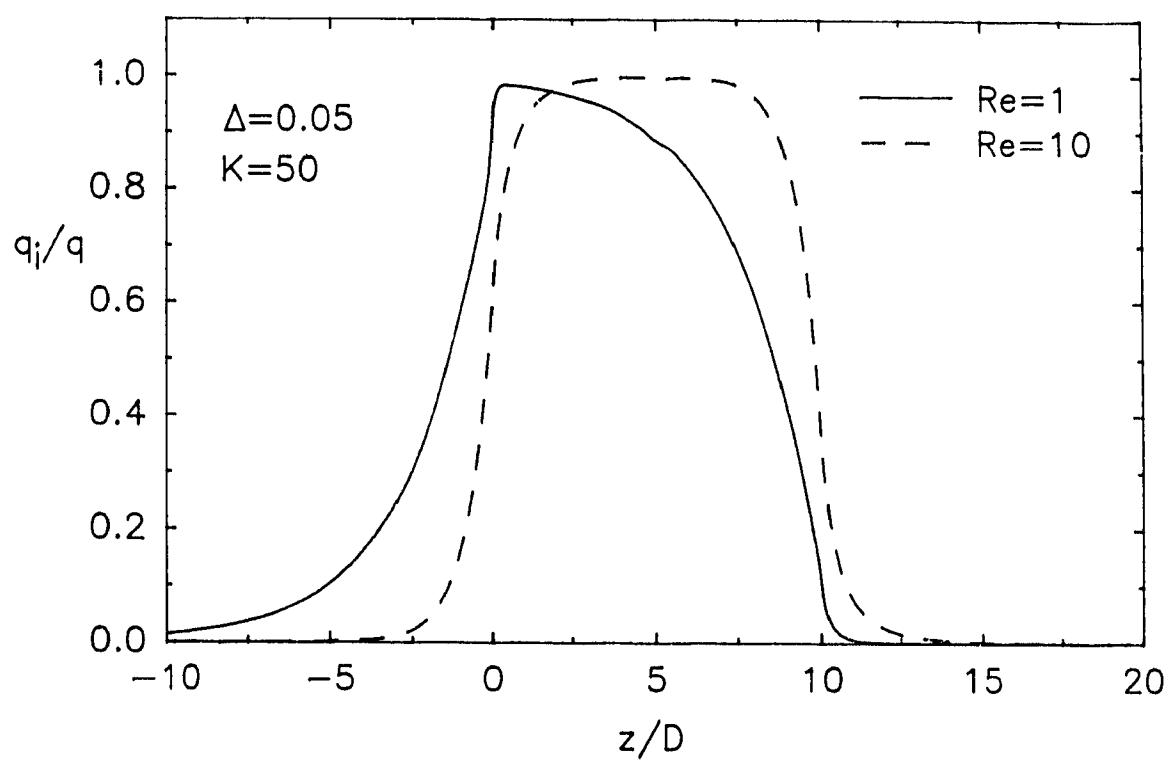


Figure 6.4: Comparison of q_i/q for two different Re . $Gr_q = 5000$, $Pr = 5$, $\Delta = 0.05$, and $K = 50$.

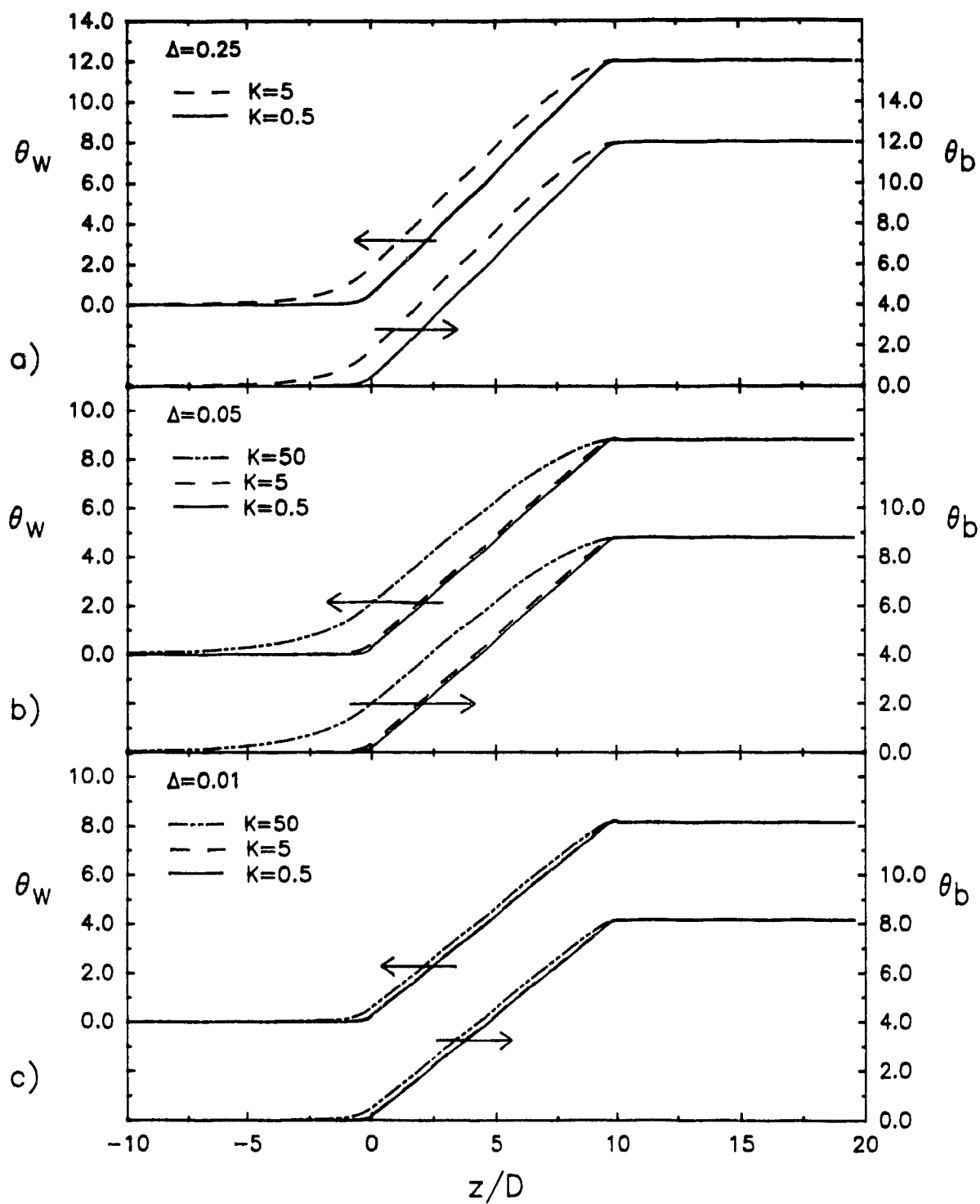


Figure 6.5: Axial variation of θ_w and θ_b for $Gr_q = 5000$, $Re = 1$, $Pe = 5$.

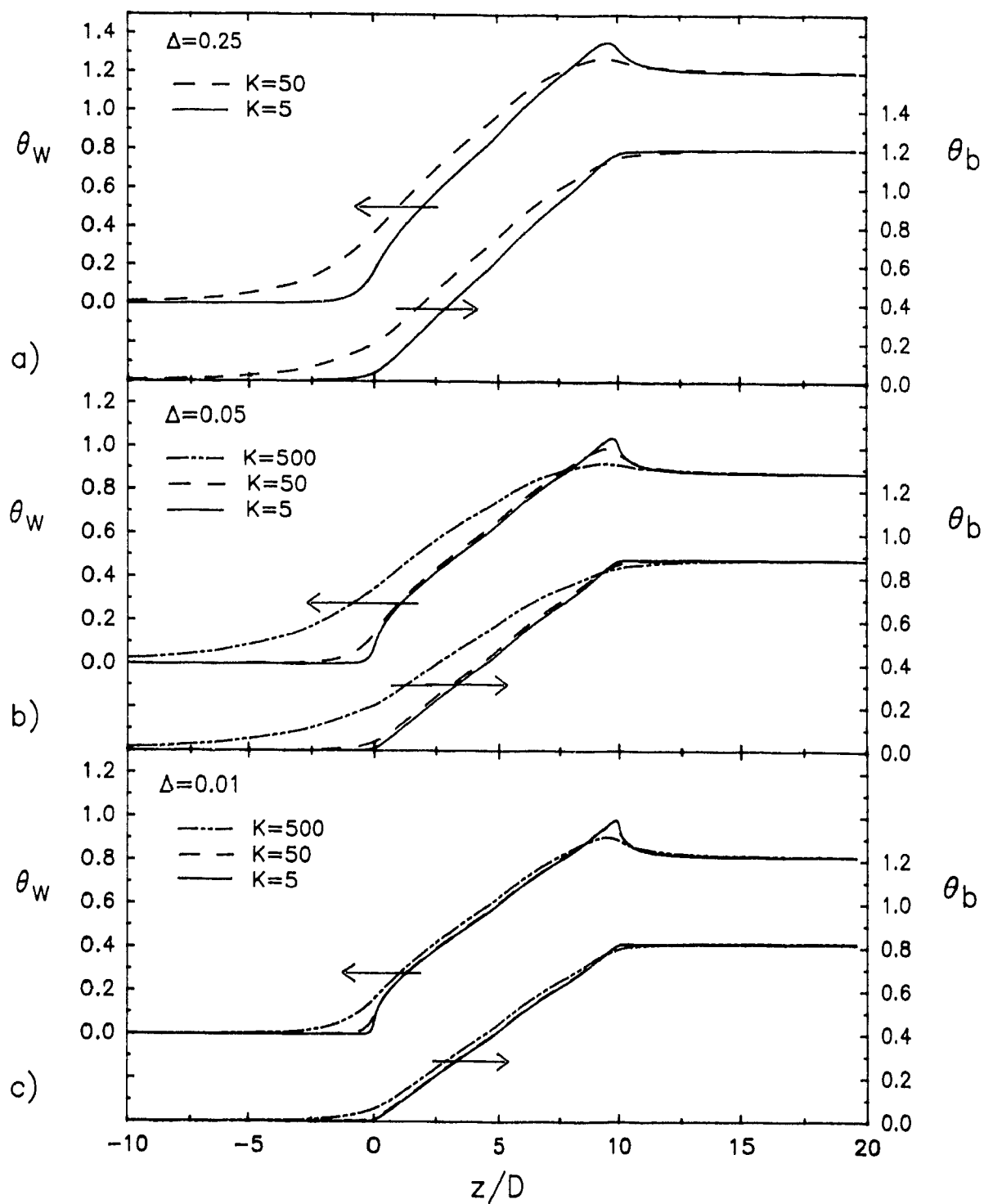


Figure 6.6: Axial variation of θ_w and θ_b for $Gr_q = 5000$, $Re = 10$, $Pe = 5$.

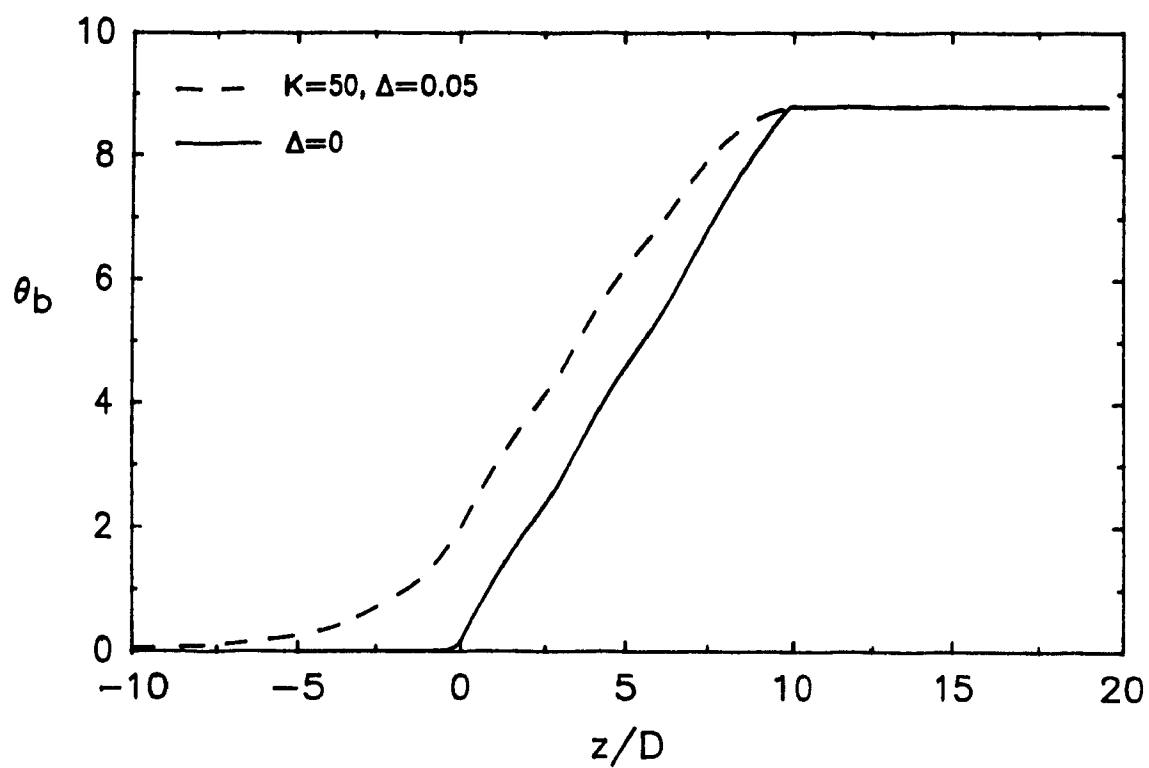


Figure 6.7: Axial variation of θ_b for cases where axial wall conduction is important ($K = 50, \Delta = 0.05$) and where it is non-existent ($\Delta = 0$). $Gr_q = 5000$, $Re = 1$, $Pe = 5$.

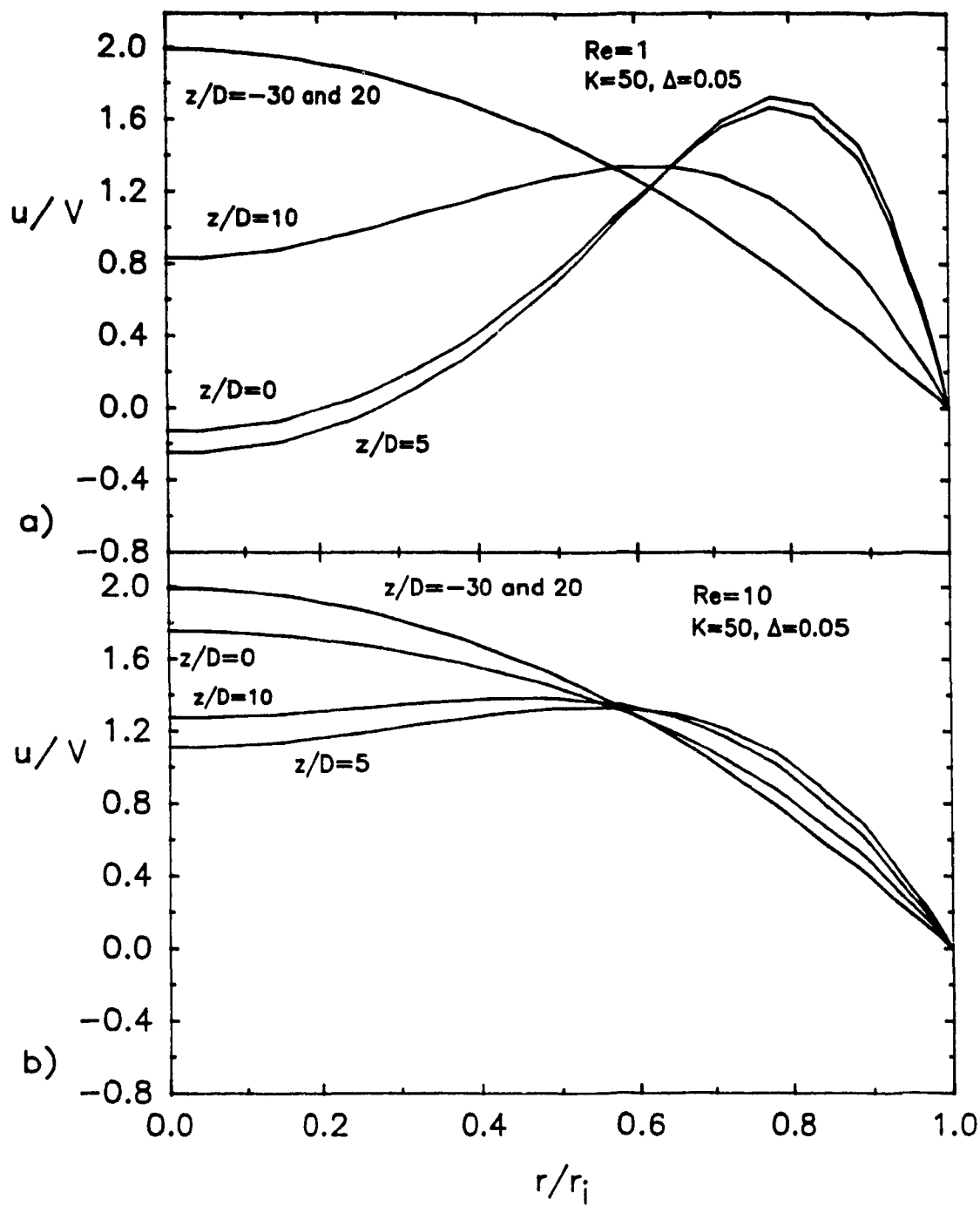


Figure 6.8: Effects of axial conduction in the wall on the velocity profiles at various axial locations for two different Re . $Gr_q = 5000$, $Pr = 5$.

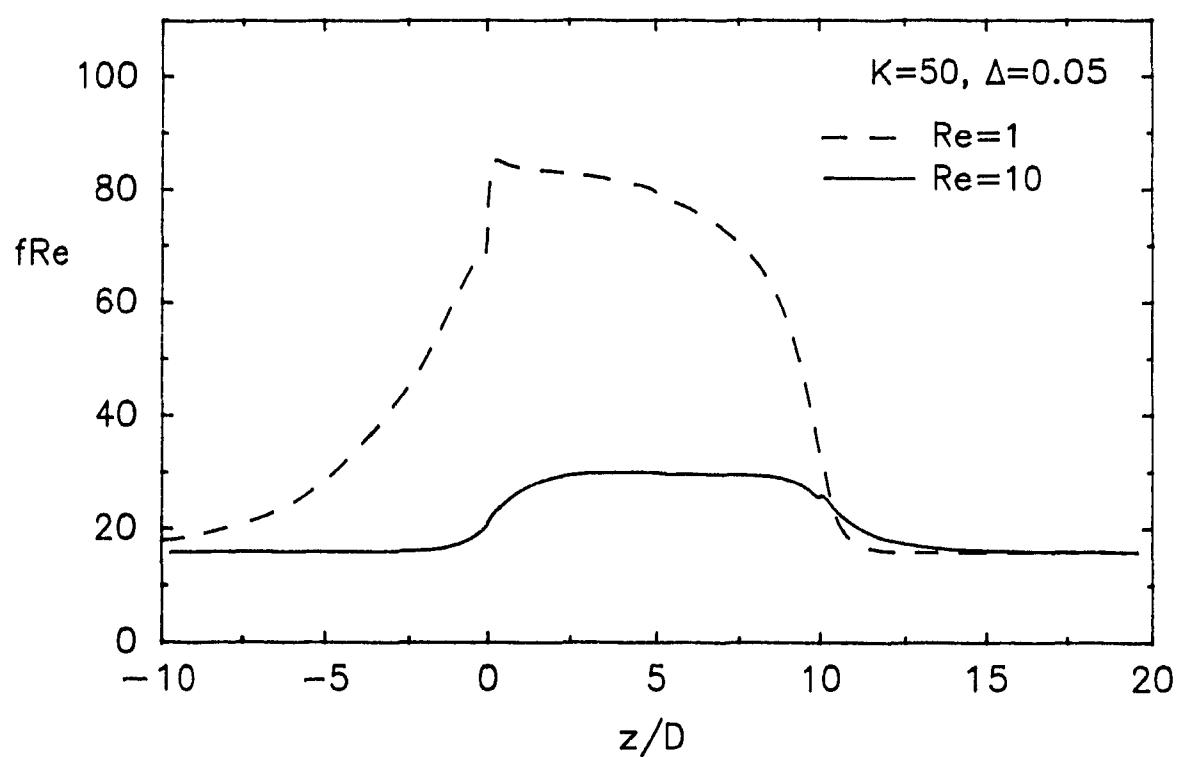


Figure 6.9: Axial variation of the fRe product for two different Re .
 $Gr_q = 5000$, $Pr = 5$.

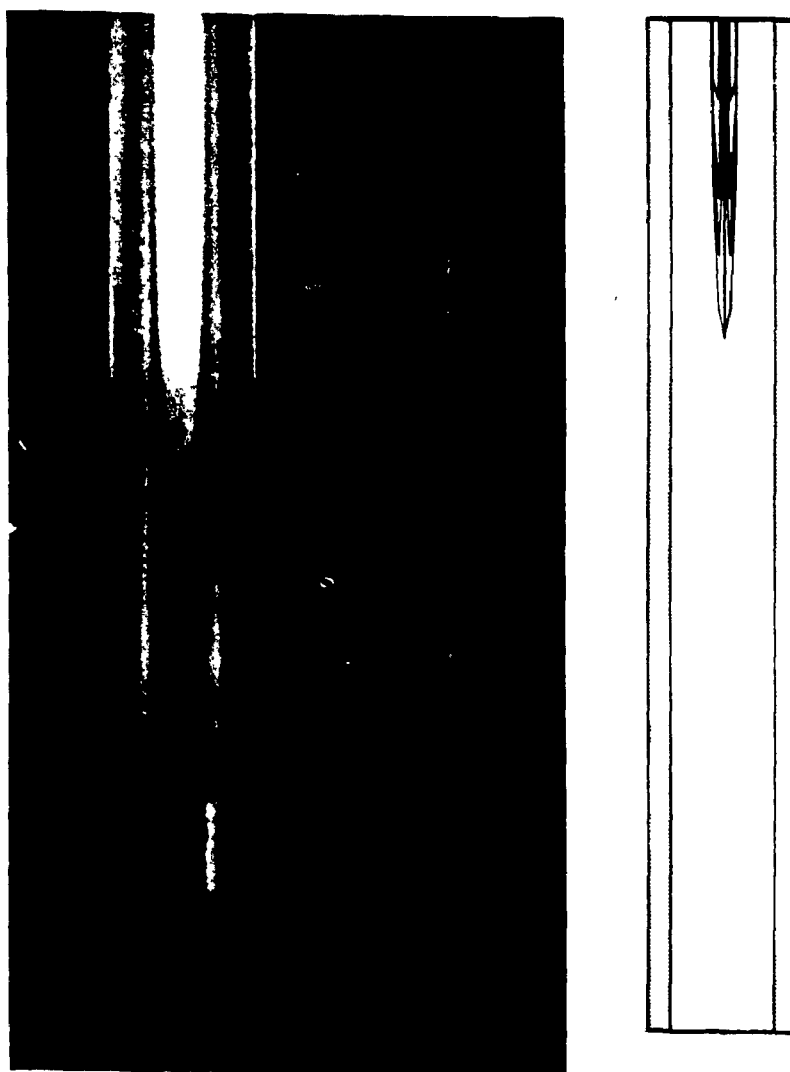


Figure 6.10: Recirculation cell in a mixed-convection flow for $Re = 90$, $Gr_q = 0.33 \times 10^6$, $Pr = 5.6$: (a) flow visualization experiments; (b) corresponding numerical streamlines.

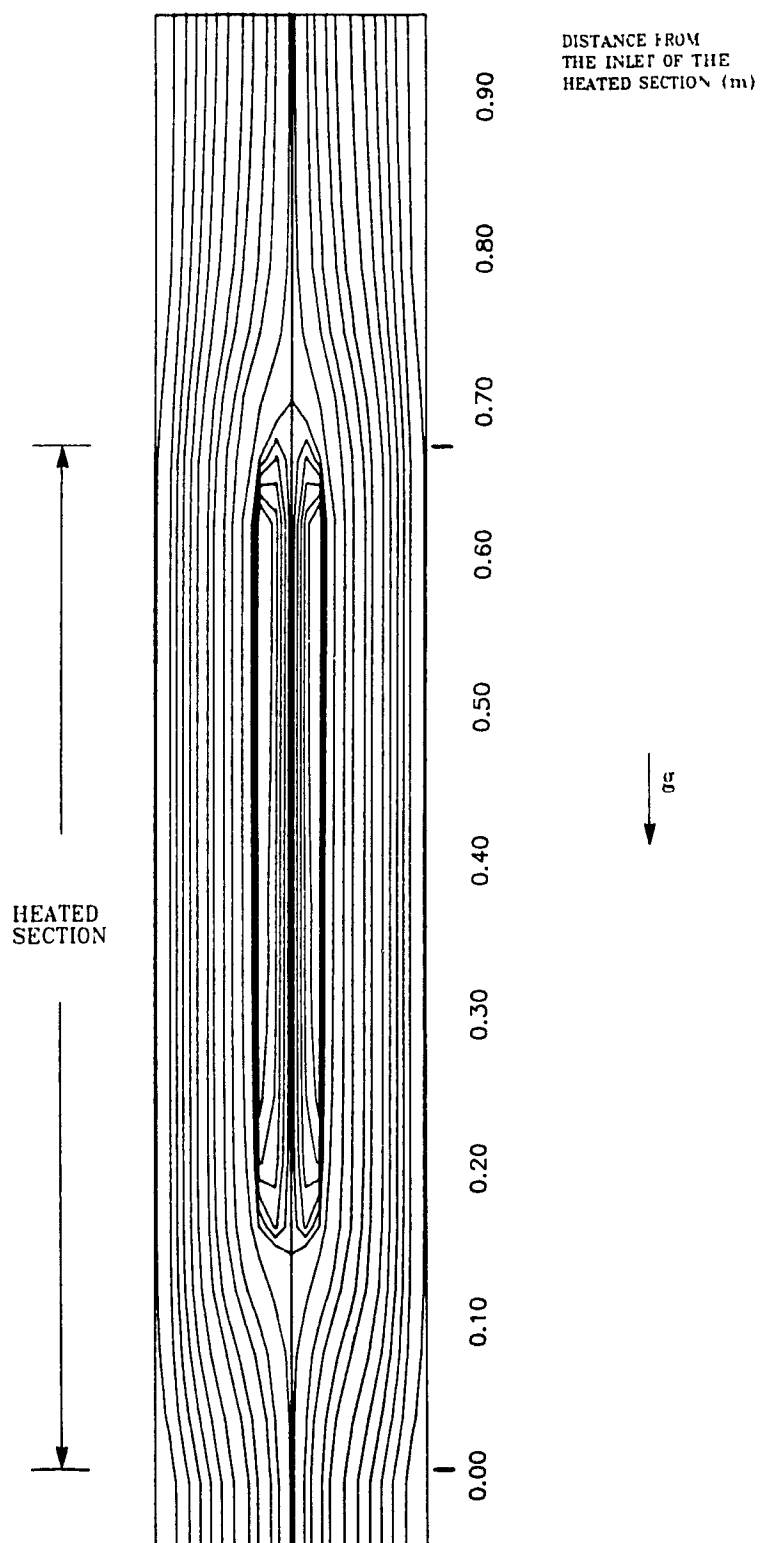


Figure 6.11: Numerically predicted streamlines over the full calculation domain for $Re = 90$, $Gr_q = 0.33 \times 10^6$, $Pr = 5.6$: Note: the scale of the radial direction is 10 times the scale of the axial direction.

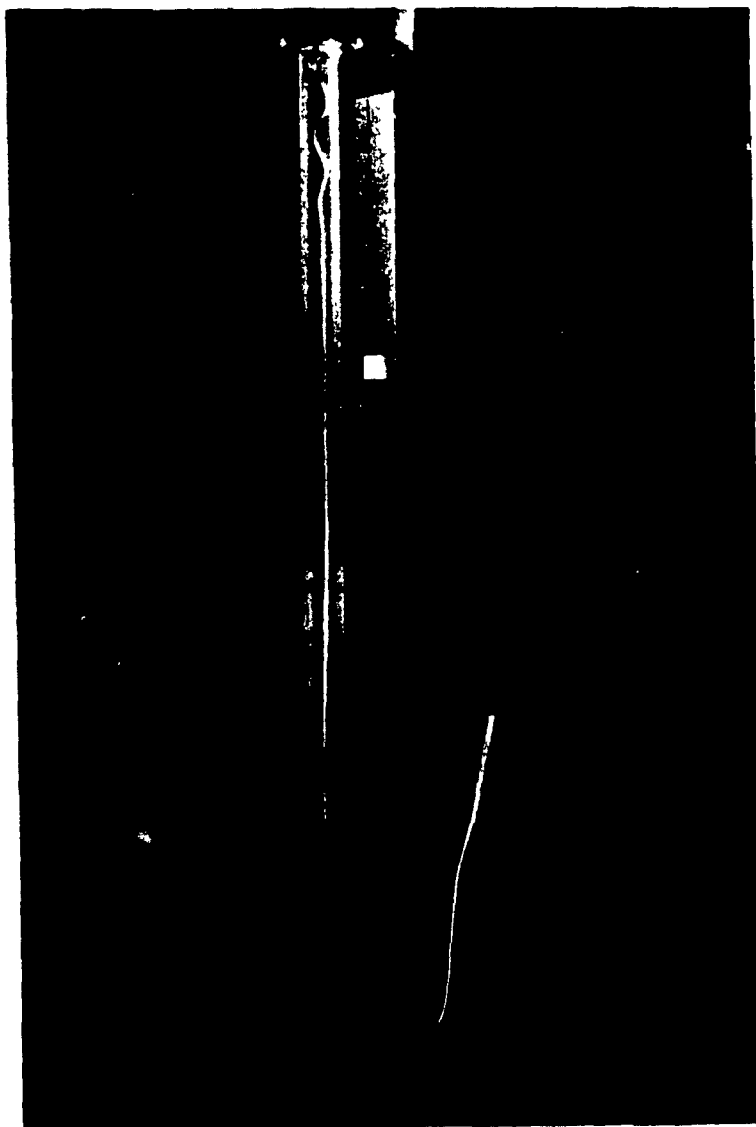


Figure 6.12: Observation of laminar-turbulent transition occurring in a mixed-convection flow for $Re = 72$, $Gr_q = 0.7 \times 10^5$, $Pr = 6.0$. The "x" indicates the start of the transition and is located ≈ 46 cm ($L/D = 25.5$) from the inlet.

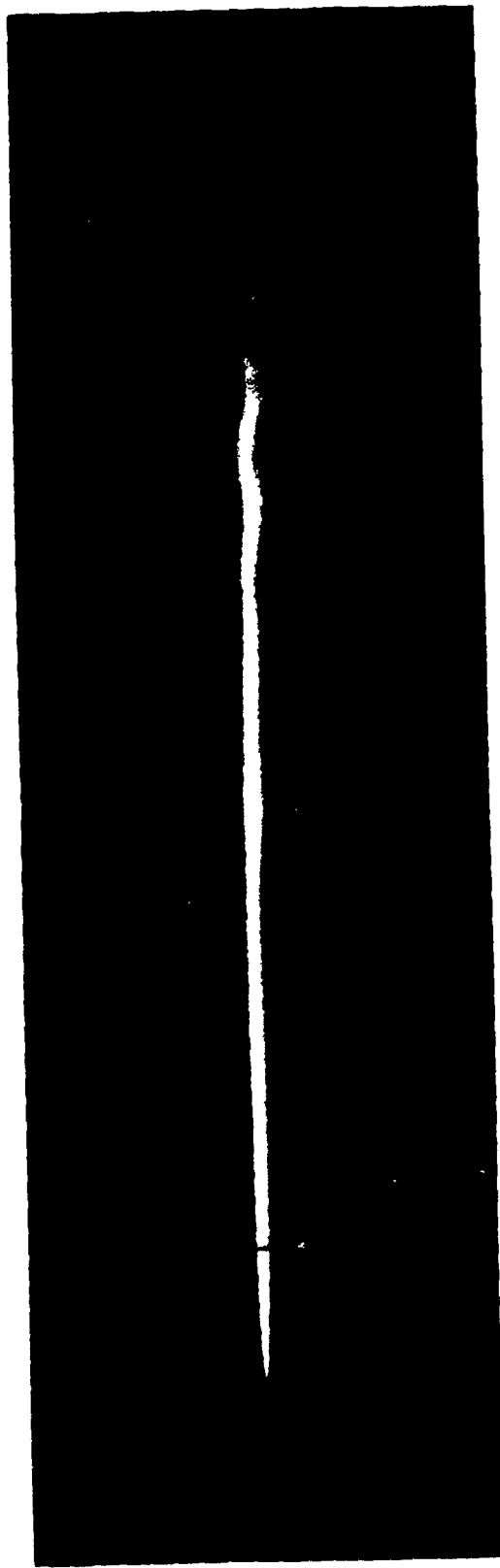


Figure 6.13: Observation of laminar-turbulent transition occurring for $Re \approx 48$, $Gr_q = 0.95 \times 10^5$, $Pr = 6.0$. Transition was noted at a distance of ≈ 50 cm ($L/D = 28$) from the inlet.

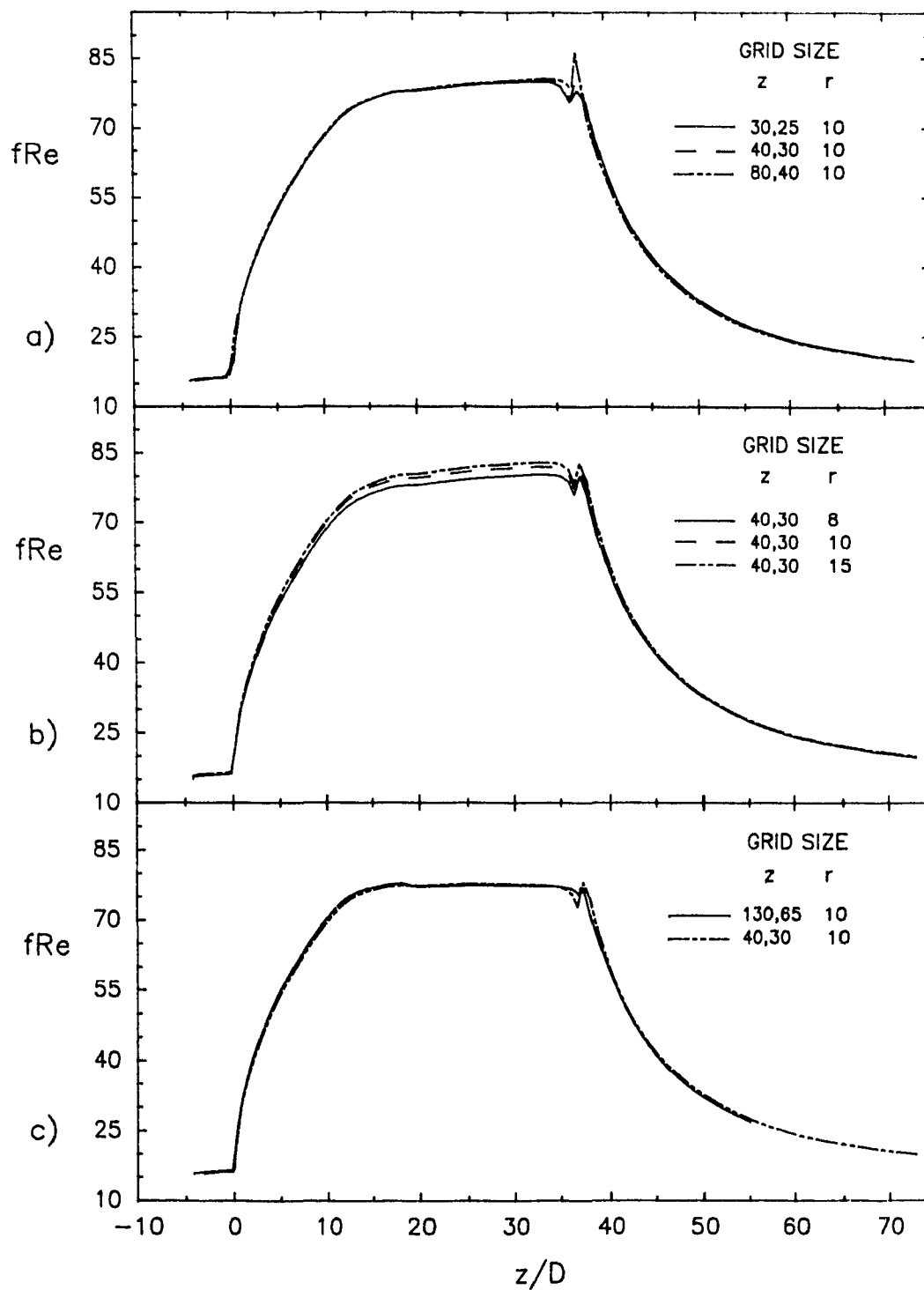


Figure 7.1: Grid independence checks performed for the conditions of experimental run #8. $Gr_m = 5078$, $Re_{ref} = 163.7$, $Pr = 6.8$, $St_m = 0.34 \times 10^{-3}$, and $\phi_\infty = 0.242$.

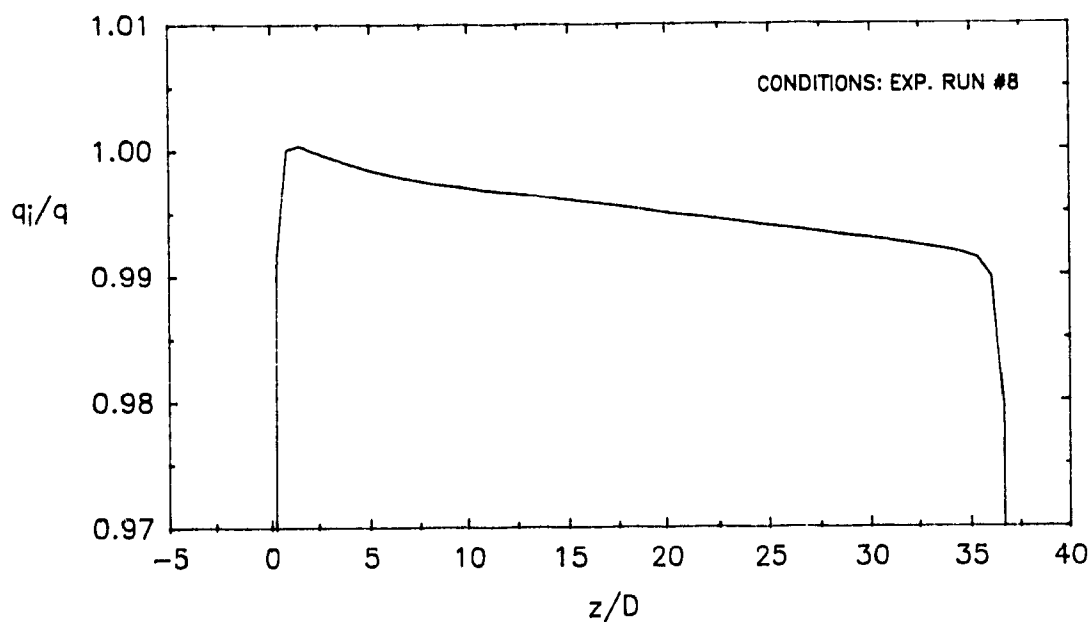


Figure 7.2: Effects of axial wall conduction and heat losses on the interface heat flux. Results of numerical simulations for $Gr_m = 5078$, $Re_{ref} = 163.7$, $Pr = 6.8$, $St_m = 0.34 \times 10^{-3}$, and $\phi_\infty = 0.242$.

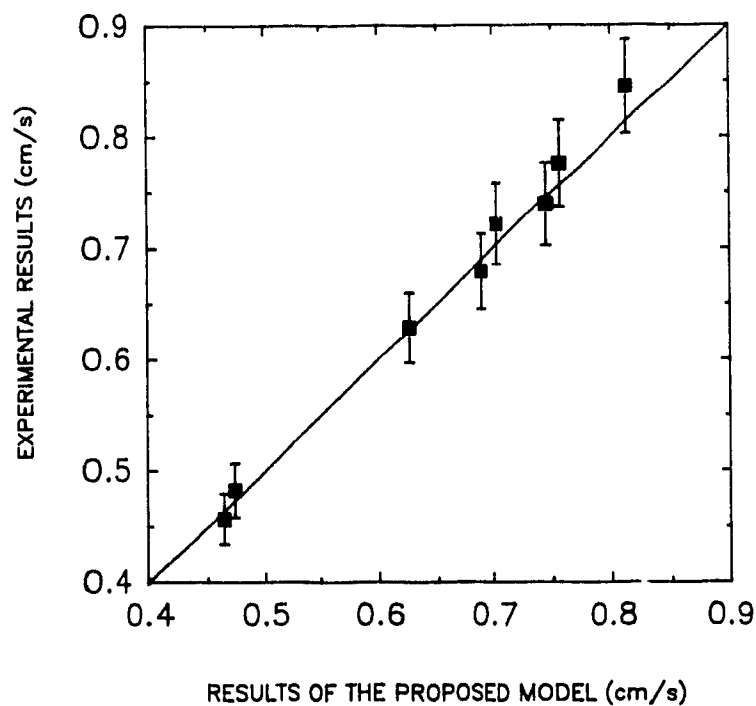


Figure 7.3: Average velocity in the heated section of the closed-loop thermosyphon. Comparison between experimental data and the results of the proposed model.

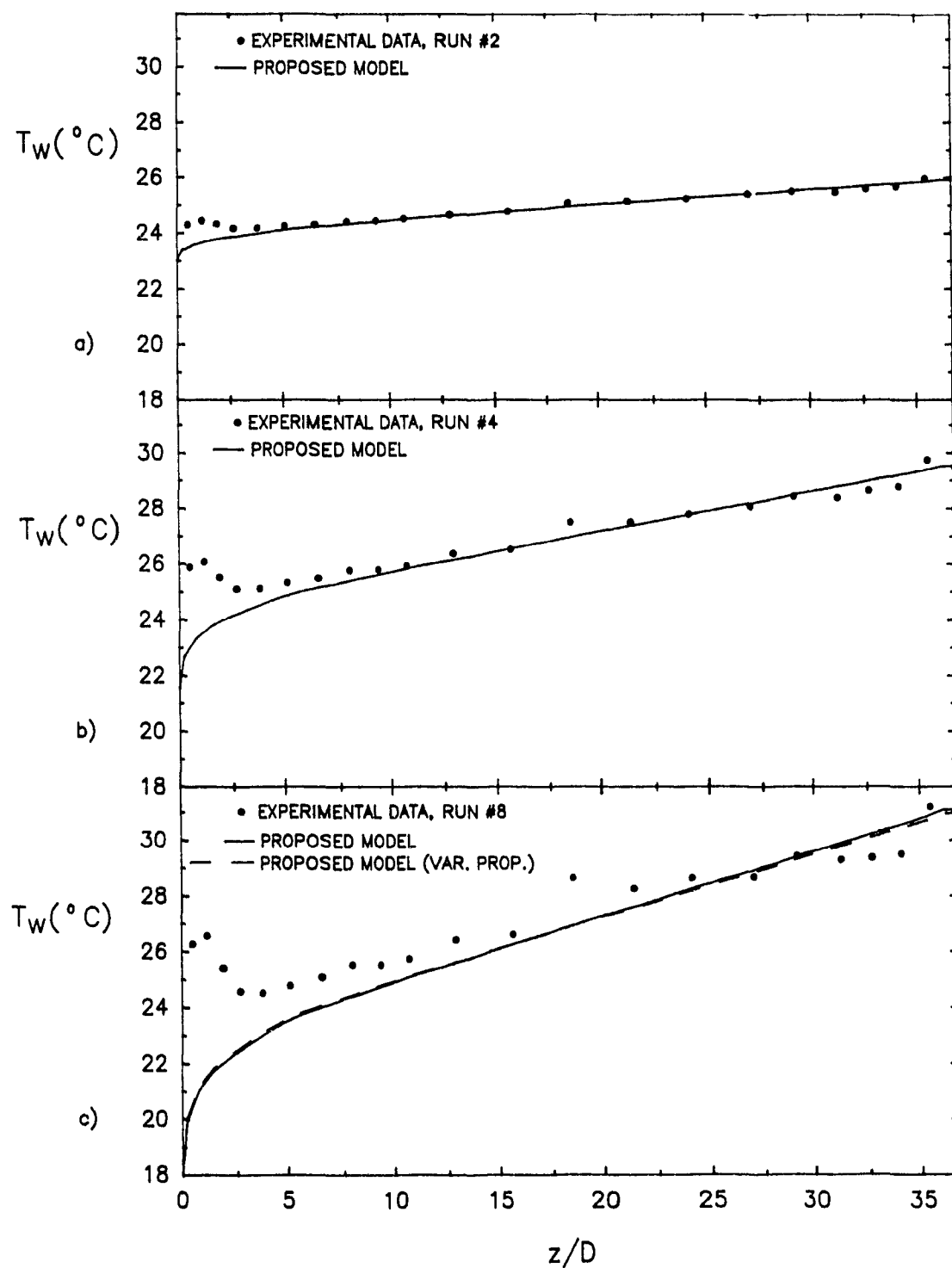


Figure 7.4: Axial variation of wall temperatures in the heated section. Comparison between experimental data and the results of the proposed model.

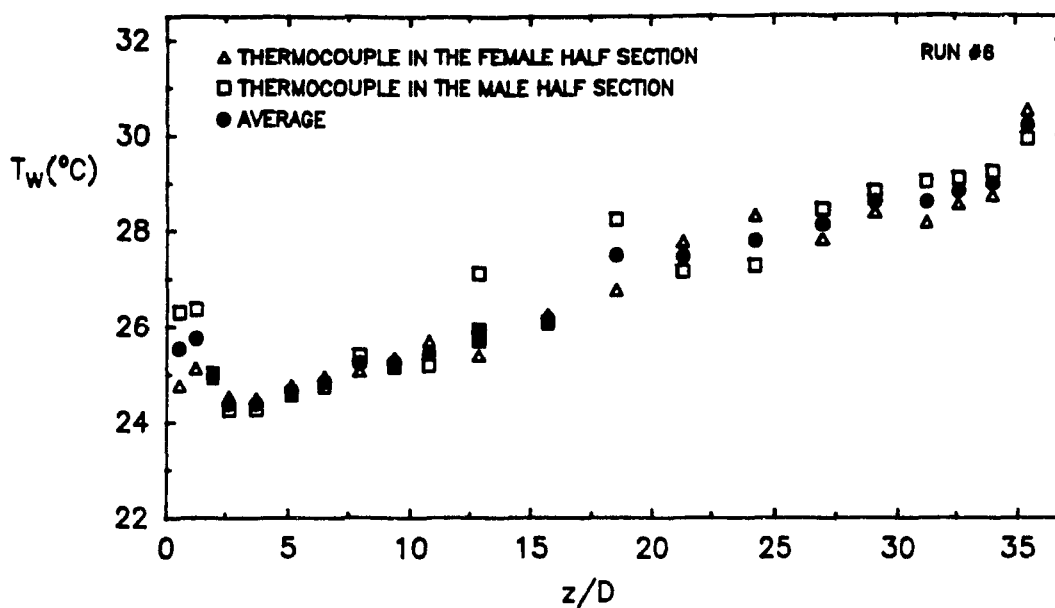


Figure 7.5: Wall temperature measurements in the male and female half sections of the heated section.

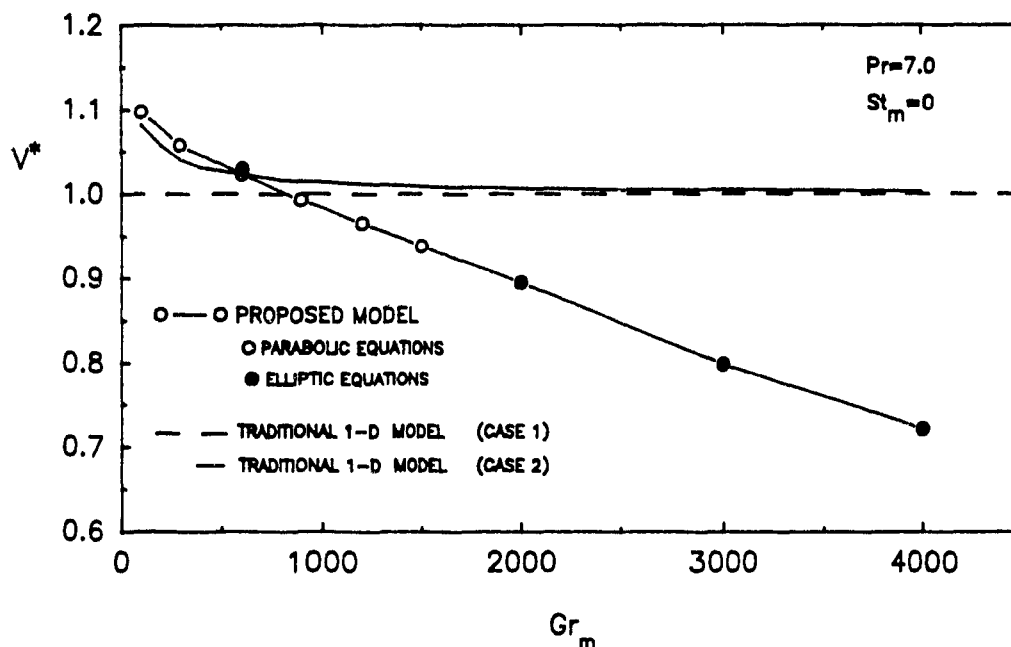


Figure 7.6: Variation of V^* as a function of Gr_m for $St_m = 0$ and $Pr = 7.0$. Comparison between the traditional and proposed models for geometry #2.

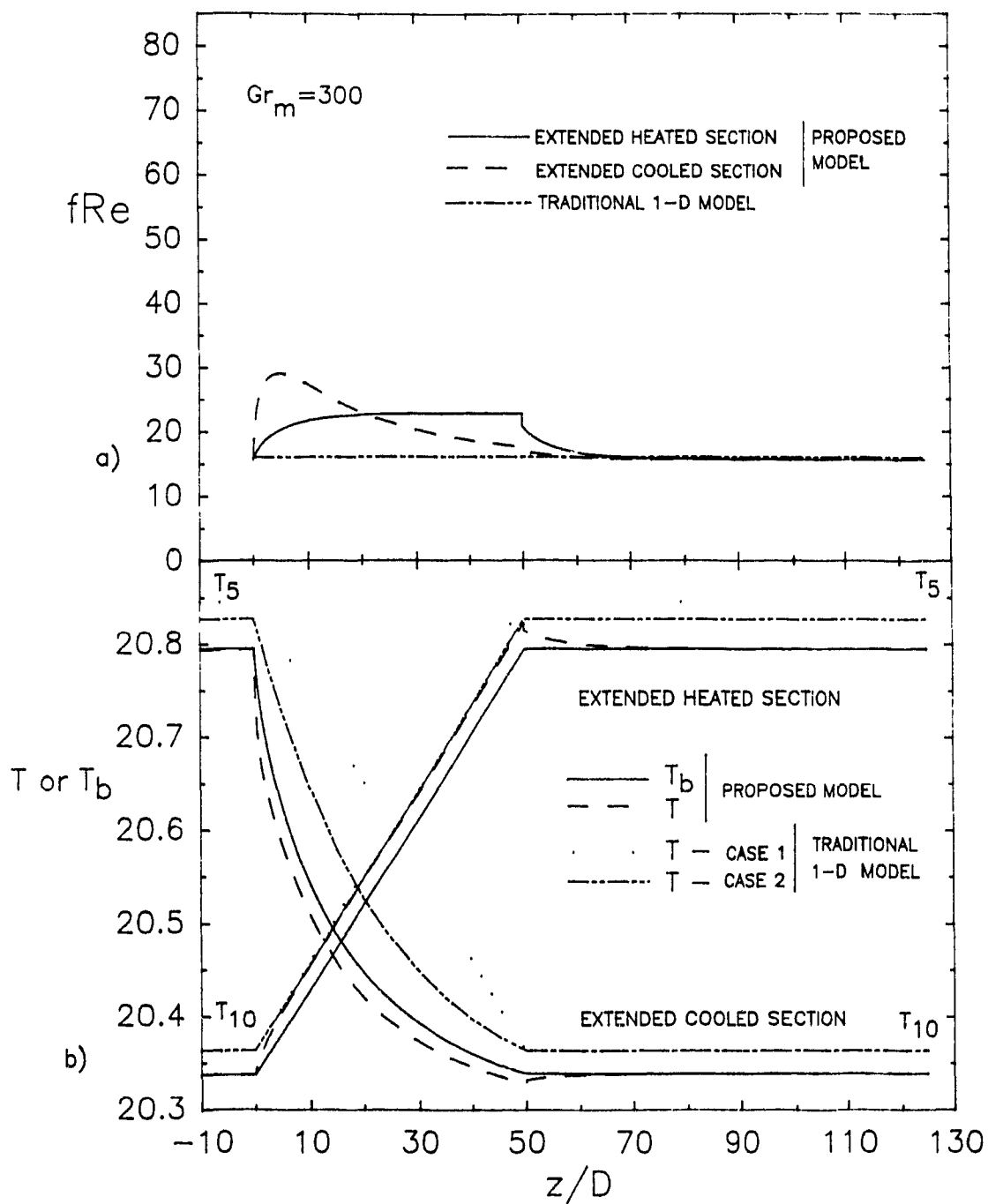


Figure 7.7: Axial variation of fRe , T (area-weighted mean temperature), T_b (velocity-weighted bulk temperature) for $Gr_m = 300$, $St_m = 0$, and $Pr = 7.0$. Comparison between the traditional and proposed models for geometry #2.

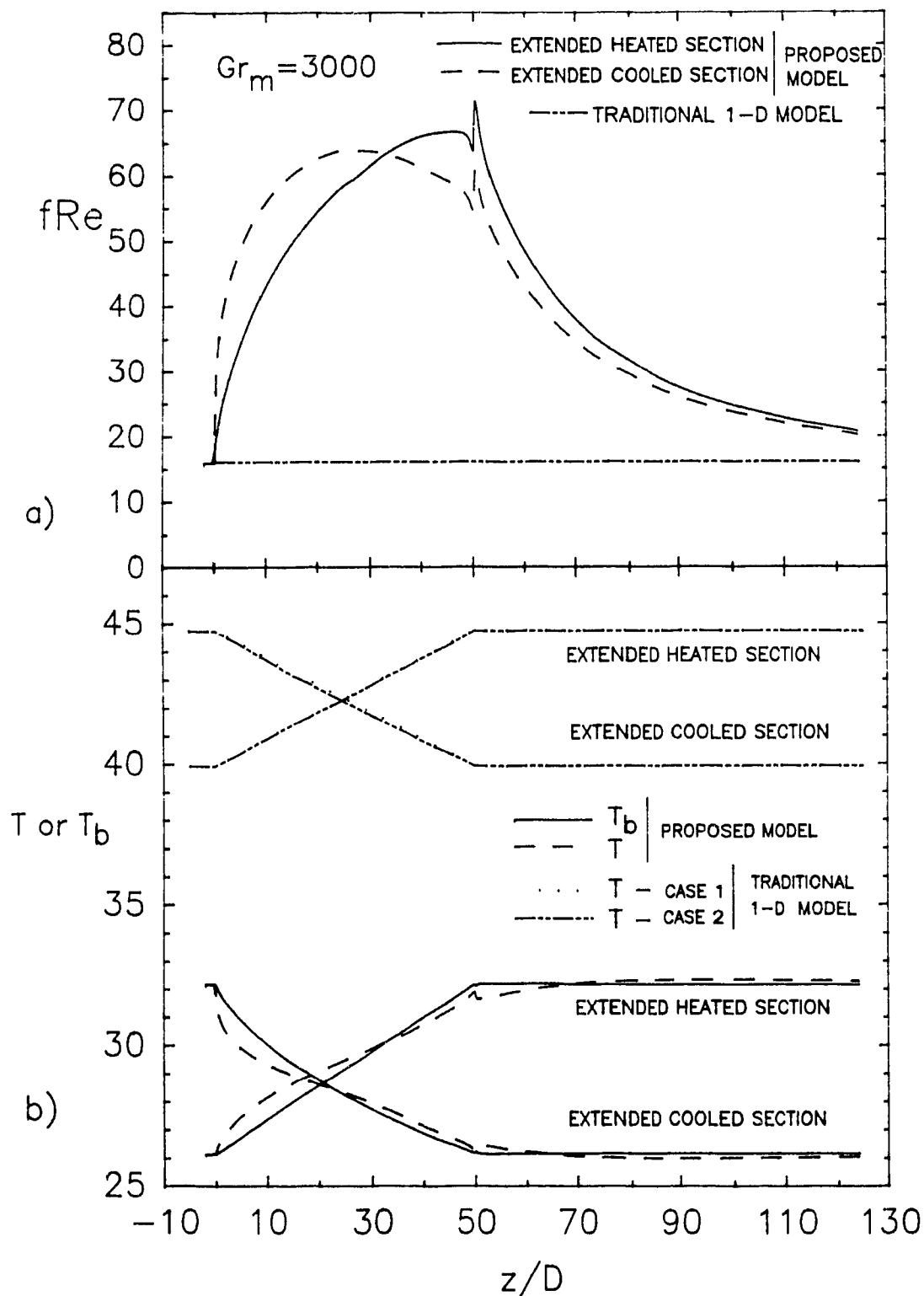


Figure 7.8: Axial variation of fRe , T (area-weighted mean temperature), T_b (velocity-weighted bulk temperature) for $Gr_m = 3000$, $St_m = 0$, and $Pr = 7.0$. Comparison between the traditional and proposed models for geometry #2.

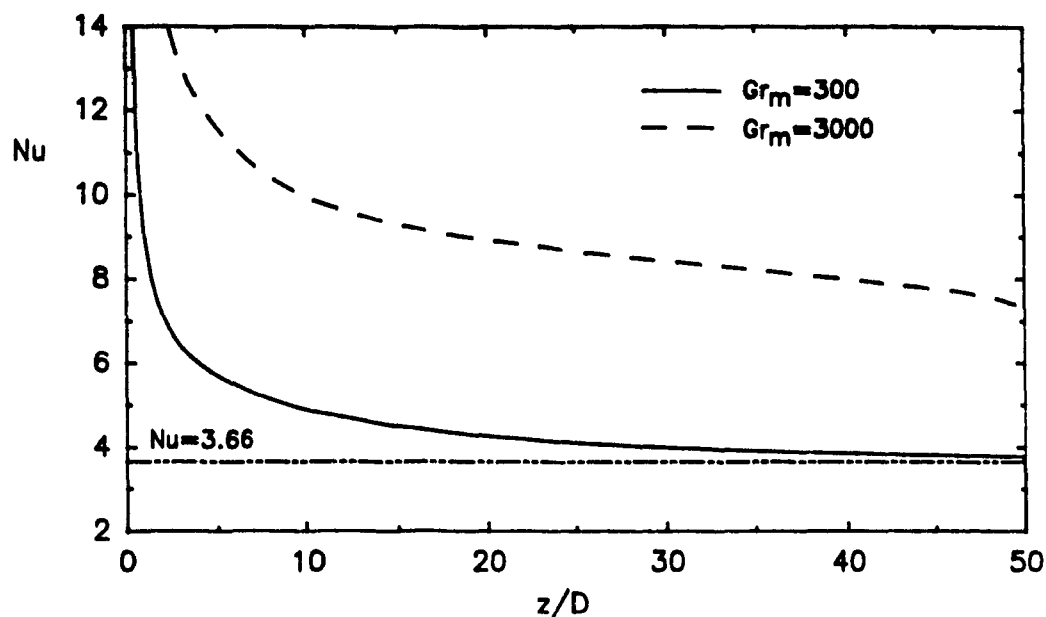


Figure 7.9: Axial variation of Nu in the cooled section of geometry #2. $St_m = 0$ and $Pr = 7.0$.

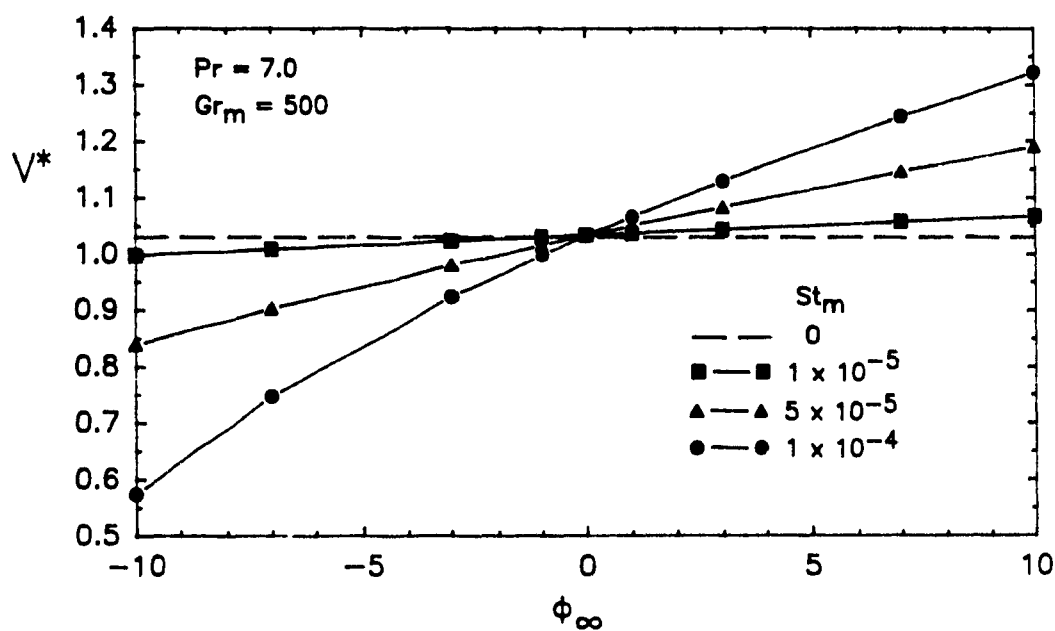


Figure 7.10: Effects of heat losses on V^* as a function of the non-dimensional ambient temperatures, ϕ_∞ , for three different values of St_m . $Gr_m = 500$ and $Pr = 7.0$.




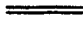
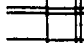
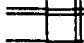
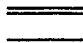

Sample and strip	Initial resistance (Ohms)	Matching	Resistance (after cutting the excess width) (Ohms)	Final † resistance measurement (with electrode) (Ohms)
A-1	265	 flow vis. section no.1	331	 165 (163)
A-2	263		324	
A-3	266		-	
A-4	274		-	
A-5	280	 heated section no.2	349	 171 (172)
A-6	275		-	
A-7	267		-	
A-8	270		-	
B-1	273	 flow vis. section no.2  heated section no.1	-	 156 (156)  178 (176)
B-2	270		311	
B-3	272		310	
B-4	282		340	
B-5	281		352	
B-6	273		339	
B-7	265			
B-8	264			
Average	271.2	† Numbers in brackets indicate the theoretical resistance obtained by connecting the two resistances of the fourth column in parallel		
Maximum difference	+ 4 %			

Table 5.1: Resistance measurements of the gold-film strips taken at various stages of construction.

Type of measurement or device	Manufacturer	Specifications of the manufacturer
4-wire resistance measurement (used during the construction of the heated sections)	Hewlett-Packard multimeter (model 3478A)	(5 1/2 digit mode, ⁺ 300Ω range, 1 year) <u>resolution</u> : 1 mΩ <u>accuracy</u> : ± 56 mΩ [for a 300 Ω meas.]
Data acquisition and control unit with thermocouple multiplexer	Hewlett-Packard (model 3497A)	(5 1/2 digit mode, ⁺ 0.10V range, 1 year) <u>resolution</u> : 1 μV <u>accuracy</u> : ± 3 μV [for V=1.2 mV (~20°C)]
Current in the heated section	Hewlett-Packard multimeter (model 3478A)	(5 1/2 digit mode, ⁺ 3A range, 1 year) <u>resolution</u> : 10 μA <u>accuracy</u> : ± 1 mA [for a 0.5 A meas.]
Voltage across the heated section	Keithley multimeter (model 195A)	(5 1/2 digit mode, ⁺ 300V range, 1 year) <u>resolution</u> : 1 mV <u>accuracy</u> : ± 33 mV [for a 100 V meas.]
DC Power Supply	Sorensen (model DCR300-3B)	<u>Range</u> : 0-300 Volts 0-3 Amps. <u>Drift</u> : (8 hours) 0.3 Volts 4.5 mAmps
⁺ These specifications were checked against a calibrated voltmeter and a standard resistance cell. This verification indicated that these instruments did not have any noticeable bias errors and that the measurements were all well within the accuracy limits quoted by the manufacturer.		

Table 5.2: Specifications of various instruments used in this study.

Gold-film sections	Length [L _h] (m)	Mass of the of the gold-film sections		Water [†] density [ρ] (kg/m ³)	Resulting average internal diameter [D] (mm)
		(empty)	(full)		
		[m _e] (g)	[m _f] (g)		
Heated section no.1	0.682	725.7	903.2	997.5	18.2
Heated section no.2	0.680	732.5	904.3	997.5	18.0
Flow vis. section no.1	0.683	721.7	898.1	997.5	18.2
Flow vis. section no.2	0.681	739.5	917.4	997.5	18.3
$D = \left[\frac{[(m_f - m_e)/\rho]4}{L_h \pi} \right]^{1/2}$				[†] Water temperature during these measurements was 20°C ± 2°C	

Table 5.3: Results of the determination of the average internal diameter of the gold-film sections.

Thermocouple number and half section		Distance from inlet (m)
male	female	
T01	T02	0.0095
T03	T04	0.0220
T05	T06	0.0350
T07	T08	0.0475
T09	T10	0.0665
T11	T12	0.0920
T13	T14	0.1175
T15	T16	0.1430
T17	T18	0.1685
T19	T20	0.1940
T21 *	T22 *	0.2320
T23	T24	0.2825
T25	T26	0.3335
T27	T28	0.3840
T29	T30	0.4350
T31	T32	0.4868
T33	T34	0.5240
T35	T36	0.5620
T37	T38	0.5875
T39	T40	0.6130
T41	T42	0.6330
T47 *	T48 *	0.2320
T49 *	T50 *	0.2320
* These 6 thermocouples are positioned 60° apart at the same axial location		

Table 5.4: Axial location of each thermocouple inside heated section no.2.

Geometry #1 (corresponds to the dimensions of the experimental apparatus)		Geometry #2	
$D = 2r_i = 0.018$ (in the heated section)		$D = 0.02 \text{ m}$	
$L_1 = 0.165 \text{ m}$	$L_1/D = 9.2$	$L_1 = 0.50 \text{ m}$	$L_1/D = 25.0$
$L_2 = 0.707 \text{ m}$	$L_2/D = 39.3$	$L_2 = 0.50 \text{ m}$	$L_2/D = 25.0$
$L_3 = 0.664 \text{ m}$	$L_3/D = 36.9$	$L_3 = 1.00 \text{ m}$	$L_3/D = 50.0$
$L_4 = 0.664 \text{ m}$	$L_4/D = 36.9$	$L_4 = 1.50 \text{ m}$	$L_4/D = 75.0$
$L_5 = 0.047 \text{ m}$	$L_5/D = 2.61$	$L_5 = 1.50 \text{ m}$	$L_5/D = 75.0$
$L_7 = 0.443 \text{ m}$	$L_7/D = 24.6$	$L_7 = 1.00 \text{ m}$	$L_7/D = 50.0$
$L_8 = 0.612 \text{ m}$	$L_8/D = 34.0$	$L_8 = 1.00 \text{ m}$	$L_8/D = 50.0$
$L_9 = 0.612 \text{ m}$	$L_9/D = 34.0$	$L_9 = 1.50 \text{ m}$	$L_9/D = 75.0$
$L_{10} = 0.580 \text{ m}$	$L_{10}/D = 32.2$	$L_{10} = 1.50 \text{ m}$	$L_{10}/D = 75.0$
$R = 0.265 \text{ m}$	$R/D = 14.7$	$R = 0.2 \text{ m}$	$R/D = 10.0$
$L = 6.16 \text{ m}$	$L/D = 342.2$	$L = 11.26 \text{ m}$	$L/D = 563.0$
$\Delta Z = 0.294 \text{ m}$		$\Delta Z = 2.00 \text{ m}$	

Table 7.1: Dimensional and non-dimensional lengths related to geometries #1 and #2.

Run #	Power input (Watts)	Experimental data		Proposed Model	
		Measured velocities (cm/s)	Uncertainty (cm/s)	Constant properties (cm/s)	Variable properties (cm/s)
1	9.97	0.483	± 0.024	0.473	0.472
2	9.83	0.457	± 0.023	0.465	0.464
3	25.18	0.628	± 0.031	0.626	0.623
4	39.84	0.722	± 0.036	0.704	0.699
5	39.89	0.679	± 0.034	0.690	0.683
6	54.83	0.776	± 0.039	0.756	0.748
7	54.80	0.739	± 0.037	0.746	0.737
8	74.58	0.845	± 0.042	0.814	0.803

Table 7.2: Summary of the average velocities measured experimentally and determined using the proposed model.

$Gr_m = 300$	T_{hot} (°C)	T_{cold} (°C)	$T_{hot} - T_{cold}$ (K)	\overline{fRe}	v^*
Traditional 1-D model Case 1	20.701	20.508	0.193	16	1.00
Traditional 1-D model Case 2	20.688	20.487	0.201	16	1.041
Proposed Model	20.664	20.447	0.217	17.11	1.055

Table 7.3: Summary of average hot and cold side temperatures and average frictional resistance obtained with the traditional one-dimensional model and the proposed model for $Gr_m = 300$.

$Gr_m = 3000$	T_{hot} (°C)	T_{cold} (°C)	$T_{hot} - T_{cold}$ (K)	\overline{fRe}	v^*
Traditional 1-D model Case 1	43.304	41.374	1.93	16	1.00
Traditional 1-D model Case 2	43.285	41.349	1.94	16	1.005
Proposed Model	30.739	28.095	2.64	27.43	0.799

Table 7.4: Summary of average hot and cold side temperatures and average frictional resistance obtained with the traditional one-dimensional model and the proposed model for $Gr_m = 3000$.

$Gr_m = 500$	Q_L/P_w	T_{hot} (°C)	T_{cold} (°C)	$T_{hot} - T_{cold}$ (K)	\overline{fRe}	v^*
$St_m = 0$	0	21.019	20.650	0.369	17.86	1.030
$\phi_\infty = 10$ $St_m = 1 \times 10^{-4}$	1.23	21.547	21.064	0.482	18.24	1.317
$\phi_\infty = -10$ $St_m = 1 \times 10^{-4}$	-1.27	20.196	20.004	0.193	16.81	0.571

Table 7.5: Summary of average hot and cold side temperatures and average frictional resistance obtained with the proposed model for three different heat losses (gains) conditions.